

2014 NSF/REU

**RESEARCH EXPERIENCE
FOR UNDERGRADUATES
IN PHYSICS**



Notre Dame Science
The College of Science at the University of Notre Dame

STUDENT RESEARCH PAPERS

VOLUME 25



REU DIRECTOR UMESH GARG, PH.D.

REU Student Research Papers – Summer 2014
University of Notre Dame – Department of Physics

Student	Research Title	Page No.
Luis Abrego National Autonomous University of Mexico	Characterization of Thin Foils as Target Materials for Nuclear Reactions	1
Emily Bell Monmouth College	Plasmid DNA Damage Induced by Helium and Oxygen Atmospheric Pressure Plasma Jet	11
Ian Broderick University of Notre Dame	CMS Upgrades	21
Guillermo Bustos Ramírez University of Guanajuato	Simulation of a Gas Cell to Stop Radioactive TWINSOL Beams	31
Devon Courtwright Norfolk State University	Investigation into Anisotropic Nature of Ferromagnetic Resonance in Fe-GaMnAs	43
Patrick Fasano University of Notre Dame	Modernizing Plunger Control with Low-Cost Digital Electronics	53
Michelle Gervais University of Wisconsin Eau Clair	Alignment Sensitivity Study of the St. ANA Beam Line	63
Ben Guerin University of Notre Dame	Graphitization Line for AMS Measurement of Carbon-14	73
Zeyu Hao Xi'an Jiaotong University	Gamma-ray Burst Analysis in Project GRAND and Flare Seeking in UW Crb	81
Kevin Howard Canisius College	Study of the Pure Double Folding Optical Model for 100 MeV/u Deuteron Scattering	91
Patricia Huestis Missouri University of Science & Technology	Modal Noise Mitigation in Optical Fibers with Small Circular Diameters	101
Lee Hyatt Furman University	Modeling the Accretion and Feedback Processes of Galaxies Similar to the Milky Way	111
Yi Jia Xi'an Jiaotong University	Beamline optimization for Long Baseline Neutrino Experiment	121
Timothy Khouw University of Notre Dame	The Notre Dame Nuclear Database: Nuclear Data Made Easily Accessible	131
Samantha Koutsares Old Dominion University	Search for Higgs Bosons Produced in Association with Top-Quark Pairs and Decaying to Hadronic Taus	141
Allan Leishman Kent State University	GRAS _{ANS} P Multi-File Fitter: A User's Guide	153
Chuanhong Liu Xi'an Jiaotong University	Search for Gamma-Ray Sources from a Measurement of the Muon Angular Distribution with High Statistics	163
Marcus Lowe University of Wisconsin La Crosse	Measurements of Internal Conversion Electron Emission Cross-Sections for ¹⁵⁴ Gd, ¹⁵⁶ Gd, ¹⁵⁷ Gd	173
Catie Luck Thomas More College	Damage of DNA by Helium and Oxygen Atmospheric Pressure Plasma Jet	183
Mitch McNanna University of Notre Dame	Natural Orbitals for a Two-Particle System in One Dimension as a Testbed for Use in the Nuclear Many-Body Problem	193

Student	Research Title	Page No.
Patrick Moran Temple University	Search for a Higgs-Top Quark Pairing in the Opposite-Charged Dilepton Channel	203
Emily Morgan University of Notre Dame	Analyzing Deuteron Scattering at 100 MeV/u Through Optical Model Parameters	213
Catherine Nicoloff Wellesley College	Simulating a Multi-Reflection Time-of-Flight Mass Spectrograph for the Purification of Radioactive Isobars	225
Marina Paggen University of Texas El Paso	Filaments: Understanding the Math that Defines Them	235
Lindsey Riordan Northern Arizona University	Graphitization Line for AMS Measurement of Carbon-14	73
Adrián Rivera Torres University of Puerto Rico	Fluid Dynamics - From Helping Messi Goal to Modeling the Evolution of a Galaxy	247
Jason Saroni University of Notre Dame	Analysis of Schematic One-Level and Two-Level Nuclear Shell Models	257
Ethan Sauer University of Notre Dame	Implementation of OpenACC for GPU Acceleration of Astrophysical Fluid Dynamics Code	267
James St. Germaine-Fuller Grinnell College	Coupling Algorithm for Sp(3,R) Irreducible Representations	277
Daniel Votaw James Madison University	Finding Optimal Parameters for Use of Position-Sensitive Ionization Chamber	289
André Wilson Morehouse College	High Purity Germanium Detectors and Angular Distribution of $^{27}\text{Al}(p,\gamma)^{28}\text{Si}$	299

Characterization of thin foils as target materials for nuclear reactions

Luis Abrego

2014 NSF/REU Program

Department of Physics, University of Notre Dame

Advisors: Ani Aprahamian, Khachatur Manukyan

Abstract

An accurate measurement of thickness of targets is crucial for the study of nuclear reactions, specifically in determining the absolute cross section for a given reaction. Existing methods show some strengths and limitations. One of the most standard ways of measuring target thickness is by the loss of energy of alpha particles produced by an accelerator. My project this summer was focused on introducing a new method from material science to measure target thicknesses. We focused on the application of an ion beam coupled to a scanning electron microscope (FIB/SEM). This instrument has taken its place in several fields as a standard method due to its versatility to characterizing materials with high resolution; here we apply it to a more precise determination of target thickness to use in reducing the errors in measuring nuclear cross sections due to target thickness. Focused ion beam instrument from the Notre Dame Integrated Imaging Facility (NDIIF: a general facility available in the colleges of Engineering and Science at ND) is used to determine the geometrical thickness of thin self-supporting film targets. We compared thicknesses obtained by energy loss measurements of alpha particles from a radioactive source with energies of 3.183MeV (^{148}Gd) and 5.486MeV (^{241}Am); discrepancies will be discussed with the energy loss method. Future investigations include comparisons with Rutherford scattering and the use of well known resonances.

1. Introduction

Cross section data provides parameters such as radioisotopes production yield for a particular reaction type or determines the particle energies and optimal energy ranges required. Particularly, to gain a better understanding on the astrophysical fusion and fission processes, experimental cross sections for particle-induced nuclear reactions are needed. It is shown that an accurate determination of number of atoms per unit area is mandatory [1, 2] by definition, which means that an accurate target thickness measurement plays an important role for determining absolute cross sections.

Some authors have published cross section data with systematic uncertainties that contribute up to the 20% [3, 4] arguing this dependence lies in the thickness, which is experimentally obtained, as such, it is imperative to seek for new ways to determine it.

In the last century, several methods were proposed [5-8] and those are being used currently, but as in any case, each technique has its strengths and limitations. Namely, measurements based on the determination of the weight and area by the means of a microbalance and optical microscope are done. This technique is widely used but it has been argued that it is highly sensitive and does not permit the identification of the surface contaminations, which could influence the foil thickness and could contribute to increase the

thickness of a pure sample. Additionally, this method is not able to characterize the roughness of the sample, which leads to some discrepancies in the cross section measured.

Other methods, such as energy loss of charged particles and Rutherford Backscattering Spectrometry (RBS) are used. Both require knowledge of stopping powers for given energies, which are typically obtained either experimentally or are taken from tables [9]. Then, an important source of error is the uncertainty on stopping powers, which increases gradually at greater thickness, and then approximations must be done [2,10]. Furthermore, in the both methods the depth resolution is limited by the energy straggling of the incident beam. To quantify these limits, the energy straggling must be known. However, there is a lack of energy straggling data for alpha particles. Moreover, the former method does not provide information about uniformity and composition of the sample of interest, but provides an average thickness of certain area of study, while the latter provides additional information about the composition which can be useful to identify contaminated samples with a high resolution. In spite of that fact, this method presents problems in some cases e.g. when ${}^6\text{Li}$ target is used with alpha ion beam, since the alpha-deuteron clustering of ${}^6\text{Li}$ causes deviations from Coulomb scattering below the Coulomb barrier of this system.

Since a complete characterization of the target which are used by nuclear experiments is of vital importance, as can be seen, we have pioneered the Focused Ion Beam Technique, which allows us to observe a sample from a wide range of magnifications while imaging, mapping any virtually region of interest, with the ability to prepare site-specific cross-sections by milling, which permits to observe in-situ subsurface microstructures, independent of the material [11].

The present report will discuss measurements of geometrical thicknesses of a wide range of thin foils made by different techniques using Focused Ion Beam Technique and energy loss of alpha particles, with the aim of seeking the feasibility of this method to determine thickness of thin foils used in nuclear reactions.

2. Experimental

2.1. Preparation of Target Foils

Different targets were obtained by either a commercial supplier, were prepared by evaporation in high vacuum or were rolled. In table 2.1 it is summarized the data according to the samples both self-supported and supported with the method of preparation.

Particularly, carbon films served as backing for evaporation of LiF, and CaF₂. As specified, three different areal densities were used; the estimation of the thickness is given by the supplier.

All the samples were supported by an aluminum frame which had an opening of 10.4 cm diameter. Additionally, in next sections we will refer to carbon of 20 ug/cm² and 60 ug/cm² as C-20 and C-60, respectively.

Table 2.1. Preparation of used thin foils, with the analysis done: energy loss of alpha particles and FIB/SEM

Target/Backing		Preparation	Alpha Energy Loss	Microscopy (FIB/SEM)
Self-Supported targets	Carbon	20 ug/cm ²	Purchased	○
		60 ug/cm ²	Purchased	○
	Aluminum	Purchased	○	
	Tin	Purchased	○	
	Samarium	Rolled foil	○	○
	Platinum	Rolled foil	○	○
	Copper	Purchased	○	
	Gold	Purchased	○	○
Supported targets	⁶ LiF /Carbon (20 ug/cm ²)		Evaporation	○
	⁶ LiF/ Carbon (60 ug/cm ²)		Evaporation	○
	CaF ₂ / Carbon	10 ug/cm ²	Evaporation	○
		20 ug/cm ²	Evaporation	○
		60 ug/cm ²	Evaporation	○

2.2. Energy loss of alpha particles

When a fast ion passes through the matter, it loses energy by the means of electronic and nuclear interactions with atoms of the target, which gives to the ion a definite range of penetration. This stopping of high velocity light ions, such as alpha particles in matter, is commonly given in terms of the stopping power S , i.e. the energy loss per amount of material in units of $\text{keV} \cdot \text{ug}^{-1} \text{cm}^2$, which is a function of the composition of the target, the atomic mass and energy of the ion.

Commonly, an initially monoenergetic beam is used. After going through the target, it is shown a spreading in its distribution of energy, instead of a delta-like function due to individual collisions with atoms, which undergo small-angle scatterings, making path length differences in outgoing paths. As a consequence, it is observed a Gaussian-like distribution with its peak of the mean energy shifts down by the mean energy loss and peak width δE . The characterization of the distribution of energy loss depends mainly in the stopping power and energy straggling.

For thin absorbers, we can use the approximation of first order for the energy of the ion [2, 10].

Letting $\lim_{\Delta x \rightarrow 0} \frac{\Delta E}{\Delta x} \equiv \frac{dE}{dx}(E)$ and regarding x as a function of E , it is straightforward getting the thickness integrating dx , from E to some initial energy E_0 and replacing $\left(\frac{dE}{dx}\right)^{-1}$ by its value at the energy E_0 because for regions near the surface x is small, in this way $\left(\frac{dE}{dx}\right)$ remains almost constant (surface mean energy approximation).

$$x = (E_0 - E) \left(\frac{dE}{dx}\right)^{-1} \Big|_{E_0} \quad (2.1)$$

Thus, the stopping power is defined by $S = -\left(\frac{dE}{\rho dx}\right) \Big|_{E_0}$ which is obtained theoretically by the well known Bethe-Bloch's formula and it is found typically in tables [9]

Hence, the energy loss when an ion reaches a transversal distance is expressed by $\Delta E = (\rho\Delta x) S$. Therefore, by determining the energies of alpha particles from radioactive sources before and after transmission through thin films it is possible to determine the thickness $\rho\Delta x$ in units of $\mu\text{g}/\text{cm}^2$

This condition is satisfied when $\Delta E \ll E_0$, thus we can assume that the stopping power remains constant, otherwise, when the deviation is not too appreciable, approximations must be done [2, 10].

In this experiment a mixed alpha source has been used with energies of 3.183 MeV (^{148}Gd) and 5.476 MeV (^{241}Am). The energy loss of alpha particles from our source was determined, in vacuum, for each of the films exposed in section 1. The source was located 12.8 cm in front of a solid state detector with an active area of 8.33cm^2 . In the vacuum vessel four supported films were mounted on a rotating wheel between the source and detector, leaving one blank position on the wheel in order to get the alpha energy unshifted spectrum. For each running, the system was evacuated up to 32-34 μ , and the bias voltage was increased gradually up to 35V. Finally, alpha spectra were recorded on a multichannel pulse height analyzer.

2.3. Scanning Electron (SEM) and Focused Ion Beam Microscopy (FIB)

Scanning electron system uses an electron beam to image a sample surface. Electrons are accelerated and focused onto the sample surface. Due to the interaction of electrons with atoms of the material there is an emission of excited electrons by the electron beam from the sample, called secondary electrons.

The recording of secondary electrons by a detection system enables us to image size, shape and texture of three dimensional objects, while other signals enable us to obtain the composition of material. On the other hand, the FIB system uses accelerated Ga^{3+} ions in order to mill material from a defined area with a typical resolution of square microns. This is possible by the means of focused ions into a specific site; when an ion hits an atom, its mass is comparable to the mass of the sample atom. Due to that, it will transfer enough momentum to remove it from the matrix. This gives to the FIB the ability to prepare site-specific

cross-sections in a highly controlled manner, leaving a very clean hole or surface. As in the case of SEM, there exists an emission of secondary electrons which are detected and gives us the possibility of imaging. The dual beam incorporates both a FIB column and SEM column in a single system. This combination is especially useful for cross-section sample preparation using the electron beam to view the cross-section face as the ion beam mills normal to the sample surface [11]. To enable ion milling and electron imaging of the same region, dual beam typically have a coincident point where the two beams intersect with the sample.

All experiments are carried out in a FIB (FEI-Helios dual beam), utilizing a beam of 30 keV with a current of 86pA. Firstly, a permanent marker of platinum is deposited, which serves as a protection layer against FIB damage. Subsequently, FIB cuts away the material, as shown in figure 2.1.

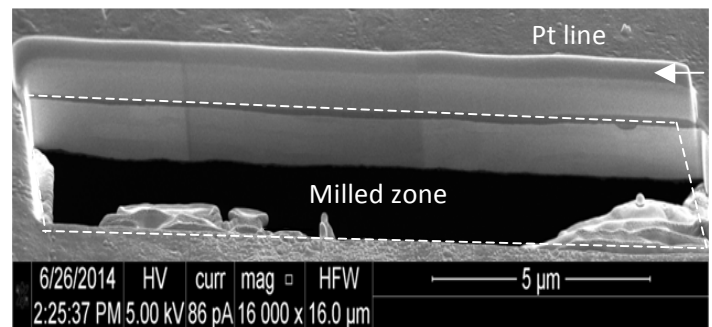


Fig.2.1. SEM image of cross-sections FIB trenches in ^{195}Pt . It can be observed the Pt layer over the sample.

3. Results and discussions

All thicknesses of samples were analyzed by energy loss of alpha particles, and specific samples were analyzed by FIB/SEM in order to compare (table 2.1). Data are summarized in table 3.1.

Images of cross sections using FIB/SEM of C-20 and C-60 are exposed in fig. 3.1(a)-(d). In (a)-(b) it is shown two different images from different transversal areas of the sample C-20, as well, in (c)-(d) correspond to C-60. In both cases, there are not inhomogeneities.

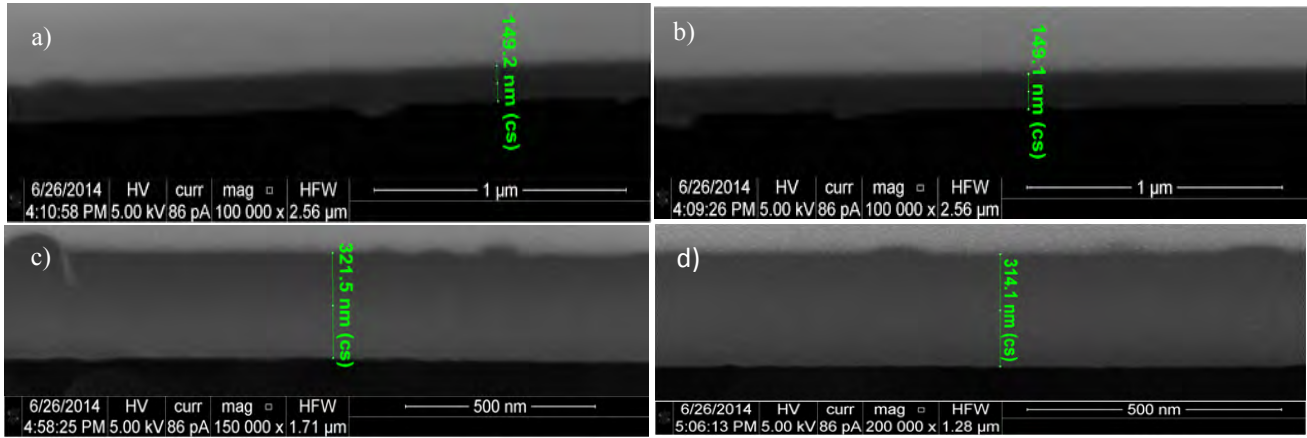


Fig. 3.1. SEM images of FIB prepared cross section of: a)-b): carbon 20ug/cm², c)-d) carbon 60ug/cm²

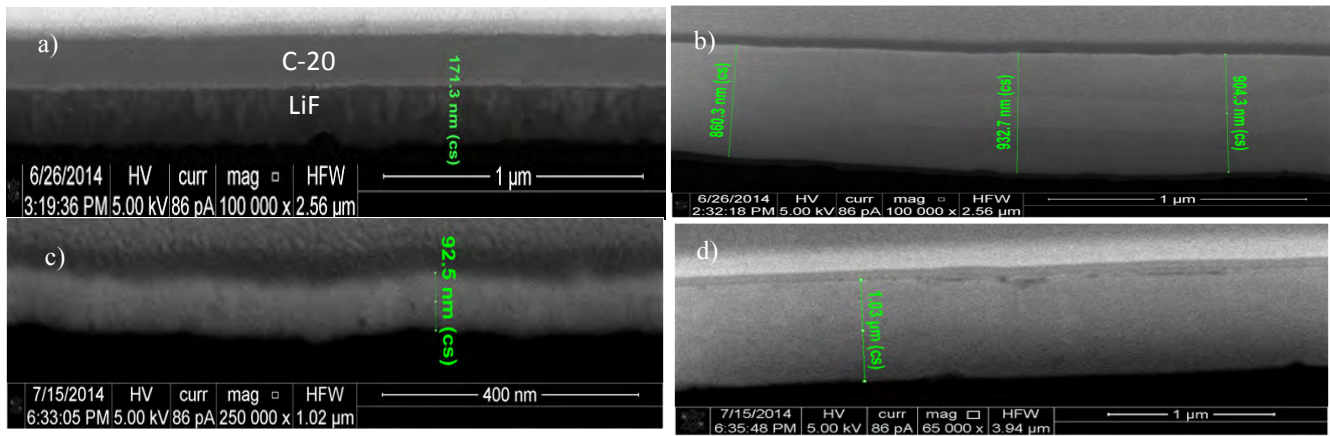


Fig. 3.2 SEM images of FIB prepared cross section of: a) LiF/C-20, b) Pt, c) Au and d) Sm

Table 3.1. Geometrical thickness both methods, energy loss of ¹⁴⁸Gd alpha particles and FIB/SEM. The latter is selected as a reference in order to compare, only.

Target	Energy shift (keV)	$\frac{dE_0}{E}\%$	Film thickness		Discrepancy (%)
			Energy loss of alpha (nm)	FIB/SEM (nm)	
C-20	29.49	0.93	138.01 ± 9.29	150.9 ± 3.6	8.6
C-60	65.78	1.10	307.57 ± 16.76	321.6 ± 7.3	4.4
LiF	68.02	2.15	151.28 ± 9.02	163.9 ± 8.6	7.7
Pt	572.20	18.00	886.92 ± 44.48	903.9 ± 28.7	6.6
Au	67.20	2.11	103.73 ± 6.91	90.3 ± 3.7	14.8
Sm	391.19	12.29	1263.1 ± 8.51	1020 ± 16	24

Thicknesses on different points were measured from cross section images, obtaining an average for each one. In this case, the uncertainties from this method are owing to the standard deviation of this measurement, using Image J software.

On the other hand, the measurements done by the energy loss are summarized in table 3.1. we compute $\frac{\Delta E}{E} \%$ where it is readily seen the final energy does not change too much, but for Pt and Sm approximations were done by dividing each sample in several thin foils assuming certain energy loss for each one, such that the sum of each loss gave us the total energy loss. In this way we obtain the sum of thicknesses from many thin foils that satisfy the condition $\frac{\Delta E}{E} \sim 1\%$.

We are interested in compare between both techniques, therefore we use FIB/SEM as a reference in order to see discrepancies among both. We get consistent results for C-60 and Pt, and small discrepancies for C-20 and LiF, which can be due to we are selecting a very small area, while the thickness by energy loss considers the total area. To overcome this, we can select more cross sections within the area of analysis for FIB/SEM.

Thickness of sammarium and gold samples shows an appreciable discrepancie in this case. In the former, we observe stragling plays an important role, where there is a considerable deviation from a Gaussian-like behavior. We fit a peak to the Sm spectrum, obtaining $\sigma = 82.27$ keV and a energy stragging 72.77 keV while using the SRIM code, we simulate the energy stragging using the ^{48}Gd (3.183MeV) alpha energy and the experimental thickness (1263.1 nm), obtaining a standard deviation for the theoretical energy spectrum of 18.33keV which means, that possibly, the sample is either very thick and also that some irregularities on the surface can be found.

While for gold, discrepancies of typically 10% are found. At first sight, we attribute this discrepancy due to the fact we have just one localized area, while the method of energy loss takes an average. Future measurements must been done in order to clarify this.

Conclusions

It has been demonstrated that FIB/SEM technique provides a reliable characterization of solid targets for nuclear reactions and it could be used as a complementary tool for exiting methods (e.g. energy loss of charged particles and RBS).

It allows precise measurement of the thickness for different thin targets. Our results shows that in many cases (e.g. carbon, platinum, lithium fluoride) measurements by FIB/SEM are in good agreement with the measured thicknesses by conventional approaches, such as energy loss of alpha particles. Some discrepancies were found for other foils (samarium and gold), which needs to be addressed in future. In addition to thicknesses measurements, FIB/SEM analysis also provides some information on the uniformity and the presence of possible impurities.

Acknowledgements

This work was supported by the National Science Foundation as part of the Notre Dame REU program.

We are also pleased with Professor U. Garg for the dedication and attentions given to this program. As well as we acknowledge Wanpeng Tan, for the fruitful support to our research.

References

- [1] Krane, K.S., 1988. Introductory Nuclear Physics. 2nd. edn. Wiley
- [2] W.K. Chu, J.W. Mayer, and M.-A. Nicolet. Backscattering Spectrometry, (Academic Press, New York, 1978).
- [3] Beck C et al 2003 Phys. Rev. C67 054602
- [4] B.W. Filippone et al., Phys. Rev. Lett. 50 (1983) 412 and Phys. Rev. C 28 (1983) 2222
- [5] L. Yaffee, Annu. Rev. Nucl. Sci., 12 (1962) 153
- [6] V. E. Lewis, Nucl. Instr. and Meth. 64 (1968) 29
- [7] H. L. Anderson, Nucl. Instr. and Meth. 12 (1961)111.
- [8] K. Muskalla, Th. Pfeiffer and W. Müller, Thin Solid Films 76 (1981) 259
- [9] J. Ziegler, Helium - Stopping Powers and Ranges in All Elements, volume 4 of The Stopping and Ranges of Ions in Matter, Pergamon Press, New York, 1977
- [10] J. Tesmer and M. Nastasi, editors, Handbook of Modern Ion Beam Materials Analysis, Materials Research Society, Pittsburgh, Pennsylvania, 1995.
- [11] L.A. Giannuzzi, F.A. Stevie, Introduction to Focused Ion Beams, Springer, New York, 2005.

Plasmid DNA Damage Induced by Helium and Oxygen Atmospheric Pressure Plasma Jet

Emily Bell

2014 NSF/REU Program

Physics Department, University of Notre Dame

Advisor: Sylwia Ptasinska

Contributors: Xu Han, Catie Luck

ABSTRACT

It is well known in the biophysics community that plasma sources may have beneficial properties in medicine. Plasma is made of various components, including ions, radicals, free electrons, and photons, which are highly reactive. Previous studies at the University of Notre Dame have shown that these components in helium plasma sources can induce significant damage to plasmid DNA, and studies performed by other groups have established that reactive oxygen species (ROS), especially hydroxyl radicals ($\text{OH}\cdot$), are main contributors to DNA damage in cells. Following these discoveries, it is important to quantify how much DNA is damaged in the presence of increasing amounts of oxygen. In these experiments DNA is irradiated with plasma containing varying amounts of oxygen at various distances and for various times.

INTRODUCTION

Plasma, often referred to as ‘the fourth state of matter’ in the physical sciences, is easy to create. When a high voltage is applied to a gas, the gas breaks down into different constituents, called plasma. Plasma can be categorized into several different types. It can exist at different temperatures and pressures: high-pressure, atmospheric pressure, non-thermal, and thermal plasmas are terms used to describe plasma parameters. Atmospheric pressure, non-thermal plasma is particularly advantageous for several reasons. The ability to generate plasma at atmospheric pressures requires no additional equipment (i.e. a vacuum chamber), and is thus cost-, time-, and energy-efficient. Non-thermal plasmas maintain low temperatures and enable application of plasma directly to the body without severe heat damage. Non-thermal plasmas can induce sub-lethal cell damage, and are useful in applications such as surface healing and

intracellular treatment. In the case of this study, the ultimate goal is to use plasma as a new form of cancer treatment. Plasma exposure can, in theory, can be used to induce cell death (apoptosis), an act which cancer cells are unable to perform and which makes them lethal.

Species generated within plasma include uncharged specimen; ions, which are charged particles; radicals, which are charged particles with an unpaired valence electron or an open valence shell; photons, or light radiation; and free electrons. Free radicals are especially reactive species. When DNA is concerned, radicals referred to as reactive oxygen species (ROS) are of special interest because oxygen has been proven to be highly responsible for DNA damage, even in normal cell metabolism. For example, ROS called hydroxyl radicals ($\text{OH}\bullet$) attack both the backbone and the bases of DNA, and are produced both in cell metabolism and from exposure to ionizing radiation, i.e. plasma. In plasma treatments, ROS are generated both in the plasma itself — from the plasma's reaction with atmospheric oxygen or from oxygen within the plasma's gas source — and also in the sample being irradiated, as secondary radiation caused by the plasma. Effects from both sources of ROS (the plasma and its interaction with the sample) are felt by the DNA because it is in aqueous solution for our experiments.

Our goal is to quantify how much damage is done to DNA in relation to the amount of oxygen in the plasma source. This could further understanding of how oxygen radicals are created in the plasma, in its interaction with the atmosphere, and in the DNA solution, and could further our understanding of DNA damage mechanisms.

EXPERIMENTAL SETUP

The plasma jet is formed by applying a high voltage to two electrodes attached to a thin tube. Helium and oxygen are piped to the tube at fixed flow rates, and the gas breaks down between

the electrodes, igniting the plasma. The plasma is accelerated downward out of the tube onto the sample. The distance between the end of the plasma tube and the surface of the sample plate is measured manually with a ruler. The high voltage source is connected to a transformer, pulse generator and an oscilloscope. The flow rates of both helium (4 L/min) and oxygen (0.04 - 0.2 cm³/m) are recorded to precisely calculate oxygen concentration.

Preparation of samples involves dilution, irradiation, and recovery. The stock solution used is 0.5 µg/µL pUC18 plasmid DNA. Before plasma irradiation, it is diluted with deionized water to 0.01 µg/µL. 10 µL of 0.01 µg/µL solution is placed in a well on a glass plate, and 5µL of deionized water is added to prevent too much evaporation (the relatively small amount of heat generated by the plasma is still enough to cause some evaporation of the aqueous solution). The plate is placed on a small metal stand and moved so that the well containing the sample is directly beneath the plasma

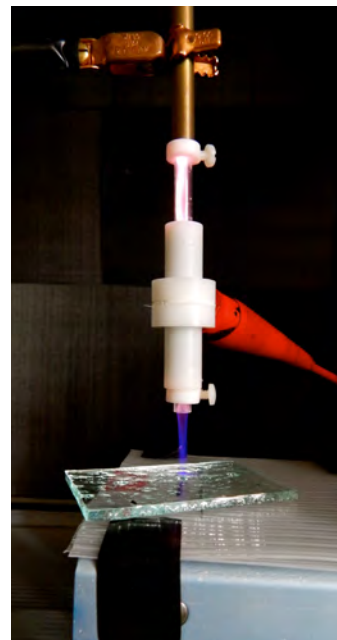


Fig 1. APPJ at 99.9% He + 0.1% O₂. The top brass electrode is grounded and the bottom is connected to a high voltage source supplying 10.8 kV. In this picture, the distance from the orifice of the tube to the sample is 2.5cm.

jet. After the full exposure time, recovery of the sample involves pipetting out the remaining irradiated sample and rinsing the well twice with 5 µL of PBS buffer per rinse. After irradiation and recovery, the total volume of the sample is around 25 µL. The sample is labelled and frozen until gel electrophoresis.

Control samples used are: stock control, which is prepared as 10 µL DNA sol'n + 5 µL DI water, with no PBS; glass control, in which the 10 µL DNA and 5µL water is placed onto the sample plate and recovered (without PBS) without exposure to gas or plasma; and flow control,

which is prepared and recovered as an irradiated sample, but exposed to only the He and O gas mixture rather than the ignited plasma.

Before being loaded into the gel, loading dye is added to the samples, which both increases sample density for efficient loading and changes the color so that the sample's movement through the gel is observable to the naked eye. For samples without PBS (containing 15 μL solution), 3 μL of dye are added, and for samples with PBS (containing 25 μL solution), 5 μL of dye are added. Samples are then ready to be loaded.

DATA ANALYSIS: GEL ELECTROPHORESIS AND GEL IMAGING

Gel electrophoresis is used to analyze DNA damage. The principle of gel electrophoresis is that when charged molecules are placed in a gel matrix and a voltage is applied, an electric field is created and the charged molecules move through the gel. Molecules of different sizes, shapes, or charges get separated as they move through the gel's pores.

In this case, DNA is negatively charged, and moves towards the positive electrode of the electrophoresis chamber. The DNA becomes separated by differences in shape, or conformation, due to plasma-induced damage. There are two main types of observed breakage which affect the conformation.

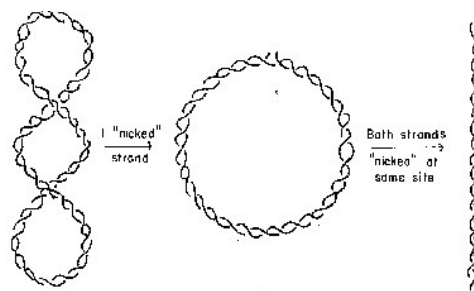
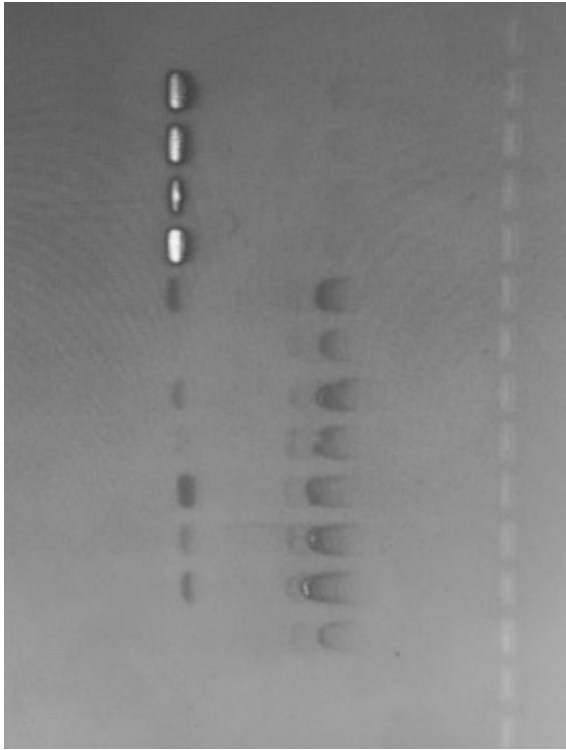


Fig 2. Depiction of supercoiled DNA (left), single strand breakage (middle), and double strand breakage (right). [<http://www.science-projects.com/PDCB101/Lectures/Lecture2A.htm>]

Single strand breakage (SSB) leaves the DNA strand in a loose circular shape and moves very slowly through the gel, traveling very little distance. Double strand breakage (DSB) produces a linearized strand of DNA which moves through the gel more efficiently than SSB DNA.

Undamaged, supercoiled (SC) DNA moves the fastest and furthest through the gel because of its compact structure.

We use agarose gel for electrophoresis because the pore size works best for the size of DNA molecules in our samples. Our gels are 1.2% agarose powder with 1x TBE buffer. 1x



TBE, diluted from 10x stock (Bio-Rad Laboratories, Inc.), is also used as the running buffer in the chamber, in which the gel is submerged, and which provides ions for current flow and a means of keeping the pH relatively constant.

Our gel is run at 50 V for 780 minutes for optimal band separation and resolution.

After the run, we image the gel using a UV machine (Molecular imager Gel Doc XR+ System, Bio-Rad Laboratories, Inc.). Before it is set, the gel itself is loaded with a dye, SYBR Green I, which, on its own, is not very fluorescent, but after binding to the minor groove of DNA, increases in fluorescence 1000-fold [4]. The imaging machine excites the dye with UV light, and takes an image of the green light that the dye, now attached to the DNA, emits upon relaxation, giving us a visualization of the position of the DNA in the gel.

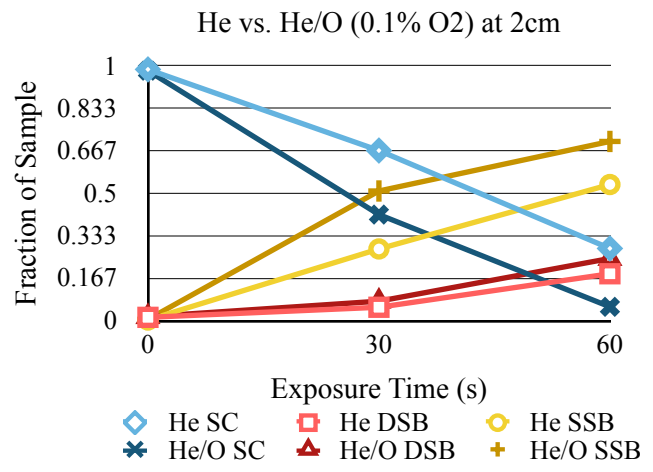
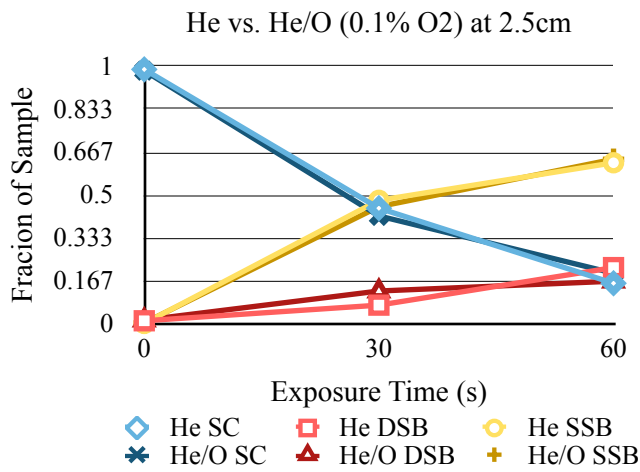
Fig 3. Example gel image. Loading wells on right side of image. Leftmost column is undamaged SC DNA, faint middle column is DSB, rightmost column is SSB. Samples loaded from top to bottom as follows: **1.** Stock control **2.** Glass control **3.** He flow control **4.** He/O flow control **5.** 2.5cm He 30s **6.** 2.5cm He 60s **7.** 2.5 cm He/O 30s **8.** 2.5 cm He/O 60s **9.** 2cm He 30s **10.** 2cm He 60s **11.** 2cm He/O 30s **12.** 2cm He/O 60s. The difference in fluorescence between control samples and irradiated samples is evidence of a problem with recovery.

Once the image is obtained, we use a gel image analysis software (Quantity One, 1-D Analysis Software, Bio-Rad Laboratories, Inc.) to determine volume of damaged and undamaged

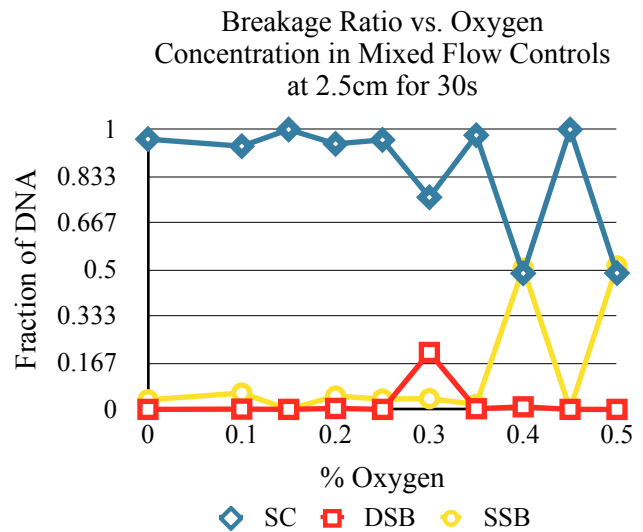
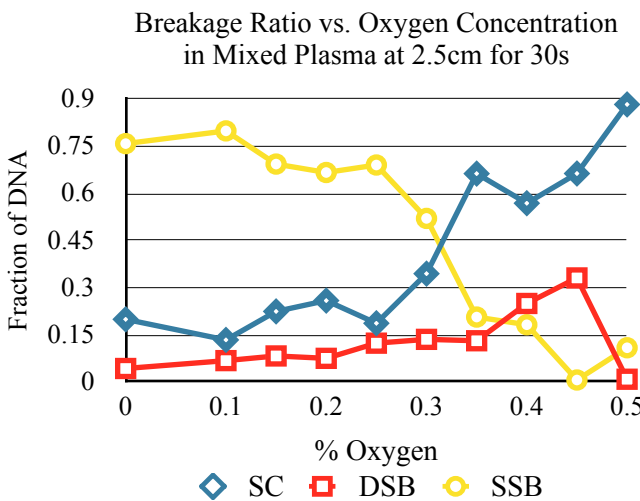
DNA. The program uses the intensity of fluorescence and area of fluorescence on the image to calculate a volume for each DNA band. We use the volumes of the bands to calculate the ratio of SC, SSB, and DSB DNA in each sample.

RESULTS

1. Helium-only plasma versus 0.1% O₂ He/O mixture at varying distances:



2. He/O mixtures at varying concentrations, for plasma and flow controls:



DISCUSSION & FUTURE PROSPECTS

In experiment **1**, less damage is induced by helium-only plasma at a distance of 2 cm. This can be explained by the plasma having less time and space to react with the atmosphere and create ROS. This trend has been observed in previous experiments. This experiment also reveals more damage from He + O₂ at 2 cm, so it appears that moving the sample closer to the jet corrects for jet instability. The difference between helium and the helium/oxygen mixture is also more defined, and closer to the expected difference, at 2 cm, and this seems to be due to the drastic change in damage done by helium at that close distance.

The results from experiment **2** are not what we hoped for. We expected to see a decrease in SC undamaged DNA and an increase in at least DSB (because double strand breaks in DNA cannot be repaired), if not both DSB and SSB. We do see an increase in DSB up to 0.45% O₂, but the SC DNA increases consistently. It's clear in the graph of control data that the instability of the jet is significant after the concentration of O₂ rises above 0.3%. Unreliable data gives skewed averages and makes the control data, which should be very consistent, look wild.

One aspect of our experiments that we were unable to improve was the amount of DNA recovered after irradiation: it was consistently low. We had difficulty getting the PBS to stay in the well when rinsing, and if it escaped the well it was hard to recover with the pipette. Perhaps in future a different well could be used for irradiation, making the recovery process more efficient and the data more reliable.

In the future, more concentrations of oxygen should also be tested to produce a more reliable trend. The experiments should be repeated to confirm the validity of the results, and a

means of keeping the jet more stable at higher oxygen concentrations should be investigated. A wider variety of exposure times should be tested as well to test the limits of the amount of damage induced by the plasma. Eventually, irradiation of cancer cells should be attempted. Dosimetry should also be used to test the presence of particular radicals in the mixed plasma.

References

1. X. Han, W. Cantrell, E. Escobar, S. Ptasinska, *Eur. Phys. J. D* (2014)
2. X. Han, M. Klas, Y. Liu, S. Stack, S Ptasinska, *Appl. Phys. Lett.* **102**, 233703 (2013)
3. Th. von Woedtke, S. Reuter, K. Masur, K.-D. Weltmann, *Physics Reports* 530 (2013)
4. A.I. Dragan, R. Pavlovic, J.B. McGivney, J.R. Casas-Finet, E.S. Bishop, R.J. Strouse, M.A. Schenerman, C.D. Geddes, *J Fluoresc* Vol. 22 No. 4 (2012)
5. M. Cooke, M. Evans, M. Dizdaroglu, J. Lunec, *The FASEB Journal* Vol 17 No. 10 (2003)

CMS UPGRADES

IAN BRODERICK

2014 REU PROGRAM

PHYSICS DEPARTMENT, UNIVERSITY OF NOTRE DAME

ADVISORS:

MITCHELL WAYNE

DANIEL KARMGARD

Abstract

As part of the next scheduled shutdown of the Large Hadron Collider (LHC), new upgrades to the Compact Muon Solenoid (CMS) are planned to be implemented. Among these include redesigns to the Optical Decoder Units (ODU) to interface with the fibers carrying light from the detector, as well as the new radiation and magnetic field resistant Silicon Photomultipliers (SiPM). In addition, the endcaps, which experience the most amount of radiation damage, may be replaced with a candidate “shashlik” detector configuration. A prototype shashlik detector was recently assembled at the QuarkNet Center and sent to the Fermilab test beam for preliminary analysis.

1 Context

Following the first long shutdown of the Large Hadron Collider in 2013 to prepare for accelerator operation at 14 TeV, the next scheduled shutdown will occur in 2017 and will further prepare the LHC for operation at higher luminosities [1]. Due to the high velocities and low masses of the particles present in the accelerator pseudorapidity can be used to describe the angle, θ , of a particle with respect to the beam. Pseudorapidity, η , of a particle is given by

$$\eta = -\ln\left[\tan\left(\frac{\theta}{2}\right)\right]$$

Since particles detected are approximately constant as a function of pseudorapidity, it is clear that the majority of detections, and therefore radiation damage, occur at the endcaps of the detector. Consequently, the CMS detec-

tor is scheduled to have this area upgraded in order to withstand this damage. Another problem that will be addressed during the next long shutdown is the problem with the current photosensors. Currently, hybrid photodiodes (HPD) are used, but these are sensitive to their local magnetic fields, can be damaged by the high amounts of radiation present in the detector, and require a high voltage (on the order of kV) to run. These HPDs are scheduled to be replaced by SiPMs.

2 Silicon Photomultipliers

Silicon photomultipliers are photosensors capable of detecting single photons by utilizing avalanche photodiodes. The SiPM accomplishes this when the photon creates a large enough electric field in the silicon to trigger an ionization cascade, which amplifies the effect of the photon into a macroscopic current [3]. These photosensors are preferable to HPDs since they are more radiation resistant, unaffected by magnetic fields, can run at much lower voltages (tens of volts), and can detect single photons.

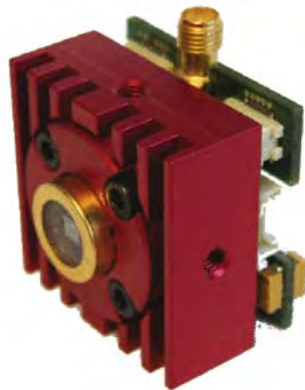


Figure 1: Cooled SensL Silicon Photomultiplier [5]

Silicon Photomultipliers are promising new photosensors, but they come with several new challenges of their own. The main problem with SiPMs is that they have a much higher noise to signal ratio compared to the HPDs currently in use. The best way to suppress this noise is to cool the SiPM to an ideal temperature of -20°C using a Peltier cooler [4]. However, there remains the challenge of how to most efficiently cool all 25,000 units that will be installed in the detector. In addition, there is a problem with the possible saturation of pixels in the SiPM. Since the SiPMs are sensitive devices, light signals hitting the same pixels repeatedly before they can recover could cause the SiPM to give inaccurate readings. As a solution, thick mixer fibers will be used to scramble the light signal and spread it out, preventing the same pixels from being stimulated in a short amount of time. Before the SiPMs can be installed, more studies need to be done in order to best optimize the devices for the detector.

3 Optical Decoder Units

The optical decoder units that currently act as the interface between the fibers carrying light signals from the detector to the HPDs need to be redesigned to interface with the SiPMs instead. The fibers in the ODU reconfigure the light signals from the detector into a configuration that is more useful for the SiPM. These fibers need to be tested to ensure that they transmit light properly within a certain tolerance. After precisely machine cutting the fibers, they are mounted on a configuration with an LED at one end and a photodiode at the other, measuring the light output. Then, after the out-

put is measured for each fiber, it is compared to the “golden” fibers (fibers used as a standard). If the fiber outputs the same amount of light with a tolerance of 10%, it passes and can be used in a prototype ODU. The golden fibers were machine cut at Fermilab and are retested every day to ensure that they maintain their quality. Further statistical analysis will be done on the light output of these fibers to determine the range of the fiber quality.



Figure 2: Prototype Optical Decoder Unit

4 Shashlik Detector

A prototype shashlik detector was constructed as a possible design for replacement of the CMS hadronic calorimeter (HCAL) endcaps. The detector consists of 16 “stacks” made up of alternating tungsten and scintillating tiles. 4 waveshifting Y11 fibers run through each stack, carrying out the light from any scintillation interaction that took place in the detector. These 64 fibers were diamond cut and tested using an LED at one end and a photodiode measuring the light output at the other to ensure that they each transmitted

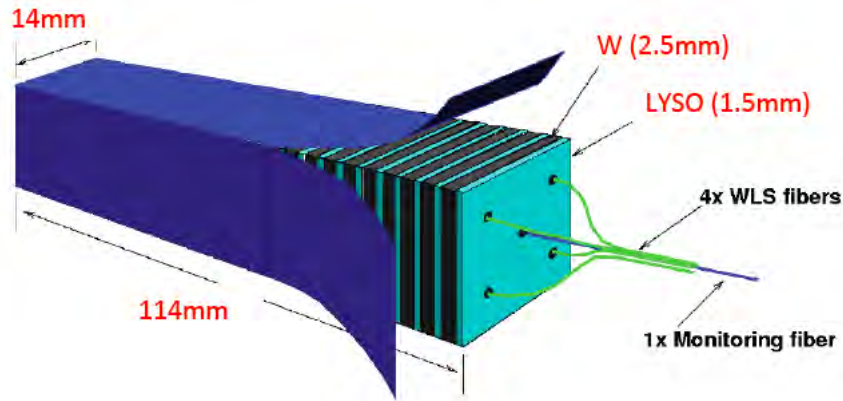


Figure 3: A Shashlik Stack
[2]

light about the same within a certain tolerance. The purpose of the tungsten is to absorb any light emitted from the adjacent scintillator, achieving a relatively small spatial resolution for the particle's trajectory, about 1 cm^2 .

As the particle travels through the detector, it deposits its energy into the scintillator, which converts it to light. The collection and measuring of this light output (using SiPMs) allows for the determination of the initial energy of the particle. Each stack contains a larger hole down the middle so that the detector may be carefully calibrated using a laser.

After sending the shashlik detector to the Fermilab test beam, it is necessary to confirm that the device was calibrated accurately. To determine this, a study of the linearity of the beam energy vs. the detector response was required. Analysis of electron and positron data was done using ROOT. A pedestal correction was necessary to filter out the noise. A plot of the pedestal corrected response to 2 GeV beam energy is displayed in Figure 6.

Data from approximately 20 runs using beam energies of 2, 4, 10, 20, 30,

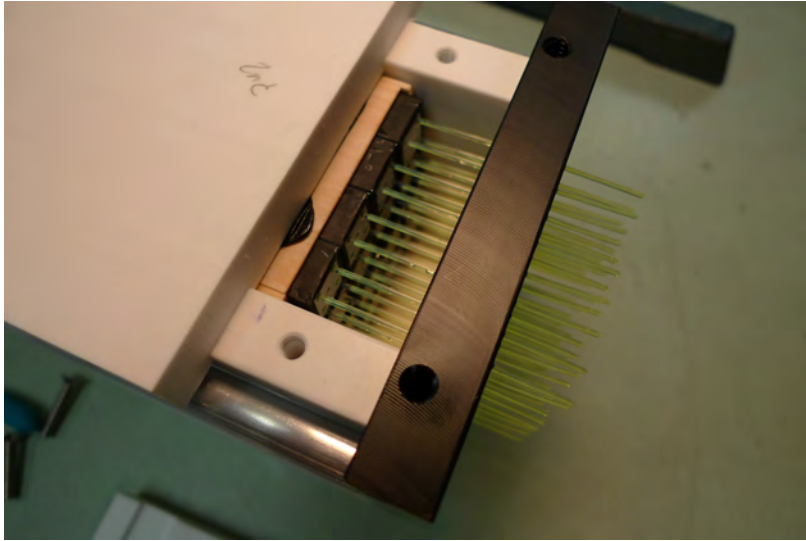


Figure 4: Prototype Shashlik Detector Stacks [6]

and 40 GeV were available. Figure 7 shows a plot of the beam energy vs. the mean detector response for the pedestal calibrated data. Preliminary shows that the beam energy vs. response relation is approximately linear. However, there are still too few runs and insufficient data to confidently determine the strength of the linearity.

5 Conclusion

During the next scheduled long shutdown of the Large Hadron Collider in 2017, several new technologies will be installed to help the CMS detector deal with the new luminosities that the accelerator will be running at. Among these are the radiation and magnetic field resistant silicon photomultipliers as light sensors, as well as a more durable and more accurate detector design in the shashlik detector. Further studies will be needed to continue optimizing SiPMs and to confirm the viability of the shashlik design. At a later time,

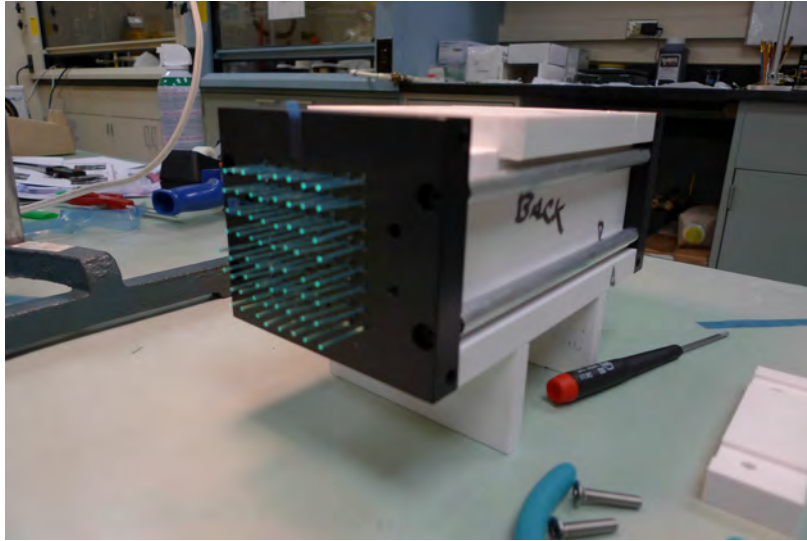


Figure 5: Prototype Shashlik Detector [6]

the possibility of replacing the waveshifting fibers with quartz capillary tubes filled with liquid scintillator will be explored. This would allow for easier maintenance. In addition, the capillary tubes would resist radiation better than Y11 fibers. These upgrades will be necessary for the accelerator to be run most effectively at the highest ever energy levels and to pursue new physics beyond the Higgs boson.

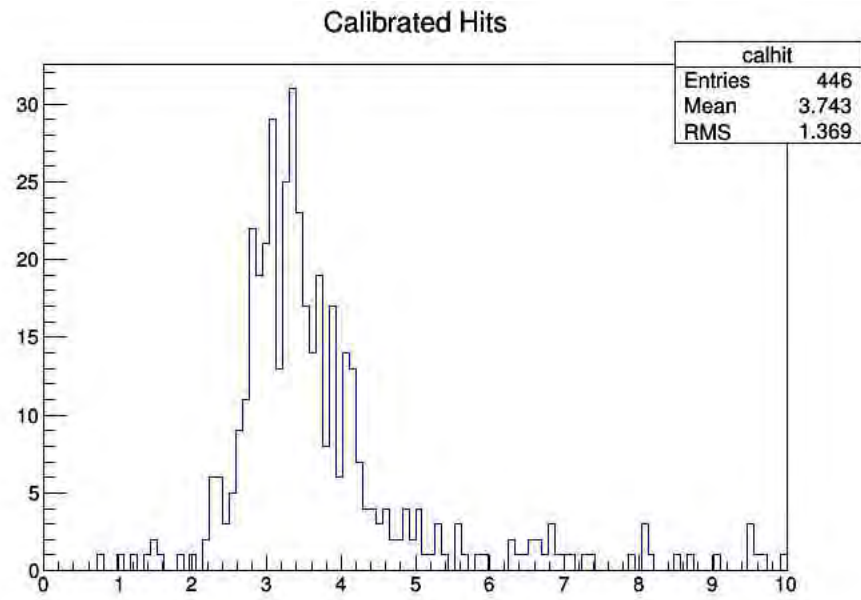


Figure 6: 2 GeV Beam Energy Calibrated Response

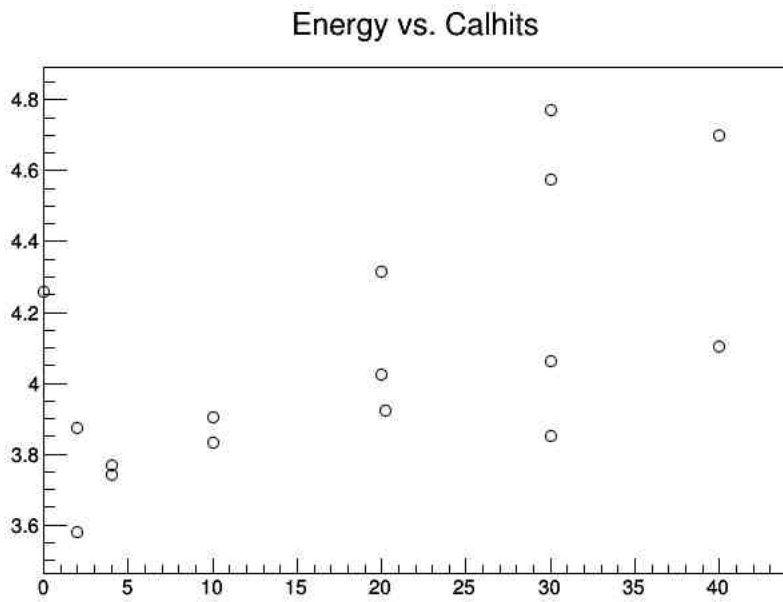


Figure 7: Beam Energy Vs. Calibrated Response

References

- [1] CMS Collaboration. Technical proposal for the upgrade of the cms detector through 2020.
- [2] Randal Ruchti. Shashlik stack.
- [3] SensL. *Introduction to the SPM*.
- [4] SensL. Silicon photomultiplier modules.
- [5] SensL. Sipm peltier cooler.
- [6] Mark Vigneault. Shashlik detector.

Simulation of a gas cell to stop radioactive TWINSOL beams

Guillermo Bustos Ramírez

2014 REU Program

Physics Department, University of Notre Dame

Nuclear Science Laboratory

Advisor:

Maxime Brodeur

Summer of 2014. Notre Dame, IN.

Abstract

The TWINSOL facility at the Nuclear Science Laboratory of the University of Notre Dame can produce various kinds of low-energy light radioactive beams, including nuclei that beta decay to their mirror neighbour. Decay spectroscopy of such mirror transitions in ion traps can provide valuable information to test the electroweak interaction. However, the energy of the TWINSOL beams is not low enough to be used in trapping experiments. The typical method used at other facilities to produce very low-energy radioactive beams consists in slowing down the energetic beam using a gas cell. Such systems include a solid degrader to slow the beam down, a He-filled gas volume to thermalize the ions and a radiofrequency carpet to extract the ions from the device. Simulations of stopping and extraction of ions were made considering the characteristics of the radioactive beams that TWINSOL can produce. A preliminary design of the stopping station is presented according with the obtained results.

Introduction

An activate field of research of nuclear physics is the study of the structure of exotic nuclei. Experiments using radioactive ion beams (RIB) are important, as they lead to discover the nature of exotic nuclei. Large laboratories have facilities that can produce high energy radioactive beams, like the Nuclear Superconductive Cyclotron Laboratory at Michigan State University [1], RIKEN [2], and GSI [3]. But some efforts have also been devoted at small laboratories like the TWINSOL facility at the Nuclear Science Laboratory (NSL) in the University of Notre Dame to produce low-energy light radioactive beams.

TWINSOL consist of a pair of large in-line superconducting solenoids with a maximum central magnetic field of 6 tesla, and they are used to produce, collect, transport, focus and analyse both stable and radioactive nuclear beams, and especially to study nuclear reactions involved in astrophysical processes. More information about TWINSOL characteristics can be found in [4], and in the website [5].

Although TWINSOL is well suited to carry out a wide variety of experiments, it is not well suited to perform very low-energy experiments, most specifically, trapping experiments. This kind of experiments can be used for correlation measurements of nuclear β - decay, as they provide ideal conditions for precision

measurements. It opens the possibility to probe the structure of the weak interaction, determine fundamental weak interaction properties in processes that involve the lightest quarks, test discrete symmetries and to perform Lorentz invariance violation tests [6].

Some efforts have been spent at high-energy radioactive beams facilities to create very low-energy radioactive beams by stopping the energetic ion beams in a gas cell and extracting them with RF ion guide techniques [7],[8], [9]. These efforts are culminating with the next generation of RIB facilities such as FRIB [10], that will allow to perform a wealth of new experiments.

A gas cell of this kind is proposed to be installed in the NSL, but the characteristics of the ion beams that TWINSOL can produce are very particular, since these ions are lighter and less energetic than the ones produced by [1], [2] and [3], so an adaptation of the chamber must be made.

The typical method to product low-energy radioactive beam consist of first slowing down the fast beam in a solid degrader, and to thermalize them inside of a gas cell. Electrodes placed inside the stopping chamber can be used to transport the stopped ions to a small orifice by a combination of static and RF electric fields. When trapping experiments are used for radioactive ions, extraction times should be on the order of a milliseconds to seconds, depending on the half-lives. New methods of RF systems have been developed in recent years, with an efficiency of nearly 100 % of ion transport [11]. After the extraction, the ions are guided through a different focusing stages before being re-accelerated to the desired energy.

This report have basically two sections. The first section is devoted to stopping ions in a gas cell. A variable solid degrader was added in order to keep the gas chamber short. To simulate this part of the experimentn the SRIM [12] code was used. The second section is devoted to extracting the ions of the buffer gas chamber. The method of extraction is the use of an RF carpet and a uniform electric field to push the ions towards the carpet. Simulations using SIMION [13] constructions of the electric field and the IonCool[14] code to simulate the motion of the ion were made.

Stopping ions

Ions passing through matter will interact with the atoms of the buffer gas. These interactions cause the ions to lose energy gradually until they finally stop. There are some energy loss models that describe this phenomena, and they have been studied for several decades and in many ways; since there are a lot of processes that have to be considered in a complete description of energy loss. However, for the purposes of this work, only the main concepts will be discussed, in order to have a general idea of the physical background.

Certainly, an important quantity is the linear stopping power. In nuclear physics, the stopping power is defined as the differential energy loss of the ion in the absorber divided by the corresponding differential path length [15].

$$S = -\frac{dE}{dx}.$$

In other words, the linear stopping power is the retarding force acting on charged particles due to interaction with matter, resulting in loss of particle energy. This interaction is mostly through Coulomb force between the ions and orbital electrons of the absorber atom, such that we can only associate a stopping power to stop charged particles. Other kind of interactions are possible, but they do not contribute too much to the energy loss of the ions.

Naturally, the range or the total path length R of an ion can be defined as

$$R(E_0) = \int_0^{E_0} \frac{dE}{S},$$

where E_0 is the initial energy of the ion. The energy loss along the path length is also named specific energy loss, which is described by de Bethe-Bloch formulation and it can be derived almost completely from classical arguments [16]. A detailed description of the process can be found on [17].

Another important concept is beam straggling, which is the spread in the longitudinal distribution over which the ions stop. This spread is due to the statistical distribution of collisions of the ions with the atoms in the absorber material.

SRIM code

The Stopping and Range Ions in Matter (SRIM) is a collection of software packages which calculate many features of the transport of ions in matter. The mathematical background of this collection is based in many models, including a correction of the Bethe-Bloch model. One software of this collection is TRIM (Transport Ions in Matter), which uses Monte Carlo simulations to calculate the interactions between transported ions [18]. All the simulations that were made to stop ions in the gas chamber were made using TRIM.

The stopping gas station

The TWINSOL facility can produce radioactive ion beams with energies typically between 10 to 40 MeV. The ions in which we are interested are ^{11}C , ^{15}O and ^{17}F . The goal of this part of the project was to determine the parameters of the gas cell that will thermalize these ions at the energy range. Similar studies had been dedicated to similar purposes [19], but at higher energies and heavier ions.

The characteristics of the gas cell were chosen as follows. The used gas in the simulation was helium. Since is a noble gas, undesirable ion recombinations with the gas atoms can be avoid, and since helium have the highest first ionization potential of any element, minimal neutralization will occur.

After several simulations, it was decided to use a $2.2\ \mu\text{m}$ Havar window to seal the gas chamber. This is a strong material that can be made thin, allowing to minimize the energy loss of the ion beam. This is important as it allows to have a better control on the energy loss by using a solid variable degrader. It is noticeable that at higher pressure, we have higher stopping power and less straggling, allowing the use of high pressure in the chamber to thermalize the full range of the ion beam. However, at higher pressures we also have less ion mobility, which can be problematic for the extraction, and will be discussed in the next section. It finally was decided to keep the pressure at 100 mbar, which is a middle point between good ion mobility and good stopping power.

To achieve high efficiency, the gas cell must have a stopping volume large enough to contain the full

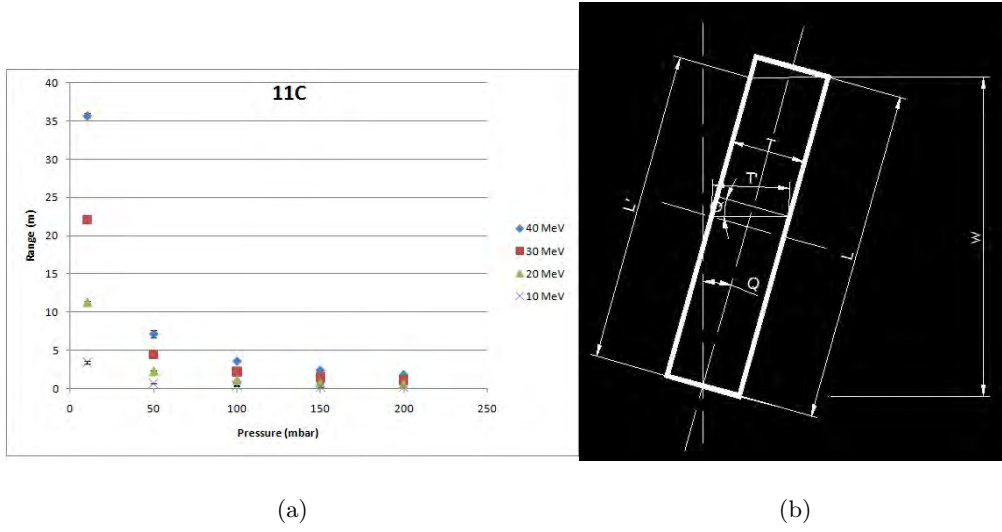


Figure 1: (a) Simulation of ^{11}C ions stopped ranges in $2.2 \mu\text{m}$ Havar window and Helium gas at energies of 10, 20, 30 and 40 MeV. (b) Variable Be foil.

range straggling of the beam. As it can be seen in Fig. 1 (a), it can be of several meters, which is not practical for use in the laboratory, so other parameter have to be managed to maintain the cell size small (in the order of centimeters). This parameter is the thickness of a solid degrader. After several simulations, it was decided that a beryllium foil is a convenient material to degrade the energy of the ion, due to his low atomic number. As can be seen in Fig. 2 (a), (b) and (c), one micrometer of Beryllium can change up to 10 cm of ion range, so the foil surface shall be as uniform as possible. In order to have a continuous range in the beryllium thickness, the foil have to be installed in a system that allow it to rotate, as can be shown in Fig. 1 (b). In this figure w is the beam width, L is the longitudinal size of the foil, T is the thickness of the foil, T' is the modified thickness and Q is the angular rotation. To obtain the complete range $[T, T']$ of the thickness, this two equations have to be solve for Q and T' ,

$$T' = \sec(Q)$$

$$w + \sin(Q)(L - T \tan(Q)) = 0$$

A precise control of the angular rotation is vital to have the ions stop inside the cell. It will be preferable to have only one beryllium foil, and rotate it to get to stop all kinds of ions. Unfortunately, as can be seen on Fig. 2, this thickness would be around 12 or 14 μm . Solving the equations above with a one inch ion

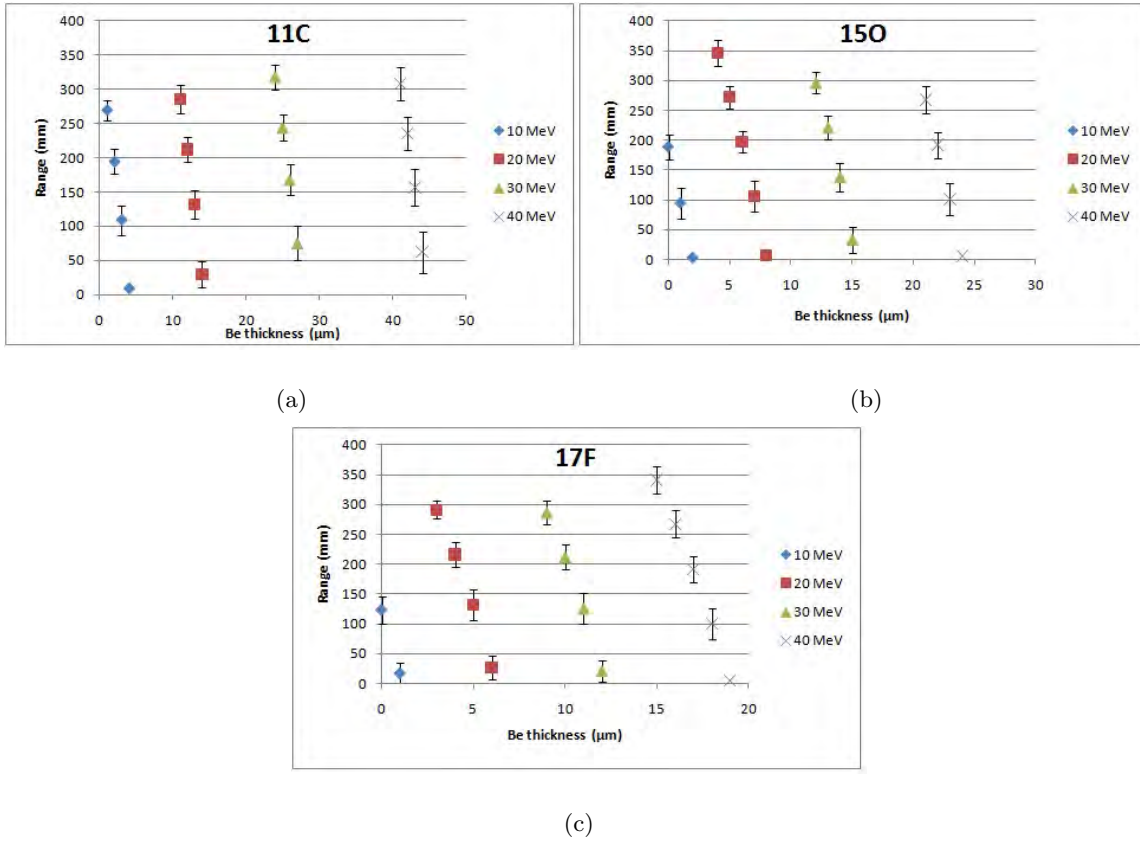


Figure 2: Simulations of ^{11}C (a), ^{15}O (b) and ^{17}F (c) stopping ranges in the gas cell. The error bars indicate the beam straggling.

beam, which is around the size of the beams that TWINSOL produce and 2 inches of longitudinal size of the foil, which is the regular size that can be found in the market for this thickness, the range can vary around $2 \mu\text{m}$, which is not enough to cover the whole range of thickness to stop all the ions. If energy of the beam can be controlled too, it translated in a better control of the ion range.

Extracting ions

After being thermalized in the gas cell, the ions will be extracted using a combination of static and RF electric fields. An important quantity that has to be considered in this process is the ion mobility K , which is a measure of how 'well' the ions can move inside the buffer gas in the presence of an electric field. It is defined as the proportional factor between the velocity of the ion in the gas and the magnitude of the electric field.

$$v = KE.$$

A correction in the density is commonly reported as the reduced mobility, and can be expressed as

$$K_0 = K \frac{n}{n_0} = K \frac{TP_0}{T_0P}.$$

As can be seen, the reduced mobility is inverse proportional to the pressure of the gas, so a low pressure chamber would be ideal to transport the ions, but as it was mentioned before, an equilibrium point between good stopping power and good ion mobility have to be established.

Ion surfing

An RF carpet consist of a pattern of thin concentric circle electrodes printed in a surface. An alternating voltage is applied to the electrodes. Adjacent electrodes are π rads out of phase. An static electric field is used to push the ions towards the carpet, so that the ions will be oscillating near the surface of the carpet. Ion surfing is a method to transport the ions along the RF carpet, and it has been proven experimentally by [20] and [11] but with heavier ions. A traveling potential wave is applied to the electrodes. To achieve this, adjacent electrodes are $\frac{\pi}{2}$ out of phase, so the potential in each electrode of the carpet is a superposition of the two alternating voltages.

$$V_n = V_{RF} \sin(\omega_{RF}t + n\pi) + V_w \sin(\omega_w t - \frac{n\pi}{2}),$$

for $n = 0, 1, 2, 3$, where V_{RF} is the amplitude of the alternating voltage, V_w is the amplitude of the potential wave, ω_{RF} and ω_w are the frequencies of the RF potential and of the traveling wave, and t is the time. An schematic of ion surfing is showed in Fig. 3 (a).

In this configuration, the velocity of the ion is determined by the traveling wave amplitude and speed, and it could be, a), equal to the wave speed if the ion is trapped in the traveling potential or b), lower than the wave speed if the ion is not trapped but is slipping above the wave.

Finally, the extraction efficiency is defined as the ions that were extracted over the total number of ions.

Code

Although an analytical model to transport ions in RF carpets in vacuum have been studied [21], a numerical approximation is necessary to model the motion of the ions in a buffer gas cell. IonCool is a

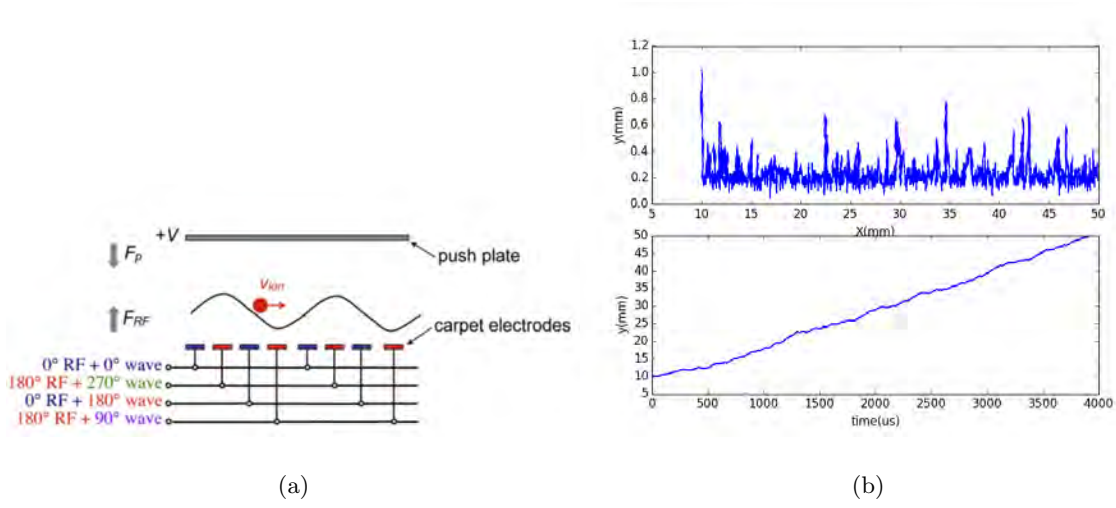


Figure 3: (a)Scheme of ion surfing. Source [20]. (b)Typical simulated trajectory of ion surfing technique. The parameters in this particular simulation were RF frequency of 20 MHz, push voltage 2 V/cm, and wave velocity of 20 m/s.

software that does exactly that. It uses Monte Carlo simulations to model the effect of the buffer gas by realistically collisions between ions and a buffer gas in presence of arbitrary electric or magnetic fields[14]. In this work, the electric fields are created by SIMION [13]. A simulated trajectory of an ion can be seen in Fig. 3 (b).

The extraction system

The extraction system consists in an RF carpet and a uniform electric field to push the ions towards the carpet. This field can be achieved by locating ring shaped electrodes along the axis of the cell, connect them with equal resistors, and setting a potential between the first one and the last one. In this configuration, the potential difference between the rings will be the same, so as the electric field magnitude. The objective of this part of the project was to maximize the efficiency and velocity of the ions in the gas cell as a function of the parameters. These parameters are the RF amplitude and frequency , the velocity and amplitude of the wave, and the magnitude of the push electric field.

The maximum RF amplitude is limited by the voltage breakdown in the helium gas. It depends on the distance between electrodes and the pressure of the gas. This voltage was fixed at 75 V, which is close to the breakdown point.

It is expected that it will be harder to transport ions with masses closer to helium mass. The ion that

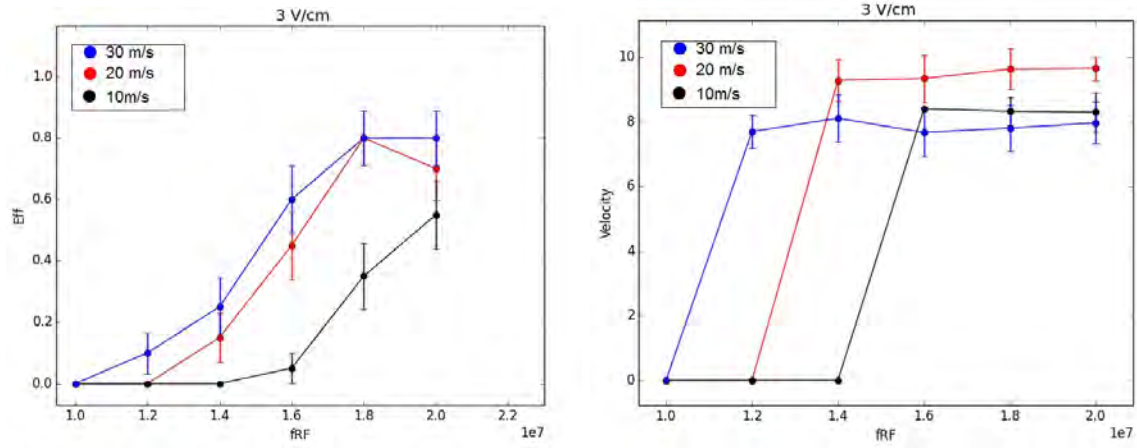


Figure 4: Efficiency and average velocities of transported ions in the RF carpet in function of RF frequency

was simulated was ^{11}C , since is the lightest of the ions in which we are interested. Hence, if it is possible to transport this kind of ions, it will be possible to transport ^{15}O and ^{17}F as well. The simulations were made by placing ions one by one at one centimeter above the carpet and 4 centimeters away from the extraction hole. After several simulations, it was noticed that for good efficiency the RF frequency has to be higher than 15 MHz, the push voltage has to be lower than 3 V/cm to avoid ions crashing in to the carpet, and the wave velocity has to be at least 20 or 30 m/s. The extraction times are in the order of a few milliseconds, as was desired. Fig. 4 shows the efficiency and the average velocity of ions of ^{11}C at 10, 20 and 30 m/s with a 3V/cm push voltage in function of the RF frequency. As can be seen, the ion velocity is better if the wave velocity is set at 20 m/s but the efficiency is higher if the wave velocity is increased. However, is difficult to tell, because of the huge statistical error.

Conclusions

Although it was demonstrated in the simulations that a stopping gas cell in TWINSOL facility is possible and efficient, other considerations have be looked more carefully in order to have a more accurate prediction of the behaviour of the ions in the gas cell. This considerations are gas flow, ion recombination and beam contamination. Finally, experimental proof of this work is necessary to validate a stopping gas cell as a viable option to produce low energy radioactive beams at the TWINSOL facility.

Bibliography

- [1] D.J.Morrissey et al., Nuclear Instruments and Methods in Physics Research B 204 (2003) 90–96
- [2] T. Kubo, T. Nakamura, K. Asahi et al., Nuclear Instruments and Methods in Physics Research B70 (1992) 309–319
- [3] H. Geissel et al., Nuclear Instruments and Methods in Physics Research B70 (1992) 286–297
- [4] J.J. Kolata, M.Y. Lee et al., TWINSOL: A DUAL SUPERCONDUCTING SOLENOID SYSTEM FOR LOW-ENERGY RADIOACTIVE NUCLEAR BEAM RESEARCH (1996)
- [5] <http://research.physics.lsa.umich.edu/twinsol/>
- [6] N. Severijns and O. Naviliat-Cuncic, Phys. Scr. T152, 014018 (2013)
- [7] L. Weissman, et al., Nucl. Instr. and Meth. A 540 (2005) 245
- [8] G. Sikler, et al., Nucl. Instr. and Meth. B 204 (2003) 482
- [9] M. Wada, et al., Nucl. Instr. and Meth. B 204 (2003) 570
- [10] <http://www.frib.msu.edu/>
- [11] F. Arai et al., International Journal of Mass Spectrometry 362 (2014) 56–58
- [12] <http://www.srim.org/>
- [13] <http://simion.com/>
- [14] Stefan Schwarz, Nuclear Instruments and Methods in Physics Research A 566 (2006) 233–243
- [15] G. F. Knoll. *Radiation Detection and Measurement*. John Wiley & Sons, Inc., New York, 3rd edition, 2000.
- [16] Alfons Weber, *Interactions of Particles with Matter*, CCLRC & University of Oxford, Graduate Lecture 2004
- [17] B.A. Weaver, A.J. Westphal, Nuclear Instruments and Methods in Physics Research B 187 (2002) 285–301
- [18] J. F. Ziegler J. Appl. Phys / Rev. Appl. Phys., 85, 1249–1272 (1999)
- [19] Patrik Andrew Lofy, *Development of a high-pressure, gas-filled ion source for a radioactive beam facility*, Ph.D. Thesis, Michigan State University, 2003
- [20] M. Brodeur et al., International Journal of Mass Spectrometry 336 (2013) 53–60
- [21] S. Schwarz, International Journal of Mass Spectrometry 299 (2011) 71–77.

Investigation into Anisotropic Nature of Ferromagnetic Resonance In Fe-GaMnAs

Devon Courtwright

Dr. Furdyna-Dobrowolska

Dr. Yoo

2014 Summer REU

Abstract

In this research we investigate the magnetic properties of a metal/semiconductor layered material grown by Molecular Beam Epitaxy (MBE) and characterized by x-ray diffraction. A Ferromagnetic Resonance Machine (FMR) is used to study what the magnetic field strength is required to allow the sample to absorb incoming microwave radiation. Our specimen sample is a thin film of Fe grown on GaMnAs grown on GaAs substrate with an additional GaAs buffer layer grown to reduce defects. The resonance peaks are demonstrated to have an angular dependence, while the emergence of multiple peaks are dependent on the direction of the applied field. Analysis of these peaks allows us to determine the anisotropic nature of the sample.

Spintronic Devices

Computer memory is reliant on transistors, which can either be in a binary state of either 'on' or 'off'. As computers become more powerful, and we are rapidly approaching the limit on how small transistors can be produced, scientists and engineers are working on new ways to store memory. One such possibility is to create memory devices based on the spin states of single atoms, which also can be in a binary state of 'up' or 'down'. The ability to manipulate spin states would overcome the size limits. "Changing the information from a '1' to a '0' would consist of applying a small magnetic field, which... can be a real magnetic field or an 'effective' field, to coherently rotate the spin by 180°" [5]

"Ferromagnetic (FM) semiconductors have recently attracted a great deal of attention due to their possible 'spintronic' applications." [3] Gallium Arsenide has gained a great deal of attention in the field of condensed matter research for its magnetic properties.

Ferromagnetic Resonance

When a strong external magnetic field is applied to a material, its unpaired electrons begin to resonate with the field, and may switch between an up- and down- spin, if it absorbs a photon with a frequency of γB , where h is Planck's constant, $\gamma = 2.21 \times 10^5$ m/A*s is the gyromagnetic ratio of the material, and B is the strength of the applied magnetic field. A hybrid sample of Iron layered on GaMnAs

was created as the focus of this research, for its “promise of integrating ferromagnetic and nonmagnetic semiconductors, with an eye on developing new devices that depend on electron charge as well as on its spin”. [3]

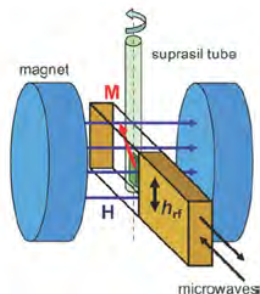


Fig. 1: Diagram of FMR device

FMR is a spectroscopic tool which is used to study the electron environment of materials with unpaired electrons and can be used to learn about various properties of the material. Electron spin, which can have quantum number $+\frac{1}{2}$ or $-\frac{1}{2}$, are the two possible values for the z-component of the angular momentum of an electron. This spin gives the electron a magnetic moment and makes the electron act like a small bar magnet. When an external magnetic field is applied, the paramagnetic electrons can either orient themselves parallel or antiparallel to the field, which results in two distinct energy levels. Electrons will prefer to align themselves parallel to the field since it results in a lower energy. FMR is a technique where a fixed frequency of microwave irradiation to excite the electrons from the lower field to the higher field. This will only happen in a magnetic field of specific strength, and in order to find this strength we measure the absorption of energy over a range of magnetic field strengths.

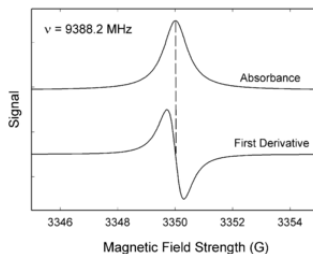


Figure 2: Theoretical Graph describing behavior of electrons in high strength magnetic field

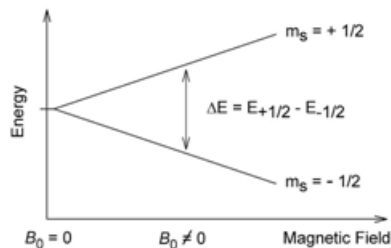


Fig. 3: Graph depicting the energy required to change a particle's spin state

A material's electrons have a preferred direction, and as the magnetic field increases, a greater amount of energy is required to switch them from one state to the other.

Anisotropy

Materials that display a multiaxial anisotropy may give rise to memory devices that have more than 2 states.

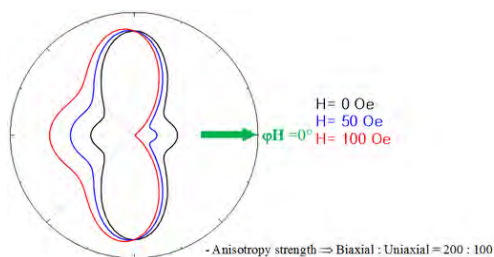


Fig.4: Theoretical graph simulating biaxial anisotropy and its magnetic field dependence

Equipment

The magnetic field that is applied come from two large helmholtz coils with a current running through it to produce an electromagnet. Between the two coils is a cavity, or resonator which amplifies the microwave signal after it comes in contact with the sample. The microwave bridge provides the source for the microwaves and detects the signal response. There is also a console to control the magnet, the microwave bridge and the process the microwave signal. The computer controls the spectrometer and allows for control of parameters and to visually process the information.



Fig. 4: Ferromagnetic Resonance machine, produced by Bruker

Procedure

An Iron sample, smaller than 1mm in size, was placed in a Bruker FMR machine and exposed to a magnetic field over a range of 0 to 12,000 Gauss. The sample was then bombarded with microwave radiation, and the FMR machine recorded how much of the radiation was absorbed as the field strength increased.

The FMR scans were repeated by rotating the θ_H around 360 degrees, every 6 degrees. The sample was characterized over four different orientations:

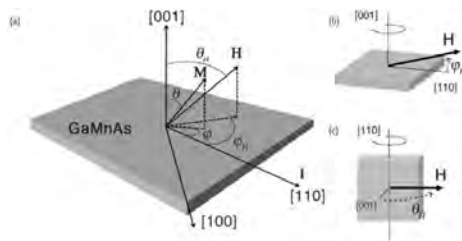


Fig. 5: Orientations of the sample in the machine, image taken from [8]

Orientation 1: $\theta_H=0^\circ$, $\phi_H=0^\circ$

Orientation 2: $\theta_H=0^\circ$, $\phi_H=45^\circ$

Orientation 3: $\theta_H=0^\circ$, $\phi_H=90^\circ$

Orientation 4: $\theta_H=90^\circ$, $\phi_H=0^\circ$

Our sample was Iron on top of Gallium Manganese Arsenide, capped with Gold for the purpose of preventing oxidation without interfering with the magnetic resonance. The sample was created through a

process known as low temperature molecular beam epitaxy. Initial experiments were done at room temperature. Further experiments will involve cooling the sample down with liquid nitrogen in order to bring it below its Curie Temperature. This is possible because the sample is doped with Manganese which has a temperature dependent magnetic property.

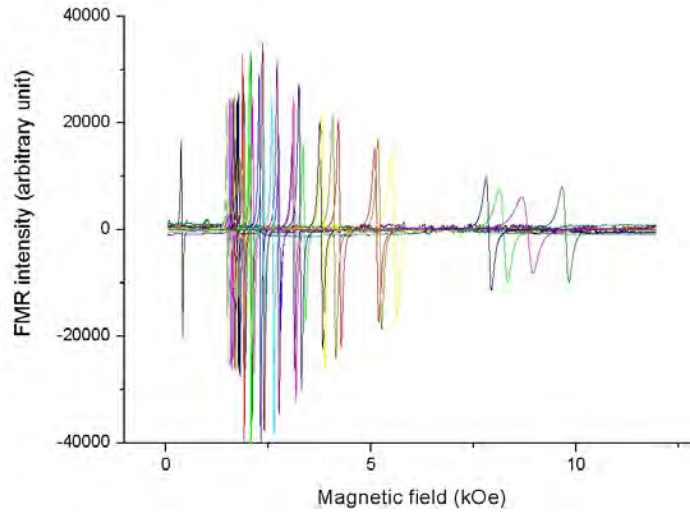


Fig 6: Resonance curves for Orientation 1

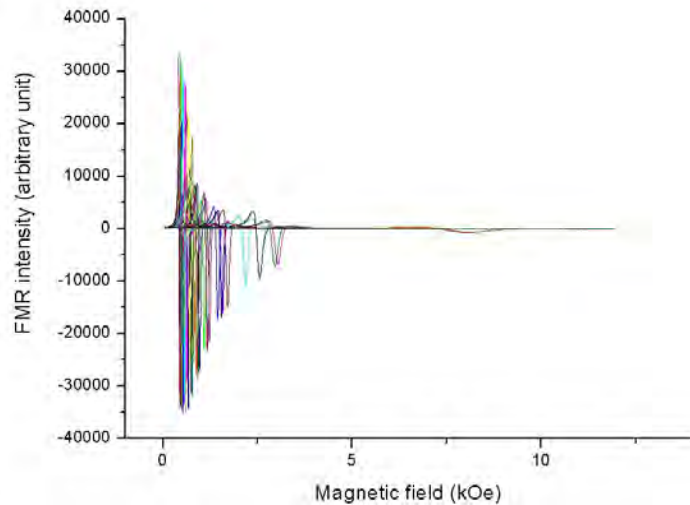


Fig 7: Resonance curves for Orientation 2

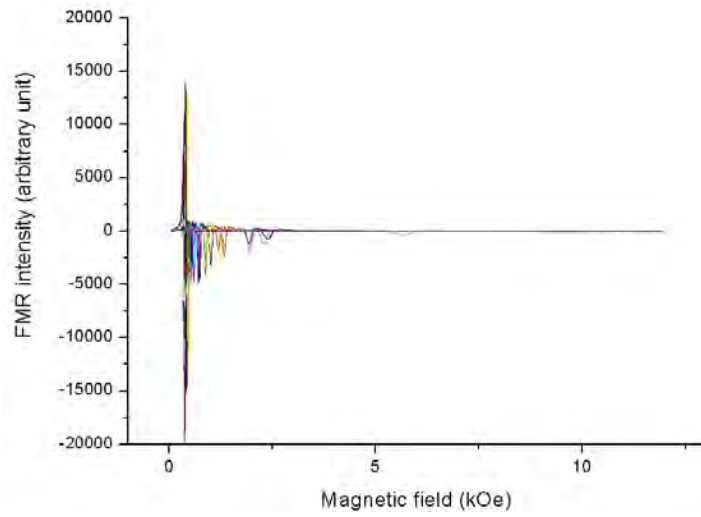


Fig. 8: Resonance curves for Orientation 3

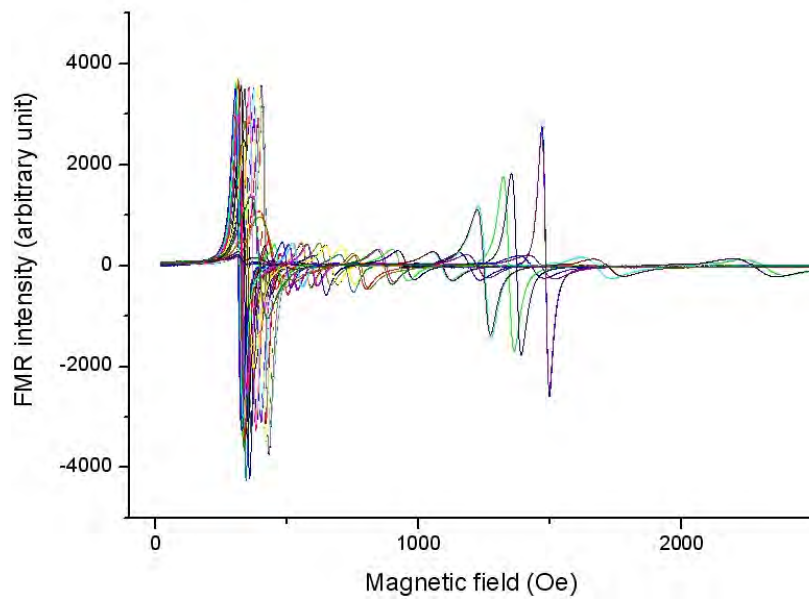


Fig. 9: Resonance curves for Orientation 4

After compiling the data, the peak values from each scan were extracted, as well as the minimum and midpoint values. The midpoint was compared to H_{eff} , the distance between the peak and minimum.

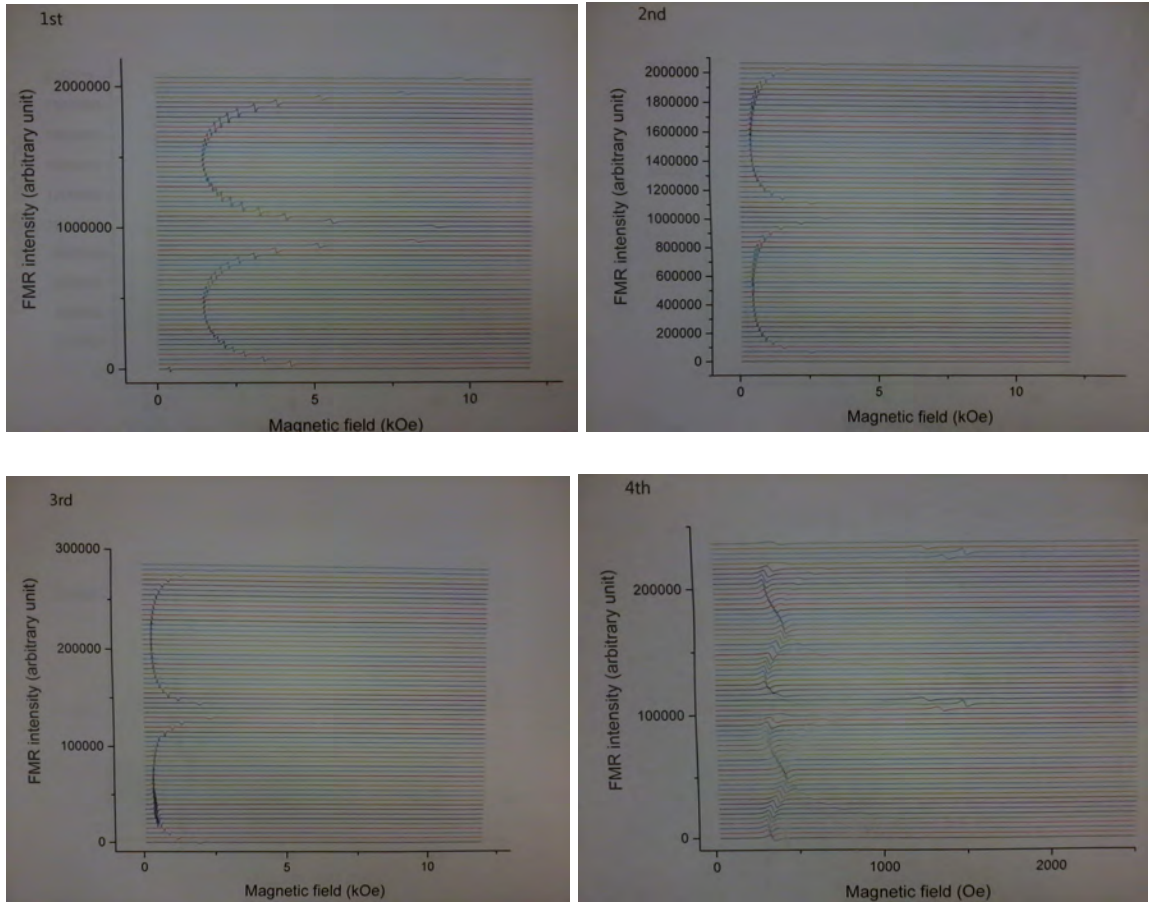


Fig 10: Graphs showing the angular dependence of FMR spectra

The plots above show where the resonance peaks occur at every angle, from 0° at the bottom and increasing to 354° at the top. A quick qualitative analysis reveals the biaxial anisotropy along the 180 axis. Further study is needed to obtain a complete quantitative analysis of the sample's anisotropic strength.

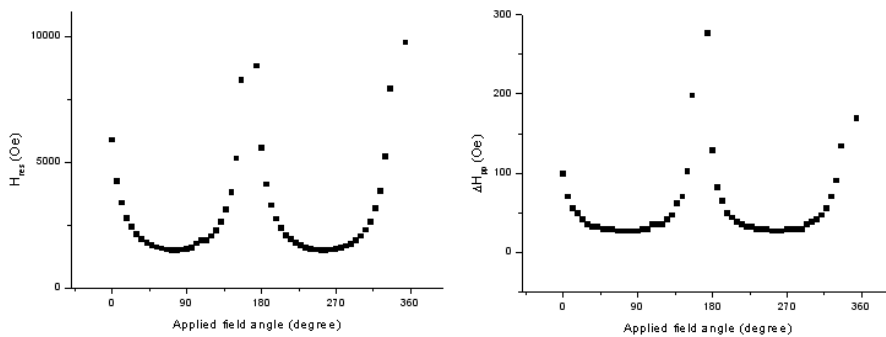


Fig 11: Resonance peaks and curve width for Orientation 1

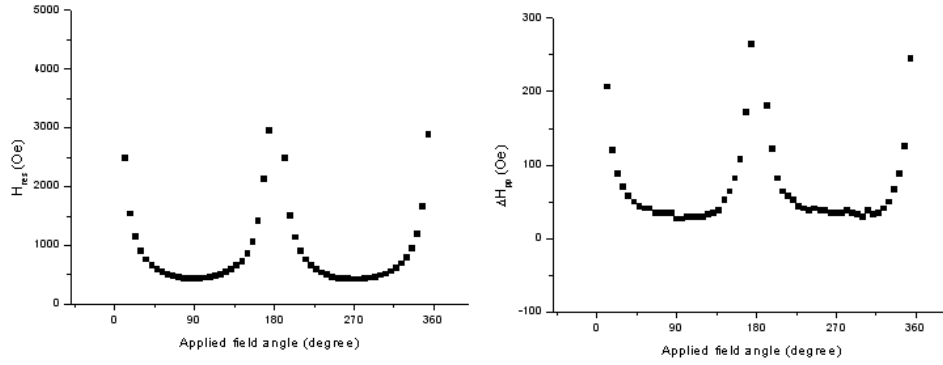


Fig 12: Resonance peaks and curve width for Orientation 2

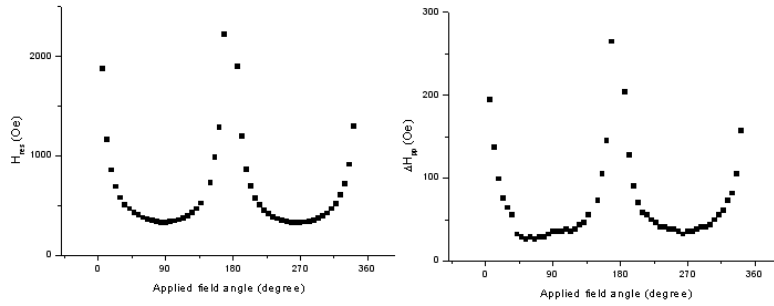


Fig 13: Resonance peaks and curve width for Orientation 3

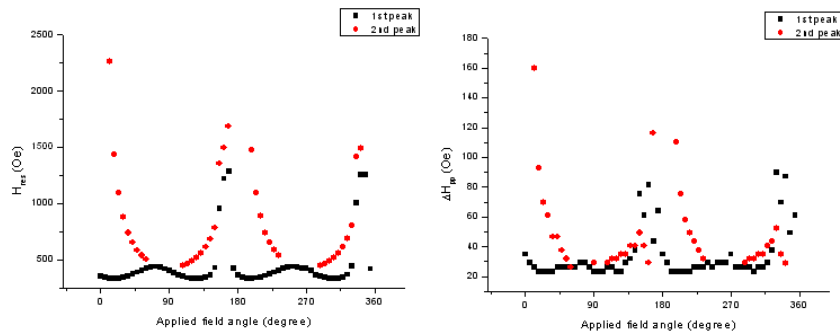


Fig 14: Resonance peaks and curve width for Orientation 4

Future Work

The next phase in our research will be to cool the sample down below room temperature using liquid helium and repeat the FMR scans see how the resonance changes when the field is interacting with both the metal and semiconducting layers. These results will later be compared to nanowires grown in the same MBE machine to determine how the direction of the wires might affect the direction of the magnetic field.

Acknowledgments:

^[1] K. Tivakornsaithorn *Magnetic Properties of Hybrid Fe/Semiconductor Structures*, Dissertation (July 2012)

^[2] Wiley, *Electron Paramagnetic Resonance: Elementary Theory and Practical Applications* (2007)

^[3] X. Liu, Y. Sasaki, and J. K. Furdyna *Ferromagnetic resonance in $Ga_{1-x}Mn_xAs$: Effects of magnetic anisotropy*
Physical Review B 67, 205204 (2003)

^[4] S. V. Vonsovskii, *Ferromagnetic Resonance* (Pergamon, Paris, 1966)

^[5] *Challenges for Semiconductor Spintronics*. Nature (2007).

^[6] Ohno, H. et al. *Electric-field control of ferromagnetism*. Nature 408,944–946 (2000).

^[7] N. Banaree, et al. *Evidence for spin selectivity of triplet pairs in superconducting spin valves*. Nature, (2014).

^[8] Sanghoon Lee, et al. *Ferromagnetic Semiconductor GaMnAs*. Materials Today (April 2009)

With special thanks to:

Xinyu Liu

Si Ning Dong

Sergio Mellon

Xiang Li

Shibo Wang

Qingyang Zhang

James Vogel II

Modernizing Plunger Control with Low-Cost Digital Electronics

Patrick Fasano
2014 NSF/REU Program
Physics Department, University of Notre Dame
Nuclear Science Laboratory

Advisor: Prof. Ani Aprahamian

Abstract

The plunger technique provides a valuable tool for measuring lifetimes of excited states in the 1-100 ps range. The plunger consists of a thin foil target and stopper foil separated by some controllable distance; beam-induced reactions occur in the target and the resulting nucleus of interest leaves the target foil and is completely stopped by the stopper foil. The Doppler-shift in γ -ray energy due to the velocity of the de-exciting recoiling nucleus is used to count the fraction of transitions which occur during the flight time, thus giving the mean lifetime of the gamma-ray depopulating a specific nuclear state directly. This technique, called the Recoil Distance Doppler-Shift (RDDS) method, requires precise and stable positioning of the foils over periods of hours or longer while correcting for beam-induced deformations to the foils.

The Notre Dame Nuclear Science Laboratory has a plunger device which is approximately 30 years old. Our work this summer included the upgrade and full rebuilding of the electronics to control the plunger system. In the Notre Dame plunger apparatus, the separation between foils is measured via capacitance between the foils and is used to control the position of three servo motors. We have made two major upgrades to the plunger device: (1) a newly-applied, precision capacitance-measuring circuit based on the phase-shift of a sinusoidal signal, (2) and low-cost microcontroller-based feedback loop for precisely controlling servo motors with quadrature encoder outputs. The capacitance measurement follows a development in the mid 1990's that will now be applied to the ND plunger. The microcontrollers are also a significant modernization of the plunger. Once we have demonstrated that all the mechanical parts of the plunger work as desired, we will carry out reactions in the Nuclear Science Laboratory and will measure the lifetimes of excited states in several rare earth nuclei.

1 Introduction

The Nuclear Science Laboratory (NSL) at the University of Notre Dame is one of the oldest continuously-operating facilities dedicated to research in low-energy nuclear physics. While no longer being known as the Nuclear Structure Laboratory, the NSL maintains a strong program dedicated to research on nuclear structure; a current push exists within the NSL to develop the capability to measure lifetimes of nuclear states via different methods. One such technique we are implementing is the plunger method. Work this summer has focused on upgrading and overhauling the Notre Dame plunger and its control electronics.

1.1 Nuclear States and Lifetimes

Much in the same way as atomic electrons have discrete states and transitions at low energies, so too does quantum mechanics predict nuclei with a finite set of allowed states for energies near the ground state; this fact contrasts with the popular notion of a nucleus as a tightly-packed ball of protons and neutrons without any real internal structure. Models for describing this internal state often fall between two extremes in simplification: the first models the nucleus as having shells, much like the electrons in the atom; the second treats the nucleus as a drop of positively-charged fluid which can oscillate or rotate, as well as be deformed at its lowest energy. To explain the behavior of many heavier nuclei, a combination of both models must be invoked, such as a nucleus with a "hard core" of nucleons (protons and neutrons) from the shell model and "valence" nucleons which exhibit fluid-like behaviors around the core [2]. Much of nuclear structure, then, studies how these two models (among others) combine to explain the phenomena which are observed.

One of the most essential tools for understanding nuclear states and the transitions between them is gamma-ray spectroscopy. In the same way that electronic transitions between energy levels produce light in the UV range and near UV, nuclear transitions produce photons in the 100 keV to 1 MeV range. Simply measuring the energy of photons emitted by excited nuclei can help determine the energies of the levels. Measurement of the angular distribution and angular correlations of emitted gamma rays can provide additional information about the angular momentum of states. However, these methods do not directly give much information about the relationship between states, such as how they are coupled via the electromagnetic force; one of the most important quantities for understanding how two states are related is the mean lifetime of a transition, τ_{if} . The mean lifetime is inversely related to the transition probability, λ_{if} , which is in turn related to the "matrix element" M_{if} by Fermi's golden rule [4, p. 41]

$$\frac{1}{\tau_{if}} = \lambda_{if} = \frac{2\pi}{\hbar} |M_{if}|^2 \rho_f \quad (1)$$

where ρ_f is the density of final states; in systems with well-separated states, such as nuclei at low excitation energy, this number is small or 1. The matrix element describes the relationship between the initial wavefunction Ψ_i and final wavefunction Ψ_f

$$M_{if} = \langle \Psi_f^* | V' | \Psi_i \rangle \quad (2)$$

The matrix element, then, expresses how much the wavefunction Ψ_f overlaps with Ψ_i after Ψ_i has been changed by the potential V' . In simpler terms, measuring the lifetime directly gives a measure of how similar or dissimilar the initial and final states are, as well as how many different ways there are to get from state i to state f . This knowledge can help determine which states have more of an aggregate (or collective) character, such as a drop, or a single nucleon character, such as the shell model.

2 Recoil Distance Doppler-Shift (RDDS) Technique

The Recoil Distance Doppler-Shift technique, known as the plunger method, allows direct measurement of lifetimes of nuclear excited states. The technique, which is capable of measuring mean lifetimes in the 1-100 ps range, exploits the fact that photons emitted by a moving body will be Doppler-shifted compared to photons emitted at rest. In the case of RDDS, the Doppler-shift is used to distinguish between photons emitted while traveling through some known distance from photons emitted after being stopped. In general, a device called a plunger is used to position a target foil and a stopper foil in parallel, shown schematically in Fig. 1a, with some separation x between them. Beam-induced reactions occur in the target foil, and the excited nucleus of interest recoils with some velocity v toward the stopper foil, where it is stopped completely. The flight time is thus $t_f = x/v$; any de-excitation photons which occur during that time t_f will be Doppler-shifted with energy

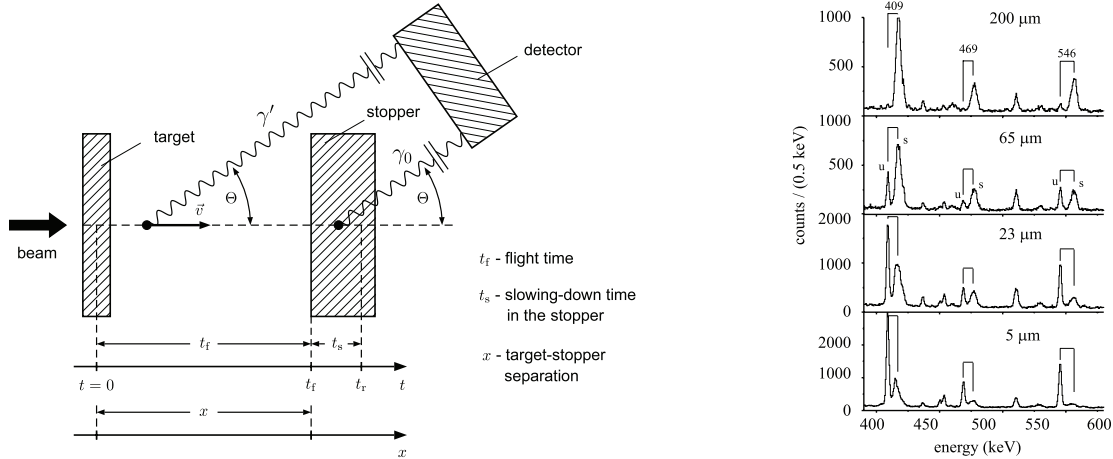
$$E = E_0 \frac{\sqrt{1 - \beta^2}}{1 - \beta \cos(\theta)} \quad (3)$$

where E_0 is the unshifted energy and $\beta = v/c$, while any de-excitations after stopping in the stopper foil will have energy E_0 . This results in a gamma-ray spectrum with shifted and unshifted peaks, as shown in Fig. 1b. The lifetime τ is related to the area of the shifted I_s and unshifted I_u and the flight time t_f peaks via the decay equation

$$\frac{I_u}{I_u + I_s} = n_0 \exp(-t/\tau) \quad (4)$$

where n_0 is the initial number of excited states [3]. In practice this analysis is much more complex due to level-feeding (higher levels de-exciting into the level of interest), so a related system of differential equations is solved instead. This process is repeated for several different separations; the name ‘‘plunger’’ comes from the fact that plunger devices can move one or both foil(s) in and out.

Figure 1: The Recoil Distance Doppler-Shift technique.



(a) Plunger schematic [3]. Excited nuclei are produced in a target foil, and are stopped by a stopper foil, with a well-defined flight time. (b) Example plunger spectra [5]. The relative areas of the two peaks change as a function of separation.

3 Plunger Device Rebuild

3.1 The Notre Dame Plunger

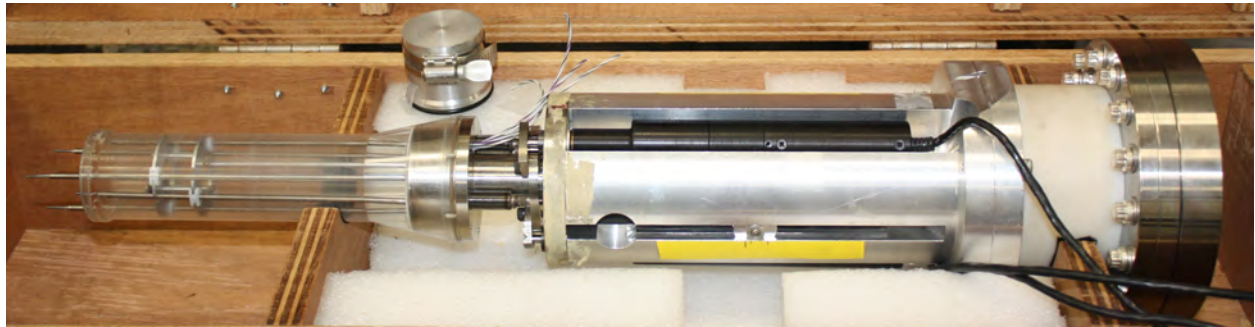


Figure 2: The Notre Dame Plunger

Notre Dame possesses a plunger device (shown in Fig. 2) which was built for the Notre Dame-Argonne Bismuth Germanate (BGO) detector array. The device itself is of the “coaxial” geometry type, with motors arranged around the beam path; the motors press against a plate which is connected at three points to rods which hold the foils. The three Newport 850B motors move independently and provide sufficient degrees-of-freedom to adjust the foils to be parallel as well as change the spacing between them. The motors are controlled by a $\pm 12\text{V}$ analog supply; they output quadrature-encoded pulses geared to produce 20,000 pulses/mm. The quadrature encoding (two square waves out of phase by 90°) gives information on both the relative position as well as the direction of motion.

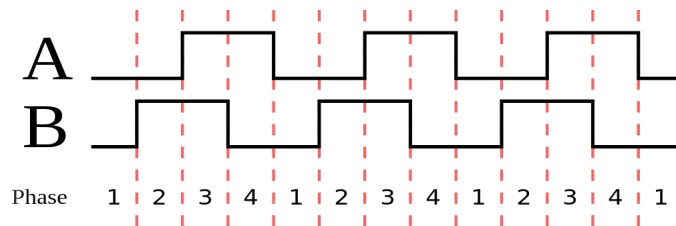


Figure 3: Quadrature encoder waveforms [7].

3.2 Electronics Upgrades

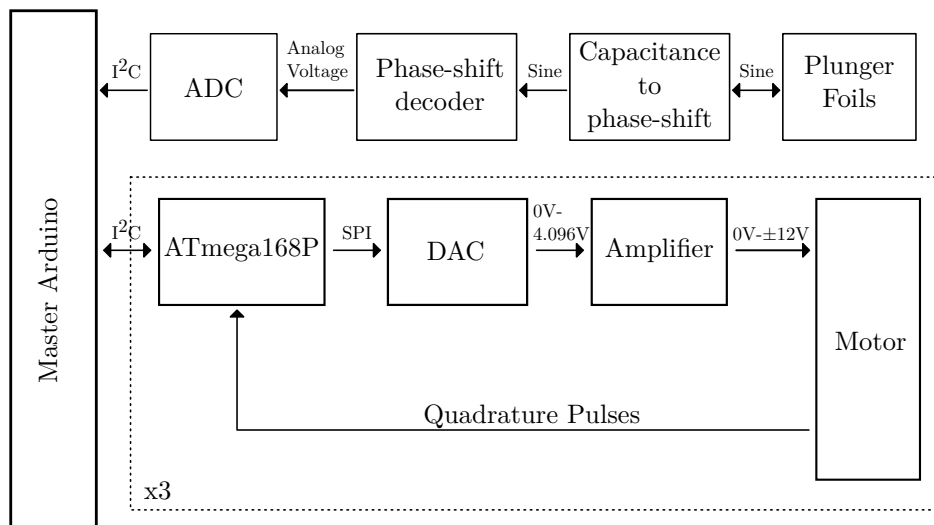


Figure 4: Block diagram of new plunger control electronics.

The major task we undertook for this summer 2014 was a complete rebuild of the electronic controls for the Notre Dame plunger. The previous circuitry used an type of “track-and-hold” capacitance-measuring circuit that did not have sufficient precision to detect small changes, especially when performing the parallelism adjustment. In addition, the earlier control used discrete and programmable logic; a major goal was to replace the logic with microcontrollers which would be easily upgradable and more flexible in the logic they implement.

3.3 Capacitance Measurement

A functional diagram of the new electronics is shown in Fig. 4; it consists of two major components, the capacitance measurement circuit and the motor control loop. These two pieces are coordinated by a master Arduino-based microcontroller. The capacitance circuit is based on a capacitance-to-phase shift circuit first published in 1999 [1]; the circuit exploits the fact that the test capacitance will cause a small phase-shift of an input sine wave. In particular, the sine wave passed through the foils is added to a sine wave which is almost

180° out of phase with the input signal and passed through a reference capacitor. This allows us to solve for the cotangent of phase-shift

$$\cot(\phi) = -\frac{C_X A}{C_0 B \sin(\psi)} \cot(\psi) \quad (5)$$

where C_X is the capacitance between the foils, C_0 is the reference capacitance, and A and B are arbitrary scaling constants. By using a phase sensitive detector circuit, the phase shift is converted to a ratio of voltages such that

$$\cot(\phi) = \frac{V_C}{V_S} \quad (6)$$

which is then measured by an analog-to-digital converter (ADC). According to its author, the limits of precision on this type of circuit is something like 1-in-10,000 at the range of capacitances applicable to the plunger, which is more than precise enough.

3.4 Motor Control Feedback Loop

The second major upgrade is to the motor control circuits. The previous circuits, based on programmable logic, are replaced with cheap, easily upgradable microcontrollers with significantly more computational power. The Atmel ATmega168P microcontrollers are responsible for communicating with the master Arduino and executing commands to move the motors. Communication between the microcontrollers is executed by the industry-standard I²C protocol, and is handled in dedicated hardware in the microcontroller. The slave microcontrollers run the FemtoOS real-time operating system (RTOS) to easily handle switching between communication and calculation tasks. A command voltage is sent over the SPI protocol to a digital-to-analog converter (DAC) which is subsequently amplified by a high-current operational amplifier. The quadrature pulse output from the motor is decoded by an optimized, interrupt-driven routine. The information about speed and position is fed into a PID-like feedback loop. PID loops are standard feedback loops for systems where

the detailed parameters cannot be known [6]; the relationship between supply voltage and actuator speed is an excellent example of such a system. PID controllers operate based on a three-term equation which contains a proportional, integral, and derivative term with respect to an “error” term, the difference between the desired value and the measured value. By taking the basic PID equation for controlling the velocity of the actuator by varying the supply voltage

$$V(t) = k_1 (v(t) - v_0) + k_2 \int_0^t (v(t) - v_0) dt + k_3 \frac{d}{dt} (v(t) - v_0) \quad (7)$$

and choosing to make the target velocity proportional to the remaining distance $v_0 = \sigma(x(t) - x_0) = \sigma\epsilon_x$, we substitute to derive

$$V(t) = k_1 \dot{x}(t) + k_2 x(t) + k_3 \ddot{x}(t) - \sigma \left(k_1 \epsilon_x(t) + k_2 \int_0^t \epsilon_x(t) dt + k_3 \frac{d}{dt} \epsilon_x(t) \right) \quad (8)$$

This equation is then implemented in software and controls the output value of the DAC.

4 Future Work and Experiments

In addition to performing upgrades on the plunger, we began studying the feasibility of several different reactions for measuring lifetimes in the rare-earth region. Because the plunger technique depends on sufficient recoil velocity to detect a Doppler-shift, the energies and momenta necessary to populate states with light beams available with the Notre Dame FN and 5U accelerators. In order to explore possible reactions, two simple Python scripts¹ were developed for calculating allowed kinematic outcomes. The script uses a subset of the AME2012 Atomic Mass Evaluation² [8] to calculate all possible combinations of target and recoil for an input projectile and ejectile over a range of energies. These values can then be plotted to visualize the reactions which might be possible for use with the plunger technique

¹Source code is attached to this PDF and can be retrieved by clicking [here](#).

²[Data](#) and [parser](#) script are also attached.

at Notre Dame.

5 Conclusions

The plunger technique is a valuable technique for measuring lifetimes of excited states, an important nuclear property. The Notre Dame plunger is in good condition electromechanically, but has seriously outdated control mechanisms. We have designed a new set of electronics for the plunger and will continue to implement them in the future. In addition, we have shown via kinematic calculations that the plunger technique is a feasible method for measuring lifetimes at the University of Notre Dame Nuclear Science Laboratory.

References

- [1] Ashkan Ashrafi and Hossein Golnabi. “A high precision method for measuring very small capacitance changes”. In: *Review of Scientific Instruments* 70.8 (1999), p. 3483.
- [2] Ashok Das and Thomas Ferbel. *Introduction to Nuclear and Particle Physics*. 2nd Ed. Hackensack, N.J.: World Scientific, 2003.
- [3] A Dewald, O Mller, and P Petkov. “Progress in Particle and Nuclear Physics”. In: *Progress in Particle and Nuclear Physics* 67.3 (July 2012), pp. 786–839.
- [4] Kenneth S Krane. *Introductory nuclear physics*. Hoboken, NJ: John Wiley & Sons, 1987.
- [5] R Krucken et al. “B(E2) Values in N150d and the Critical Point Symmetry X(5)”. In: *Physical Review Letters* 88.23 (May 2002), p. 232501.
- [6] Bob Pease. *What’s All This P-I-D Stuff, Anyhow?* June 1995. URL: <http://electronicdesign.com/analog/whats-all-p-i-d-stuff-anyhow>.
- [7] sagsaw. *Quadrature Diagram.svg*. Wikipedia, the free encyclopedia. Oct. 2007.
- [8] M Wang et al. “The AME2012 atomic mass evaluation (). Tables, graphs and references”. In: *Chinese Physics ...* (2012).

Alignment Sensitivity Study of the St. ANA Beam Line

Michelle Gervais

2014 NSF/REU Program

Physics Department, University of Notre Dame

Advisor: Manoel Couder

Mentor: Hyo Soon Jung

Mentor: Kiana Setoodehnia

Abstract

The St. ANA (STable Accelerator for Nuclear Astrophysics) accelerator is being prepared for use with the St. George recoil mass separator. The accelerator is in working condition for use in direct kinematic experiments but the St. George separator works with inverse kinematics and requires a highly controlled beam restricted by severe position and divergence parameters that are not achieved at the present time. A systematic sensitivity study was conducted using a simulation of the beam line in order to assess the impact of a misalignment in each optical element or in the beam itself. Tests were done with the beam to analyze how the beam behaves at various points in the line and to compare this data with simulation results to determine possible causes of misalignment. The results of these tests and simulations are that the beam characteristics are now better understood and the possible causes of the limitations have been narrowed down.

Introduction

St. George is a recoil mass separator designed for use in the study of nuclear reactions of astrophysical interest. The separator will be used to analyze (α,γ) reactions at low energies, the capture of a helium nuclei by a heavier element. St. George uses a heavy beam and a He gas target in order to reduce the effects of background radiation [1]. St. George is coupled to the St. ANA accelerator, to be of use, the beam of St. ANA must meet stringent position and angular specifications. The St. ANA accelerator is now in the process of being calibrated to the necessary parameters.

St. George requirements

The St. ANA accelerator is an upright 5MV electrostatic accelerator with a self-contained ion source. The accelerator is currently usable for direct kinematic experiments but the main purpose of the St. ANA is for use with the St. George recoil separator. St. George is a very sensitive recoil separator that requires a much more controlled beam. The beam's behavior must be well known as to its position and divergence, its position must stay within $\pm 0.5\text{mm}$ and it cannot diverge more than $\pm 1\text{mrad}$ from the central axis.

Beam line description

To produce a good beam that is useable for St. George there are many elements along the line that need to be aligned and tuned correctly. Figure 1 shows the various elements that control the beam and the permanent analysis elements used in tuning the beam.

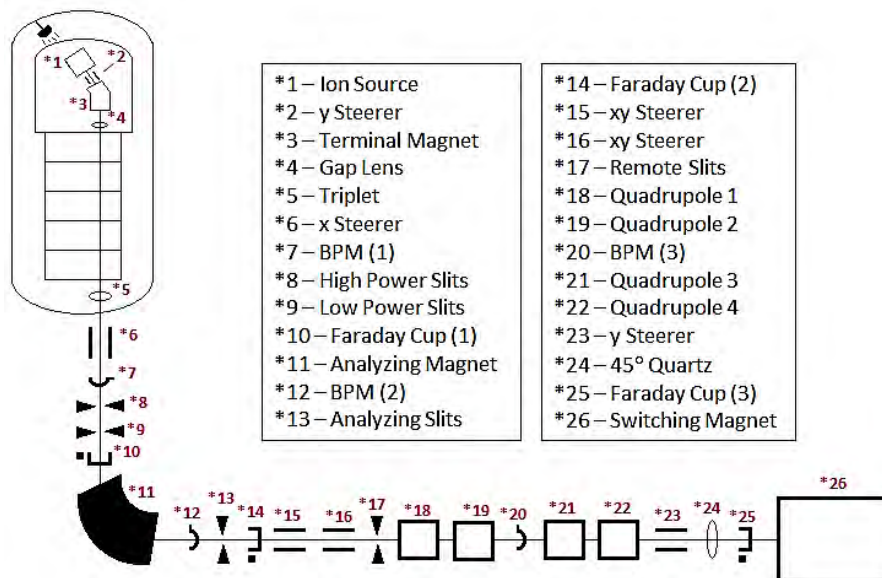


Figure 1: St. ANA permanent beam line elements

Beam tuning anomalies

The St. George line is connected to the 13° port on the switching magnet, thus for tuning purposes a beam visualization quartz was put on the 0° port which is the same distance away, to ensure a good tune of the beam at that distance. When hit with a beam the electrons in the quartz become excited and through fluorescence show the position of the beam upon it, a camera and video feed are then used to monitor this at a safe distance from the radiation. From the use of this quartz it was determined that all four of the magnetic quadrupoles steered the beam. The quadrupole's purpose is to focus the beam along one of the axes but if either the incoming beam or the quadrupole is misaligned in some way they can instead physically move the center of the beam spot around instead of only focusing. This leads to problems because if the beam needs to be focused at a different point in the beam line or retuned, a change in the quadrupoles would move the beam's position and take it off target, rendering it unusable.

Another main problem for testing is the current unreliability of several of the diagnostic elements. It was noticed that the amount of current on the remote slits was not physically possible; the current readings on cup 2, the remote slits, and cup 3 did not add up, the reading on the remote slits was far too high. The use of a volt meter showed that the individual slits were not electrically isolated from each other. This means that currently these slits can only be used to know when they cut the beam but not the amount of beam they are stopping.

Another variable to be aware of is when turned off the switching magnet has a non-zero residual field which deflects the beam to the right. To correct for this during

testing, the field in the magnet was turned on to oppose the residual field and a Hall probe was used to find when they were cancelled out.

From former tunings it was found that in order to center the beam on the quartz the two x steerers before the remote slits were needed (numbers 15 and 16 in Figure 1). This indicated that there was at least one misalignment of the beam in the x direction. It was also found that with the best possible tune quadrupoles 1 and 2 did not steer very much and quadrupoles 3 and 4 did.

The stability of the beam is also a concern; the spot itself has a wiggle or bounce to it that is not fully understood. This wiggle can be seen in both slit mode and GVM mode (Generating Volt Meter). It is thought that this may be a natural property of the beam itself at the energies being used.

Beam simulations

In order to understand the reason why the quadrupole magnets are steering and the possible impact on the beam from a misalignment in each of the elements, a systematic sensitivity study was conducted using a beam tracing program [2]. The simulated beam line starts at the analyzing slits and ends after the switching magnet. The program imitates the effects of the four magnetic quadrupoles and reference lines were put in to represent the various analyzing elements and restriction points. The output of the simulation has a graphical representation of the beam's path (Figure 2) and the coordinates of the center of the beam at the start, BPM 3 (Beam Profile Monitor), and at the final quartz. The remote slits were intentionally left out as they cannot be used in regular analysis of the beam.

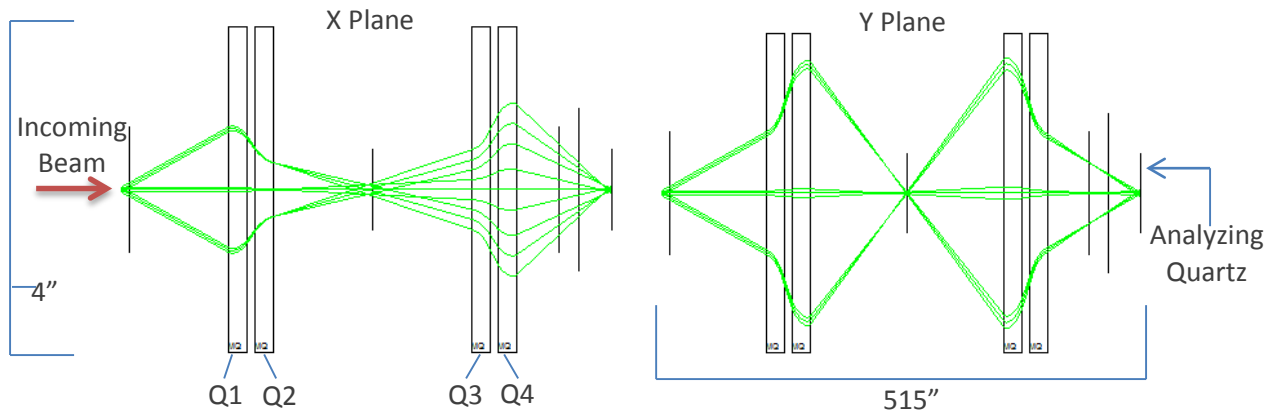


Figure 2: Projection of characteristic rays on the horizontal and vertical plane

Each of the magnetic quadrupoles and the initial beam were tilted and translated along the four cardinal axes to determine the effect of each element and to see if any type of misalignment or any one element had a more dramatic effect than the others. The quadrupoles were also rotated on axis around the beam. The magnitude of the misalignments used was made large enough to be noticed in the simulation but not so large as to be far outside the realm of reality. For translations this came out to be $\pm 1\text{mm}$ for both the quadrupoles and the initial beam, for tilts the quadrupoles were moved ± 1 degree and the initial beam was tilted ± 0.5 degrees. The radial offsets were 1 degree clockwise and counterclockwise.

The severity of the different types of misalignments were assumed to be somewhat comparable to each other, with that assumption it was found that overall a misalignment in the tilt of an element had a effect on the final beam spot than did translations. A radial offset in a quadrupole only changed the focus and not the position of the spot as would be assumed.

From here the elements underwent further analysis to see if the misalignments produced the same steering effect in the quadrupoles as was seen during actual runs, where quadrupoles 1 and 2 hardly steered and 3 and 4 did. This was done by inserting a misalignment and then altering each of the quadrupole field values one at a time by $\pm 10\%$ of their ideal value. As it was known from trials that there was a misalignment in the x direction, these misalignments were looked at to determine a possible cause for this. A tilt in either quadrupole 2 or 3 showed the greatest displacement in position on the quartz and when analyzed for steering properties they both showed the desired pattern. But a tilt in quadrupole 2 had a significant amount more steering making it the more harmful misalignment. Since a 1 degree tilt in a quadrupole is a rather large offset the amount of the tilt was then reduced in gradual steps and the beam's sensitivity to the change recorded. It was found that non negligible steering was still present in the quadrupoles when quadrupole 2 was tilted only 0.05 degrees (Figure 3). To determine what a 0.05 degree tilt translated to on an actual quadrupole several measurements were taken and some geometrical calculations were done to determine how much the quadrupole would need to be shifted to obtain the theoretical tilt amount. It was found that the downstream side of the quadrupole would need to be shifted about 0.5 mm while keeping the center of the upstream side in place, an amount easily within the mechanical error range.

Q2 Tilt Steer Check				
0.05 deg +x				
initial position [m]:	5.858E-04			
Quad	Up or Down (10%)	X Quartz Position [m]	Difference [m]	% Diff
1	+	5.858E-04	0.000E+00	0.000%
1	-	5.858E-04	0.000E+00	0.000%
2	+	6.266E-04	4.072E-05	6.951%
2	-	5.455E-04	-4.033E-05	-6.883%
3	+	1.633E-04	-4.226E-04	-72.133%
3	-	9.987E-04	4.128E-04	70.468%
4	+	1.835E-03	1.249E-03	213.196%
4	-	-6.903E-04	-1.276E-03	-217.824%

Figure 3: Q2 Tilt steering check

Experimental testing

In order to determine the behavioral characteristics of the incoming beam the line was broken just upstream of the first quadrupole and a quartz was put in. The analyzing magnet was set to send the beam through the center of the analyzing slits for this trial. From this it was found that even at this early point in the line the beam was already high and to beam right. The analyzing magnet could be used to pull the beam down but if it were to be centered in this way the beam would have a tilt and wouldn't be usable down the line. Several x and y field value pairs were found for the electrostatic steerers (numbers 15 and 16 in Figure 1) that placed the beam in the center of the quartz. The steerers were set to oppose each other in the direction of their change so that the combined effect might make the outgoing beam parallel to the ideal beam path axis.

Unfortunately it is unknown whether the beam hitting the quartz is tilted or only translated. To determine this additional testing will need to be done. One proposed way to test this is, with the quartz positioned before the first quadrupole, record the beam's position when the accelerator is ideally tuned. Then record the field values of

the steerers that center the beam and then go through several field values for each of the steerers individually and record the beam's position on the quartz. Once this is done the quartz is to be moved down the line either between the second and third quadrupoles or after the fourth. With this set up and all the quadrupoles turned off the same settings should be tested and the position on the quartz recorded. With this information and the measured distance between the two quartz positions the tilt if any of the incoming beam should be calculable. As the settings of the steerers that centered the beam on the nearer quartz placement probably will not create a centered beam further down the line, the influence of each of the steerers can be determined as well and a setting calculated from this that should yield field values that could be used.

Conclusion

In order to use the St. George separator we need the St. ANA accelerator to meet severe parameters. Currently one of the main issues is that the magnetic quadrupoles steer the beam. Through the simulation study and beam line testing the nature of the beam is now better understood. The type and magnitude of the influence that the various elements have on the beam can now be characterized such as how sensitive one quadrupole is compared to another. The most sensitive of the misalignments is a vertical tilt in the initial beam entering the line or a horizontal tilt in either the first or second quadrupole. Also it is well verified that by the time the beam arrives at the first quadrupole it is high and to the right and there is a way to test and see if this is caused by a tilt or translation of the beam.

Acknowledgements

Special thanks to Manoel Couder for assistance along the way and to Hyo Soon Jung and Kiana Setoodehnia for the mentoring during the experiment.

References

- [1] M. Couder, G.P.A. Berg, J. Görres, P.J. LeBlanc, L.O. Lamm, E. Stech, M. Wiescher, J. Hinnefeld, Nucl. Instr. and Meth. A 587 (2008) 35-45

- [2] COSY INFINITY Version 9: Nuclear Instruments and Methods in Physics Research
Section A: Accelerators, Spectrometers, Detectors and Associated Equipment
Volume 558, Issue 1, 1 March 2006, Pages 346–350

Graphitization Line for AMS Measurement of Carbon-14

Ben Guerin

Lindsey Riordan

2014 NSF/REU Program

Physics Department, University of Notre Dame

Advisor: Philippe Collon

Abstract

The Accelerator Mass Spectrometry (AMS) group at Notre Dame is currently working on implementing a reliable method to perform an AMS measurement of the Carbon-14 concentration in a sample. Carbon-14 is the most commonly measured element in AMS due to its applications in many different areas of study including biology, archeology, environmental science, and hydrology. There are two standard procedures for sample preparation. The procedure we need to perform depends on whether the ion source relies on solid or gas cathode material. Our summer project was focused on the development of a graphitization line. This line will enable our group to run carbon-14 samples in the accelerator by having a simple and brief process that converts a sample into graphite, which is essential for a reliable AMS measurement of carbon-14.

Introduction

Accelerator mass spectrometry is a very precise method to measure isotopic ratios in a given sample. The sample is loaded into the cathode, ionized, and launched through the beamline. In our tandem accelerator, ions are then passed through a stripper foil, where they lose their electrons. These newly charged particles are accelerated again as they approach ground potential. The first filter they pass through is a magnet that bends out the ions according to their mass per charge (M/Q) ratio. A Wien filter is also used. This functions as a velocity selector when the particles pass through its orthogonal electric and magnetic fields. The ions enter the detector and the counts are recorded.

With so many applications in AMS, one can see why having a way to measure carbon-14 concentrations could be quite significant in experimental research. The applications of carbon-14 AMS include: carbon dating, tracing ocean currents, and environmental studies. In comparison to previous carbon-14 measurements, in which the decays of carbon were directly counted, the AMS carbon-14 technique is a much more effective approach. This technique is more precise and time efficient since it is measuring the concentration directly with an accelerator, instead of waiting for individual beta decays to occur [beta]. Through this technique, the sample carbon is chemically separated from the original sample, converted into graphite, loaded into a cathode, and is then placed into a sputter ion source of an accelerator. The previous and still widely used method of carbon-14 measurements involved counting the number of decays. The only advantage to this approach is the lesser need for resources.

Carbon dating involves the measurement of carbon isotopic ratios. Carbon atoms are created in the atmosphere by the collision of solar rays with the atmosphere which produce

excited neutrons. The excited neutrons collide with nitrogen-14 producing carbon-14. These carbon atoms then enter the biosphere in two ways. The first is absorption into rain and precipitation; the second is photosynthesis. The carbon-14 concentration in an organic sample depends on the concentration in the atmosphere while the sample was alive since carbon enters the biosphere through photosynthesis. This required the scientific community to map the carbon-14 concentrations in the atmosphere as a function of time. To do this, they measured carbon-14 concentrations of samples with known ages. For example, the age of trees can be determined by their tree rings. Measuring the carbon-14 concentration of the tree will tell you how much carbon-14 was in the atmosphere when the tree was alive. With this standard correlation of concentration and time, the age of a sample can be determined.

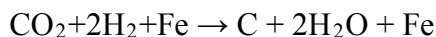
Methods

There are two standard methods for sample preparation when trying to measure isotopic ratios of carbon via accelerator mass spectrometry. The method we must do is called graphitization since we have an ion source that relies on solid cathode material and we are trying to perform an AMS measurement of carbon-14. Our methods are a combination of two different graphitization procedures performed by the Department of Archeology at Simon Fraser University and the Keck Carbon Cycle Accelerator Mass Spectrometry Facility/University of California, Irvine (KCCAMS/UCI).

To convert the carbon in a sample to graphite, we must first convert the carbon to carbon dioxide (CO_2), then to graphite. The sample is burned at nine hundred degrees celsius in the presence of copper(II) oxide (CuO). The carbon dioxide is then brought through the line to the prepared iron catalyst for the actual graphitization step. The reaction that occurs here is termed the Bosch reaction which requires a catalyst. We use iron (Fe) because of its reliability in past

attempts at graphitization and since its presence in the cathode will not deter the sputtering process. The Fe serves as a catalyst for the oxygen from the CO₂ to bond with the hydrogen (H₂), making water. The trap with the dry ice and ethanol serves to trap the water produced by this reaction, leaving graphite and Fe. This product is what will be loaded into the cathode wheel.

The process of creating graphite from a carbon sample has five general steps: preparing the line, preparing the catalyst, conversion of carbon to CO₂, transfer of CO₂, and the graphitization. Line preparation consists of flushing the whole line with H₂ several times. To prepare the catalyst, it must be heated to 400°C in the presence of H₂. The reaction will run until the H₂ is consumed [Nĭmec]. The conversion of carbon into CO₂ is a several hour process. The next phase is the actual graphitization. This is the step in which the Bosch Reaction occurs:



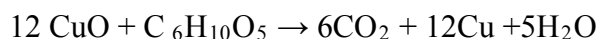
This is a chemical reaction between carbon dioxide and hydrogen that produces elemental carbon in the form of graphite, water and a 10% return of invested heat. This reaction requires the introduction of iron as a catalyst and requires a temperature level of 600°C[wiki]. What is left over at the end of the graphitization step (the Fe and Graphite) is what will go into a cathode which will then be used in AMS measurements.

Results

After ensuring the first section of our line was leak tight, we ran a test to convert the CuO and wood sample into carbon dioxide. After heating the mixture for two hours at nine hundred

degrees celsius, the heater was removed. Upon removing the heater, a clear visual of copper was left over, indicating the reaction had occurred. The quartz tube was tinted with a brown soot and bright orange-red dust was evidently left over in the base of the tube from this chemical reaction.

According to the equation for this reaction:



it is clear that we did in fact create CO_2 , which was expected. Because of the low precision on our pressure gauges, we could not quantify the product amounts.

Upon completing this step, we would then convert the carbon in the CO_2 into graphite. The CO_2 that was created would flow into the tube with the iron catalyst after opening the necessary valves. Performing an AMS measurement of a prepared sample's carbon concentration will determine how successful we were. We will be able to do this in a few weeks since our accelerator recently had difficulties with the charging chain.

Conclusion

Though we could not perform a measurement of the carbon-14 concentration of a sample, we do know how to improve on the line we currently have. The major modifications include larger tubing, a more powerful vacuum pump, and more precise pressure gauges. The small tubing we used did not allow the pump to pump down to the pressure we wanted. We will need to increase the internal diameter of the tubing. This will require disassembly and replacement of several parts. The only pump we had access to was not powerful enough to pump down to the pressure we needed even without the graphitization line attached and the vacuum pump closed off. Lastly, the pressure gauges we were using did not register readings small enough for our

purposes. We will need new pressure gauges. The AMS group hopes to accomplish these improvements in the near future.

"Accelerator Mass Spectrometry Radiocarbon Dating." *Accelerator Mass Spectrometry*. N.p., n.d. Web. 30 July 2014.

"Beta Analytic." *Introduction to Radiocarbon Determination by the Accelerator Mass Spectrometry Method* (n.d.): 1-16. *Beta Analytic Inc.* Web.

Beauchemin, Diane, Richard M. Caprioli, Michael L. Gross, and Dwight E. Matthews. *The Encyclopedia of Mass Spectrometry*. Amsterdam: Elsevier, 2010. Print.

"Bosch Reaction." *Wikipedia*. Wikimedia Foundation, 22 July 2014. Web. 30 July 2014.

"Graphitization Protocol - Hydrogen Reduction Method." (2004): 0-20. *UCI KCCAMS Facility*. Web. 14 June 2004.

Litherland, A. E. "Ultrasensitive Mass Spectrometry with Accelerators." *Annual Review of Nuclear and Particle Science* 30.1 (1980): 437-73. Web.

Němec, Mojmír, Lukas Wacker, and Heinz Gäggeler. "Optimization Of The Graphitization Process At Age-1." (n.d.): 1380-393. Web.

Vogel, J.s., J.r. Southon, D.e. Nelson, and T.a. Brown. "Performance of Catalytically Condensed Carbon for Use in Accelerator Mass Spectrometry." *Nuclear Instruments and Methods in Physics Research Section B: Beam Interactions with Materials and Atoms* 5.2 (1984): 289-93. Web.

W. Kutschera, *Int. J. Mass Spectrom.* (2013), <http://dx.doi.org/10.1016/j.jms.2013.05.023>

Gamma-ray Burst Analysis in Project Grand and Flare Seeking in UW CrB

ZEYU HAO

2014 NSF/REU Program

Physics Department, University of Notre Dame

ADVISOR(S): PETER GARNARVICH

ABSTRACT

Gamma-ray bursts (GRBs) represent “the most powerful explosions in the universe since the big bang” and the nature and the origin of GRBs remain a mystery. Understanding these can help us understand the stellar evolution, how black hole works, etc. However, most detections of Gamma-ray burst are limited in the low energy range. For example, Swift (Swift Gamma-Ray Burst Mission) covers the energy range 0.3-150keV; Fermi (Fermi Gamma-ray Space Telescope) covers the energy range 10keV-300GeV. Project GRAND is an air-shower detector array which is sensitive to 30-300GeV and 100-100 000TeV energies. Using the data from GRAND, we analyzed some of the GRBs which were detected by the satellite mission. Specifically, we extracted GRAND data during the time when GRBs happened and tried to find the increase of muons number to decide if we had observed the GRBs within our energy range. Another line of research this summer concerned UW Coronae Borealis (UW CrB). UW CrB is a low-mass X-ray binary system with a neutron star primary. Here we present the photometry made from the CCD images taken by LBT (Large Binocular Telescope) on June 30th while it simultaneously obtained spectra. We found a flare in the photometry, which represents an X-ray burst event from fusion on the neutron star. We confirm the flare and two other possible flares in an analysis of VATT (The Vatican Advanced Technology Telescope) photometry taken the same night as the LBT data.

Keywords: Gamma-ray bursts GRAND UW CrB photometry X-ray burst

Gamma-ray Burst Analysis in Project Grand

INTRODUCTION

Gamma-ray bursts were first discovered by Ray Klebesadel at Los Alamos National Laboratory. Since then, several experiments and spacecraft missions such as Compton Gamma Ray Observatory (CGRO), Swift, Fermi have been launched to study the phenomenon of GRBs. Every instrument detects the cosmos in limited energy ranges. BATSE, the instrument on CGRO, has channel 1, 2, 3 and 4, covering energy ranges 20-50keV, 50-100keV, 100-300keV, and $E > 300\text{keV}$, respectively. Swift's Burst Alert Telescope (BAT) covers energy range 15 - 150keV. Fermi has two instruments: LAT, which covers 30MeV-300GeV and GBM, which covers 150keV-30MeV. Higher energy range detections may help crack the mysteries of GRBs and answer some long standing questions across a broad range of questions.

Project GRAND in Notre Dame is an extensive array of proportional wire planes that measures the angles of individual muon tracks to within ± 0.25 degree. Muons are secondary particles produced by high-energy radiation incident (e.g., Gamma-rays) on the Earth's atmosphere. So by detecting the muons hit on GRAND, we can get information of GRBs. Project GRAND is sensitive to two energy band: 30-300GeV and 100-100 000TeV. Given that first band overlaps with the LAT energy detection range, we tried to correlate high energy bursts visible to LAT with data from GRAND.

METHODOLOGY

The GRBs we correlated are most from the circular archive of GCN (The Gamma-ray Coordinates Network). GCN is a system which distributes Locations of GRBs and other Transients (the Notices) detected by spacecraft. It also distributes the reports of follow-up observations made by ground-based, space-based and other particle observers.

We collected 22 GRBs detected by LAT from 2008, when Fermi was launched to 2013.

Our position (41.7057° N, 81.2196° W) allows us to see the sky in the range of declination -49° -- 90° . However, as a result of the structure of the detectors of GRAND, we can't cover the sky below the altitude 28.18° . So there are only several of the 22 GRBs we could see. Actually, after calculation, there are 7 in our range of sight.

	RA(hour, min,sec)	dec(deg, min, sec)	trigger	T90/s	T90 start	Alt	azi
GRB081024A	01 51 36.0	+61 18 00	10/24/2008 5:53:09	0.832	-0.832	69.9313	349.9307
GRB081224A	13 26 48.0	+75 06 00	12/24/2008 21:17:55	16.448	0.736	32.1362	345.6558
GRB090217A	13 39 36.0	-08 24 00	2/17/2009 4:56:43	33.281	0.832	9.0654	108.7584
GRB090323A	12 42 48.0	+17 06 00	3/23/2009 0:02:43	135.17	8.192	6.5165	72.8651
GRB090510A	22 14 24.0	-26 36 00	5/10/2009 0:23:00	0.96	-0.048	-72.6663	337.9451
GRB090626A	11 20 02.4	-33 30 00	6/26/2009 4:32:09	48.897	1.536	-17.784	241.9681
GRB090902A	17 39 45.4	+27 19 28	9/2/2009 11:05:08	19.328	2.816	-17.4526	337.6208
GRB091003A	16 46 04.8	+36 37 29	10/3/2009 4:35:46	20.224	0.832	15.6597	305.4555
GRB100116A	20 20 04.8	+14 27 00	1/16/2010 21:31:00	102.53	0.576	41.4178	250.0968
GRB100325A	22 00 57.6	-26 28 12	3/25/2010 6:36:08	7.104	-0.384	-50.3225	80.2078
GRB100414A	12 48 26.9	+08 41 30	4/14/2010 2:20:22	26.497	1.856	40.4194	119.5426
GRB100707A	23 24 16.8	-06 34 12	7/7/2010 0:46:39	81.793	1.088	-40.2733	53.9209
GRB100724A	07 58 23.8	+75 51 22	7/24/2010 0:42:06	114.69	8.192	36.6421	342.9226
GRB100826A	18 56 00.0	-23 11 24	8/26/2010 22:58:23	84.993	8.704	9.7999	132.9133
GRB110120A	04 06 24.0	-12 00 00	1/20/2011 15:59:39	28.417	0.256	-49.3869	52.3079
GRB110328B	07 50 36.0	+43 06 00	3/28/2011 12:29:19	141.315	1.024	-4.6223	351.9924
GRB110428A	00 21 12.0	+64 48 00	4/28/2011 9:18:30	5.632	2.688	34.7052	31.0098
GRB110625A	19 06 55.2	+06 45 18	6/25/2011 21:08:18	26.881	3.84	-30.5111	44.925
GRB110721A	22 09 49.4	-38 37 41	7/21/2011 4:47:44	21.822	0.003	-0.4489	143.7141
GRB110731A	18 42 01.0	-28 32 14	7/31/2011	7.485	0.003	-31.7791	259.9462

			11:09:30				
GRB130518A	23 43	46 03	5/18/2013 13:54	48.577	9.92	85.0849	333.1859

Table 1. The GRBs we tried to correlate. The GRBs highlighted are the GRBs in our sight range.

To extract the data corresponding to a certain GRB, we need appropriate time window and angle window to include the GRB's T90 and position in them.

In terms of time window, T90 is the duration during which 90% of the burst fluence was accumulated. The start of the T90 interval is defined by the time at which 5% of the total fluence has been detected, and the end of the T90 interval is defined by the time at which 95% of the fluence been detected. Muons number we detect at a fixed direction (i.e., fixed altitude and azimuth) is changing with time as a result of rotation of earth and the change of distance in the atmosphere that muons have get through to hit GRAND. So not only the data within T90, but also the data before and after T90 is needed so that we can get the information of background muons.

In terms of angle window, GRAND's resolution of altitude is about $\pm 4^\circ$ so we should add and subtract altitude and azimuth 4° to get the angle window which covers the position where the GRB happened.

After extracting the data we need, we made the graph of muons number v.s. time. This is similar to a light curve since the number of muons produced by GRB is positively relative to the intensity of the GRBs.

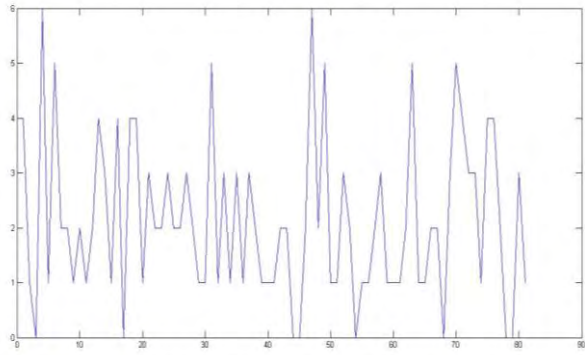


Figure 1. GRB100414A Total number of muons: before T90: 65, during T90: 52, after t90: 56

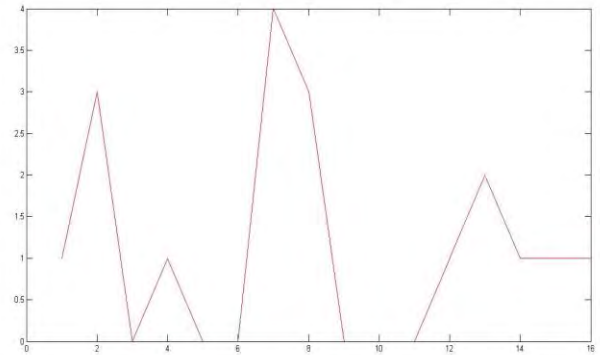


Figure 2. GRB110428A Total number of muons: before T90: 5, during T90: 7, after t90: 6

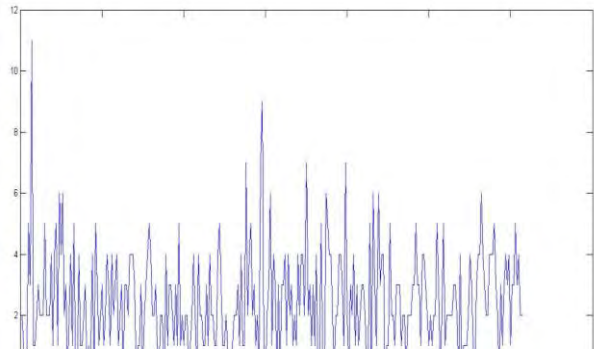


Figure 3. GRB100106A Total number of muons: before T90: 244, during T90: 252, after t90: 259

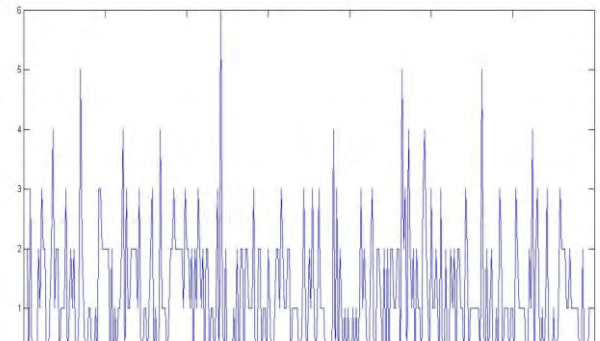


Figure 4. GRB100724A Total number of muons: before T90: 157, during T90: 125, after t90: 142

CONCLUSION

In conclusion, we didn't find the increase of number of muons we expect during T90.

And conversely, sometimes the numbers of muons within T90 are even less than the time before and after T90. Two causes may lead to these results. One is that the GRBs we were trying to correlate are not with enough energy. However, according to the detection of spacecrafts, this cause is less likely for it's not rare to detect the photons with high energies. Another cause is that GRBs are just covered by the noise around it. Even if GRBs can produce muons, the increase led by the GRBs are easily covered by statistical errors if there are more other gamma-ray sources such as the sun.

Flares Seeking in UW CrB

INTRODUCTION

UW CrB (also known as MS1603+2600) was discovered during the Einstein medium sensitivity survey (Morris et al. 1990). Morris et al. also identified the optical counterpart of the X-ray source. Since then, UW CrB has remained a peculiar source for there is not a firm classification for it. Our current understanding is that it is an Accretion Disc Corona (ADC) low mass X-ray binary. In this report, we will present the photometry of UW CrB made from the CCD images taken by LBT (Large Binocular Telescope) on June 30th. We will show the flare we found in the photometry. We will also show the VATT photometry of UW CrB taken at the same night as the LBT data.

METHODOLOGY

LBT has two 8.4 meter diameter primary mirrors and the two mirrors are mounted with a 14.4 meter center-center separation, which make telescope be equivalent in light gathering power to a single 11.8 meter instrument. The images we got are taken on June 30th from 6:17:29 to 7:55:24. LBT took a picture every 35 seconds, 17 seconds of which are exposure time while the rest was used to process the CCD images.



Figure 1. One of the images taken by LBT. Star 1 and star 2 are comparison stars. Star V is UW CrB.

At the same time, another telescope was also taking pictures of UW CrB. VATT is a 1.8m Alice P. Lennon Telescope located at the Mount Graham International Observatory (MGIO) in southeastern Arizona. It took 270 pictures in total from 7:13:46 to 9:41:45.

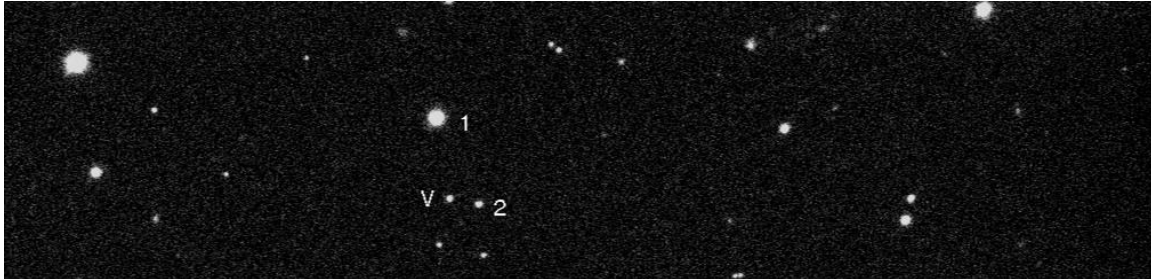
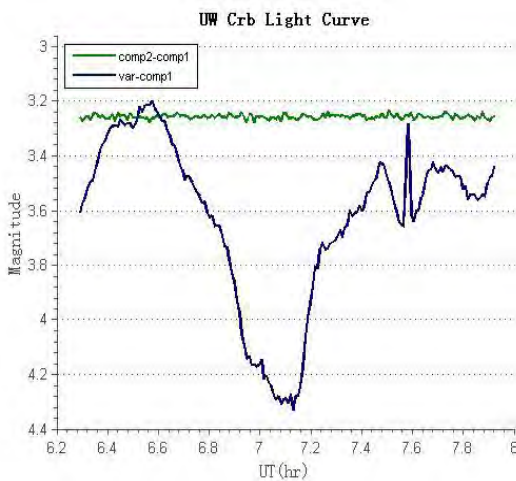
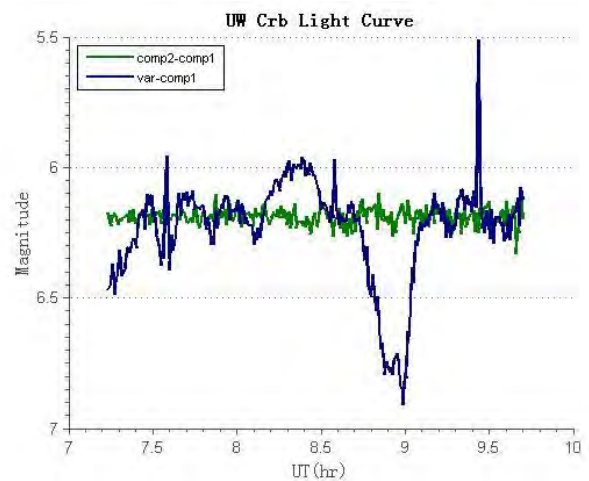


Figure 2. One of the images taken by VATT. Star 1 and star 2 are comparison stars. Star V is UW CrB.

We used Iraf (Image Reduction and Analysis Facility) to make the photometry of every image. We assume the star 1 and star 2 are ordinary stars with constant magnitudes and we use them as comparison stars. Star V is UW CrB, which we are studying. Since LBT is a ground-based telescope, the absolute magnitude we measure for each star will be influenced by the weather factors (e.g., weather). So we measured the difference between the magnitudes of star 1 and star 2 and the difference between the magnitudes of star 1 and UW CrB.



*n by Li
r stana*



There can be seen there is a spike at the time about 7:36 in the LBT's photometry. And in the photometry of VATT, there are three spikes in total. Since star 1's magnitude is

constant, the spike represents a sudden increase of the brightness of UW CrB, which is a flare. And according to the time when these flares happened, the first flare in LATT's photometry is corresponding to the flare in the photometry of LBT.

CONCLUSION

We found an optical flare in the photometry of UW CrB made from CCD images taken by LBT. And using the CCD images taken by VATT, we confirmed the flare which happened at 7:36. Meanwhile, we found two more flares from the VATT's CCD images. Both LBT and VATT were using V filter, which is in visible range. So the flares actually are optical bursts, which are caused by X-ray bursts. Our founding may help to find the phase distribution of optical bursts and may further help to explain the mechanism of optical bursts of UW CrB.

REFERENCE

- [1] Morris S.L., Liebert J., Stocke J.T., Gioia I.M., Schild R.E. Wolter A., 1990, Ap.J, 365, 686.
- [2] GCN-The Gamma-ray Coordinates Network: <http://gcn.gsfc.nasa.gov/>
- [3] FERMIGBRST-Fermi GBM Burst Catalog:
<http://heasarc.gsfc.nasa.gov/W3Browse/fermi/fermigbrst.html>
- [4] Fermi Gamma-ray Space Telescope: <http://fermi.gsfc.nasa.gov/>

Study of the Pure Double Folding Optical Model for 100 MeV/u

Deuteron Scattering

Kevin Howard

2014 NSF/REU Program

Department of Physics,

University of Notre Dame

Advisor: Prof. Umesh Garg

(Dated: July 31, 2014)

Abstract

The centroid energies of the giant monopole resonance (GMR) in nuclei are important because they are directly related to the nuclear incompressibility, an important quantity in the nuclear equation of state. It is necessary to examine the properties of the GMR in nuclei far from stability using advanced experimental techniques. The optical model for deuteron scattering is of interest from the point of view of performing these studies in inverse kinematics. Most studies on deuteron optical potentials have been done at lower energies and using the phenomenological optical model. However, this model has been shown to overestimate the cross sections for the low-lying discrete states in the case of light mass nuclei. Recent developments in theory allow for the optical model real and imaginary volume potentials to be calculated using a double folding model with the help of the computer code `dfpd5`. For the first time these calculations are used to model the elastic and inelastic angular distributions in ^{28}Si , ^{58}Ni , and ^{116}Sn nuclei. The experiment was performed at the Research Center for Nuclear Physics, Osaka University, Japan, using a 100 MeV/u deuteron beam. The double folding model is found to well-replicate the experimentally observed angular distributions, and proves to be a viable alternative to the phenomenological model with less restrictions on its range of applicability (e.g., higher energy beams, lower mass targets).

Introduction

The three important properties of the nuclear equation of state are the binding energy per nucleon at saturation density ($E/A|_{\rho=\rho_0}$), the saturation density of the nucleus (ρ_0), and the nuclear incompressibility (K_∞). This equation of state is crucial in the understanding of various astrophysical phenomena, including the lifetimes of neutron stars and the behaviors of supernovae. It is necessary to constrain the values of K_∞ such that the curvature and structure of the equation of state can be understood. The incompressibility of finite nuclear

matter, K_A , is readily calculable in closed form from the centroid energies, E_{GMR} , of the giant monopole resonance (GMR) [1, 2] :

$$E_{GMR} = \hbar \sqrt{\frac{K_A}{m \langle r^2 \rangle}}. \quad (1)$$

From K_A , K_∞ can be obtained and it is of great physical significance to study such resonances in order to accurately determine this quantity. It has become a recent interest from an experimental standpoint to use deuterium probes on various unstable target nuclei so that these resonances can be measured and analyzed in isotopes that are far from stability. The experimental difficulties associated with the short lifetimes of these exotic nuclei can be overcome by using an inverse kinematic approach in which the heavy nuclei are made incident upon a deuterium target [3]. Moreover, deuterium can be used also as a detector gas in an active-target projection chamber (AT-TPC) apparatus. It is necessary to study the deuteron scattering with the optical model so as to become confident in the model for application to experiments using inverse kinematics. The optical model allows one to model the interaction potential; for example, the optical model potential can be used for distorted wave Born approximation (DWBA) calculations to perform a multipole decomposition analysis in the study of the giant resonances [2]. The pure double folding optical model will be assessed for its capability to model the (d,d') reaction.

Theory

The optical model potential simplifies the complicated nucleon-nucleon interactions and represents them in terms of a complex potential:

$$U(r) = -V_v(r) - iW_v(r) - V_s(r) - iW_s(r) + V_{s.o.}(r) + V_c(r), \quad (2)$$

where V and W represent the real and imaginary components of the contributions from the volume (subscript v), surface (subscript s), spin orbit (subscript $s.o.$), and Coulomb (subscript c) potentials [4, 5].

$$\begin{aligned}
V_v(r) &= V_v f(r, R, a_v) \\
W_v(r) &= W_v f(r, R, a_v) \\
V_s(r) &= -4a_s V_s \frac{d}{dr} f(r, R, a_s) \\
W_s(r) &= -4a_s W_s \frac{d}{dr} f(r, R, a_s) \\
V_{s.o.}(r) &= V_{s.o.} \left(\frac{\hbar}{mc} \right)^2 \frac{1}{r} \frac{d}{dr} f(r, R, a_{s.o.}), \tag{3}
\end{aligned}$$

where V_i and W_i represent the depths of the respective potentials, $R_i = r_{0_i} A^{1/3}$, and a_i is the diffuseness parameter. The form factors f_i take the general aforementioned two parameter Woods-Saxon form [4]:

$$f_i(r, R_i, a_i) = \left(1 + \exp \left[\frac{r - R_i}{a_i} \right] \right)^{-1}. \tag{4}$$

More recently, it has become possible to use a double folding formalism to describe the real and imaginary volume potential in terms of individual nucleon pair interactions between the projectile and target nuclei [5, 6], while using the previously mentioned Woods-Saxon to reproduce the shapes for the other potentials. Thus, in this work it is the parameters of the surface and spin orbit optical model potentials, V_i , W_i , r_{0_i} , and a_i that are used to fit the elastic angular distributions. In order to confirm the uniqueness of the optical model parameter set obtained in the elastic fitting process, the parameter set is then used to calculate the angular distributions for low lying discrete states with known $B(E2)$ and $B(E3)$ values from literature. The correct set of optical model parameters will, in principle,

accurately reproduce the angular distributions for the low-lying discrete states. [6, 7].

Analysis

Elastic and inelastic deuteron scattering data from the Research Center for Nuclear Physics (RCNP), Osaka University, Japan, at beam energy $E = 196$ MeV were analyzed with the computer code ECIS-97 [8]. The double folding calculations were computed with dfpd5, an unpublished code that was acquired via private communication from Prof. Dao Khoa. The density distribution parameters used in the double folding calculations are listed in Table I. These double folded potentials were then explicitly specified within the ECIS-97 input file. The real volume potential normalization N_R was fixed at unity during the analysis, while the normalization N_I was allowed to vary within 15% of unity [6]. It was observed that when small variations in N_I were allowed in the elastic fitting process, the agreement with experimental angular distributions noticeably increases for both the elastic fitting and discrete state calculations.

	$^{58}\text{Ni}(1)$	$^{58}\text{Ni}(2)$	^{116}Sn	$^{28}\text{Si}(1)$	$^{28}\text{Si}(2)$
ρ_0 (fm^{-3})	0.162	0.176	0.155	0.175	0.167
c (fm)	4.20	4.08	6.67	3.15	3.16
a (fm)	0.515	0.515	0.545	0.475	0.523

TABLE I. Mass density distribution parameters input to dfpd5 to compute double folded real and imaginary volume potentials. Parentheses indicate enumerations of parameter sets, if multiple sets were used. [2, 5, 6, 9]

When available, multiple sets of density distribution parameters were tested to determine their impact on the double folding calculations and on the subsequent fitting and reproductions of the low lying discrete state distributions. The elastic fits produced in this study are shown in Fig. 1. Figure 2 shows a comparison of double folding calculations for ^{58}Ni using two sets of density parameters from the literature [6, 9]. It is noted that for ^{58}Ni , the second density distribution (Par. Set 2) shows better agreement in both the elastic and

discrete state with experimental data. Similar calculations will be completed for ^{28}Si with an alternative density distribution.

Availability of experimental angular distributions for comparison in the case of the ^{116}Sn nucleus allows for better constraints on the optical model parameter sets found in the elastic fitting process. Comparison plots for the 2^+ and 3^- angular distributions for ^{116}Sn are shown in Figs. 3 and 4. The optical model parameter sets found in analyses of various target nuclei are summarized in Table II. The 3^- state calculations, when using the adopted value of $B(E3) = 0.132 \pm 0.014 e^2b^2$, underestimate the cross sections of the angular distribution by a factor of 16% [10]. The $B(E3)$ value within the error limit is able to reproduce the experimental angular distribution. The analysis of ^{116}Sn implies that having multiple available discrete level angular distributions allows for better constraints on the optical model parameter sets found in the elastic fitting process.

Beyond the density dependencies of the double folding model, it is noted that there is

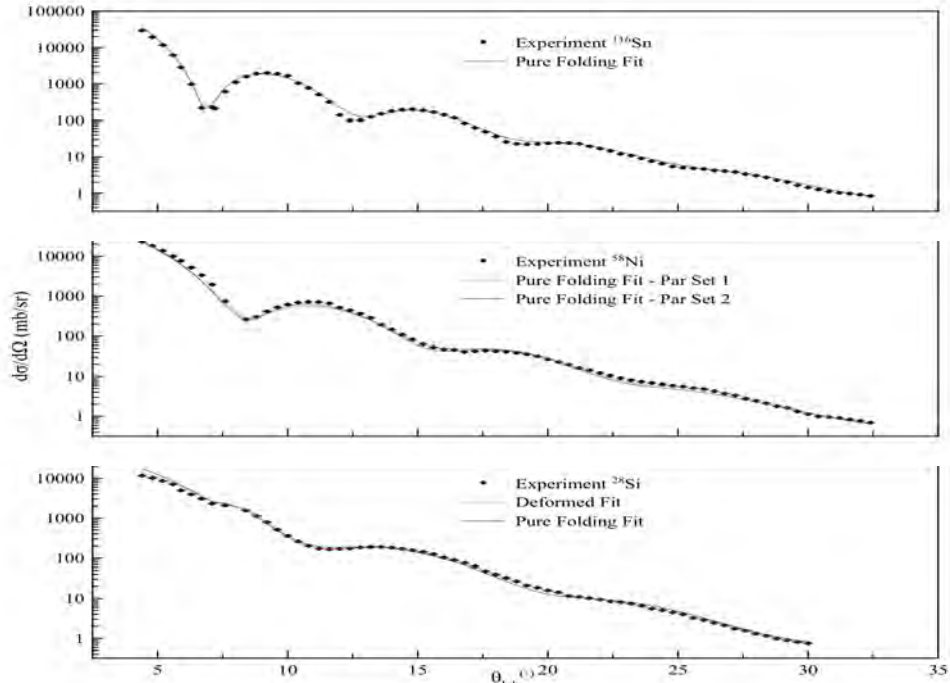


FIG. 1. Comparison of elastic fits for various models, density distributions and target nuclei with the (d,d') reaction at energy $E = 196$ MeV.

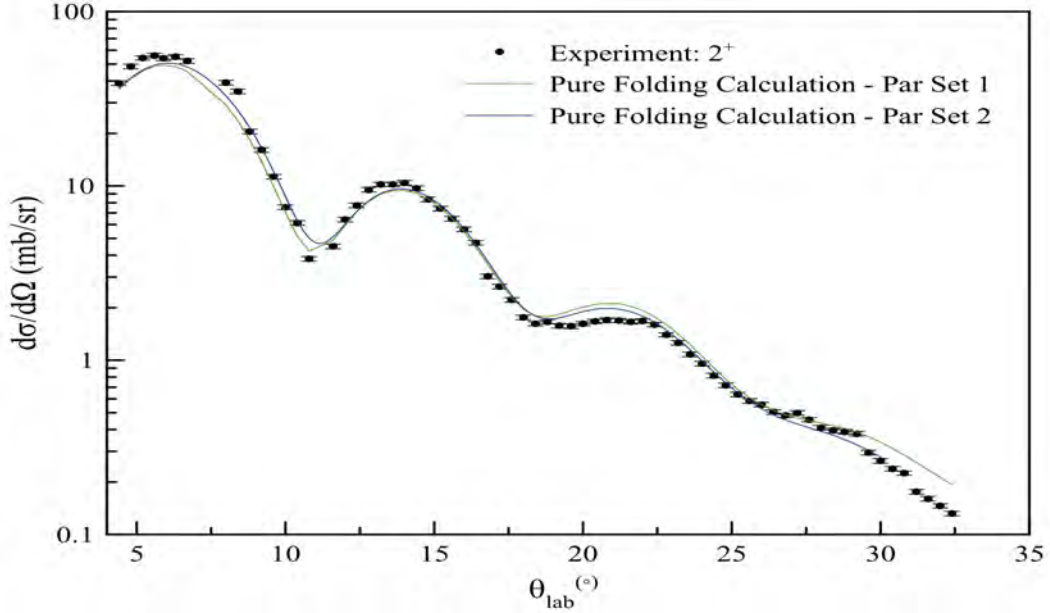


FIG. 2. Comparison of 2^+ calculations for $^{58}\text{Ni}(d,d')$ at $E = 196$ MeV using varying density parameters from Table I.

marked improvement in the reproduction of excited state angular distributions as compared to the deformed optical model. The phenomenological model - consisting of purely Woods-Saxon potentials as described in Eq. (2) - becomes incapable of reproducing behaviors for light masses [12]. This is made evident by the analysis of ^{28}Si . The improvement of the pure double folding model in reproducing deuteron scattering phenomena in light target masses over deformed model calculations is significant. When the deformed potential model is applied to $^{28}\text{Si}(d,d')$, it drastically overcalculates the cross sections by approximately 40%. The double folding model is able to reproduce the experimental distributions with better

	^{58}Ni	$V_i(\text{MeV})$	$r_{0_i}(\text{fm})$	$a_i(\text{fm})$	^{116}Sn	$V_i(\text{MeV})$	$r_{0_i}(\text{fm})$	$a_i(\text{fm})$	^{28}Si	$V_i(\text{MeV})$	$r_{0_i}(\text{fm})$	$a_i(\text{fm})$
N_I	0.86				1.13				1.00			
$V_s(r)$		-11.6	1.29	0.863		-6.79	1.27	1.12		-0.186	1.84	0.473
$W_s(r)$		13.0	0.450	0.628		22.0	0.629	0.721		0.715	1.81	0.241
$V_{s.o.}(r)$		3.18	1.26	0.987		1.11	1.48	0.983		2.05	1.38	0.742

TABLE II. Optical model parameters for analyses of ^{58}Ni , ^{116}Sn , and ^{28}Si . Double folded potentials were calculated using density parameters from Table I.

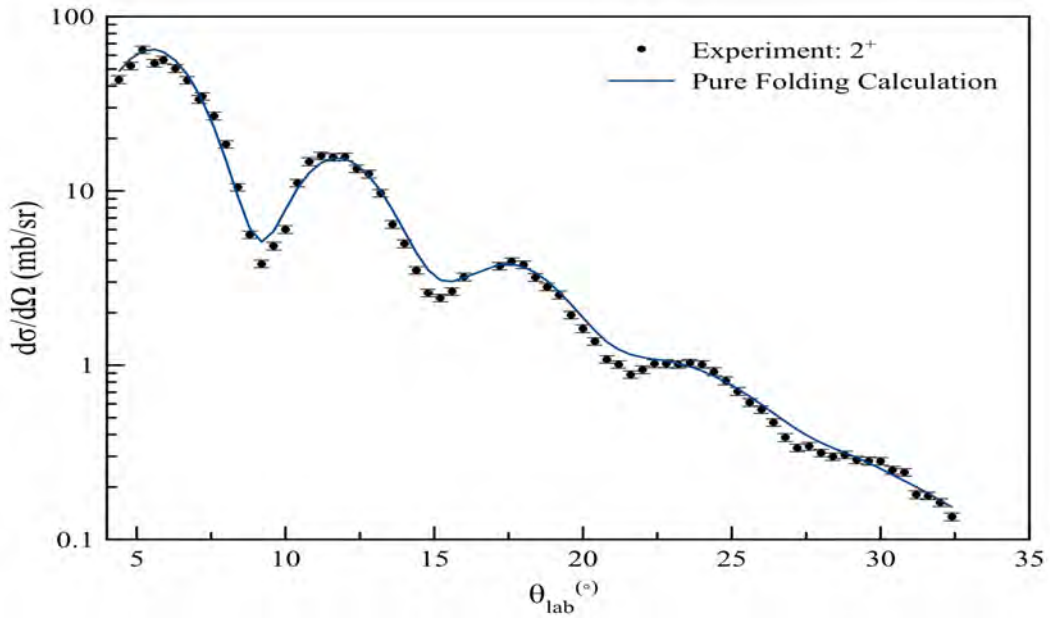


FIG. 3. 2^+ calculations for $^{116}\text{Sn}(d,d')$ at $E = 196$ MeV completed using double folding potentials with density parameters from Table I.

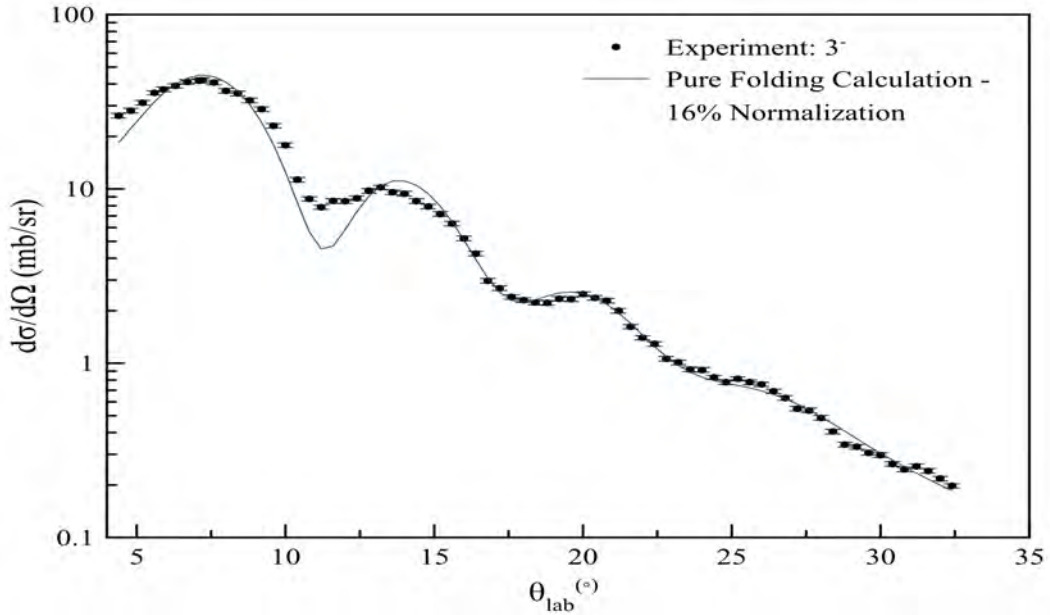


FIG. 4. 3^- calculations for $^{116}\text{Sn}(d,d')$ at $E = 196$ MeV completed using double folding potentials with density parameters from Table I.

structure; this is while using the adopted value of the $B(E2)$ value rather than a 40% lower value as for the phenomenological model calculations (Fig. 5).

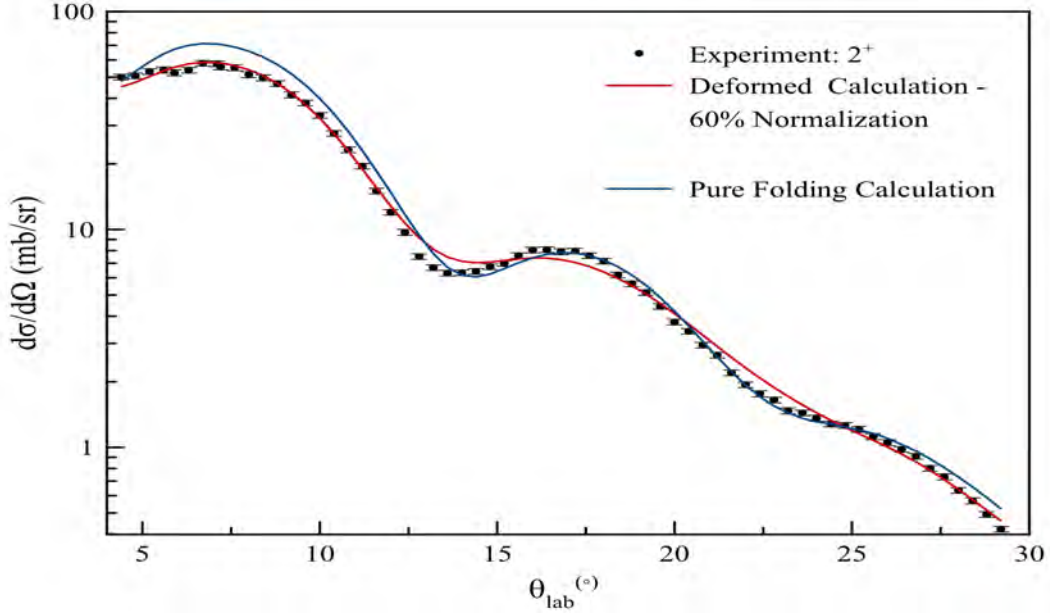


FIG. 5. Comparison of 2^+ calculations for $^{28}\text{Si}(d,d')$ at $E = 196$ MeV for both the pure double folding and deformed potential models.

Conclusions

It is noted that double folding is a new alternative to producing optical model representations of the (d,d') reaction with a series of target nuclei of varying masses. It is concluded that it is a viable alternative, to reproduce discrete state distributions from the deuterium reaction. In particular, double folding has been found to substantially improve in the modeling of the experimentally observed angular distributions for light mass nuclei.

These optical model parameters should be used for GMR and multipole decomposition analysis calculations to investigate the giant resonances in the target nuclei. In addition, for the lighter projectile deuteron reactions, it has been observed that due to the limited structure for higher angles in ^{28}Si and ^{58}Ni , more data should be taken and analyzed with this optical model at $\theta_{\text{lab}} > 35^\circ$ to better examine the structure in the angular distributions and to improve the analysis of the associated optical model parameters (Figs. 2, 5).

Acknowledgments

The author would like to thank the University of Notre Dame Department of Physics for acceptance into its Research Experience for Undergraduates Program. In particular, the author would like to thank both Professor Umesh Garg and Darshana Patel for guidance throughout the proceedings of this study.

References

- [1] M. Hedden, U. Garg, “The isoscalar giant dipole resonance in ^{208}Pb and the nuclear incompressibility,” *Nuclear Physics in the 21st Century*, 2002, (880).
- [2] T. Li, “Isoscalar giant resonances in the Sn nuclei and implications for the asymmetry term in the nuclear-matter incompressibility,” *Physical Review C* (2010) **81**
- [3] D. Patel “Excitation of giant monopole resonance in ^{208}Pb and ^{116}Sn using inelastic deuteron scattering,” *Physics Letters B* (2014) **735** 387-390
- [4] W. Daehnick “Global optical model potential for elastic deuteron scattering from 12 to 90 MeV,” *Physical Review C* (1980) **21**
- [5] G.R. Satchler, “Folding model potentials from realistic interactions for heavy-ion scattering,” *Physics Reports* (1973) **55** (3) 183-254.
- [6] D.T. Khoa, “Generalized folding model for elastic and inelastic nucleus-nucleus scattering using realistic density dependent nucleon-nucleon interaction,” *Nuclear Physics A*, (2000), **668** 3-41.
- [7] F.E. Bertrand, “Giant multipole resonances - perspectives after ten years,” Session IV: Giant resonances and other high-lying excitations, Oak Ridge National Laboratory (1981).
- [8] J. Raynal, in: *Proceedings of the Workshop on Applied Nuclear Theory and Nuclear Model Calculations for Nuclear Technology Application*, Trieste, Italy, 1988.
- [9] G.R. Satchler, “A simple effective interaction for peripheral heavy-ion collisions at intermediate energies,” *Nuclear Physics A* (1994) **579**, 241-255
- [10] T. Kibédi, “Reduced electric-octupole transition probabilities, $B(E3; 0_1^+ \rightarrow 3_1^-)$ – an update,” *Atomic Data and Nuclear Data Tables*, (2002), **80**, 35-82.
- [11] National Nuclear Data Center, *Reduced Transition Rate Probabilities*: Brookhaven National Laboratory. www.nndc.bnl.gov
- [12] A.J. Koning, “Local and global nucleon optical models from 1 keV to 200MeV,” *Nuclear Physics A* (2003) **713** (1), 231–310.

Modal noise mitigation in optical fibers with small circular diameters

Patricia Huestis

2014 NSF/REU Program
Physics Department, University of Notre Dame

Advisor: Dr. Justin Crepp, PI

ABSTRACT

“Modal noise” occurs when light propagating through an optical fiber excites specific modes and creates an interference pattern; its effects can introduce spurious Doppler shifts when acquiring precise radial velocity (RV) measurements of nearby stars in search of extrasolar planets. The severity of modal noise worsens as the wavelength of light increases and also as the optical fiber core diameter decreases. iLocator, a planet-finding instrument currently being developed for the Large Binocular Telescope, will be the world’s first diffraction-limited Doppler spectrometer. It aims to work in the near-infrared (NIR) and use optical fibers with core diameters no larger than 50 microns, so modal noise could be especially problematic. This paper discusses an inexpensive solution to reduce modal noise in 50 micron core optical fibers at a wavelength of 632.6 nm, though is also applicable to multi-mode fibers of various sizes. Our preliminary experimental results demonstrate that circular fiber motion is an effective method for spatially smearing out the modal noise pattern in small core fibers. Such mitigation schemes will aid in the design of a mechanical agitator for iLocator that will ameliorate modal noise patterns. In doing so, we will be able to achieve the first RV measurement precisions below 1 m/s in the NIR region. Ultra-precise RV measurements will allow for the detection and study of “Earth-like” exoplanets orbiting in the habitable-zone around nearby M-type stars, ultimately giving us clues to how our own planet formed and developed.

INTRODUCTION

iLocator, or the **infrared Large Binocular Telescope Exoplanet Reconnaissance spectrometer**, is an instrument currently being developed for use on the Large Binocular Telescope (LBT) in Arizona. It will be the world's first diffraction-limited Doppler spectrometer which will lead to several key advantages over previous spectrometers. iLocator will operate at near-infrared (NIR) wavelengths to detect Earth-like exoplanets orbiting M-type stars.

Modal noise occurs in optical fibers when light propagating through them excites certain modes and creates interference patterns. As the path taken by the light changes, i.e. when changes in the fiber mechanical boundary conditions change, so does the modal noise pattern. When the fiber output pattern changes, so does the illumination of the spectrograph optics, which modifies the spectrum at the detector, introducing radial velocity (RV) shifts.

The light path may be altered by introducing stress into the fiber via agitation. Modal noise may be suppressed using a mechanical agitator [Mahadevan, 2014]. In general, the fewer the number of modes, the more difficult it is to mix those modes. Doppler shifts resulting from ineffective mode mixing will result in false positive planet signals. It is therefore imperative to completely smear out the modal noise patterns to ensure the success of iLocator.

The maximum number of modes (M) for coherent light of wavelength λ in a circular fiber with core diameter d and numerical aperture NA is given by

$$M = 0.5 \left(\frac{\pi d NA}{\lambda} \right)^2$$

The number of modes decreases as the wavelength increases and as the diameter of the fiber decreases. Compared to previous generation instruments iLocator will use both larger wavelengths of starlight and smaller core diameters, exacerbating the effect of modal noise.

EXPERIMENTAL APPROACH

The setup for our experiment is shown in Figure 1. Our modal noise suppression system consists of two standard fiber coupling optics and a mechanical agitator. Information about the equipment used can be found in Table 1.

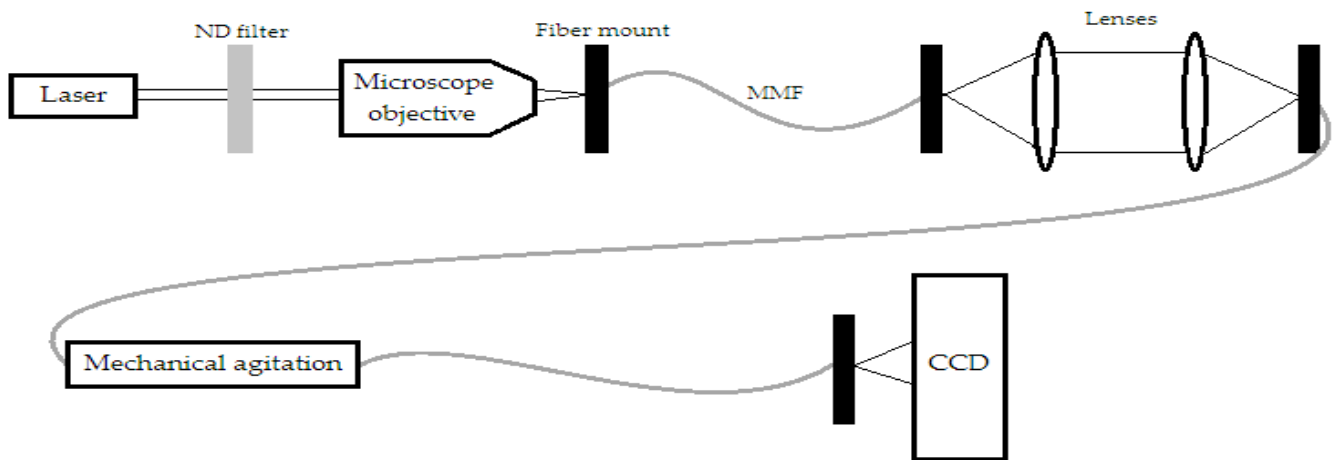


Figure 1: Schematic of modal noise experimental setup.

Table 1: Parts list and model numbers for experimental setup.

Part	Model Information
Laser	Melles-Griot 1 mW HeNe laser (Model 05LLR811-230)
Optical fibers	Thorlabs M42L0- (50 micron) and M67L0- (25 micron)
Optics (lenses, ND filters, fiber mounts)	Off-the-shelf Thorlabs
CCD	SBIG STF-8300M
Microscope objective	Olympus Plan N 10x/0.25
Software	MaximDL and MATLAB

Before designing the mechanical agitator, several hand agitation tests were conducted to see which motion best smeared out the modal noise pattern. The first motion tested was suggested by McCoy et al. (2012). The fiber was held by hand in two separate locations. The fiber was then manually moved up and down with a motion similar to a sine wave and each hand was exactly out of phase with the other. The amplitude of the motion was approximately 7 cm with a frequency of 1-2 Hz and was referred to as the “double sine wave” agitation. We compared this agitation to a “single sine wave” agitation, i.e. with the fiber being held and moved in only one spot. The same amplitude and frequency was tested. The last round of motions tested was inspired by Plavchan et al (2013) and their “woofer/tweeter” design. The “woofer” was a toy motor that provided large amplitude and small frequency agitation, while the “tweeter” was a cell phone vibration motor that provided small amplitude and large frequency agitation. The fiber was held in a single place and rotated about different

axes. Rotation about the z-axis (pointing out of the optical bench) was referred to as the “helicopter” design; rotation about the x-axis (along the axis of the fiber) was referred to as the “jumprope” design, and rotation about the y-axis was referred to as the “waterwheel” design. Each rotational case had a radius of about 4 cm and an amplitude around 1-2 Hz.

The first test suggested that circular motion was slightly better at ameliorating modal noise in the 50 micron fiber, as shown by a more uniform illumination pattern in Figure 2. The circular motion tests did not have a clear front runner, so the “helicopter” motion was selected due to the constraints in mechanical designs. The circular motion of the agitator was achieved by using a planetary gear set from a Japanese toy company. Attached to the gear set was a custom arm that provided the option of a larger amplitude, and a loose slip joint that prevented the fiber from being twisted around the base the agitator was mounted on.

RESULTS

Figure 3 shows the CCD images for the testing done with the mechanical agitator. The larger frequency does a better job of smearing out the modal noise pattern for both the long and short arms, but the effects are especially apparent for the long arm. In fact, the long arm with a higher frequency does the best in terms of the motor agitation, and it even compares with the hand agitation. Although the contrast between

the mixed mode areas is starker in the motor agitation, the modal noise pattern is overall less patchy for the motor agitation when compared to the hand agitation.

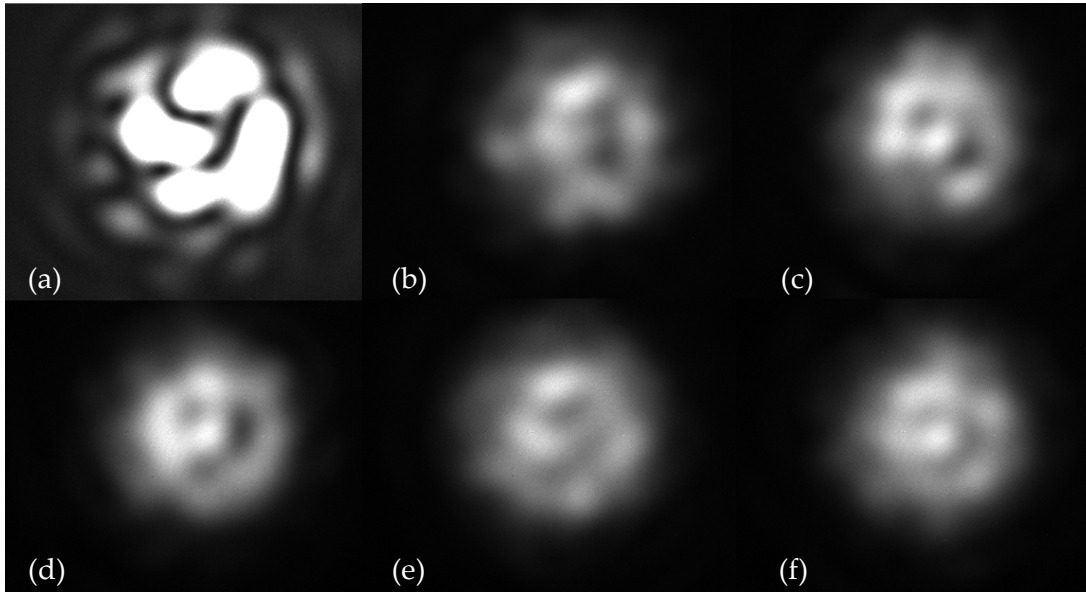


Figure 2: CCD images of (a) free 50 micron MMF; (b) 50 micron MMF with “single sine wave” hand agitation; (c) 50 micron MMF with “double sine wave” hand agitation; (d) 50 micron MMF with “jumprope” hand agitation; (e) 50 micron MMF with “waterwheel” hand agitation; (f) 50 micron MMF with “helicopter” hand agitation.

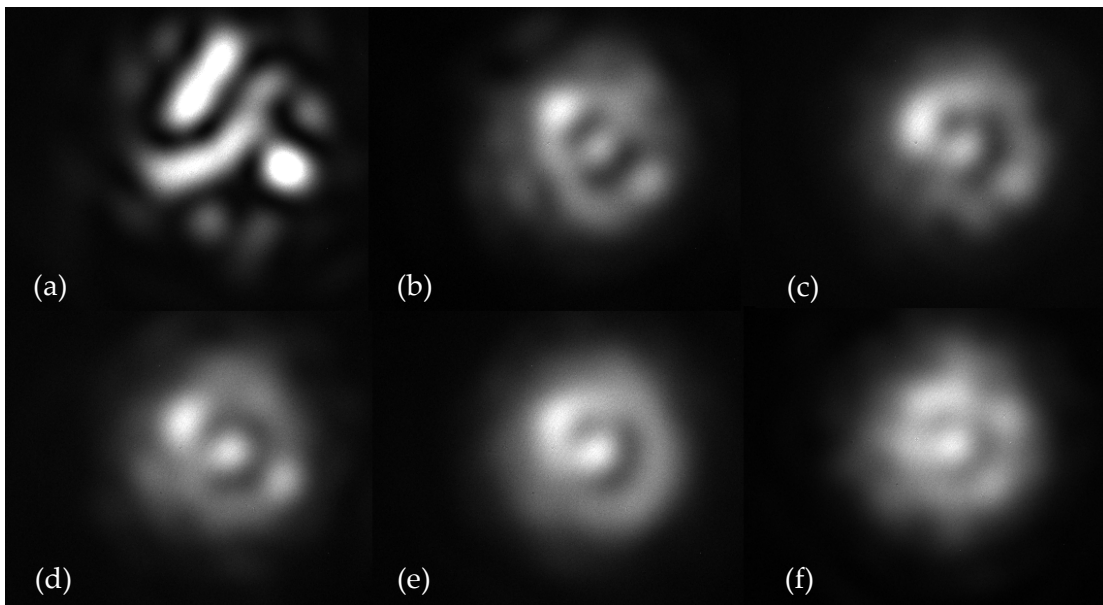


Figure 3: CCD images of (a) free 50 micron MMF; (b) 50 micron MMF with small radius 0.5 Hz frequency agitation; (c) 50 micron MMF with large radius 0.5 Hz frequency agitation; (d) 50 micron MMF with small radius 2 Hz agitation; (e) 50 micron MMF with large radius 2 Hz frequency agitation; (f) 50 micron MMF with “helicopter” hand agitation.

The desired result is one in which the modes are mixed enough to mimic the illumination pattern of a single mode fiber, shown in Figure 4. A single mode fiber's illumination pattern looks like a Gaussian, and therefore does not change as the fiber or input conditions change. Our results are well on their way to looking like the output of a single mode fiber, but there is still work to be done.

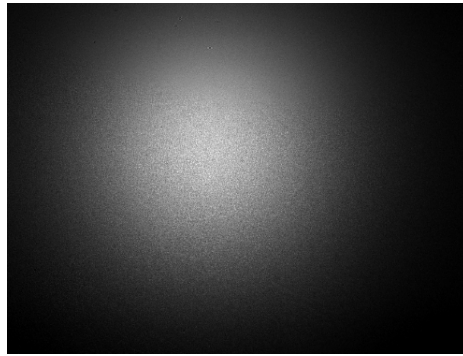


Figure 4: CCD image of a 10 micron single mode fiber.

CONCLUSION

iLocator's search for Earth-like planets will require extremely precise radial velocity measurements; down to 20 cm/s. Modal noise will make achieving this goal an impossibility if not properly alleviated. While this experiment laid some essential groundwork for modal noise mitigation in small diameter circular core fibers, there is still work to be done. Since iLocator will operate in the NIR, this experiment must be carried out with a laser that operates in the NIR region, along with the appropriate NIR equipment. The fiber used at the LBT to connect the acquisition camera to the spectrograph will be at least 40 meters in length, meaning that several agitators could be placed along the fiber. It would therefore be advantageous to test different numbers of

mechanical agitators to see the effect the number of agitated spots has on the alleviation of modal noise. In addition to the number of agitated spots, testing modal noise mitigation with longer fibers should be done. The fiber end connected to the spectrograph must be held stable, but agitation kept strictly at or near the acquisition camera end may not be optimal. Testing how the light continues to propagate when mechanically scrambled at a large distance away could be advantageous to better develop the modal noise rejection setup. Lastly, more exotic fiber solutions (such as non-circular cores or photonic lanterns) are expensive but possibly very useful.

REFERENCES

- Avila, Gerardo, et al., "Results on fiber scrambling for high accuracy radial velocity measurements", SPIE Vol. 7735, 773588 (2010)
- Avila, G., Singh, P., "Optical fiber scrambling and light pipes for high accuracy radial velocities measurements", SPIE Vol. 7018, 70184W (2008)
- Crepp, Justin R., "iLocater", American Astronomical Society, AAS Meeting 2013, #221, #149.12
- Mahadevan, Suvrath, et al., "Suppression of Fiber Modal Noise Induced Radial Velocity Errors for Bright Emission-Line Calibration Sources", arXiv: 1403.1577v1 (2014)
- McCoy, Keegan S., et al., "Optical fiber modal noise in the 0.8 to 1.5 micron region and implications for near infrared precision radial velocity measurements", arXiv:1209.2906 (2012)

Plavchan, Peter P., et al., "Precision near-infrared radial velocity instrumentation Non-Circular Core Fiber Scrambler", SPIE Vol. 8864, 88640G (2013)

Modeling the Accretion and Feedback Processes of Galaxies Similar to the Milky Way

Lee Hyatt

2014 NSF/REU Program

Physics Department, University of Notre Dame

Advisor: Professor Lara Arielle Phillips

Abstract

Composed of sheets, walls, and filaments, the cosmic web connects clusters of galaxies together and is responsible for regulating galaxy evolution by the accreting mass into galaxies via filaments [3]. In an effort to further understand the evolution of galaxies, we first study filaments and devise an interactive analytical model for disk galaxies with accurate inflow and outflow rates of matter. Using accretion rates and feedback rates from different regions in the Galaxy, it is now possible to model and predict galactic behavior for a galaxy with similar mass and morphology as the Milky Way. Other models simulate feedback or accretion processes numerically and in greater detail. Here we consolidate the rates to make one single model for the galaxy as a whole. In this model, we take the rates from other papers and use them to calculate the total mass flowed, energy used, distance travelled, and current location of the gas from the following parameters: change in time, redshift value, morphology of the galaxy, and type of active galactic nuclei (AGN) the galaxy has at its center. Although, we have just begun to make this detailed model, it will serve as the foundation for future work to be done to further understand galaxy evolution.

Introduction

Making up 90% of the universe's total mass and essentially 100% of the universe's volume, the cosmic web dwarfs the size of galaxies and is the driving force behind the creation and evolution of galaxies [3]. Galaxies are finite members of our universe and the depletion time of a galaxy greatly depends on the rates of gas and metals inflowing and outflowing from a galaxy [5]. Ranging from lengths of 5 – 100 h^{-1} Mpc, filaments are the primary source of accretion of mass onto the galactic haloes [3]. As of now, the current

rates of accretion from filaments is unknown, but we can gather a sense of how much they play a factor in galactic accretion based on other processes of gas inflows.

For our model, we are assuming $M_{\text{gal}} \approx 1.3 \times 10^{12} M_{\odot}$ [9] for the Milky Way and thus the Galaxy primarily undergoes “hot-mode accretion” (HMA), or filamentary inflows with $T_{\text{max}} > 2.5 \times 10^5 \text{ K}$ [10]. For most of our models, we are assuming a redshift (z) of zero, but our model is designed to calculate rates with varying $z = 0 - 3$. Some calculations require the star formation rate (SFR) of the Galaxy, which we approximated by knowing $M_{\text{stellar}} = 3.63 \times 10^{10} M_{\odot}$ [7] and the estimated SFR for a galaxy with $M_{\text{stellar}} \approx 3 \times 10^{10} M_{\odot}$ to be $1 M_{\odot}\text{yr}^{-1}$ [10]. By using the ratios of these two numbers, we estimated that the Milky Way has an approximate SFR of $1.21 M_{\odot}\text{yr}^{-1}$. Our result is consistent with current estimates of the Milky Way’s SFR to currently be between $0.68 - 1.45 M_{\odot}\text{yr}^{-1}$ [15]. Since we are assuming a large galaxy of $M_{\text{gal}} \approx 1.3 \times 10^{12} M_{\odot}$, we do not attribute the phenomenon of wind recycling accretion to have any effect on our data due to the fact that it is extremely efficient at masses this large [5]. Another consequence of having an enormous galaxy is that galactic collisions are fairly common -- especially at high redshifts, and play a very important role in galactic evolution for galaxies similar to the Milky Way [9]. We put spiral galaxies with similar masses of the Milky Way in the spotlight for our model [13], because spiral galaxies are the most common type of galaxy found in our universe, and it is not uncommon for disk galaxies to have $M_{\text{gal}} \approx 10^{12} M_{\odot}$ [20], thus making our model incredibly practical and useful.

Method

Using Python 2.7 for our model, we calculated the following: total mass accreted or expelled per process, total energy, total distance the gas travelled, current location of the

material, velocity of the gas, depletion time of the galaxy, and total mass accreted or outflowed from the galaxy depending on parameters such as mass rate, luminosity, origin of inflow or outflow, merger rate, SFR, redshift, and change in time in Myrs. With many resources providing a mass rate, calculating the total flow of mass per process was just a simple integration:

$$M = \int_0^{\Delta t} \dot{M} dt$$

with \dot{M} being either the mass accretion or mass outflow rate. However, this was not always the case; supernovae's (SNe) mass rate depended on the SFR of the galaxy. Thus, the mass outflow rate for SNe is the following [19]:

$$\dot{M}_{\text{SNe}} = 0.26 \left(\frac{\text{SFR}}{M_{\odot} \text{yr}^{-1}} \right)$$

Calculating the total energy is very similar to calculating the total mass accreted. To calculate the total energy over time in years we simply perform this integral:

$$E = (3.155 \times 10^{13}) \int_0^{\Delta t} L dt$$

where L is luminosity in erg s^{-1} and 3.155×10^{13} is the number of seconds in one Myr. Just as before, SNe have a special energy equation that also depends on SFR. The equation for luminosity for SNe is the following [18]:

$$L = 7 \times 10^{41} \left(\frac{\text{SFR}}{M_{\odot} \text{yr}^{-1}} \right)$$

After calculating the total energy, calculating the distance the gas travelled from its origin is simply just using the gravitational potential energy equation. Using basic algebra to move variables around we get the following equation:

$$r = \frac{-GM_{\text{gal}}}{E} \frac{M_{\odot}}{j} \frac{M_{\text{acc}}}{p}$$

with the equation giving us r parsecs. For clarification, M_{\odot} is the mass of the sun in kilograms, j is the conversion from erg s^{-1} to joules, and p is the number of meters in one parsec. The current location of the gas depends on where its origin was, and the radius of the accreted matter related to morphological measurements of the Galaxies' supermassive black hole (SMBH), galactic center, stellar bulge, thin disk, thick disk, interstellar medium (ISM), and the stellar halo. The Milky Way's galactic center is a mere 4.84×10^{-6} pc across [13]; the stellar bulge is 1kpc in diameter; the thin disk is 300 pc thick [11]; thick disk is 1000 pc wide [11]; ISM is hundreds of parsecs across [13], and the stellar halo is 100 kpc in diameter [20]. Knowing these descriptions and the radius of the flowing gas, we can easily predict and locate the region of the inflows and outflows for a given amount of time, which is very useful for improving our understanding of galaxy evolution.

```

We're going to open a table for Galaxy Accretion
with the table 'GalaxyAccretionTable.txt'.

Method of Accretion      Flow Rate(Msun/yr)      Mass Accreted(Msun)      Current Location      Total Energy
('Radio Mode'           6e-6                    ', 6.0, '                ', 'Supermassive Black Hole')
('Seyfert AGN           1.0                    ', 1000000.0, '          ', 'Spherical stellar bulge', '
('Radio AGN             100.0                  ', 0, '                    ', 'DNE', '
('Quasar AGN            100.0                  ', 0, '                    ', 'DNE', '
('BL-Lacertae           1e-3                   ', 0, '                    ', 'DNE')
('Supermassive Black Hole 9.2e-4                 ', 920.0, '                ', 'Galactic Center', '
('Central Molecular Zone 1.0                    ', 1000000.0, '          ', 'Galactic Center', '
('High Velocity Clouds  0.2                   ', 200000.0, '          ', 'Interstellar Medium', '
('Hot Mode Accretion    ', 4, '                  ', 4000000.0, '          ', 'Interstellar Medium')
('Accretion Disk        1e-9                   ', 0.001, '                ', 'Thin Disk', '
('Galactic Mergers      ', 775115.750125)

```

Figure 1: Table in Python that displays outputted data and location after 1 Myr for methods of accretion

Accretion Results & Analysis

Accretion of material of galaxies essentially comes from the following places: filaments, SMBH, active galactic nuclei (AGN), central molecular zone (CMZ) winds from the galactic center, ISM gas, and the accretion disk. Since filament accretion rates are not

currently known, we will begin with SMBH inflows. Located in the center of the galaxy [13], SMBH inflows are fueled by stellar tidal forces and convert its gravitational energy to radiative energy in order to power the galaxy's AGN [19]. SMBH range in masses of 10^6 - $10^9 M_{\odot}$, even though Milky Way's SMBH is currently known to have a mass of $4.5 \pm 0.4 \times 10^6 M_{\odot}$ [8] and an accretion rate of $9.2 \times 10^{-4} M_{\odot} \text{yr}^{-1}$ [12]. 'Radio mode' accretion is a result of HMA once a central halo has formed in the galaxy with $z \leq 2$ being when it is the most prominent. These outflows have velocities greater than 150 km s^{-1} and an accretion rate of $6 \times 10^{-6} M_{\odot} \text{yr}^{-1}$ [4]. With about 1 – 10% of large galaxies having an AGN – including the Milky Way – or galactic nuclei with the majority of its luminosity from nonstellar origin [13], AGNs have four distinct types: seyfert, radio, quasar, and BL – Lacertae [20] – all of which are accounted for in our program. Having inflows of ionized gas from a range as far as 400 pc away [16], AGNs are the most dominant method of gas accretion with $\dot{M}_{acc} \approx 100 M_{\odot} \text{yr}^{-1}$ for powerful radio and quasar AGNs [20]. Located just 180 pc from the galactic center, the CMZ has inflows of about $\dot{M}_{acc} \approx 1 M_{\odot} \text{yr}^{-1}$ [19]. Responsible for most of the galaxy's formation of stars, the accretion disk is insignificant in the grand scheme of galaxy accretion with $\dot{M}_{acc} \approx 1 \times 10^{-9} M_{\odot} \text{yr}^{-1}$ [13]. The remainder of the accretion comes from the ISM in categories of HMAs and high-velocity clouds (HVCs). Contributing to the growth of the stellar spheroid but consequently lowering SFR rates for Milky Way size galaxies, HMAs have a major impact on the accretion rates for galaxies with rates starting at $4 M_{\odot} \text{yr}^{-1}$ at $z = 0$ and peaking at $z = 3$ with $38 M_{\odot} \text{yr}^{-1}$ [10]. Driven by tidal forces and having $\dot{M}_{acc} \approx 0.2 M_{\odot} \text{yr}^{-1}$, neutral HVCs are responsible for cooling the galactic hot corona and increasing SFR rates [11]. Playing a vital role in galaxy evolution for Milky Way size galaxies, galaxy mergers increase in importance with increasing redshift values with as much as 200% of

all accreted mass at $z = 3$ is from galactic mergers [10].

Method of Accretion ($z = 0$)	Mass Rate ($M_{\odot}\text{yr}^{-1}$)	Location (@ 1Myr)	Energy Rate (erg s^{-1})	Velocity (km s^{-1})
Radio Mode	6×10^{-6}	Supermassive Black Hole		≥ 150
Seyfert AGN	1	Spherical Stellar Bulge	1×10^{43}	200-500
Radio AGN	100	Galactic Center	1×10^{46}	100 - 1000
Quasar AGN	100	Galactic Center	1×10^{47}	
BL - Lacertae AGN	1×10^{-3}	Galactic Center		
Supermassive Black Hole	9.2×10^{-4}	Galactic Center	1×10^{43}	
Central Molecular Zone	1	Galactic Center	1×10^{56} erg	
High Velocity Clouds	0.2	Interstellar Medium	3×10^{51} erg	70 - 120
Hot Mode Accretion	4	Interstellar Medium		100 - 300
Accretion Disk	1×10^{-3}	Thin Disk	4×10^{33}	

Table 1: Results for accreted gas mass at $z = 0$

Feedback Results & Analysis

Feedback processes are responsible for regulating galaxy growth and increase the metallicities of galaxies [5]. The bulk of outflowing gas occurs inside of the stellar bulge through AGN and ultrafast outflows (UFOs), but a considerable portion of outflows occurs in the disk and IGM from stellar outflows, SNe, and galactic winds. AGNs are the Galaxy's primary source of feedback with outflow rates being as high as $1020 M_{\odot}\text{yr}^{-1}$ of neutral hydrogen, ionized hydrogen and dust combined [19]. Conical radial outflow from AGNs with angles ranging from 60° - 135° while Compton heated feedback is approximately perpendicular to the disk [19]. For galaxies the size of the Galaxy, AGNs stifle star formation by heating up the disk and as a consequence move stars onto the red sequence on the Hertzsprung – Russell diagram [6]. Outflowing perpendicularly from the SMBH at relativistic speeds of $0.1c$, UFOs regulate the growth of the SMBH while having an outflow rate of $0.1 M_{\odot}\text{yr}^{-1}$ [20, 2]. Most of the stellar outflows occur from non-main sequence stars such as the asymptotic giant branch (AGB), which are located in the ISM in globular clusters, tend to be the oldest stars in the galaxy, and have the lowest metallicities of $Z \leq 0.001$ [13]. Outflow rates for AGB stars are about $10^{-4} M_{\odot}\text{yr}^{-1}$, which result in intermittent periods of helium shell burning [13]. Developing stars are located in the thick disk and

generate bipolar outflows of gas with velocities ranging from 30 – 100 kms^{-1} at angles of $10^\circ - 45^\circ$ to the base of the disk and feedback rates ranging from $10^{-4} - 10^{-6} M_\odot\text{yr}^{-1}$ [19,20]. YSOs have higher metallicities than the Sun and the time for the protostars to become main sequence stars is about 10^7 years, when hydrogen ignition at 10^7K is feasible [13]. Giants and supergiants contribute to gas outflows as well, but are relatively insignificant with mass rates ranging from $10^{-6} - 10^{-8} M_\odot\text{yr}^{-1}$ at velocities ranging from 1000 – 2000 kms^{-1} for O & B supergiants[20]. Normally located in the thick disk or globular clusters, SNe explosions are the result of unstable neutron stars that blow off the outer shells [13]. The two main types of SNe are type Ia SNe and type II SNe. Type Ia SNe explosions are caused by a thermonuclear domino effect of nuclear reaction rates and are known to not leave behind stellar remnants or nebulas [13]. Outflow rates are approximately $2.3 \pm 0.6 \times 10^{-3} M_\odot\text{yr}^{-1}$ compared to rates of the Milky Way to have been estimated to be $3.146 \times 10^{-1} M_\odot\text{yr}^{-1}$ for type II SNe with our program [18, 19]. Type II SNe or core-collapse SNe leave behind nebulas – with the Crab Nebula being the most studied – and eject mass at high speeds ranging from $10^3 - 10^4 \text{kms}^{-1}$ [13]. SNe feedback plays a much more prominent role in galaxies with $M_{\text{gal}} \leq 3 \times 10^{10} M_\odot$ because SFR rates tend to be much higher and its energy does not radiate away as quickly [19,10]. Located in the intergalactic medium (IGM), galactic winds eject neutral gas, dust, and metals with combined outflow rates

normally ranging from 0.1 to 10 $M_{\odot}\text{yr}^{-1}$ at $z \geq 1$ [5,19].

Method of Feedback (z = 0)	Mass Rate ($M_{\odot}\text{yr}^{-1}$)	Location (@ 1Myr)	Energy Rate (erg s ⁻¹)	Velocity (kms ⁻¹)
Ultra Fast Outflows	0.1	Galactic Center	1.25×10^{45}	30000
Seyfert AGN	1	Spherical Stellar Bulge	1×10^{45}	200-500
Radio AGN	100	Galactic Center	1×10^{44}	100 - 1000
Quasar AGN	100	Galactic Center	1×10^{47}	
AGB Stars	1×10^{-3}	Globular Clusters		
Young Stellar Objects	1×10^{-6}	Thick Disk	1×10^{43}	
O & B Supergiants	1×10^{-8}	Thin Disk	1×10^{38} erg	
Type Ia Supernovas	2.3×10^{-3}	Globular Clusters	3×10^{53} erg	70 - 120
Type II Supernovas	3.146×10^{-3}	Thick Disk	3×10^{53} erg	100 - 300
Galactic Winds	0 (until z = 1)	IGM	1×10^{44}	525 - 655

Table 2: Feedback rates and locations at $z = 0$

Conclusion & Future Work

Although this model is still a work in progress, it is useful for tracking the flows of matter and calculating the total mass for varying parameters such as change in time, redshift, type of AGN, and even type of galaxy. With our current knowledge of mass rates, our model aids in our understanding galaxy of evolution by being able to accurately predict how a Milky Way size galaxy will change and develop over time. More research is needed to find the remaining luminosities of processes to better track the location of the gas. A useful addition to the program would be to expand its usefulness for spiral galaxies of all masses and have rates adjust per era of galaxy evolution. Being in the current astrophysics spotlight, it is only a matter of time until filaments are better understood, which would improve this model considerably. Having the accretion rates of filaments could be the last piece of the puzzle that helps astrophysicists better predict and understand galaxy evolution.

References

- [1] Bond, Nicholas A. et al. "Crawling the Cosmic Network: Identifying and Quantifying Filamentary Structure." *Monthly Notices of the Royal Astronomical Society* 409 (2010): 156-68. *Cornell University Library*. Web. 5 June 2014.
- [2] Bourne, Martin A., "Black Hole Feedback in a Multiphase Interstellar Medium." *Monthly Notices of the Royal Astronomical Society*. Oxford Journals, 29 May 2014. Web. 14 July 2014.

- [3] Cautun, Marius, Rien Van De Weygaert, Bernard J. T. Jones, and Carlos S. Frenk. "Evolution of the Cosmic Web." *MNRAS* 441 (2014): 2923-973. Print.
- [4] Croton, Darren J., et al. "The Many Lives of AGN: Cooling Flows, Black Holes and the Luminosities and Colours of Galaxies." *MNRAS* 365 (2006): 11-28. *Cornell University Library*. Web. 16 June 2014.
- [5] Davé, Romeel, Kristian Finlator, and Benjamin D. Oppenheimer. "Galaxy Evolution in Cosmological Simulations with Outflows - II. Metallicities and Gas Fractions." *MNRAS* 416.2 (2011): 1354-376. *Cornell University Library*. Web. 2 June 2014.
- [6] Davé, Romeel, et al. "Building Galaxies with Simulations." (2005): 1-10. *Cornell University Library*. Web. 10 June 2014. <<http://arxiv.org/abs/astro-ph/0510625>>.
- [7] Ford, Amanda Brady, et al. "Tracing Inflows and Outflows with Absorption Lines in Circumgalactic Gas." *MNRAS* (2013): 1-25. *Cornell University Library*. Web. 2 June 2014.
- [8] Ghez, A. M., et al. "Measuring Distance and Properties of the Milky Way's Central Supermassive Black Hole with Stellar Orbits." *The Astrophysical Journal* 689.2 (2008): 1044-062. *IOP Science*. *The Astrophysical Journal*, 20 Dec. 2008. Web. 8 July 2014.
- [9] Keller, B. W., et al. "A Superbubble Feedback Model for Galaxy Simulations." *MNRAS* 442 (2014): 1-14. *Cornell University Library*. Web. 6 July 2014.
- [10] Keres, Dusan, Neal Katz, David H. Weinberg, and Romeel Davé. "How Do Galaxies Get Their Gas?" *Monthly Notices of the Royal Astronomical Society* 363.1 (2005): 2-28. Web.
- [11] Kruit, P.c. Van Der, and K.c. Freeman. "Galaxy Disks." *Annual Review of Astronomy and Astrophysics* 49.1 (2011): 301-71. Web. 5 June 2014.
- [12] Kuo, C. Y., et al. "Measuring Mass Accretion Rate onto the Supermassive Black Hole in M 87 Using Faraday Rotation Measure with the Submillimeter Array." *ApJL* (2014): 1-11. *Cornell University Library*. Web. 22 July 2014.
- [13] Maoz, Dan. *Astrophysics in a Nutshell*. Princeton, NJ: Princeton UP, 2007. Print.
- [14] Metuki, Ofer, et al. "Galaxy Properties and the Cosmic Web in Simulations." (2014): 1-12. *Cornell University Library*. Web. 6 July 2014. <<http://arxiv.org/abs/1405.0281>>.
- [15] Robitaille, Thomas P., and Barbara A. Whitney. "The Present-day Star Formation Rate of the Milky-Way Determined from Spitzer Detected Young Stellar Objects." *ApJL* 710 (2010): 1-12. *Cornell University Library*. Web. 20 July 2014. <<http://arxiv.org/abs/1001.3672>>.
- [16] Schnorr-Müller, Allan, Thaisa Storchi-Bergmann, Neil M. Nagar, and Fabricio Ferrari. "Gas Inflows towards the Nucleus of the Active Galaxy NGC 7213." *Monthly Notices of the Royal Astronomical Society*. Oxford Journals, 24 Jan. 2014. Web. 6 July 2014.
- [17] Stewart, Kyle R., et al. "Angular Momentum Acquisition In Galaxy Halos." *IOP Science*. University Libraries of Notre Dame, 6 May 2013. Web. 17 July 2014.
- [18] Toonen, S., et al. "Binary Population Synthesis and SNIa Rates." *ASP Conference Series* (2013): 1-4. *Cornell University Library*. Web. 17 July 2014.
- [19] Veilleux, Sylvain, Gerald Cecil, and Joss Bland-Hawthorn. "Galactic Winds." *Annual Review of Astronomy and Astrophysics* 43.1 (2005): 769-826. Web. 5 June 2014.
- [20] Zeilik, Michael. *Introductory Astronomy & Astrophysics*. Singapore: Brooks/Cole / Thomson Learning, 1998. Print.

Beamline optimization for Long Baseline Neutrino Experiment

Yi Jia

2014 NSF/REU Program

Physics Department, University of Notre Dame

Advisor: Prof. John LoSecco

abstract

One of the physics goals of Long Baseline Neutrino Experiment (LBNE) is to measure CP violation in the neutrino sector and to determine the mass hierarchy. This summer, we work on various simulations to explore an optimal design of neutrino beamline. Such an improved beam is expected to achieve by maximizing events at first and second oscillation maxima while minimizing high energy tail that produce backgrounds, eventually leading to better resolution of the CP phase. The studies were done by advanced tool G4LBNE combined with Fermilab Grid. To determine the optimizing construction with most potential to obtain our physics goals, different structures and parameters, such as adding a plug, beam power and horn current, are compared to underline their effects. The simulation results show that a plug can play a significant role to enhance our spectra. As a powerful simulation tool, Fast Monte Carlo provides detailed information including efficiencies, purities and detector response for us to understand the experiment.

1 Introduction

Although neutrinos are the most abundant of known matter particles in our Universe, it may remain the most mystery one in the particle family. The Long Baseline Neutrino Experiment (LBNE) aims to reveal some fundamental properties and parameters of neutrino, such as charge-parity (CP) violating phase δ , mass hierarchy, mixing angle θ_{13} , which can serve for considerable significant physics objectives, for example, providing a broader understanding of asymmetries between matter and antimatter, examining the Grand Unified Theory by observing the protons decay, elucidating critical information about the dynamics of supernovae explode.

Covering an approximately 800-miles distant to send a high-intensity neutrino beam

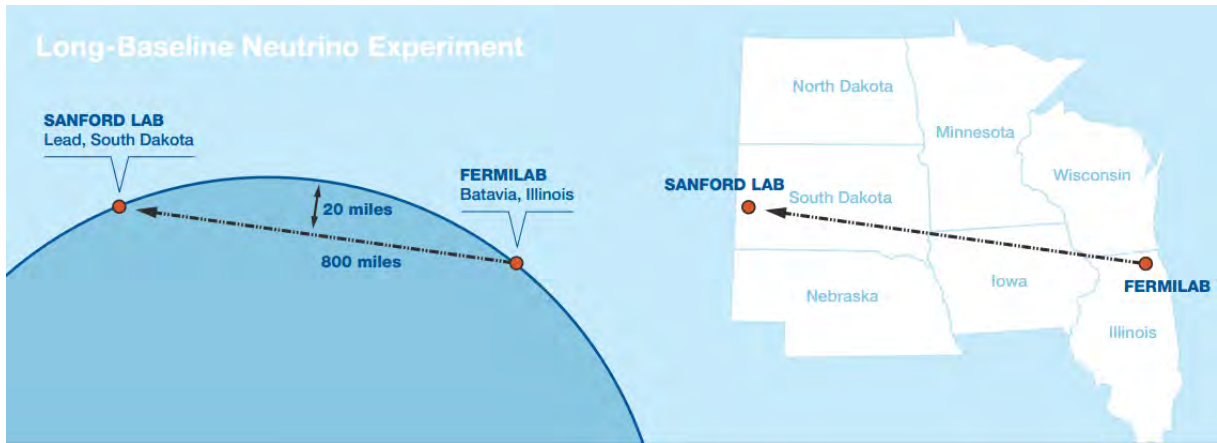


Figure 1: The 800-mile-long trip from Batavia, Illinois to Lead, South Dakota.

from Fermilab to Sanford Lab in South Dakota[1], this experiment is currently organized into four subprojects: Beamline, Near Detector Systems (ND), Liquid Argon Far Detector (FD) and Conventional Facilities (CF). For this paper, we focus on the part of the beamline design. Based on advanced methods of simulation tool like Fast Monte Carlo, the main purpose of this paper is to promote the beamline optimization by testing different beam configurations.

2 Components of the Beamline

G4LBNE is a Geant4-based simulation package of the beamline dedicated to LBNE. The components of the beamline will be designed to extract a proton beam from the Fermilab Main Injector (MI) and transport it to a target area where the collisions generate a beam of charged particles. The secondary beam, aimed toward the far detector, is then led to a decay-pipe where the particles of the secondary beam decay to generate the neutrino beam. At the end of the decay pipe, an absorber pile removes the residual hadrons [2].

In order to enhance the neutrino spectrum, a “beam plug” can act a second source

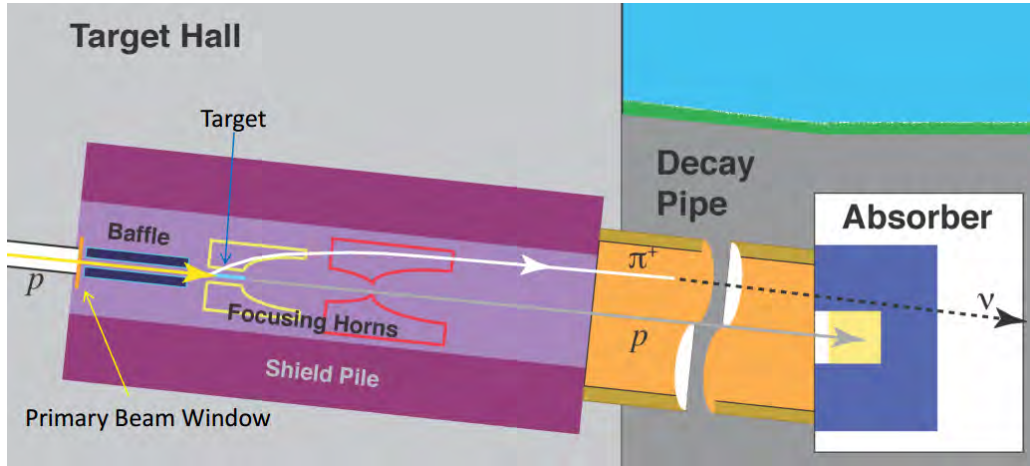


Figure 2: LBNE beamline showing major components of neutrino beam.

of desirable low energy hadrons and reduce flux in the high energy tail. On the other hand, some other parameters like the beam power on the target and the level of horn current can also be considered to achieve the same goal.

G4LBNE provides us with powerful tools to design numerous configurations involving those parameters. As shown from table 1, the running of number 2360 would be our most fundamental configuration, while other running can be compared to this baseline to highlight the corresponding effect. At this table, the length and location of the plug are both considered. Neutrino beam power has been initialized as either 0.7MW or 1.2MW, and 200kA current would be compared to 150kA. Though Beamline in LBNE will utilize a proton beam with energy tunable from 60 to 120 GeV, here we all use a proton beam with 80 GeV.

3 Comparison for 80 GeV flux

Working on Fermilab grid system, submitting and running jobs can be performed with high statistics and speed. After creating the TTree files from original macro files, we can make various plots to demonstrate the optimizing effect with those TTree files, which

Run#	Plug Length(cm)	Beam Power(MW)	Horn Current(kA)
2330	245 Upstr.	0.7	200
2360	No plug	1.2	200
2390	100 H2	1.2	200
2420	363 H2	1.2	200
2450	145 Upstr.	0.7	200
2480	No plug	1.2	150
2510	145 Upstr.	1.2	200
2540	100 H2	1.2	150

Table 1: Running configurations of beamline. “Upstr.” means putting the plug on the upstream side between horn 1 and horn 2, and “H2” refers to place it into the horn 2.

have stored all the resulting information of every single running of simulation.

Since Run# 2360 plays a baseline role of our simulation, other running configurations should be made accurate comparison with this basic one. Figure 3 shows the comparing result of No#2330 and No#2360. As first and second oscillation maximum show more physics potential, increasing flux at the low energy and decreasing flux in the high energy tail is our optimizing aim.

From figure 3, the running of No#2330 has a prominent performance to obtain the goal. Such consequence can be demonstrated by a more direct way when drawing the ratio between those two configurations. We obtain a 20% increase under 1 GeV, while reducing a large scale of events in the wide range of high energy. Further, other outcomes with a plug also show great superiority compared to those without plug.

By contrasting all the comparisons, the No#2330, No#2420 and No#2450 have been

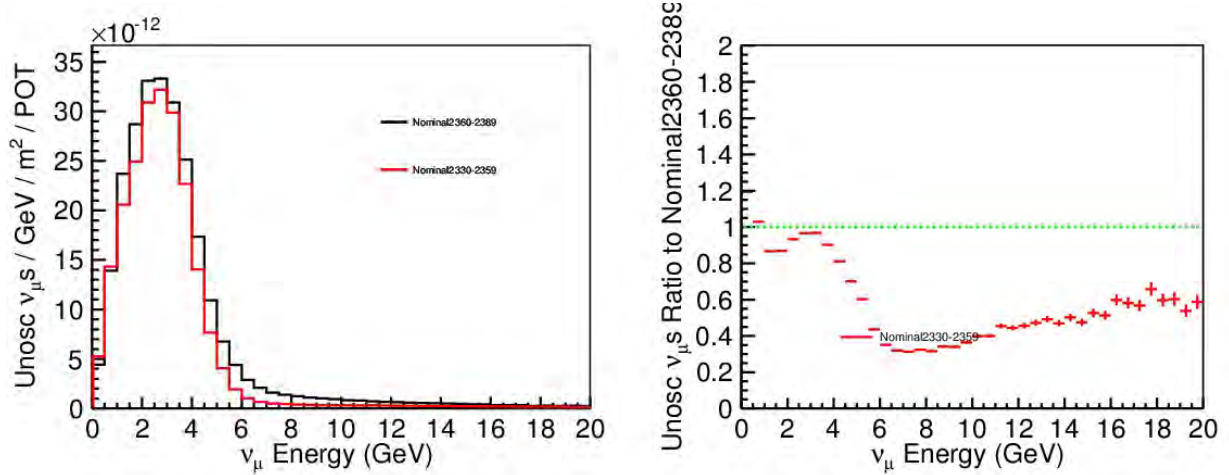


Figure 3: The flux (left) and ratio (right) comparison between Run#2360 and Run#2330.

Red line represents Run#2330 with a 245cm-length plug located upstream, while the black or green line refers to Run#2360 with no plug

selected out to be the three most desirable configurations. As No#2330 turns out to be the best one, it indicates that a 245cm-length plug located upstream is the most recommended one to be applied to practice. Thus, we can draw the conclusion that adding a plug to the system can play a significant role to enhance our spectra.

4 Fast Monte Carlo

The Fast Monte Carlo simulation is a preliminary version of full Monte Carlo. It will use a Geant4 simulation of the beamline to estimate the neutrino flux, a neutrino interaction generator (e.g., GENIE), and detailed detector simulation that mimics the real detector output for data events [3].

First, the original flux files are created by those TTree files mentioned before. Flux files with antineutrino information can be obtained by change the sign of the horn current to a minus one. Then, GENIE takes these flux files to make neutrino interaction. Finally, one should take GENIE output and produce flat TTree fastmc output, which can be the

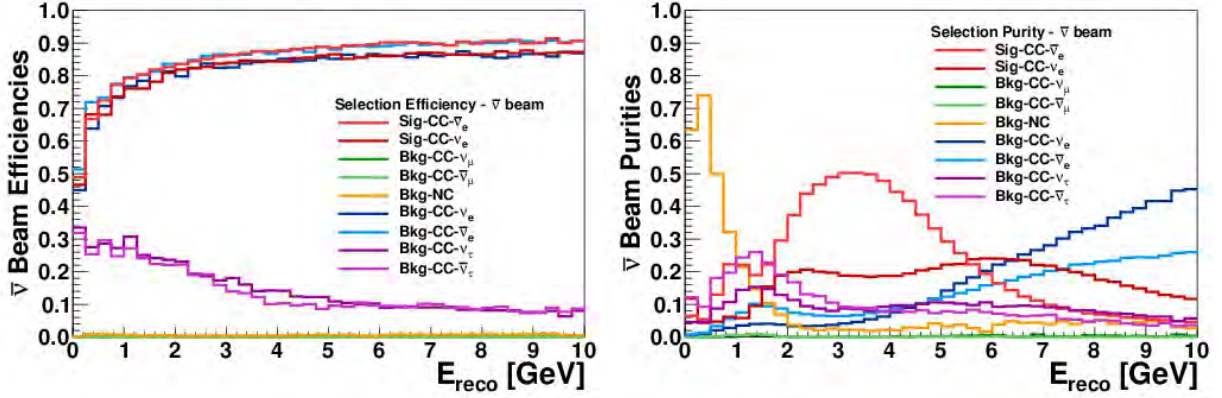


Figure 5 :The expected anti-neutrino efficiencies and purities of (top) and (bottom) appearance events in a LArTPC.

resource to plot efficiencies, purities and beam spectra showing detailed detector response.

As figure 5 shows, the detector provides excellent particle identification with high signal-selection efficiency. The corresponding plots on the right-hand side show the purity of the signal and each background sample for the Fast MC.

To accurately approximate a full MC simulation, the Fast MC is used to simulate the measured (reconstructed) energy and momentum of each final-state particle. The simulated energy deposition of the particles in each interaction is then used to calculate reconstructed kinematic quantities (e.g., the neutrino energy), and classify the type of neutrino interaction, including backgrounds and misidentified interactions.

Generally speaking, Fast MC is a powerful tool to characterize effects of uncertainties in flux, cross-sections, beamline tolerances, beam design optimizations, and so on. For this summer, I worked on the effects of putting the detector at an off-axis location with Fast MC. Figure 6 shows the original true energy spectra for on-axis and 30 mrad off-axis beam, while Fast MC provides us with the reconstructed energy distributions in Figure 7. As those figures indicate, the oscillated neutrino beam would reach a first maximum at around 3 GeV and a second maximum at around 1 GeV. Comparing to the on-axis neutrino

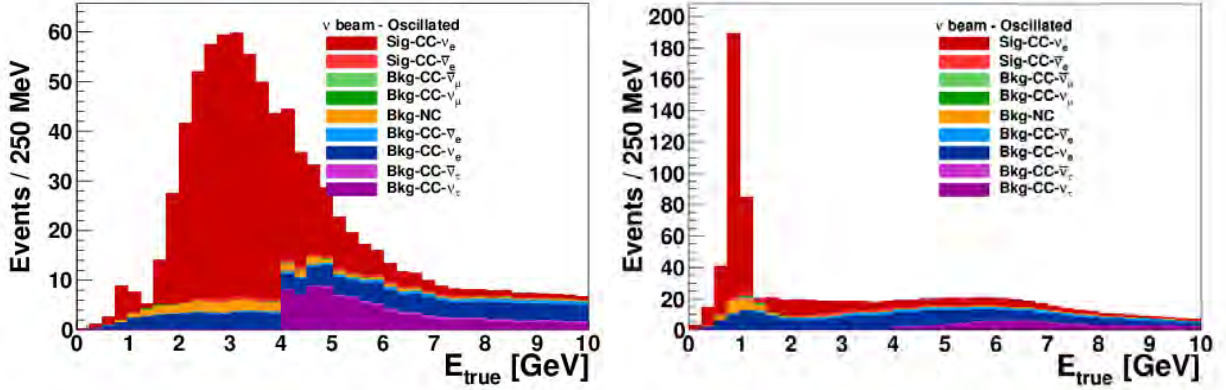


Figure 6: The true energy spectra of the signal and background of beam Run#2360. Left-hand and right-hand are on-axis and off-axis(30mR) beam, respectively.

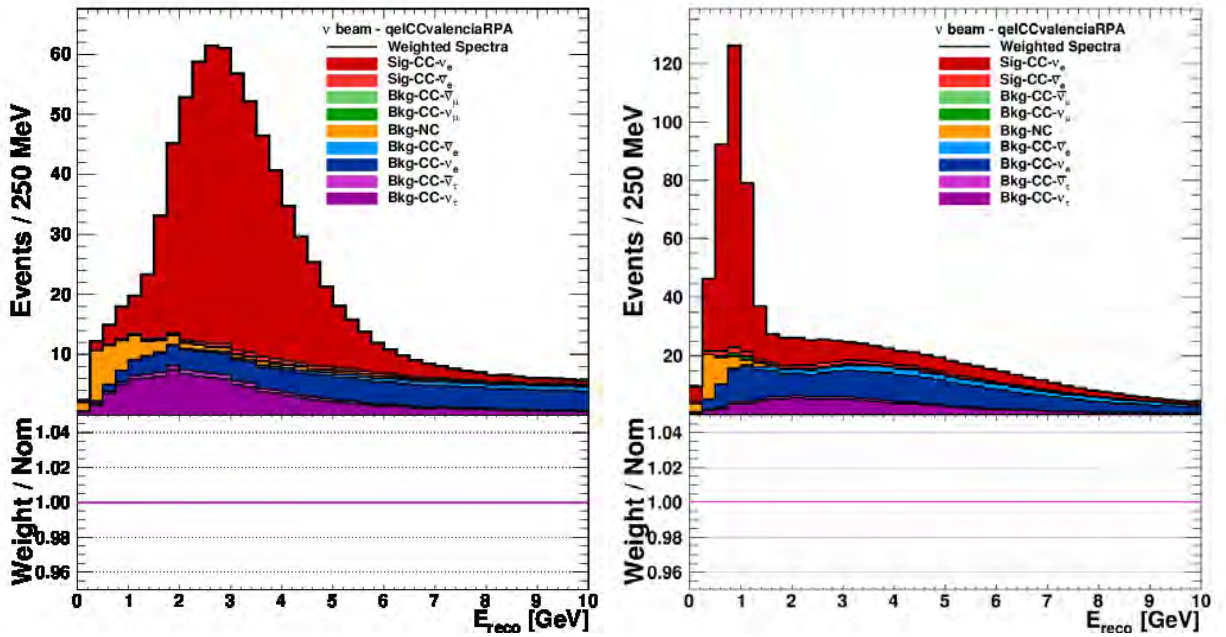


Figure 7 :The reconstructed energy spectra for the signal and background of beam Run#2360. Left-hand and right-hand are on-axis and off-axis(30mR) beam, respectively.

beam, our result shows the off-axis beam flux is much higher at the second oscillation maximum. The narrow-band beam also provides advantages in reducing backgrounds, which are generated by high-energy neutrinos [4]. Therefore, a second detector at an off-axis location can help us enhance the performance of this experiment.

5 Discussion

I'm very excited to have such an opportunity to participate in the work of beam simulation group in Fermilab. At first, I logged my laptop into Fermilab computer "gpsn01.fnal.gov", so I had to get familiar with commonly-used commands and file structure of linux system soon. Most of my results are relied on the Fermi Grid in Fermilab computer, by which users can submit numerous intensive jobs at the same time, resulting in a high-efficiency simulation.

Then, the G4LBNE, developed by Fermilab, brought me into contact with various advanced tools to perform simulations. It combines Geant4, a toolkit for the simulation of the passage of particles through matter, with a data analysis framework ROOT. In ROOT, I learnt how a TTree could store large quantities of simulation data. Once I tried to fit my histograms in ROOT, the flux files kept crashing, so I decided to change the fitting function from exponential to polynomial, finally it works! I really enjoy such a problem-solving process, leading to a sense of achievement.

One of my most important contributions this summer is to help professor determine the most optimizing construction to enhance beam spectra. I also learnt how GENIE and Fast Monte Carlo work to give us detailed information about the detector response in the simulation. I really appreciate Prof. LoSecco's guidance throughout the whole summer to witness my progress. Thanks to the University of Notre Dame and especially to Dr.

Umesh Garg for providing the opportunity for me to conduct such an awesome research for this summer.

6 Conclusion

The comparisons between various configurations and our baseline Run#2360 have shown a convincing result that a beam plug can lead to improved resolution of the CP phase. Specifically, a 245cm-length plug located upstream can increase low energy events by 20%, while reducing flux in the high energy tail by 70%. Besides, the spectra provided by Fast Monte Carlo demonstrate that a second detector at an off-axis location dedicated to the second oscillation maximum can help enhance the performance of LBNE.

References

- [1] http://lbne2-docdb.fnal.gov/cgi-bin/RetrieveFile?docid=6710;filename=LBNE_Factsheet_4Pager_050213.pdf;version=3.
- [2] Seongtae Park, Jae Yu, Timothy Watson, Amit Bashyal, Simulation Studies on LBNE Neutrino Beam Flux in Different Decay Pipe Materials, air/He, Nov. 11, 2013.
- [3] http://lbne2-docdb.fnal.gov/cgi-bin/RetrieveFile?docid=8087;filename=appendixA_update.pdf;version=5
- [4] X. Qian, J. Ling, R. McKeown, W. Wang, E. Worcester et al., A second detector focusing on the second oscillation maximum at an off-axis location to enhance the mass hierarchy discovery potential in LBNE10, arXiv:1307.7406 [INSPIRE].

The Notre Dame Nuclear Database: Nuclear Data Made Easily Accessible

Timothy Khouw

2014 NSF/REU Program

Physics Department, University of Notre Dame

Advisor: Prof. Ani Aprahamian

Abstract :

In 1994, the NNDC revolutionized nuclear research by providing a colorful, clickable, searchable database over the internet. Since then, web technology has evolved dramatically, but the NNDC's user interface has not expanded. Our project, the Notre Dame Nuclear Database, (ND)², aims to provide a more comprehensive and broadly searchable set of data while making access to the data easy and clickable. The database can be searched by an array of filters which includes metadata in addition to the nuclear parameter that is searched for, including information on the facility where a measurement is made, the author(s), or date of publication for the datum of interest. The user interface takes full advantage of HTML, a markup language that encodes the vast majority of webpages, CSS (cascading style sheets which define the aesthetics of the website), and JavaScript, a programming language that allows our website to process complex data; these are essential components of any modern website. The server-side technologies used to power the webserver are MySQL, a relational database management system, and Python, a high-level programming language that we use to access and return data. In addition, our team has developed a first-of-its-kind command-line interface that allows users to interact with the database directly on their local machines without having to open a web browser. For example, users can request to download specific, pre-parsed content in numerous data formats with a simple command. This is possible through the use of a standardized API (application programming interface) that relies upon well-defined filtering variables to produce customized search results. (ND)² also offers an innovative chart of nuclides utilizing scalable vector graphics (SVG) to deliver researchers an unsurpassed level of interactivity as well as support on all computers and mobile devices (including touch features such as scrolling and pinch-zooming). It is our hope that (ND)² will greatly benefit the nuclear physics community and accelerate nuclear research around the world.

Introduction:

The Notre Dame Nuclear Database is an ambitious project that has involved many hours of coding and collaboration. This database is makes access to nuclear data as fast and convenient as possible. Our team has developed an advanced user interface that allows researchers to access exactly what data they want, when they want it. We achieved this goal by focusing on the development of three main features: a robust search function able to retrieve search results on the basis of nuclide information and metadata (data about the data stored in the database), an interactive chart of nuclides that allows users to navigate the chart easily by zooming and scrolling and also allows users to search the chart for specific nuclide measurements, an original command-line interface that allows users to fully interact with and retrieve data from the database without having to open a web browser. We believe these components are the main things that set the Notre Dame Nuclear Database apart from other currently available nuclear databases. While there are other nuclear databases online, they lack many features that have become standard and expected over the last two decades. For example, the NNDC's chart of nuclides does not allow users to zoom or pan without reloading the page [1]. As of summer 2014, users must click buttons that correspond to set zoom levels and then wait for the page to reload. Panning the chart is only possible through an eight-directional collection of arrows in the corner of the chart. Again, a researcher must wait for the page to reload after clicking an arrow. The NNDC, while it does store metadata on its measurements, does not allow users to search by metadata. This means that if a user wants to view all mass measurements taken on a certain nuclide from year 2000 to 2014, then there is no practical way to do this. It is the mission of (ND)² to improve upon the accomplishments of databases like the NNDC's by taking full advantage of the most modern web technologies that the internet has to offer to produce the most usable and efficient nuclear data storage and retrieval system to date.

Data included in (ND)²:

As a database, (ND)²'s main purpose is to provide data to researchers. Our database stores a multitude of data for all nuclides. One type of data included in our database is raw measurements. These are measurements of a nuclide's property that come directly from an experiment that was published in a journal. For example, there have been very precise mass measurements of short-lived radioactive nuclei conducted by ISOLDE, CERN's nuclear physics facility in Geneva [2]. By using mass-spectrometry, researchers were able to measure masses at previously unmatched precision. Relative uncertainties were 1×10^{-7} or even 1×10^{-8} in special instances. However, mass measurement is not the only kind of raw data included in (ND)². The database also includes half-lives, level-lifetimes, and properties of deformation as well.

(ND)² will also contain theoretical calculations of nuclide properties. These are hypothetical values that theorists have predicted, but have not necessarily been verified by experiment. The finite-range droplet model is an example of a set of theoretical calculations that will be stored in (ND)² [3]. This model was an attempt to predict the masses of nuclides using nuclear theory.

Finally, the Notre Dame Nuclear Database provides compilation data. These are values that have been determined by an organization that has gathered many raw measurements from a variety of sources. The resulting value is generally considered the most correct number that a researcher could use in their calculations. An example of compilation data is the AME2012 atomic mass evaluation [4]. This organization, the AME, regularly re-evaluates raw measurements of nuclide masses in attempt to determine the best standard values for each nuclide. This data is very useful to researchers and will thus be included in (ND)².

Metadata included in (ND)²:

A central feature of the Notre Dame Nuclear Database is its inclusion of metadata. Metadata is data about other data. From a nuclear physicist's perspective, this often means data about where certain nuclear measurements come from, or the details of a theoretical calculation or compilation. Examples of metadata include the facility where a measurement was made, the author(s) who published the measurement, the specific device that was used to take the measurement and the type of device, the date the measurement was taken, the publication information about the paper in which the measurements were published (such as DOI), and the affiliated institutions responsible for the measurement. The Notre Dame Nuclear database includes all of these metadata as a standard part of any measurement. The database also stores metadata associated with theoretical calculations and compilations. Users are therefore able to find the organization that produced the compilation or the researchers that made the theoretical calculation, for example. One advantage of the availability of metadata is that it allows users to know where, why, and how different data disagree. By recognizing the scientists responsible for any measurement, (ND)² helps foster a dialogue between researchers when discrepancies arise. It is our hope that this will allow conflicts to be resolved more quickly and easily.

Technologies Used:

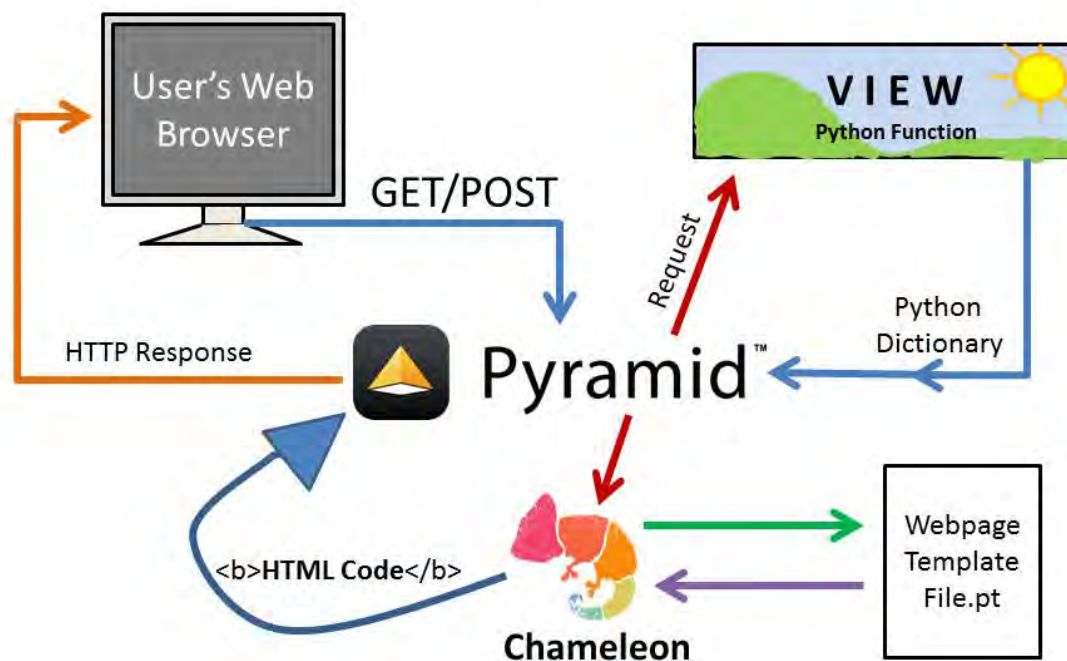
The main component powering our database is Python, a high-level programming language. Python is the main engine powering Pyramid, a web-development framework that we use to generate the website for our database. Pyramid sets up routes for each webpage we create, which are essentially URLs, and assigns each route to a view function which generates what the user will see when they visit a certain route. We also employ MySQL, a relational database management system that we use to store nuclear data in a way that connects different variables to each other very efficiently. For example, MySQL stores associations between each

mass measurement and the authors who published the measurement. This means that the authors can be accessed by simply specifying a certain measurement. SQLAlchemy is then the language we use to access data from MySQL.

Our team uses Git, a version control system, in order to facilitate collaboration. Git allows us to all work on the same code from different locations while expediting the process of sharing our work. It also provides full version control of our code which means that each modification to the database is permanently saved. Although the changes can be undone, there is always a record of how the code used to be, so it is virtually impossible to destroy the database by accidentally deleting a file. Git also pairs well with the open-source nature of (ND)². We intend to make our database an entirely open-source project meaning that all of our code will be freely available to the public. Git allows those interested to not only see the current version of (ND)², but also past versions that are no longer in use.

Basic Structure of (ND)²:

Basic Design of (ND)²



Above is the general framework by which (ND)² returns data to the user. The process of data retrieval often starts with the user's web browser. The browser will send form data to the server in the form of a GET or a POST. This form data contains filtering variables such as the nuclides that the user wants to search for and their associated metadata. Pyramid then intercepts these parameters and sends them as a request object to the view, a Python function responsible for generating the content of a webpage. Based on this request object, Python queries the MySQL database via SQLAlchemy. After receiving the resulting nuclear data, Python returns a dictionary back to Pyramid. Then, only if the webpage uses a template file, Pyramid will send the dictionary to Chameleon, a templating language, that will fill in the specified template with content from the Python dictionary. The result is standard HTML code that Chameleon sends back to Pyramid. Pyramid then converts this to an HTTP response for the user's web browser to read. This complex process is the most efficient and comprehensive mode of nuclear data retrieval to date.

How to use (ND)²:

There are three main ways to interact with (ND)²: the search page, the chart of nuclides, and the command-line interface. Our team has developed a standardized search API, application program interface, so that the same search capabilities are available across all three main components of the database. We wrote this code in Python in an object-oriented style for maximum efficiency and generality. This robust searching protocol relies upon well-defined filtering variables to select the specific data that the user requests.

Notre Dame Nuclear Database

Home Search Chart Documentation Downloads Contact login sign up

Here is what we found for you: Page 1 of 80
3997 Results

#	Z	A	Facility	Date	Device	Device Type	DOI	Author	Institution	Mass	Error
1	1	3	Manne Siegbahn		SMILETRAP			Sz. Nagy		3.0160486124463706 [u]	4.1511776650274154e-36 [kg]
2	1	3	Atomic Mass Data Center (AMDC)	2013-01-27	AME (Atomic Mass Evaluation)			M. Wang		3.01604927688 [u]	2.37253256908e-09 [u]
3	2	3	Manne Siegbahn		SMILETRAP			Sz. Nagy		3.0160286562748455 [u]	4.317224771628512e-36 [kg]
4	2	3	Atomic Mass Data Center (AMDC)	2013-01-27	AME (Atomic Mass Evaluation)			M. Wang		3.01602931905 [u]	2.50135786695e-09 [u]
5	2	4	U.		PTMS			R. S. Van		4.002603146084122	1.0627014822470185e-

Example search results page viewed in Google Chrome

The first way to use (ND)² is to simply make an online web search. By visiting the search page of (ND)², users can specify the parameters they want to filter by to generate search results. These parameters include any kinds of data and/or metadata. For example, let us assume that a researcher wants to be presented with all of the half-life measurements of all nuclides between $Z=1$ and $Z=10$ that were taken at CERN after 2005. This is as simple as setting the Z -range to 1-10, entering CERN in the facility box, and entering 2005 in the date box. All search results matching the criteria will be presented in tabulated, paginated form once you click the search button. We make this search experience possible through our standardized API.



Chart of nuclides colored by mass with shape set to circles; the filter tab is visible on the right

The second way to access data is to use our interactive chart of nuclides. This chart is revolutionary because it uses scalable vector graphics (SVG) to generate the nuclide boxes. This allows for very dynamic zooming and panning that is supported on all computers and mobile devices. We also allow the user to switch between two shapes to display each nuclide: circles and squares, with squares as the default shape. Our standardized API allows the chart to be fully capable of all of the same search features as the search page. This means that if a user types “GSI” into the facility box, all of the nuclides who were not measured at GSI will disappear from the chart without having to reload the page. Furthermore, the user is easily able to switch between displaying different data types on the chart via color scheme without ever having to reload the page. Nothing like this is currently available on the internet.

Finally, we give users the option of a command-line interface that allows users to interact with data from (ND)² without having to use a web browser. One simple command will result in downloading user-specified, pre-parsed content directly to the user’s device in a chosen data format. Available data formats to download include JSON, ASCII, and XML.

Again, this uses the same search API as the chart of nuclides and the search page to specify data. This concept is totally revolutionary as no other technology exists that is comparable in function.

Conclusion:

The Notre Dame Nuclear Database has tremendous potential to benefit nuclear research. We believe our most important accomplishment thus far is the development of the API used to search the database. This is the chief component connecting all of the front-end user interfaces to the back-end data storage. The three methods of accessing data that we've developed - the search page, chart of nuclides, and command-line interface - are huge steps toward creating the ultimate database. By greatly easing the research process for nuclear physicists, (ND)² has the potential to accelerate the rate at which researchers from all institutions expand their knowledge and make scientific breakthroughs, and our team is proud to have made such an important contribution to nuclear physics.

References:

- [1] <http://www.mdc.bnl.gov/chart/>
- [2] F Herfurth *et al*, "Mass measurements and nuclear physics—recent results from ISOLTRAP", 2003 *J. Phys. B: At. Mol. Opt. Phys.* 36 931 [doi:10.1088/0953-4075/36/5/312](https://doi.org/10.1088/0953-4075/36/5/312)
- [3] P. Moller, J.R. Nix, and W.J. Swiatecki, *Atomic Data Nucl. Data Tables* 59, 185(1995)
- [4] M Wang *et al*, "The AME2012 atomic mass evaluation", CPC(HEP & NP), 2012, 36 (12): 1603–2014 <http://amdc.in2p3.fr/masstable/Ame2012/Ame2012b-v2.pdf>

Search for Higgs Bosons Produced in Association with Top-Quark Pairs and Decaying to
Hadronic Taus

Samantha Koutsares

2014 NSF/REU Program

Physics Department, University of Notre Dame

Advisors: Dr. Hildreth, Dr. Lannon

SEARCH FOR HIGGS BOSONS PRODUCED IN ASSOCIATION WITH TOP-QUARK PAIRS AND DECAYING TO HADRONIC TAUS

Abstract

Presented is a search for the Higgs Boson produced in association with top-quark pairs and decaying to hadronic taus. This project seeks to optimize signal sensitivity (signal-to-noise ratio) of previously published analysis using new techniques. Improvements in tau identification, multivariate selection, and event categorization were studied. A maximum likelihood technique was used to generate expected limits on the sensitivity of the analysis for observing ttH production. The results use the standard model expectation for ttH production where $m_H = 125.6 \text{ GeV}$.

Search for Higgs Bosons Produced in Association with Top-Quark Pairs and Decaying to Hadronic Taus

The Large Hadron Collider (LHC) is the world's largest particle accelerator. The LHC is a 27km ring kept at 1.85 K and accelerates particles up to .999999997 the speed of light. The LHC works by accelerating two particle beams in opposite directions. Once the beams are moving fast enough, magnets are activated to align the beams causing collisions in the many detectors on the LHC. There are four major detectors, ATLAS, ALICE, LHCb, and CMS. This summer I worked with CMS. CMS stands for Compact Muon Solenoid and is one of the two detectors (ATLAS being the other) integral in the 2012 discovery of the Higgs boson.

My project this summer was to assist in the search for more information about the Higgs boson. Specifically, I worked with the team studying the Higgs boson when it is produced in association with two top quarks (ttH) and decays into two hadronic taus. Now that the Higgs has

been discovered, the next stage of measurements will determine whether or not the Higgs can really be responsible for generating the masses of the Standard Model particles or not. In order to understand this, we need to measure the strength of the coupling of the Higgs to each of the Standard Model particles. The ttH process gives direct access to the Higgs coupling to top quarks, and thus forms an important measurement in the overall Higgs study.

Yields

The Tau Identification Algorithm (TauID), is a series of programs released by CMS that are used to best identify Taus based on the data that CMS can detect. I worked with two TauIDs during this project, in this paper the original TauID will be referred to as the “Old TauID” and the updated TauID with increased isolations and improved electron and muon filters will be referred to as the “New TauID”. Yields are an account of several statistics that give us an indication of the performance of our data analysis. Yields include the ratio of the number of events that pass the cuts in both the signal and background as well as the measure of signal sensitivity $\left(\frac{s}{\sqrt{s+b}}\right)$. I ran these yields on the Old TauID in order to gain a baseline for the project. I then tightened increased the minimum standards on the AntiElectronIndex and the AntiMuonIndex in both Tau1 and Tau2 to see if changing the minimum standards helped us reduce the amount of background coming in.

Old TauID	Baseline	Minimums increased to 2	Minimums increased to 3
Signal Sensitivity: $\frac{s}{\sqrt{s+b}}$.093	.072	.066
Signal-to-noise Ratio: Data/Collisions	1.078	1.114	1.154

While the Signal-to-noise ratio does increase with each cut, it is a relatively insignificant increase. The signal sensitivity, on the other hand, decreases with each cut. This shows that

increasing the minimum standards on the Old TauID does not reduce the amount of background coming in. I then repeated this process with the New TauID.

New TauID	Baseline	Minimums increased to 2
Signal Sensitivity: $\frac{s}{\sqrt{s+b}}$.097	.089
Signal-to-noise Ratio: Data/Collisions	.903	.901

Increasing the minimums did not improve either the sensitivity or the signal-to-noise ratio.

Limits

Ideally, our observations will match perfectly with the standard model. One technique we use to measure this is by using confidence level (CL) limits. A limit is the maximum value that the background can mimic the signal. I ran limits using FinalBDTG (Final Boosted Decision Tree Gradient) as my limit variable. I first ran the limit using 6 categories as my systematics.

Category	Description	Category	Description
1b_1nb	1 b-jet and 1 non b-jet	2b_0nb	2 b-jets
1b_2nb	1 b-jet and 2 non b-jets	2b_1nb	2 b-jets and 1 non b-jet
1b_3plusnb	1 b-jet and 3 or more non b-jets	2b_2plusnb	2 b-jets and 2 or more non b-jets

My results were:

--Asymptotic-- (Limits: Final BDTG)	
Expected 2.5%: r <	5.9381
Expected 16.0%: r <	8.4809
Expected 50.0%: r <	12.9375
Expected 84.0%: r <	20.6729
Expected: 97.5%: r <	32.1947

Here the Expected 50.0% median is the important number. Our goal is to reduce the limit as much.

We wanted to see if we could reduce this number if we lumped the six groups into varying numbers of other groups. I tried running it with three categories:

New Category consisting of Original Categories	
2 jets	1b_1nb
	2b_0nb
3 jets	1b_2nb
	2b_1nb

4plusjets	1b_3plusnb
	2b_2plusnb

--Asymptotic-- (Limits: FinalBDTG)	
Expected 2.5%: r <	6.6193
Expected 16.0%: r <	9.2651
Expected 50.0%: r <	14.0625
Expected 84.0%: r <	22.2463
Expected: 97.5%: r <	34.4275

And two categories:

New Category consisting of Original Categories	
1 b-jet	1b_1nb
	1b_2nb
	1b_3plusnb
2 b-jets	2b_0nb
	2b_1nb
	2b_2plusnb

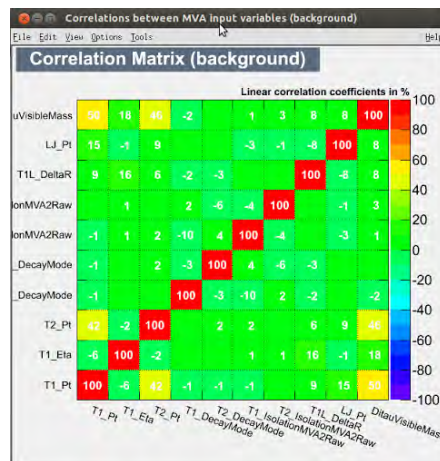
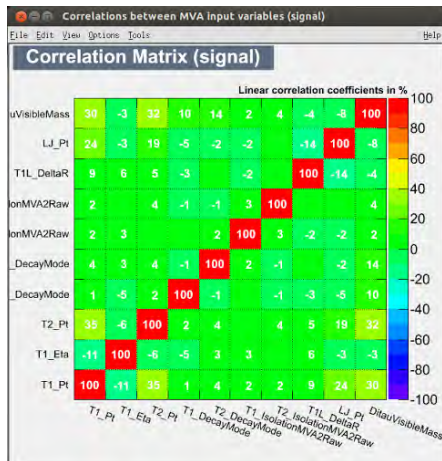
--Asymptotic-- (Limits: FinalBDTG)	
Expected 2.5%: r <	7.2616
Expected 16.0%: r <	10.2897
Expected 50.0%: r <	15.6875
Expected 84.0%: r <	25.0672
Expected: 97.5%: r <	39.0380

Neither organization improved our original 6 category outcome of 12.9375.

Variable Selection

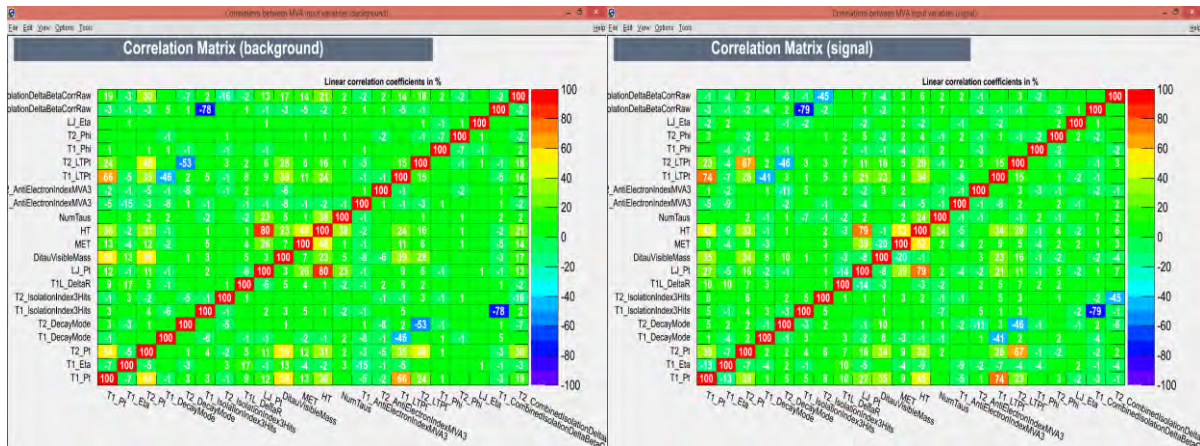
It occurred to us that the reason our data wasn't highly promising might have been because of impurities in our variable selection. To analyze the particular variables that were chosen, I ranked the variables in order of importance and then track their correlation using a TMVA correlation matrix.

Original Ranking		
Rank	Variable	Variable Importance
1	LJ_Pt	1.497e-01
2	T2_IsolationIndex3Hits	1.358e-01
3	T1L_DeltaR	1.150e-01
4	T1_Pt	1.136e-01
5	T2_Pt	1.113e-01
6	DitauVisibleMass	9.566e-02
7	T1_Eta	9.207e-02
8	T2_DecayMode	8.738e-02
9	T1_DecayMode	5.553e-02
10	T1_IsolationIndex3Hits	4.396e-02



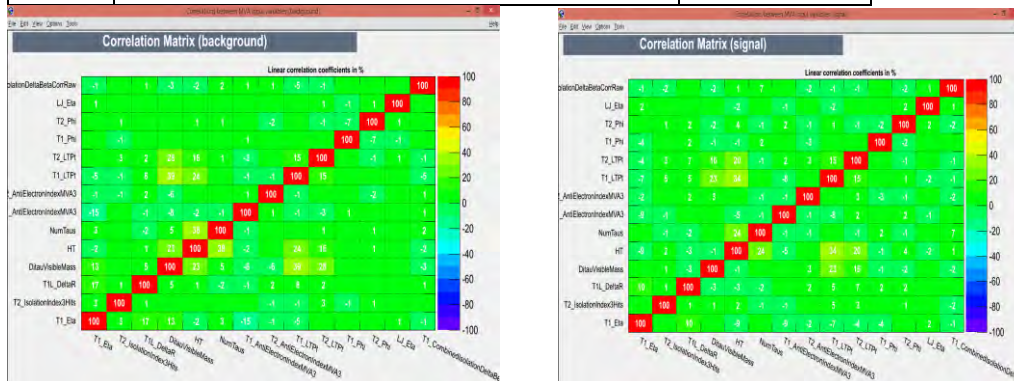
While the correlation of these variables look fairly good in the signal. There are some instances in the background where the variables are just slightly too highly correlated. So, I added every variable I could find to run one massive ranking and correlation matrix, I ended up running with 22 variables.

Ranking		
Rank	Variable	Importance
1	T2_IsolationIndex3Hits	7.798e-02
2	T2_LTPt	7.358e-02
3	HT	7.183e-02
4	NumTaus	6.595e-02
5	LJ_Pt	6.101e-02
6	T2_CombinedIsolationDeltaBetaCorrRaw	5.672e-02
7	MET	5.598e-02
8	T1_LTPt	5.170e-02
9	DitauVisibleMass	4.726e-02
10	T1L_DeltaR	4.677e-02
11	T1_Pt	4.391e-02
12	T1_Phi	4.021e-02
13	LJ_Eta	3.903e-02
14	T1_Eta	3.902e-02
15	T2_Phi	3.900e-02
16	T2_DecayMode	3.878e-02
17	T2_Pt	3.008e-02
18	T1_CombinedIsolationDeltaBetaCorrRaw	2.903e-02
19	T2_AntiElectronIndexMVA3	2.569e-02
20	T1_AntiElectronIndexMVA3	2.544e-02
21	T1_DecayMode	2.230e-02
22	T1_IsolationIndex3Hits	1.874e-02



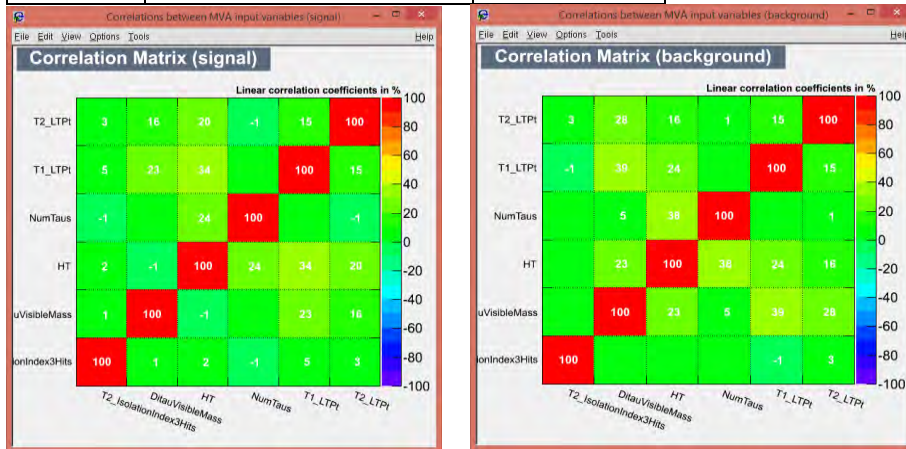
I then eliminated the high correlations by getting rid of the lowest variable in a highly correlated pair. I ended up with 14 variables. I ranked and tracked the correlations of those.

Ranking		
Rank	Variable	Importance
1	HT	2.270e-01
2	T2_IsolationIndex3Hits	2.032e-01
3	DitauVisibleMass	2.031e-01
4	T2_LTPt	1.582e-01
5	T1_LTPt	1.203e-01
6	NumTaus	8.941e-02
7	T1_CombinedIsolationDeltaBetaCorrRaw	3.532e-02
8	T1_Eta	2.868e-02
9	T1L_DeltaR	1.547e-02
10	LJ_Eta	8.742e-03
11	T1_Phi	4.887e-03
12	T2_Phi	4.571e-03
13	T2_AntiElectronIndexMVA3	1.861e-03
14	T1_AntiElectronIndexMVA3	1.221e-03



I then chose the top 6 ranked variables to run limits with.

Ranking		
Rank	Variable	Importance
1	HT	2.119e-01
2	T2_LTPt	2.055e-01
3	T2_IsolationIndex3Hits	1.666e-01
4	NumTaus	1.566e-01
5	T1_LTPt	1.529e-01
6	DitauVisibleMass	1.065e-01

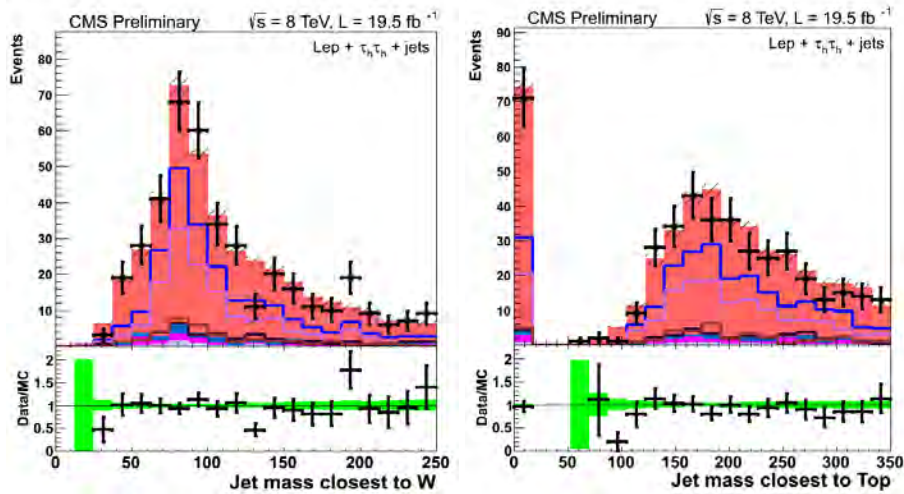


--Asymptotic-- (Limits: FinalBDTG) 6 categories	
Expected 2.5%: $r <$	5.8151
Expected 16.0%: $r <$	8.2136
Expected 50.0%: $r <$	12.5625
Expected 84.0%: $r <$	20.0737
Expected: 97.5%: $r <$	30.9782

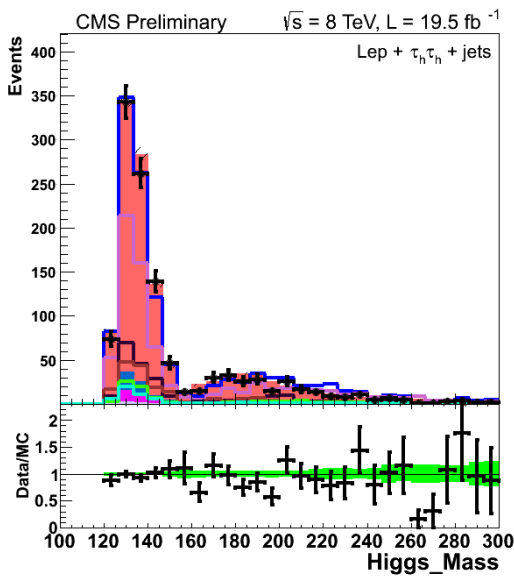
This limit of 12.5625 is an improvement on the limit we found in the previous variable set.

Reconstruction

At this point we started to wonder if we could take the data we've collected and use it to reconstruct some of the expected objects from top quark decay in order to get a more pure ttH signal. We first reconstructed the jet mass that is closest to the W boson. Then we wanted to use the data we got from the W boson to reconstruct the top quark.



After this, we decided it would be a good idea to reconstruct the Higgs. We used the missing transverse energy to calculate the neutrino energy and direction and then used that to reconstruct the Higgs mass. The peak ended up showing what we expected. The salmon area is the background and the blue line is the signal.



Despite the successful reconstruction of the Higgs mass. We were still concerned by the amount of background we were seeing.

Tracking

We wanted to see if there was more coming in the background than we expected. I then spend the next few weeks tracking each event individually. I tried to match the gentaus (“Truth” information from the Monte Carlo generator that simulated the event) to the reconstructed taus, leptons, and jets. At first I did this by hand and manually figured out which gentaus were best matched. After a while though, I decided to automate the process for all 1400 events. What I discovered was that there was a lot more going on in the background than we had originally anticipated.

In my program, I took the gentau measurements in the phi and eta directions and matched them as well as they could fit to the measurements for the taus, leptons, jets, and reconstructed taus in the phi and eta directions.

Key:	
J – Jet	L – Lepton
T – Tau	R – Reconstructed Tau
U - Unmatched	

Match Configuration	# of occurrences	Match Configuration	# of occurrences	Match Configuration	# of occurrences
JTU	21	JTT	25	LR	1
No Gentaus	152	LRT	18	JJLT	3
LT	170	RTT	9	LU	2
T	232	RTU	7	LRTT	1
TU	225	L	13	JRTT	1
JLT	28	J	12	LTUU	3
TUU	13	JLTT	3	JRT	4
TTU	42	LTT	31	RU	3
RT	47	JLTU	7	JLRT	1
U	22	JU	6	LTTU	3
LTU	35	R	4	JJLT	1
JT	104	JJT	4	UU	3
TT	205	JLU	1	RTTU	1
JR	1	LRU	2	JL	2
LRTU	1	TTUU	2	JJTT	1
RRT	2	TTT	1	LRRT	1
JJ	1				

The most interesting results we saw were the high number of events with no gentaus and the high number of events that could not be matched with the data we have. In the case where there are no gentaus it is likely that the taus we are measuring are either fake, or some from other sources.

However, because there are so many unmatched gentaus, our next steps need to address our current method of identifying taus.

Conclusions

This project showed that by subdividing the event samples, we could gain a better sensitivity. Our next step should be to analyze how we choose our taus, and how to minimize the background, now knowing that there are so many different configurations to the background.

References:

The CMS Collaboration, *Search for Higgs bosons produced in association with top-quark pairs and decaying to bottom quarks, photons, or leptons*, 2014

GRAS_{ANS}P Multi-File Fitter:

A User's Guide

ALLAN LEISHMAN

2014 NSF/REU Program

Physics Department, University of Notre Dame

ADVISOR:

MORTEN RING ESKILDSEN, PhD

COLLABORATORS:

ELIZABETH DE WAARD

STEPHEN KUHN

CATHERINE RASTOVSKI, PhD

ABSTRACT

Graphical Reduction and Analysis SANS Program (GRASP) is a program developed in MATLAB™ for the analysis of small-angle neutron scattering (SANS). The software engages the user through a series of GUI's which allow the user to view and analyze their data in a straightforward manner. Of particular interest to this group is the ability to fit Gaussian peaks to the data files with relative ease, which can be used to characterize the superconducting vortex lattice states in MgB₂. However, one weakness of GRASP is the inability to analyze large collections of files quickly, as they all must be manipulated individually and fit by hand. This problem has been resolved through the creation of Multi-File Fitter (MFF), a user module designed to analyze large sets of files rapidly and export the fit parameters in a simple manner. MFF has greatly accelerated the analysis process, from a matter of days to a matter of minutes, with little to no loss in the quality of the fits.

INTRODUCTION

Small-angle neutron scattering (SANS) is an important method for investigating vortex lattices (VLs) in Type II superconductors (SCs)¹. A common method used to analyze SANS data is Graphical Reduction and Analysis SANS Program (GRASP), a program developed by Charles Dewhurst at the Institute Laue-Langevin². In particular, GRASP has proven very effective at fitting Gaussian peaks to SANS data (Figure 1). While this is useful, a key weakness of GRASP is the inability to perform this process repeatedly on large collections of files. This can make analysis of experiments quite cumbersome, as each file must be manipulated and fitted by hand. In this manual, we describe Multi-File Fitter (MFF), a user module we have added to GRASP to automate the curve-fitting process for large collections of files. MFF is particularly optimized for the investigation of metastable VL states in MgB₂, but could be modified for use in other applications. Overall, MFF has shortened the analysis process from a matter of a few days, to a matter of a few minutes.

Multi-File Fitter was designed in MATLAB R2014a for use with GRASP v. 6.89 or later, but has been shown to work with the more recent previous versions of this software.

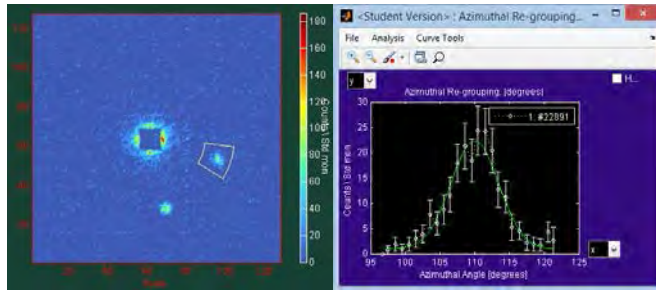


Figure 1: GRASP fitting data with a single, Gaussian peak.

BACKGROUND

We have designed MFF to aid in the investigation of phase transitions in the VL of MgB_2 . These second order transitions are characterized by a rotation in the hexagonal lattice, and have been shown to have a high degree of metastability³. Since both phases can exist simultaneously in different regions of the VL, both Bragg patterns can be seen through the transition. This can be observed as a gradual change from a one peak Bragg pattern to a two peak Bragg pattern (or vice versa), with all three peaks being visible during the intermediate steps (Figure 2). The relative intensities of these peaks allows for the calculation of what fraction of the VL is in each state over time, which can be used to better understand these transitions in the lattice. Further analysis has ruled out vortex-pinning as the cause of this high metastability⁴.

Correspondingly, MFF allows the user to fit large groups of files with three-peak Gaussians automatically, storing the appropriate fit parameters in a table for easy viewing. MFF also allows the user to export this table as a txt file should any further analysis be desired (Excel, Origin, etc.). Finally, the fraction of the lattice in the one peak state can be calculated and plotted versus file index to show the gradual transition between the states (this is shown in Figure 6).

Commented [ME1]: The coexistence in itself does not show that pinning is not the mechanism behind the metastability. Rather we did another analysis of the radial peak position to show this. I would imagine that the program could relatively easily be extended to do this analysis as well, but since this is already finished and published there's little reason to do so at the moment.

Error bars on this plot are propagated from the uncertainties calculated by GRASP for each of the fitted intensities.

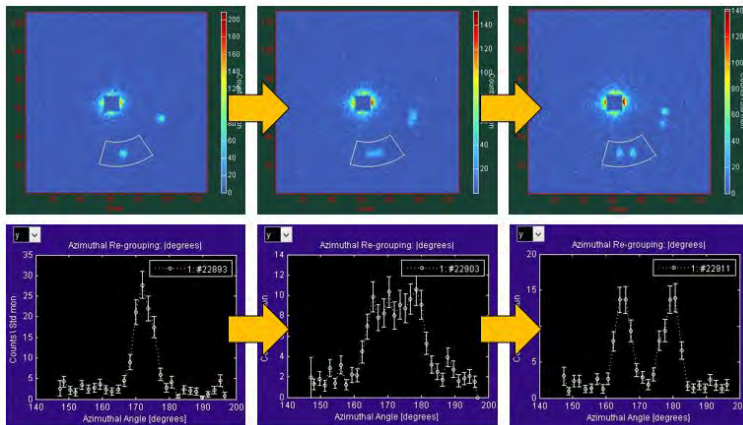


Figure 2: Transition from the metastable state to the ground state in the VL of MgB_2 . Note the characteristic shift from one central peak, to three peaks, and finally to two outer peaks.

FITTING PROCEDURE

MFF cycles through three rounds of fitting. A visual representation of the three fitting rounds can be seen in Figure 3. In each round, MFF improves the fit by manipulating some of the four fitting parameters (center position, full width half max (FWHM), background, and intensity). The most sensitive of these parameters is the FWHM and centers, as the convergence of the fit is highly dependent on them. In every fit though, the FWHM and background are “grouped”, meaning that all the peaks in one file have the same values for these parameters. This is valid since the FWHM and background are functions of the experiment and should be constant between peaks.

In order to start with good seed values, MFF first asks the user for one file which is a characteristic example of the one central peak, and for one file that is a characteristic example of

the two outer peaks. Then, using the peak centers and FWHM fitted to these files as “guess values” (values which are recommended to GRASP, but not fixed), MFF begins its three rounds of fitting.

In the first round, MFF fixes the three centers to the values extracted from the reference files and allows the FWHM to fluctuate. For each file, MFF checks if any of the peak intensities are below a user-defined ratio of the total fitting intensity (the intensity cutoff). If the central peak is below the intensity cutoff, MFF will fit the file with two peaks in the next round. If either of the edge peaks are below the intensity cutoff, only the central peak will be fit during the next round of fitting. This cutoff discourages MFF from fitting noise, which would then be weighted into future averages. In the second round, MFF cycles through the files again, fixing the FWHM to the average of the previous round, while allowing the centers to fluctuate. In the third round of fitting, the centers are fixed to the averages of the second round, the FWHM remains fixed, and each file is once again fit with three peaks. This allows the peak intensities to be compared directly, which is ideal for calculating what fraction of the VL is in each state.

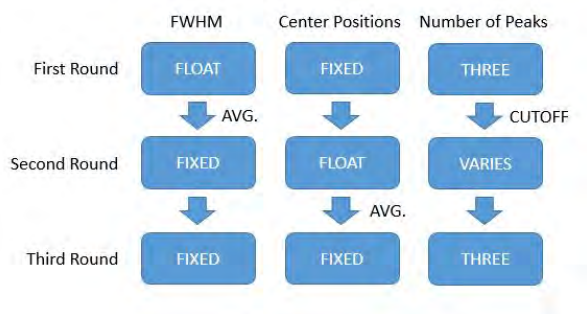


Figure 3: Three-round fitting procedure

INSTALLATION

To add Multi-File Fitter to GRASP, start by adding the MFF folder (likely the folder you found this manual in) to your MATLAB path. This can be done by right clicking on the folder in the Current Folder window and selecting **Add to Path** → **Selected Folders and Subfolders**.

Next, we need to add a button in GRASP so that we can run MFF. One simple way of doing this is to edit the **modify_main_menu_items.m** file, which can be found in the **main_interface** folder of GRASP. After opening this file, scroll down to the User Module section (approximately line 512) and add the following line of code:

```
MF FITTER - Allan 7/27/14
uimenu(grasp_handles.menu.user_modules.root,'separator','on','label','M
ulti-File Fitter','callback','mf_GUI_window','enable','on');
```

Save **modify_main_menu_items.m** after adding this line of code. This should be all the MATLAB coding required to use MFF. (Note: If you cannot/ do not want to modify GRASP code, MFF can be accessed and ran by returning the command **mf_GUI_window** in the Command Window while running GRASP).

BASIC OPERATION

Before starting MFF, make sure your data files are loaded into GRASP using the standard method (**Set File & Data Directory**, type in the Numors, etc.). (Note: It is not recommended to load “junk” files into GRASP. These have a tendency to mess up the center averaging and distort the fits that MFF produces). To start MFF, click on the **User Module** tab in GRASP, then select **Multi-File Fitter**. After a few seconds, a window like Figure 4 should open. Below is a description of each part of the interface:

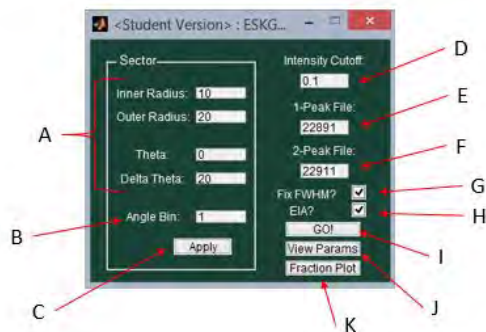


Figure 4: Main interface for MFF

- A. **Sector Selection:** Allows the user to modify the desired polar coordinate sector in the exact same manner as the default GRASP Sector Window, without having to open a separate window. The current sector can be viewed in the main GRASP window
- B. **Angle Binning:** Allows user to modify the binning for the azimuthal intensity plot to their choice. This can be changed to improve the quality of fits. These typically vary from 1.5 to 2 degrees.
- C. **Apply Sector Button:** Applies current sector and angle binning, and opens a window showing what one of the plots looks like with these parameters. (Note: You may have to use the plot that this window generates to open the Curve Fit window. Sometimes the fitting algorithm does not work without the Curve Fit window being open.)
- D. **Intensity Cutoff:** Allows user to select what fraction of intensity will be used as a cutoff to define a peak. The default setting is 0.1. (This means that any peak with an integrated intensity of less than 10% of the total for that file will be excluded from the final averaging of the centers). The value can be varied to improve fits.

- E. **1-Peak File**: User inputs Numor of one file that is the best representation of the single, center peak (this defaults to the first file in the stack).
- F. **2-Peak File**: User inputs Numor of one file that is the best representation of the two, outer peaks (this defaults to the last file in the stack).
- G. **Fix FWHM**: This checkbox controls whether or not the full width at half maximum (FWHM) is fixed to an average value for all files in the final round of fitting. The FWHM is fixed by default, as statistically speaking, all peaks should be the same width, but this feature can be turned off.
- H. **EIA**: For use in only the most awesome of circumstances.
- I. **Go! Button**: Starts fitting cycle as described above. Please make sure that all of the previously mentioned settings have been set to your desires before hitting this button. To cancel the fitting cycle while running, hit Ctrl + C in the Command Window. At the end of all three cycles, a table (Figure 5) will open showing the fit parameters for all files.
- J. **View Parameters Button**: Reopens the table of fit parameters (Figure 5) for the most recently ran cycle (in case you accidently close the window).
- K. **Fraction Plot Button**: Calculates and plots the fraction of the VL in the 1-peak state vs. the index of the file. An example of this can be seen in Figure 6.

After hitting the **Go! Button**, the fitting procedure will begin (~ 3 to 5 min). After fitting all files, the program will display a table containing all the fit parameters, as well as the chi-squared for the fit. An example of this table is shown in Figure 5.

Numors	Chi-Squared	FWHM	I	I Error	J1	J2 Error	J3	J3 Error	J4	J4 Error	J5	J5 Error	J6	J6 Error	J7	J7 Error	J8	J8 Error	J9	J9 Error	J10	J10 Error	J11	J11 Error	J12	J12 Error	J13	J13 Error	J14	J14 Error	
1	22001	1.9553	5.8544	-2.0544	3.5200	105.0243	0	143.2084	11.0192	172.5412	0	2.3210	4.1279	179.6453																	
2	22002	1.2783	5.9857	13.2648	4.9172	179.9384	1.1489	146.4287	9.8264	172.9548	0.1075	7.6274	3.2761	189.1017																	
3	22003	2.1349	6.0558	9.1782	4.6564	165.0343	0	171.0875	14.2796	172.5412	0	2.8038	6.8716	179.6453																	
4	22004	0.9913	5.9887	82.0979	9.9489	171.2659	0.5279	89.8230	8.8987	173.9073	8.4028	0.9189	4.4235	179.1371																	
5	22005	1.0813	5.9887	8.9022	3.6791	168.6544	1.5889	139.8281	8.8022	172.9064	0.1841	25.7043	4.1794	179.3746																	
6	22006	1.0889	5.9346	-25.8733	4.6837	168.0543	0	179.8289	12.9782	172.5412	0	-13.4188	0.8123	179.9475																	
7	22007	1.7261	5.9887	21.5979	7.8957	168.1915	-1.1528	89.7063	10.8756	171.7029	0.3883	43.1996	0.4688	179.1891																	
8	22008	0.9937	5.9987	13.8511	3.9589	163.8096	0.6959	170.4981	7.1883	171.6227	0.1981	38.2247	4.8875	179.1570																	
9	22009	1.7188	5.9987	18.7488	6.8712	167.8239	1.1456	87.2873	10.7664	172.5025	0.2272	39.0469	7.9134	178.7239																	
10	22010	1.4559	5.9987	38.9082	7.4210	167.5899	0.4268	73.0595	9.2448	172.6947	0.4459	46.1882	7.4211	179.5359																	
11	22011	0.8976	5.9987	35.9329	4.4969	159.4080	1.5482	31.9587	10.5547	169.2282	1.9854	76.4967	15.0565	179.5729																	
12	22012	1.8888	5.9987	38.4170	4.8884	169.7917	0.3647	72.2480	9.8981	172.4437	0.2758	44.3928	4.9687	179.2617																	
13	22013	1.6989	5.9987	42.0579	4.4482	165.6943	0.3205	43.0791	4.7965	171.6798	0.4331	35.2904	4.8269	179.3936																	
14	22014	1.7271	5.9987	58.7979	3.9856	166.9156	0.2463	46.7834	4.0395	172.4598	0.3122	52.6982	3.9162	179.1381																	
15	22015	2.5721	5.9987	42.5198	6.8872	165.9382	0.4982	36.0169	6.8238	179.9642	0.6193	63.5177	7.4277	179.6095																	
16	22016	1.2445	5.9987	52.2705	3.9412	165.5876	0.3431	31.4071	5.5170	179.4961	0.5887	64.4937	15.3686	179.6027																	
17	22017	2.1389	5.9987	37.2207	4.8875	164.4688	0.3593	44.2951	5.0300	169.8258	0.5990	54.2560	5.3238	179.4403																	
18	22018	2.1881	5.9987	59.2188	5.2732	165.7938	0.2736	21.8653	4.4562	179.8709	0.7192	72.8969	5.5493	179.2159																	
19	22019	1.3916	5.9987	81.9099	4.5384	165.8888	0.2118	39.4817	4.8232	173.0587	0.5120	69.2980	4.8370	179.8044																	
20	22020	1.2422	5.9987	47.0244	6.8568	165.5949	0.4821	24.5143	6.0223	169.9814	0.7760	48.6946	7.0214	179.8916																	
21	22021	1.7173	5.9987	1.059e+03	6.1971	166.2211	0.9166	-887.7882	8.8431	166.3180	0.8178	72.1770	0.8442	179.0064																	

Figure 5: Table of fit parameters

- A. **Fit Parameters:** Table of calculated fit parameters, including the FWHM, all three centers, all three intensities, and all associated uncertainties. The chi-squared of the fit is also calculated and displayed in the second column.
- B. **Examine Fit:** Allows the user to reexamine a fit of their choice by inputting the appropriate index (row number, NOT Numor).
- C. **Update Table:** Reopens window to implement any changes that have been made to the fit parameters since it was opened.
- D. **Negative Intensities:** Calls the user's attention to any fits which have negative values for at least one of the intensities (ideally, they should all be positive or zero).
- E. **Export to .txt:** Allows the user to export the fit parameters to a .txt file. Upon pressing this button, the user will be allowed to pick where they would like the file to be saved.

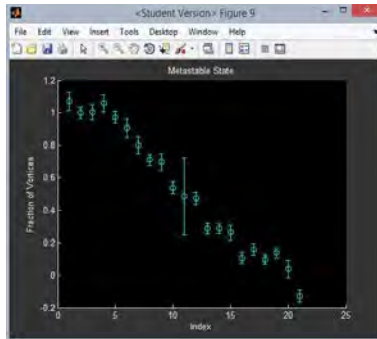


Figure 6: Fraction of VL in the metastable one-peak state

CONCLUSIONS & FUTURE WORK

Multi-File Fitter has greatly accelerated the analysis process, through both the ability to fit files sequentially and the simplification of exporting data. Analysis which once took C. Rastovski several days has been reduced to 5 – 10 minutes for the largest collections of files. More data must be run through the software to work out any quirks in the program. Hopefully, this can be done after our next set of experiments (November 2014).

REFERENCES

1. M. R. Eskildsen, “Vortex lattices in type-II superconductors studied by small-angle neutron scattering”, 2011, *Front. Phys.*, 6(4), 398 – 409
2. C.D. Dewhurst, “GRAS_{ANS}P: Graphical Reduction and Analysis SANS Program for MATLABTM”, 2001, Institute Laue Langevin
3. P. Das, C. Rastovski, T.R. O’Brien, K.J. Schlesinger, C.D. Dewhurst, L. DeBeer-Schmitt, N.D. Zhigadlo, J. Karpinski, and M.R. Eskildsen “Observation of Well-Ordered Metastable Vortex Lattice Phases in Superconducting MgB₂ Using Small-Angle Neutron Scattering”, 2012, *Physical Review Letters*, 167001
4. C. Rastovski, K.J. Schlesinger, W.J. Gannon, C.D. Dewhurst, L. DeBeer-Schmitt, N.D. Zhigadlo, J. Karpinski, and M.R. Eskildsen “Persistence of Metastable Vortex Lattice Domains in MgB₂ in the Presence of Vortex Motion”, 2013, *Physical Review Letters*, 107002

Search for Gamma-Ray Sources from a Measurement of the Muon Angular Distribution with High Statistics

Chuanhong Liu^{1,2,3}

Advisor John Poirier¹

¹Dept. of Physics, University of Notre Dame, IN 46556, USA

²Dept. of Physics, Xi'an Jiaotong University, Xi'an, Shannxi, 710049, China

³Dept. of Physics, Texas A&M University, College Station, TX 77845, USA

Abstract

Project GRAND is an array of proportional wire chamber stations which detects secondary muons produced by cosmic ray primaries. It has been used to detect muons since 1995. In this report, 6.5 years of data has been analyzed in order to construct a high statistic angular map of muon flux in celestial coordinates (right ascension, declination) and in solar coordinates (solar hour of day EST and declination). We search for muons in coincidence with gamma-ray sources with GRAND using data from 1 Jan 2007 to 30 Jun 2013.

1 Introduction

Many physical processes both in space and atmosphere generate muon flux. On Earth, most naturally occurring muons are created by cosmic rays, which consist mostly of protons, many arriving from deep space at very high energy (1). About 10,000 muons reach every square meter of the earth's surface a minute; these charged particles form as by-products of cosmic rays colliding with molecules in the upper atmosphere (2). When a cosmic ray proton impacts atomic nuclei in the upper atmosphere, pions are generated. Pions will decay in such a short distance into muons, and muon neutrinos. From high energy cosmic rays, muons generally continue in approximate the same direction as the very original proton. At a velocity near the speed of light, the time dilation effect of special relativity allows secondary muons to survive during the flight to the Earth's surface. In order to detect and identify the direction of the cosmic ray sources, especially Gamma ray sources, the angular distribution of the secondary muons need to be measured with high precision. Project GRAND, a distributed array, is built to measure these secondary muons. The angle of each incident muon is determined with a resolution of better than 0.5° , in each of two projected planes. This, along with accurate information on the arrival time of the muon, allows for the creation of a map of muon counting rates in right ascension and declination. Data are collected over five years and used in the construction of such an angular map. This paper updates previous work (3), and references therein. Secondary muons from those distant Gamma ray sources, eg. Crab Nebula and Cygnus X-3, only take up a very small percentage of total muons compared those muons from the cosmic rays omitted by relatively close sources like Sun. Six and a half years' data will help to subtract the dominate background influence and reveal the real distant source's direction from the periodic noise.

2 Background

Project GRAND is an array of 64 detector stations located north of the University of Notre Dame at $41.7^\circ N$ and $86.2^\circ W$ at an altitude of $220m$ above sea level. Two experiments are run simultaneously at the array: the tracking of low energy single muon events and the detection of high energy air showers. The single track muon experiment is increasingly sensitive to primary energies $> 10GeV$ with a median value of $50GeV$ for vertical tracks. Each station contains four proportional wire chamber (PWC) plane pairs. These eight $1.29m^2$ PWC planes yield a total active area of $82m^2$. Each of the four chambers in a detector contains a horizontal plane of wires running north-south and another plane of wires running east-west. When a charged particle passes through the chamber, it leaves a trail of ions which accelerate toward the closest signal wire. As they gain energy, they collide with more gas molecules and release more charged particles in a process known as gas amplification which further increases the charge collected on the signal wire resulting in a small current. By identifying the hit wires in each plane and comparing the event position for each plane, the angle of the muon track can be reconstructed to within 0.5° , on average, in each of two projected planes: up-east and up-north. A $50mm$ thick steel plate is situated above the bottom two PWC planes to discriminate between muon tracks which penetrate the steel and electron tracks which stop, shower, or are deflected by the steel. The array collects data at a rate of 2000 identified muons per second. Added details are available at: <http://www.nd.edu/grand>.

The array records approximately 1700 muons per second. Time information with millisecond precision is obtained from a radio receiver tuned to WWVB in Boulder, CO. A one MHz crystal clock is used as a backup time reference in case the WWVB signal is lost. The data are stored in records of 900 muons each. The start and end times of these records are recorded as well as the incident angle of each muon in both the north-up and east-up planes.

3 Data Analyzing

3.1 Periodic Influence

Data were collected from 1 Jan. 2007 until 29 Jun. 2013. In this study, 2372 solar days were analyzed to average out the periodic trends in flux. As the earth is rotating along its axis, the right ascension right above the same place on the earth will change 15° per hour.

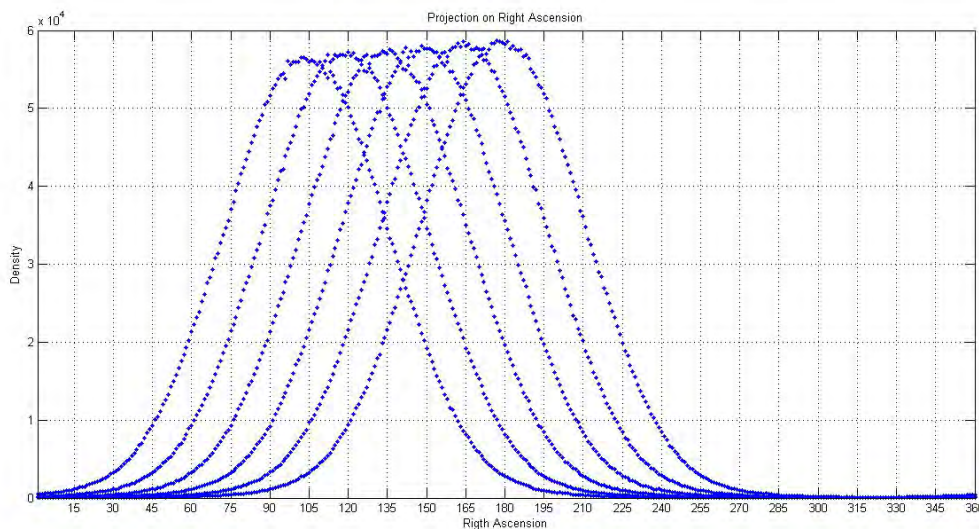


Figure 1: The projection on declination of muons for the first six hours first day of year 2012.

Compared with right ascension, the density of muon on declination cannot be flat because the axis of earth's rotation. In addition, the quantization of the PWC makes the projection on declination more irregular, shown in Fig.3. The peak around 35° is out of the location of the GRAND array. The decrease of the density of muon to -20° and to 90° is mostly due to the fact muons will travel a longer distance of atmosphere.

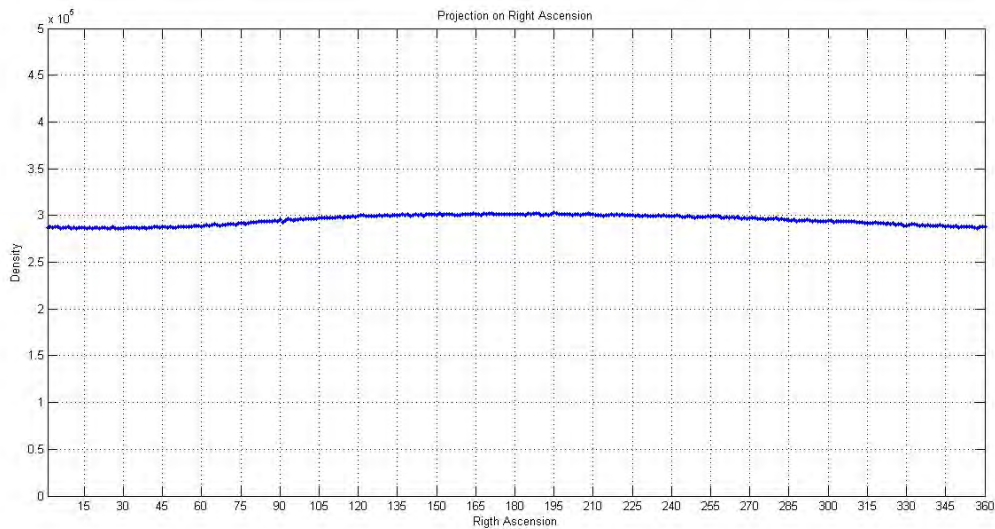


Figure 2: The projection on declination of muons for the first six hours first day of year 2012.

3.2 Angle

As mentioned before, the incident angle (right ascension and declination) of each muon needs to be calculated based the time and the location of the array in earth. The location of the array stays the same, while the time changes. With the help of WWVB in Boulder, CO, we can store the time information for muon with millisecond precision. However, if there is extreme weather condition like storm, the WWVB signal can be lost. In such case, a one MHz crystal clock, which is always running separately from the WWVB, is used to back the time up. The one MHz crystal clock is with a much higher precision, $10^{-6}second$. All the data files are stored in solar time coordinates. For distant gamma ray sources, we need to convert the solar time coordinate to sidereal time coordinates. For those days when the clock works with high precision, we just cut the difference between a solar day and sidereal day from the last hour file for each solar day. There are $86400seconds$ in one single solar day and $86164seconds$ in one single sidereal day. Thus $236seconds$ will be subtracted from the last hour file. For those particular days, when both the WWVB clock and one MHz crystal clock are not working, the fraction of muons has been

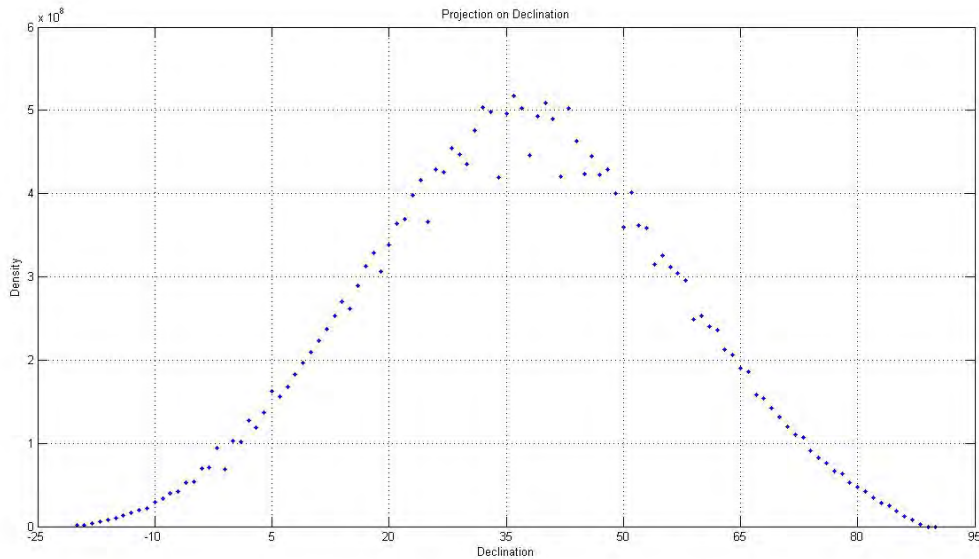


Figure 3: The projection on declination of muons from the required sidereal days of the first 180 days of year 2010.

used to deal this problem. The rate of the muon changes very slightly during one day, so we can use the total number of muons detected by array as a 'clock'. Apart from the 236 seconds, we have 24 seconds gap in total for each day as a result of the computer's data store. Thus, 260 seconds need to be subtracted from the last hour to make it a complete sidereal day. During the last hour, we have 3600 seconds, the ratio of muon we are supposed to get is $1 - 260/3600$, and which is 0.92778. For example, we have a total number of 4299471 muon for the last hour of 1 Jan. 2012 and $4299471 * 0.92778 = 3988963$. Then, when the program will stop at the 3988963th muon.

4 Results and Summary

After data selecting and basic analyzing, we have $2.52836 * 10^{11}$ muons in the matrix. Fig.4 shows the angular distribution of density on right ascension and declination, which agrees with Fig.2 and Fig.3, in which the distribution and right ascension is rather flat as the declination is

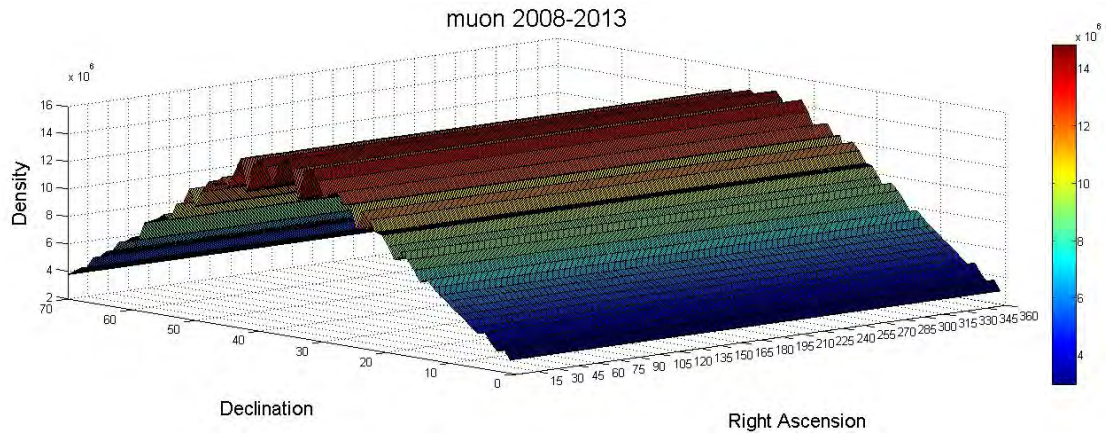


Figure 4: The angular distribution of secondary muon is displayed in the three dimensional plot.

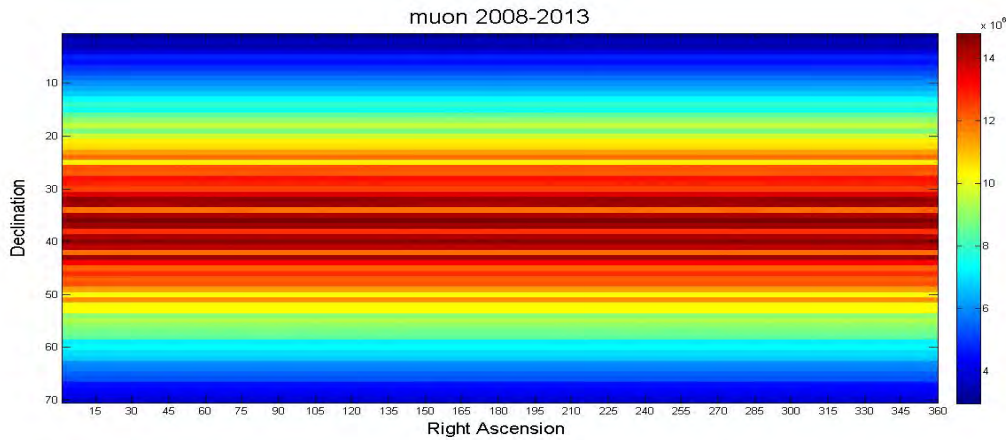


Figure 5: A two dimensional colorbar map of the distribution of the muon density

not. We have two different ways to find the Gamma ray sources from the matrix.

4.1 Certain Angle

We chose a window of 6° (in right ascension) by 5° (in declination) as the location of some certain source. We need to get the amplitude of the both the signal and the background area. As shown in Fig.4, the amplitude of the density does not vary so much as the right ascension varies. In this condition, we choose two nearby windows with the same declination as the background. And calculate the σ from the background and signal area. Here are two known Gamma ray

sources, Crab Nebula (RA: 83.6° , Dec: 22.0°) and Cygnus X-3 (RA: 308.1° ,Dec: 40.6°). For The result for Crab Nebula is 38035 ± 24086 ($\approx 1.58 : 1$) and Cygnus X-3 is 619222 ± 26809 ($\approx 2.31 : 1$). It will be better if we can have a ratio more than 3σ , with which we will have more confidence to declare this window covers a distant Gamma ray source.

4.2 Normalization

Using normalization, we can easily tell direction we may be interested just simply by looking at Fig.6 or Fig.7. The pixels were normalized using the following equation: $Diff = \frac{N - \langle N \rangle}{\sqrt{\langle N \rangle}}$

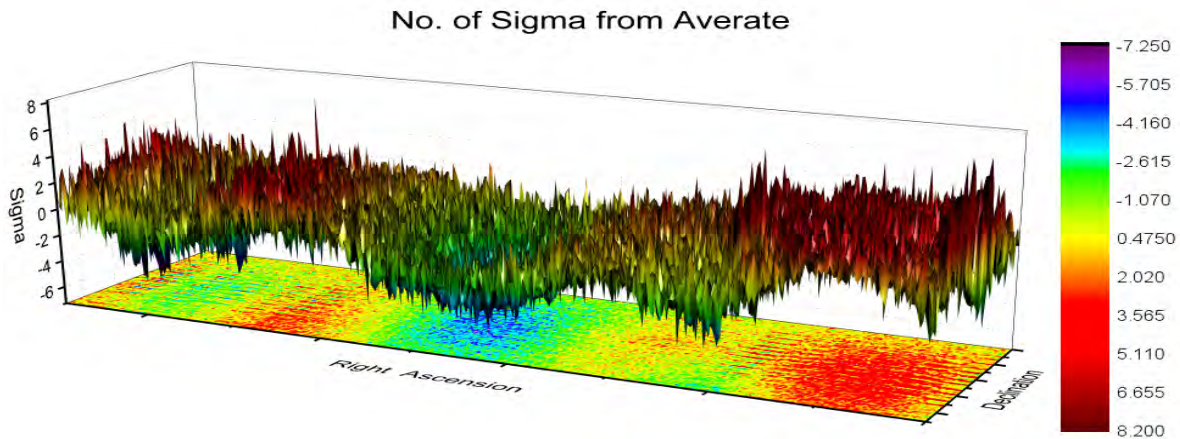


Figure 6: The results are given as a function of Declination versus Right Ascension. Although the statistical deviations can be large $\pm 8\sigma$, the absolute variations are small ($< 1\%$) due to the large numbers of identified single muons in each box.

5 Acknowledgment

Thanks to the Center for Research Computing for providing the on-campus data backup system that contributed to the 24/7 continuous operation and security of the data. Project GRAND was constructed with assistance from the National Science Foundation and is operated by gifts from The University of Notre Dame and private individuals.

References and Notes

1. S. Carroll *Spacetime and Geometry: An Introduction to General Relativity*, Addison Wesley, p. 204 (2004)
2. Mark Wolverton *Muons for Peace: New Way to Spot Hidden Nukes Gets Ready to Debut*, Scientific American 297 (3) 2628. (September 2007)
3. C. DAndrea and Poirier, J. *A Measurement of Secondary Muon Angular Distribution with High Statistics*, ICRC. 06. 1293 (2011)
4. Poirier, J. and C. DAndrea in Proceedings of the 27th ICRC. 3923-2926 (2001)

Measurements of Internal Conversion Electron
Emission Cross-Sections for ^{154}Gd , ^{156}Gd , ^{157}Gd

Marcus Lowe; Wanpeng Tan, Ani Aprahamian, Shelly Lesher

August 11, 2014

Abstract

To study the nuclear structure of deformed nuclei, in particular, $0+$ excited states in several gadolinium isotopes, we plan to perform (α, n) and $(\alpha, 2n)$ reactions on enriched samarium targets utilizing coincidence and time of flight techniques to measure conversion electrons, gamma rays and neutrons by populating the levels in gadolinium. As a preliminary experiment, natural samarium targets were used. Alpha particles, 16-21 MeV in energy, produced at the Nuclear Science Laboratory's Tandem van de Graaf accelerator at the University of Notre Dame, were incident upon a series of four natural samarium targets with the primary aims to measure cross sections of the selective $(\alpha, n/2n)$ channels and test the samarium targets for improvements for when the enriched material is used to produce the targets. Data were collected via an Internal Conversion Electron Ball array (ICEBall) containing six Si(Li) detectors and accompanying neutron and gamma-ray counters. Spectra were observed in ICEBall from both beta decay and conversion electrons emitted from a range of reaction channels both in ground state and excited states of gadolinium. The focus was set on $(\alpha, n/2n)$ channels that were more easily observed and identified with conversion electron peaks emitted from gadolinium-154, 156 and 157. We will present the results on conversion electron emission cross-sections as well as neutron and gamma fluxes for corresponding reactions and compare with TALYS calculations. These data give insight for performing future experiments that will use enriched targets so as to allow optimum beam energy for particular reaction channels while maintaining a neutron flux that is non-destructive for HPGe detectors

1 Introduction

Much debate has been had over the course of, approximately, the past decade on the cause of particular deformations in rare earth nuclei, such as gadolinium. As of 2002, there was the discovery of unexpected $0+$ excited states in ^{158}Gd [1]. This mismatch of predictions and experimental observation began a number of subsequent experiments for further investigation.

These subsequent experiments included measurements of absolute transition probabilities. By 2014 four separate isotopes; ^{154}Gd , ^{156}Gd , ^{158}Gd and ^{160}Gd , had been investigated for $B(E2)$ values. These were calculated through data obtained by an angular distribution experiment that utilized the inelastic neutron scattering reaction $(n, n' \gamma)$ [2].

At the present day, it is still debated what is actually seen when these low lying $0+$ excited states are observed. It is theorized by some that they are automatically described by vibrations within the nuclei, but others think this may be a hasty conclusion and are still investigating further.

The motivation for the content of this paper is then to allow further investigation of this debated topic. By testing natural samarium targets with an incident alpha beam we can induce both (α, n) and $(\alpha, 2n)$ reactions which create a large number of gadolinium isotopes due to it being a natural target. By selecting the correct peaks in the produced spectra it is possible to calculate cross sections of the desired reactions. By doing this, as well as varying target thicknesses and measuring the neutron and gamma fluxes produced, we can optimize parameters for experimenting with enriched targets and have a high intensity of the selected reaction channels

while maintaining a relatively low neutron flux.

Internal conversion is a competing process with gamma decay. It is an interaction between the excited nucleus and inner shell electrons which will cause the nucleus to emit these electrons instead of a gamma ray. It is important to note, this is a different process from beta decay, where a proton or neutron is converted into the other and the nucleus emits a newly created electron. Internal conversion involves already existing inner shell electrons.

2 Experiment

The FN tandem Van deGraaf accelerator in the Nuclear Science Laboratory was used to accelerate 16-21 MeV alpha particles into a natural samarium target within ICEBall, inducing $(\alpha, n/2n)$ reactions. The neutrons were detected by two liquid scintillators. The product nuclei will not necessarily be in ground state so they will begin to decay via gamma rays and conversion electrons. Gamma rays will also interact with the liquid scintillators and be counted for further use in analysis.

There is a unique feature about conversion electrons in that they do not carry orbital angular momentum. This feature allows for measuring $0+$ excited state transitions, which are mentioned in the introduction as being of interest. Since we are interested in a specific transition that does not change its spin, internal conversion electrons are the only way possible to detect these transitions.

3 Analysis

The end goal of this experiment is to locate the energy that will optimize the probability the conversion electrons at the desired energy will be emitted while maintaining a neutron flux that is not dangerously high for the High Purity Germanium (HPGe) detectors that will be used in the future for detecting gamma rays. HPGe's contain a germanium crystal that is very expensive and sensitive if it is to be useful for an experiment. They are known for having good resolution but this is dependent on the crystal remaining of good quality. It is required that they operate at a very low temperature so they are cooled with liquid nitrogen. Biasing them too quickly, or at too high of a temperature will damage their crystal structure. The concern here is for too many neutrons to strike the crystal. Since they are reasonably thick, even though neutrons have a low probability of interaction they interact with the crystal and diminish the detector's resolving capabilities. Performing this experiment with ICEBall will yield the spectra in Figures 1 and 2.

The neutron gate holds the information for total neutron count for that specific run, there is a gamma gate for the same information on gamma rays that looks the same. The Si(Li) detector is what actually detects the electrons. The spectra is a plot of number of counts on the y-axis and channel number on the x-axis. This is important to note because these channel numbers are much higher than the energies of the electrons themselves. The electrons of interest for this information possessed energies of 149keV, 191 keV and 198 keV. We are interested in electrons of higher energy if we can identify them, but only to a point. At too high of an energy they can be mistaken for electrons created in pair production, a phenomena that occurs

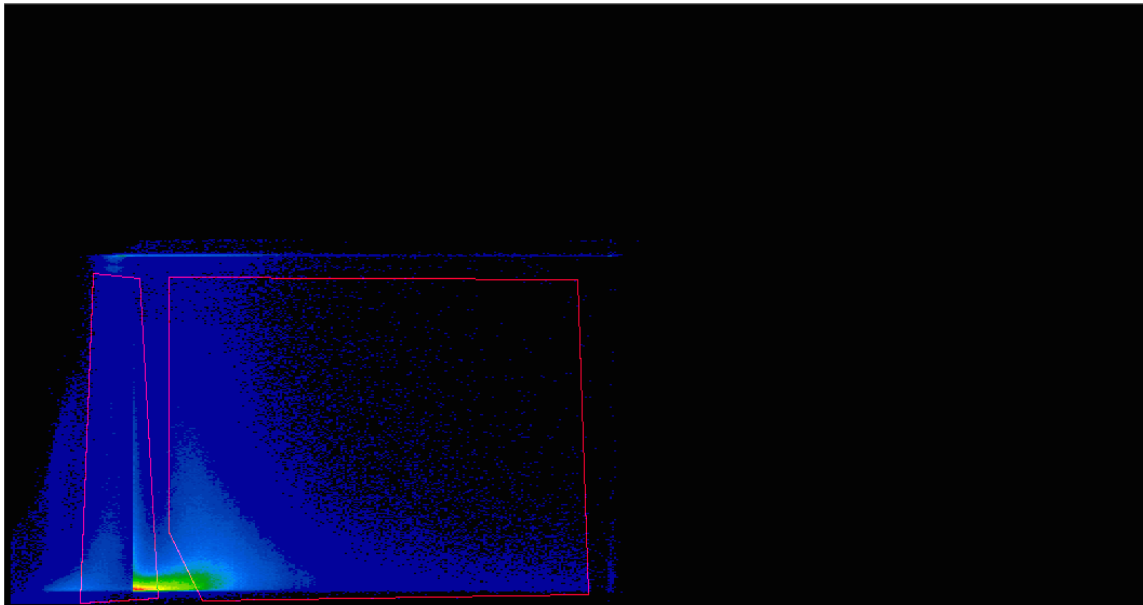


Figure 1: Neutron Gate 1

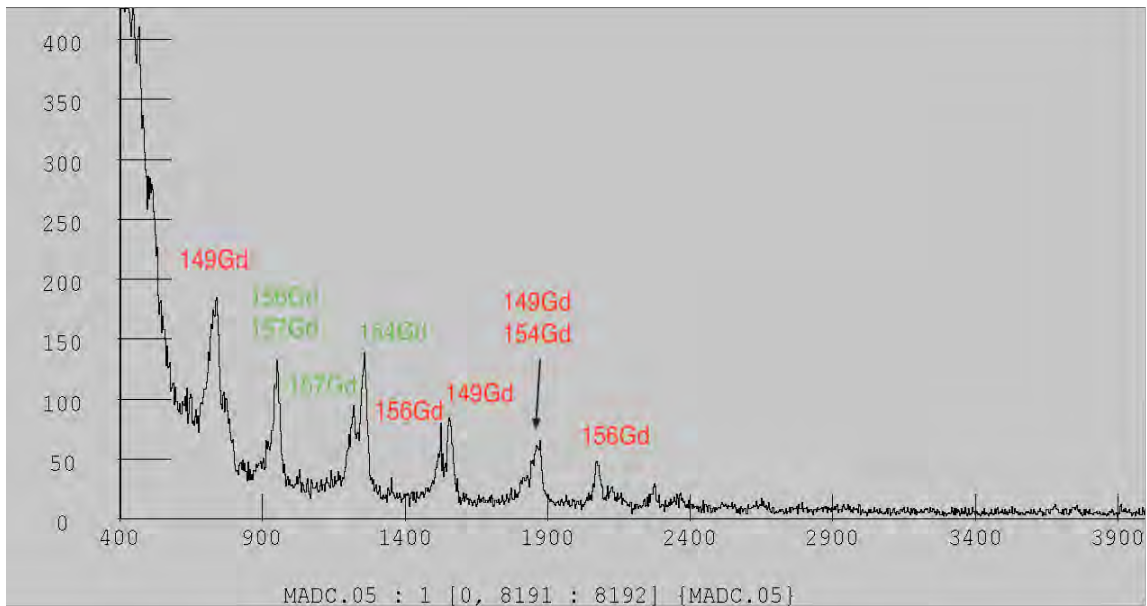


Figure 2: Si(Li) Detector 6

between gamma rays and a detector. The reason that provides a cutoff for an energy range is because the gamma ray must possess the energy to create this pair, which is 1022keV, the rest mass of two electrons. Each electron or positron will then have 511keV. Focusing on lower energies allows us to cut out pair production. Beta decay is also a contributing factor to our spectra, but they are of a continuous distribution and will appear as background. By analyzing strictly the peaks in the spectra we can cut these out as well.

By analyzing these spectra for the number of counts under the peaks of interest and neutron counts, along with compiling data from the National Nuclear Data Center (NNDC) about these peaks we can get an idea of what isotopes we are seeing and, specifically, what excited states by knowing the peak energies. Also involved in calculations will be knowing the target thickness (Δx), beam intensity (I) and energy dependent efficiency of the detectors at each energy. Target thickness is measured prior to the experiment, beam intensity is measured during the experiment and, given that you know the parameters from Figure 3, the efficiency of the detector can be calculated with the following equation (where x is the particle energy):

$$\text{eff} = \frac{1+P_0}{1+e^{-\frac{x-P_1}{P_2}}} \times (P_3 + P_4 \times x)$$

With those numbers known, neutron and gamma flux can be calculated:

$$\text{flux} = \text{Neutron Count} / \text{Run Duration} / \Delta x / I$$

Beam intensity should be normalized to integrated charge (Q) and target thickness should be normalized to particles per cm^2 . This requires dividing the beam intensity by the charge state times the electron's charge and dividing the target

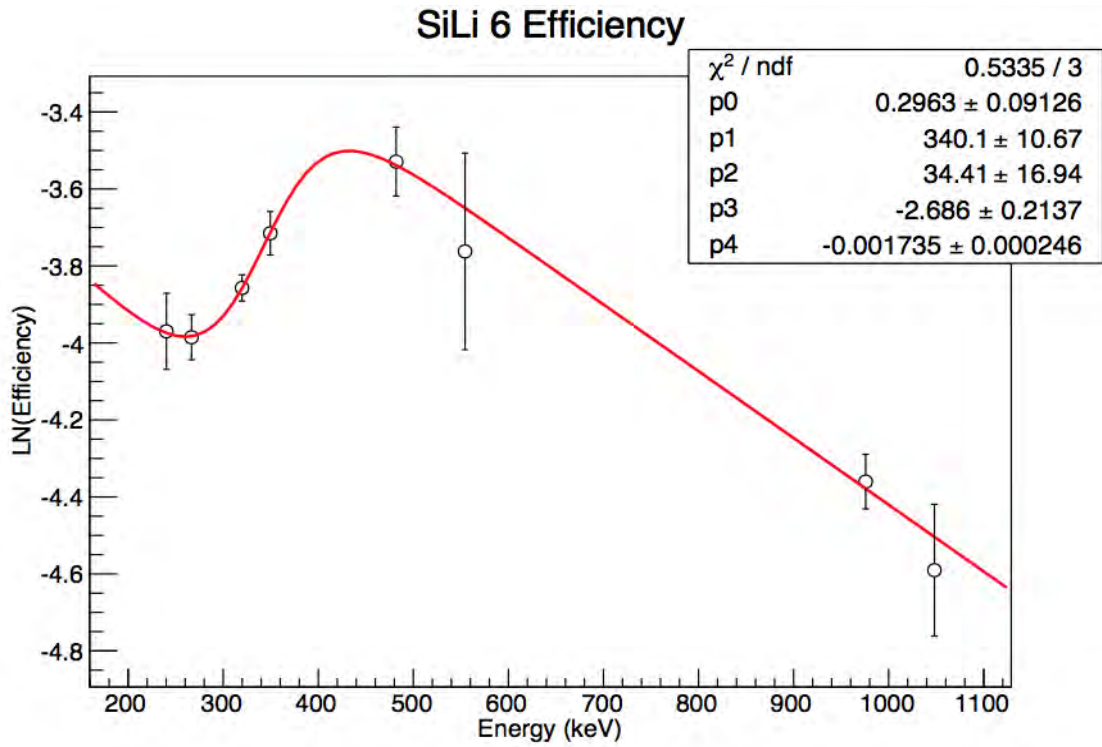
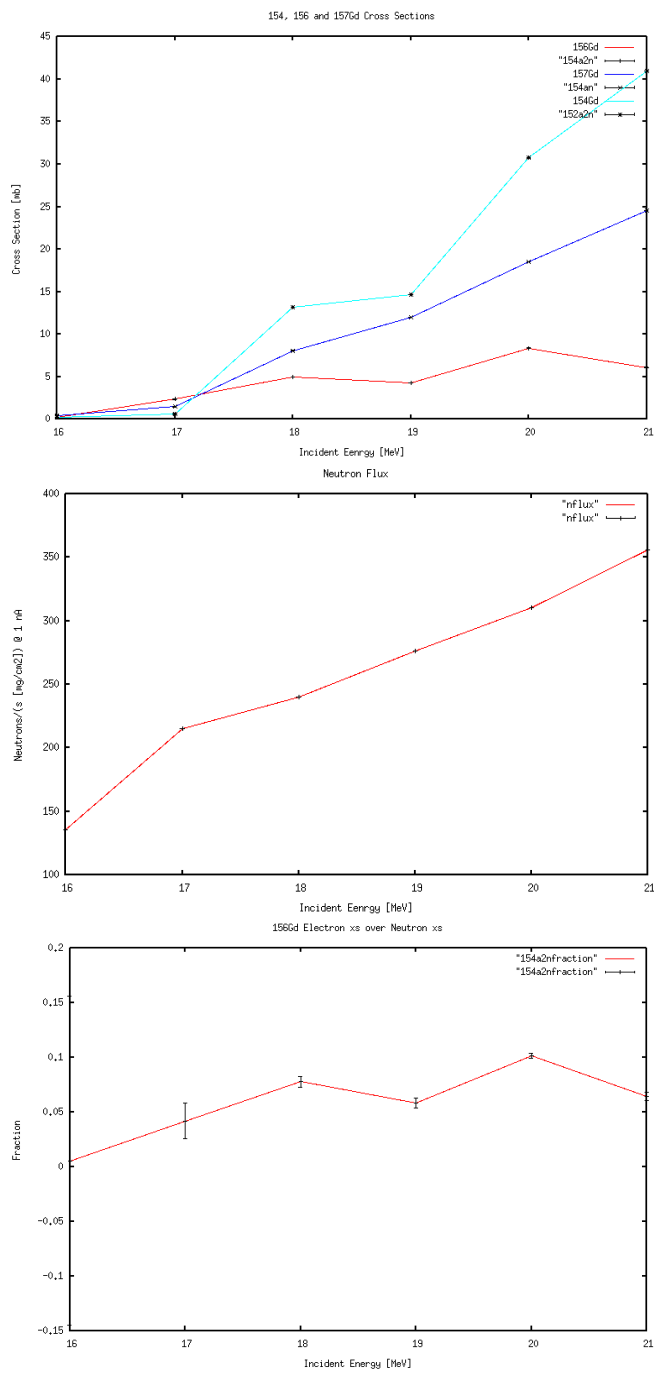


Figure 3: Si(Li) Energy Dependent Efficiency Plot [3]

thickness by average atomic mass times Avogadro's Number. Once that is done cross-section can finally be calculated:

$$\text{Cross Section} = \frac{\text{Yield}}{\Delta x * Q * \epsilon_{eff}}$$

By dividing the cross section by the neutron flux you can directly plot the fraction that, at its maximum, will give the energy to be used when running the experiment with enriched targets to provide the largest number of electrons per neutron.



The above plots, from top to bottom, are the cross-sections for the specific elec-

trons in the reaction channels, the neutron flux and then the fraction we are interested in. As can be seen from the bottom plot, the most optimum energy is 20MeV.

4 Conclusion

Though natural targets are not advisable for experiments that will pinpoint one reaction, they can be effective for low cost target testing and parameter optimization. From the data collected for a 16-21MeV energy range of alpha particles, the most valuable reaction in question, $^{154}\text{Sm}(\alpha, 2n)^{156}\text{Gd}$, has an optimum ratio of conversion electron emission cross section to neutron flux at an incident energy of approximately 20 MeV. Also, normalized for a target thickness of $1 \frac{\text{mg}}{\text{cm}^2}$ and a 20MeV beam at 1nA, we expect a neutron flux of $310.5 \frac{\text{neutrons}}{\text{second}}$.

5 References

[1] Lesher, S. R., A. Aprahamian, L. Trache, A. Oros-Peusquens, S. Deyliz, A. Gollwitzer, R. Hertenberger, B. D. Valnion, and G. Graw. "New 0^+ States in ^{158}Gd ." Physical Review C. The American Physical Society, 27 Nov. 2002. Web. 29 July 2014. <http://journals.aps.org/prc/abstract/10.1103/PhysRevC.66.051305>.

[2] Lesher, S. R., C. Casarella, B. P. Crider, R. Ikeyama, I. Marsh, E. E. Peters, F. M. Pradosestevez, M. K. Smith, Z. Tully, J. R. Vanhoy, A. Aprahamian, and S. W. Yates. "Inelastic Neutron Scattering in ^{160}Gd ." Epj-conferences.org. EDP Sciences, n.d. Web. 30 July 2014. <https://www.google.com/url?q=http://dx.doi.org/10.1051/epjconf/20146602>

[3] (Anthony Battaglia, personal communication, July 14, 2014)

Damage of DNA by Helium and Oxygen
Atmospheric Pressure Plasma Jet

Catie Luck

2014 NSF/REU Program

Physics Department, University of Notre Dame

Radiation Laboratory

Advisor: Sylwia Ptasinska

Abstract

An emerging, highly interdisciplinary field in physics has been created which combines plasma technology with biomedical applications. Plasma has been used for sterilization purposes and in the areas of dentistry and cosmetics but is more recently being researched for various medical advancements, including wound care and oncology. In my research project, the plasma is in the form of a non-thermal jet, which can be created under ambient conditions, which is an advantage, as it does not require a vacuum chamber for the jet to be sustained. My project is aiming to understand how the plasma jet affects the cells and to analyze the damage induced to DNA depending on plasma exposure duration. The DNA can be damaged due to the production of single strand breaks (SSB) and double strand breaks (DSB). By using agarose gel electrophoresis we are able to analyze irradiated DNA and see what type of damage has occurred, as well as the amount of DNA that remained intact during radiation. In order to enhance DNA damage, which can have benefits in cancer treatment, we use a helium plasma jet with oxygen (O₂) admixture. Moreover, we try to reveal how the presence of oxygen affects the DNA. As higher concentrations of oxygen (up to 0.5%) are used in the helium plasma jet, we see more breakage most likely due to the formation of reactive oxygen species (ROS). ROS are known to be highly reactive and can create damage to DNA.

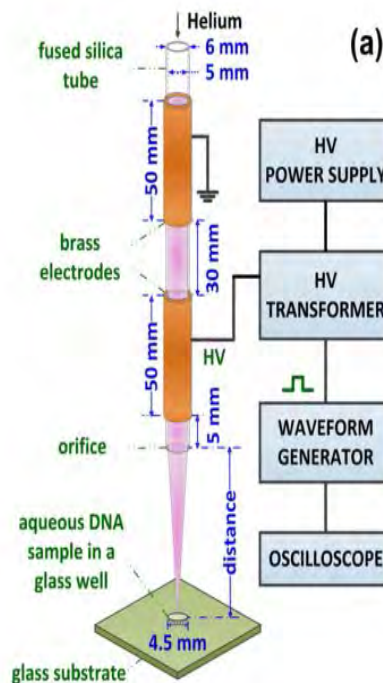
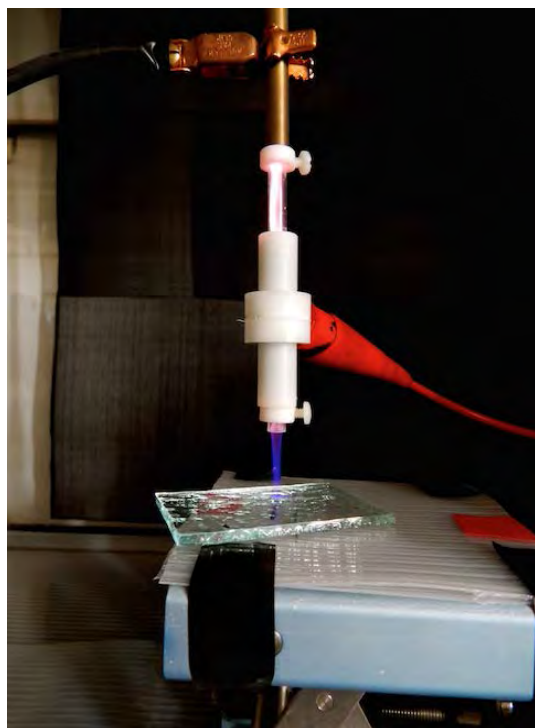
Introduction

The atmospheric pressure plasma jet (APPJ) is a non-thermal jet that is created in ambient conditions and composed of UV light, radicals, free electrons, and neutral and charged particles [1]. A non-thermal jet is significant because it can be directly applied to the body without visible damaging effects. It is also important that the jet is created in ambient conditions

at atmospheric pressure because it can be ignited and sustained without the need for a vacuum chamber, which allows us to treat humans with the APPJ. The APPJ used in our experiment is a helium source; operating in a noble gas environment because it has a low breakdown voltage and long plasma sustainability. Helium has a thermal heat conductivity much larger than other gases, which renders heat removal from the discharge, causing it to be more efficient. Cell interaction with plasma can lead to either inhibition or stimulation of cellular function [2] so when DNA is irradiated with the helium plasma jet, damage occurs. The plasma jet generates both reactive oxygen species (ROS) and reactive nitrogen species (RNS) which lead to cell arrest and cell apoptosis [3]. Because of this, oxygen (O_2) is sometimes mixed with the helium plasma jet to create even more ROS that induce damage. The damage comes in two forms: single strand breaks (SSB) or double strand breaks (DSB) [4]. The type of breakage affects the size and conformation of the DNA. These two factors affect the way the DNA travels through a gel when we run a process called gel electrophoresis to analyze our irradiated DNA. When DNA travels through a gel during electrophoresis, it separates into bands and we calculate ratios of each damage that occurs using a program on the computer.

Setup

Plasma is usually operated in one of two ways: the corona discharge and the barrier discharge. For our experiment, we use plasma with the barrier discharge method. Both methods can operate in ambient conditions, which require no vacuum to be used [5]. The barrier discharge suppresses large currents by dielectric barriers on the electrodes. With a barrier discharge, the feed gas, helium, flows between two electrodes. One of the electrodes has a high voltage (HV) applied, which can be measured on the oscilloscope that is connected to the HV

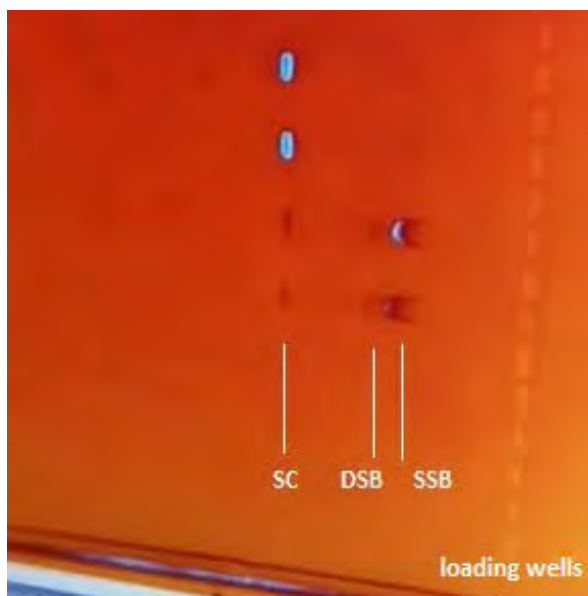


power supply, and the other electrode is grounded. An electric field is formed between the electrodes, which accelerates electrons. As the electrons collide with molecules in the atmosphere, radicals, reactive oxygen species, and reactive nitrogen species are formed and cause damage to DNA. We place our samples to be irradiated in wells on a glass tray and place the tray underneath the plasma jet. For each of our experiments, we place the sample 2.5 cm away from the orifice on the jet apparatus. This distance allows the jet to be concentrated fully on our sample but leaves enough room so that the atmosphere can still react with our sample, producing the nitrogen and oxygen radicals found in the atmosphere and causing damage to our DNA cells. Hydroxyl radicals ($\text{OH}\cdot$) are an important ROS because they induce DNA damage [6] and help to cause cell apoptosis.

Experiment

For our research project, we mixed O₂ with our helium plasma source at several different concentrations to determine what concentration of oxygen produced the most damage to the DNA. The presence of extra O₂ causes more ROS to be present, which aid in damaging the cells in the DNA.

From our stock sample of DNA, we prepare a dilution that is 0.1 μg of DNA for every 10 μL of water. When we irradiate the DNA, we pipette the sample onto a glass well, with 10 μL of



DNA and 5 μL of distilled water. The purpose of the water is to try and minimize evaporation of our diluted DNA sample. We irradiate our samples at different concentrations of oxygen mixed with helium to see how the variation in concentration affects the condition of the DNA. We then put our sample in a test tube and pipette the well with 5 μL of PBS buffer twice to make sure that all the DNA is recovered. When

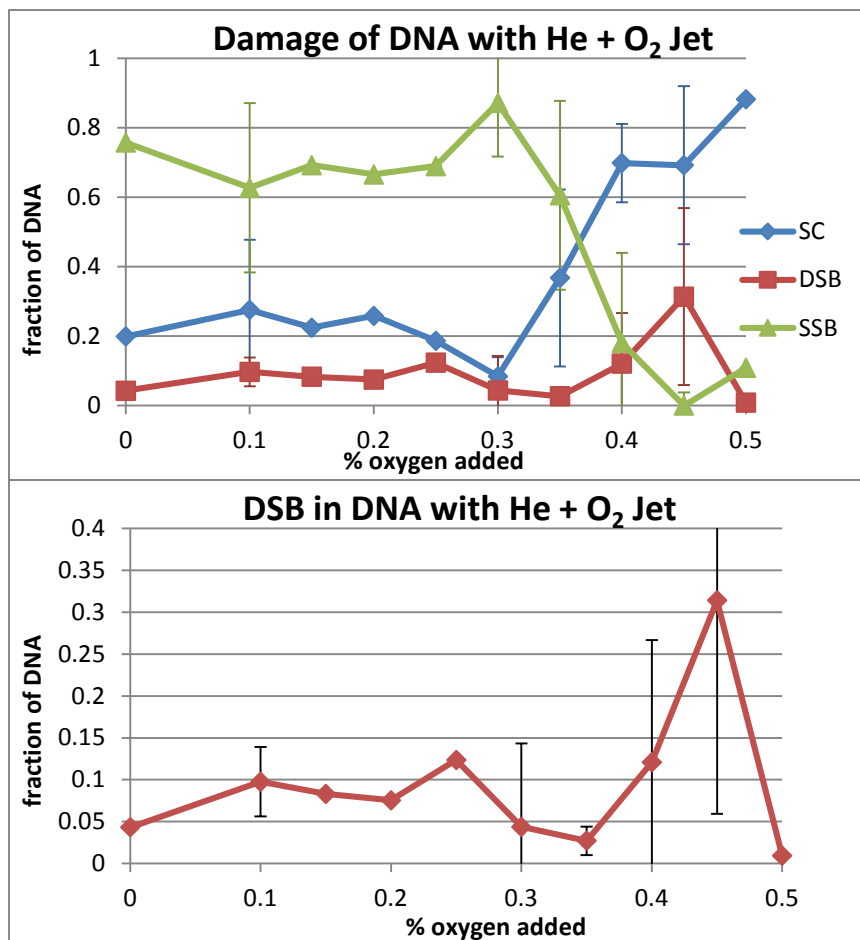
analyzing the DNA, we use a process called gel electrophoresis. We prepare a porous gel using 3.24 g of agarose powder and 270 mL of TBE buffer. We heat the mixture so that the powder completely dissolves in the buffer and then we let it cool to 60°C. Once the mixture cools, we add 6 μL of SYBR Green—a dye used to fluoresce the gel when it is exposed to UV light. We pour the mixture into a tray and allow it to cool, forming a gel. A comb is placed in the mixture before it cools completely, giving us wells into which we can load our DNA samples. We add about 5 μL of loading dye to our DNA samples and load them into the wells of the gel. The

loading dye helps the DNA samples to sit down in the well so that we can run a current through the gel and see how our samples travel through the gel. DNA is negatively charged, so it travels through the gel toward the cathode of the chamber and separates into bands according to size and conformation. Single strand breaks form a circular shape, making it more difficult for them to travel through the pores of the gel because they are met with more resistance. Double strand breaks form a linear shape, allowing them to move further through the gel, but not as far as undamaged, or supercoiled DNA, which is tightly compacted. We apply a voltage of 50 volts to our gel for 13 hours and analyze our results by exposing the gel to a UV light source and taking an image of it, using the Quantity One program on the computer. The program makes it possible for us to obtain numerical values for the intensity and area of the bands so we can determine what fraction of the DNA has undergone each type of damage and what fraction of DNA remains intact.

The time of irradiation for each sample was 30 seconds. Keeping the time constant allows us to see if the concentration alone had an effect on the damage that was done to the DNA. We irradiated DNA samples with ten different concentrations of oxygen added in with the helium plasma jet, ranging from 0.0% oxygen to 0.5% oxygen.

Results

When varying the concentration of oxygen up to 0.5%, we find that as more than about 0.3% of the jet is comprised of oxygen, the stability of the jet lessens. This leads to a decrease in damage of the DNA because not enough of the jet is concentrated on our DNA sample. Because of this, it is difficult to determine if the incorporation of oxygen does induce more damage in DNA. If we look at only the DSB plot in our graph, however, we can see that the amount of

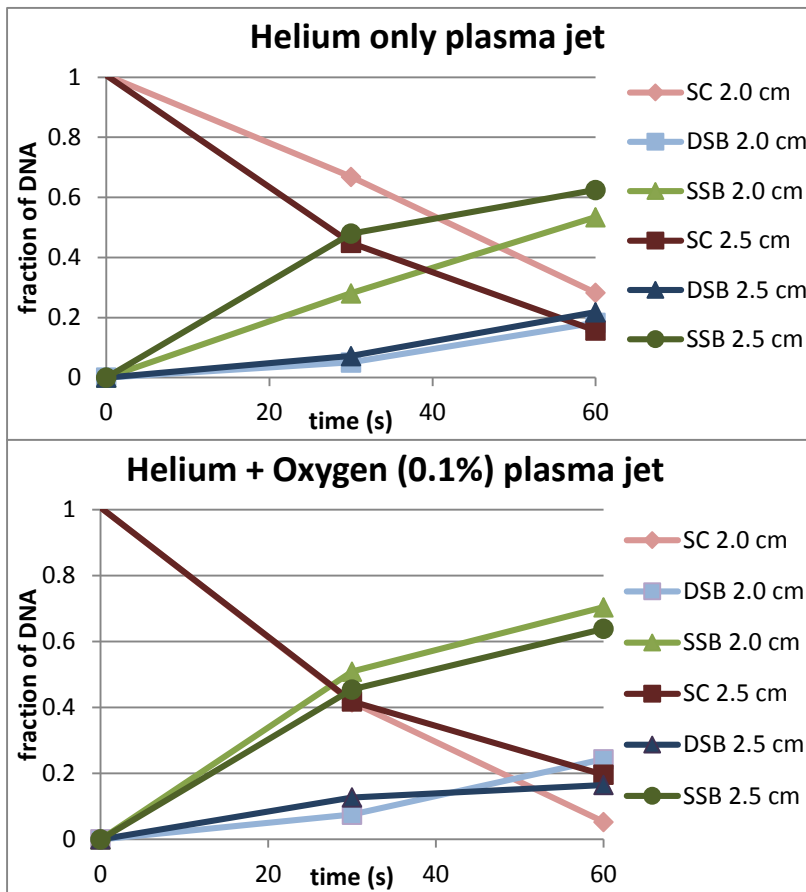


damage increases to a peak at 0.25% oxygen incorporation. It then decreases due to jet instability until it hits another peak at 0.45% oxygen. More DSB occur at this point than at any other point on the graph so there must have been enough jet stability at 0.45% oxygen incorporation to get ROS to interact with our sample and

cause substantial damage to the DNA, comparatively. Double strand breaks are much more significant than single strand breaks because cells are not able to easily repair themselves from DSB so the damage in DNA due to DSB is of much more interest to us.

In an attempt to generate more damage to the DNA, we irradiated samples that were 2.0 cm away from the orifice on the device rather than 2.5 cm to see if the closer distance would have an effect on the ROS that were created due to the incorporation of O₂. We found that for the helium only plasma jet, the closer distance had the opposite effect of what we wanted. There was less damage done to the DNA at a closer distance than there was when the plasma jet was 2.5 cm away from the sample. For the helium and oxygen admixture jet, it seems that there was more damage done to the DNA at the distance of 2.0 cm, however, the damage done is not

substantially more at a particular distance. The reason for the lack of increased damage when the jet is moved closer to the sample is that the closer distance doesn't allow as much interaction between the jet and the surrounding atmosphere. The radicals that cause damage to DNA are generated by the plasma jet, but also by the oxygen and nitrogen molecules that are found in the atmosphere.



In the helium jet that has oxygen incorporated, there is oxygen available in the jet so it is likely that there was enough oxygen to create ROS without the need for the oxygen that is usually found in the atmosphere.

Conclusion

Plasma science is still an emerging field in the physics industry, so it continues to be studied and improved for many applications, especially medical processes. Plasma can be a time and cost efficient way to perform medical processes, one being the treatment of cancer. We know from past experiments that an atmospheric pressure plasma jet with either nitrogen or helium as a feed gas can cause damage to DNA but our experiment focused on the incorporation

of oxygen to a helium plasma jet. In theory, as more oxygen is added to the jet, more damage to the DNA should occur due to an increase in the presence of ROS. We found that this does happen, but only up to a certain concentration, as the jet becomes too unstable as a certain amount of oxygen is added. Our DNA was increasingly damaged as the concentration increased, but only to about 0.25% oxygen. Our jet then became unstable until about 0.45% oxygen, where we saw another spike in DNA damage for DSB. The reason for the spike at 0.45% oxygen concentration is uncertain, because the other concentrations greater than about 0.3% were not stable enough to cause any significant damage to our DNA. The APPJ is particular, and something as small as a draft can cause the jet to become slightly unstable while irradiating samples. The peak at 0.45% oxygen concentration does reinforce our theory that DNA will incur more damage as the concentration of our oxygen and helium admixture jet is increased, but more trials of this experiment can be conducted in the future to offset the inconsistencies that we have experienced. We can also conclude that our DNA sample must be a certain distance from the plasma jet (2.5 cm) in order to interact with the atmosphere most effectively and cause the most damage to DNA.

References

- [1] Nehra, Vijay, Ashok Kumar, and H K Dwivedi. "Atmospheric Non-Thermal Plasma Source." *International Journal of Engineering* 2.1 (n.d.): 1. Print.
- [2] Woedtke, Th. Von, S. Reuter, K. Masur, and K.-D. Weltmann. "Plasmas for Medicine." *Physics Reports* 530.4 (2013): 291-320. Web.
- [3] Han, Xu, Matej Klas, Yueying Liu, M. Sharon Stack, and Sylwia Ptasinska. "DNA Damage in Oral Cancer Cells Induced by Nitrogen Atmospheric Pressure Plasma Jets." *Applied Physics Letters* 102.23 (2013): 233703. Web.
- [4] O'Connell, D., L. J. Cox, W. B. Hyland, S. J. McMahon, S. Reuter, W. G. Graham, T. Gans, and F. J. Currell. "Cold Atmospheric Pressure Plasma Jet Interactions with Plasmid DNA." *Applied Physics Letters* 98.4 (2011): 043701. Web.
- [5] Pârvulescu, V. I., Monica Magureanu, and Petr Lukes. *Plasma Chemistry and Catalysis in Gases and Liquids*. Weinheim, Germany: Wiley-VCH, 2012. Print.
- [6] Dorfman, Leon M., and Gerald E. Adams. "Reactivity of the Hydroxyl Radical in Aqueous Solutions." (1973): n. pag. US Department of Commerce. Web.

**Natural orbitals for a two-particle system
in one dimension as a testbed for use in
the nuclear many-body problem**

Mitch A. McNanna

2014 NSF/REU Program
Physics Department, University of Notre Dame

Adviser: Mark A. Caprio

Abstract

Natural orbitals have been applied in atomic and molecular electronic-structure theory to increase the accuracy of calculations of observables for a many-particle system. However, unlike the electron-structure problem, the nuclear problem is translationally invariant. We created a testbed code to test the usefulness of natural orbitals as they may apply to translationally invariant problems. The relative Hamiltonian matrix of a two-particle system in one dimension is first calculated in a basis of antisymmetric products of the harmonic oscillator eigenfunctions. The natural orbitals are then calculated for the resulting ground state, and the Hamiltonian matrix is recalculated using a two-particle basis built from the natural orbitals. The effect of basis size on the accuracy of the ground state energy calculation is explored.

Introduction

Due to the complex nature of the nucleus, calculations in nuclear physics are never exact, and physicists strive to improve their approximations using various techniques, one of which is explored in this project. Rather than calculating an observable by diagonalizing its matrix representation in an arbitrary basis, this technique allows us to select an optimized basis of “natural orbitals” which improves accuracy. Natural orbitals have already proven useful in the case of electron-structure ^{[1] [2] [3]}, but this does not necessarily imply usefulness for nuclear potentials due to their translational invariance. We test natural orbitals’ use in calculating the ground-state energy of a relative Hamiltonian for a two-particle system in one dimension. This can later be generalized to measure any observable for a many-particle system in three dimensions. The accuracy of the calculations with natural orbitals is shown to be superior to those using the harmonic-oscillator basis when both bases are truncated according to the N_{\max} scheme, which is outlined later. With the usefulness of natural orbitals established, the increased accuracy from their implementation in the nuclear many-body problem may improve our knowledge of nuclear physics as a whole.

Initial Hamiltonian calculation

First, we begin by defining the harmonic oscillator basis functions in the usual way:

$$|n\rangle \equiv \varphi_n(x) = \sqrt{\frac{b}{2^n n! \sqrt{\pi}}} e^{-\frac{(bx)^2}{2}} H_n(bx), \quad (1)$$

where H_n are the Hermite polynomials, and b is the length parameter $b = \sqrt{\frac{m\omega}{\hbar}}$. We chose to

study Hamiltonians of the form (setting $\hbar = \omega = m = 1$)

$$H = \frac{1}{2}(p_1 - p_2)^2 + V(x_1 - x_2), \text{ and with } V(x_1 - x_2) = \frac{1}{2}(x_1 - x_2)^2,$$

$$H = \left(\frac{p_1^2}{2} + \frac{1}{2}x_1^2 \right) + \left(\frac{p_2^2}{2} + \frac{1}{2}x_2^2 \right) - p_1 p_2 - x_1 x_2 \quad (2)$$

since we know our basis functions solve

$$H_1 |m\rangle = \left(\frac{p_1^2}{2} + \frac{1}{2}x_1^2 \right) |m\rangle = \left(m + \frac{1}{2} \right) |m\rangle \quad (3)$$

To create a two-particle basis, we combine the one particle functions such that the result is antisymmetric and normalized

$$\psi_i(x_1, x_2) = |i\rangle = |mn\rangle = \frac{1}{\sqrt{2}} (|mn\rangle - |nm\rangle) = \frac{1}{\sqrt{2}} (|m\rangle|n\rangle - |n\rangle|m\rangle) \quad (4)$$

This also defines some notation used throughout this paper: i and j are used when referring to a two particle state, and m and n (along with μ and ν) when referring to a single particle state.

Furthermore, for a two-particle state, a sharp bracket indicates an antisymmetric state, whereas a curved bracket indicates a simple product. The antisymmetry is necessary since we hope to apply the techniques developed here to nucleons which are in general fermions.

Since there are an infinite number of harmonic oscillator functions, our two particle basis is also infinite in size. This means we must truncate our basis at some point, which will create a built-in inaccuracy in the calculations. Having more basis functions will result in a better approximation, but also needs more computing power. This project seeks, in addition to

establishing the usefulness of natural orbitals in nuclear physics, to quantitatively explore the effect of basis size on accuracy. The two methods of truncation for the two-particle basis used will be called “single-particle truncation” and “ N_{\max} truncation.” In single-particle truncation, the two-particle basis contains all possible antisymmetric products of single-particle states where the energy quantum number n for any single-particle states does not exceed some maximum N . In N_{\max} truncation, we include all antisymmetric products such that the *sum* of the two contributing quantum numbers $m+n$ does not exceed some maximum N .

Although for this project we are most interested in the relative Hamiltonian, we first set up code which calculates and diagonalizes the Hamiltonian for any given potential $V(x_1, x_2)$, employing the standard kinetic energy for a two-particle system $\frac{p_1^2}{2m} + \frac{p_2^2}{2m}$. This allows us to test our code using potentials whose eigenvalues and eigenfunctions are known.

Now, since the momentum operators act only on one particle, the calculation of the matrix element $(mn|H|\mu\nu)$ reduces using

$$\begin{aligned} (mn|H|\mu\nu) &= (mn|T|\mu\nu) + (mn|V|\mu\nu) = \\ &\langle n|v\rangle\langle m|p_1|\mu\rangle + \langle m|\mu\rangle\langle n|p_2|v\rangle + (mn|V|\mu\nu), \quad \langle m|\mu\rangle = \delta_{m\mu} \end{aligned} \quad (5)$$

Calculating the full matrix element $\langle i|H|j\rangle$ then requires combining the two terms in the bra $\langle i|$ with the two terms in the ket $|j\rangle$ (see (4)) for four total terms in the form of (5), each identical up to a permutation of the quantum numbers.

For the momentum operators, rather than keeping the wavefunction in coordinate space, we replace the wavefunction with its Fourier transform to simplify the integral. With the length parameter set to 1, the Fourier transform $\tilde{\varphi}_n(p)$ can be written simply in terms of the coordinate-space wavefunctions:

$$\tilde{\varphi}_n(p) = (-i)^n \varphi_n(p) \quad (6)$$

The simplicity of the Fourier transform is very useful in helping reduce the number of needed

calculations and a reason for the choice of the harmonic oscillator functions as a basis.

The calculation for the relative Hamiltonian (2) is even simpler than (5). Using (3),

$$(mn|H_1 + H_2|\mu\nu) = \left(\mu + \frac{1}{2}\right)(mn|\mu\nu) + \left(\nu + \frac{1}{2}\right)(mn|\mu\nu), \text{ so}$$

$$\langle i|H_1 + H_2|j\rangle = \delta_{ij}(m+n+1) \quad (7)$$

All that is left is to calculate the contribution from the cross terms. Since the x operators only act on one particle, the matrix element can be simplified:

$$\langle mn|x_1x_2|\mu\nu\rangle = \langle m|x_1|\mu\rangle\langle n|x_2|\nu\rangle - \langle m|x_1|\nu\rangle\langle n|x_2|\mu\rangle \quad (8)$$

The same is done for momentum, and taking advantage of (6), we can rewrite $\langle mn|p_1p_2|\mu\nu\rangle$ entirely in terms of (8):

$$\langle mn|p_1p_2|\mu\nu\rangle = (i)^{m+n-\mu-\nu} \langle mn|x_1x_2|\mu\nu\rangle \quad (9)$$

Therefore, the matrix $\langle m|x|n\rangle$ along with (7) gives us all the information we need to calculate the relative Hamiltonian matrix in the two-particle basis.

However, since the full Hamiltonian for the nuclear problem can be separated into $H = H_{CM} + H_{rel}$, there are several degenerate eigenstates of the relative Hamiltonian which are not eigenstates of the center of mass Hamiltonian. Because of this, a contribution of

$a \cdot \left(\frac{1}{2m}(p_1 + p_2)^2 + \frac{1}{2}(x_1 + x_2)^2 \right)$, $a \gg 1$, is added to the relative Hamiltonian to lift the

degeneracy. Note that the only difference between this and (2) is the sign on the cross terms, so no new calculations are necessary. Although this will certainly change the Hamiltonian matrices in both single-particle and N_{max} truncation, due to the nature of N_{max} truncation this will not affect the natural orbitals, other than to ensure that the ground state is the *true* ground state and not one of several degenerate ground states. Once we have the correct ground state, we can subtract out the approximately known effect of the center of mass Hamiltonian from the ground state energies to obtain the eigenvalues of the relative Hamiltonian alone.

Natural Orbitals

Once the Hamiltonian matrix is calculated, the resulting ground state eigenvector ψ (some linear combination of the harmonic oscillator functions) is used to create the density matrix $\rho_{\alpha\beta} = \langle \psi | a_{\beta}^{\dagger} a_{\alpha} | \psi \rangle$, where α and β run through the single particle states (m and n) from 0 through N, the truncation parameter used in calculating the Hamiltonian matrix. a_{β}^{\dagger} is the creation operator for state β ; that is, if $|\psi\rangle$ contains some set of single-particle states $|\gamma\delta\varepsilon\dots\rangle$, $a_{\beta}^{\dagger} |\gamma\delta\varepsilon\dots\rangle = |\beta\gamma\delta\varepsilon\dots\rangle$, or 0 if β is already one of the states. Similarly, a_{α} is the annihilation operator for state α : $a_{\alpha} |\gamma\delta\varepsilon\alpha\dots\rangle = (-1)^{\sigma} |\gamma\delta\varepsilon\dots\rangle$, or 0 if α is *not* already a state, where σ is the sign of the permutation needed to bring α to the front of the list while keeping other entries in order.^[4]

The inner products of the eigenvectors of the density matrix with the set of single-particle harmonic oscillator basis functions give us the natural orbitals: if the matrix whose columns are the eigenvectors is

$$\begin{pmatrix} a_{00} & \cdots & a_{N0} \\ \vdots & \ddots & \vdots \\ a_{0N} & \cdots & a_{NN} \end{pmatrix} \quad (10)$$

then any given natural orbital, denoted $|\tilde{m}\rangle$, is

$$|\tilde{m}\rangle = \sum_n a_{\tilde{m}n} |n\rangle \quad (11)$$

We can build an antisymmetric, normalized two-particle basis $\{ |\tilde{i}\rangle \}$ in the same way we did previously, truncated in the same way.

Finding the Hamiltonian matrix in this new basis requires no new calculation, taking advantage of (11):

$$\langle \tilde{i} | H | \tilde{j} \rangle = \langle \widetilde{mn} | H | \widetilde{\mu\nu} \rangle = \left[\sum_{m < n} (a_{mm}^- a_{-m}^- - a_{mn}^- a_{-nm}^-) \langle mn | \right] H \left[\sum_{\mu < \nu} (a_{\mu\mu}^- a_{-\nu\nu}^- - a_{\mu\nu}^- a_{-\nu\mu}^-) | \mu\nu \rangle \right] \quad (12)$$

Note that in the N_{\max} truncation scheme, some of the matrix elements on right-hand side of (12) will not be part of the original Hamiltonian matrix. For this reason, even when using N_{\max} truncation, the first step in the whole process is to calculate the Hamiltonian matrix in the original two-particle basis using single-particle truncation. From there, rows and columns which would not have appeared in N_{\max} truncation are deleted, and diagonalization proceeds with this new matrix. Then, when it comes time to recalculate the Hamiltonian matrix in the two-particle natural orbital basis using (12), that original matrix in single-particle truncation is referenced. Once the matrix in (12) is calculated, its eigenvalues and eigenvectors are calculated.

Code Verification

To make sure our code is doing what we want, we did a few simple tests. First, using the code which takes a general potential as an input, we found the Hamiltonian matrix

for $H = \frac{p_1^2}{2m} + \frac{p_2^2}{2m} + \frac{1}{2}x_1^2 + \frac{1}{2}x_2^2$, which is the Hamiltonian for which our basis functions are

eigenfunctions. As expected, we got a diagonal matrix whose elements are

$\langle i | H | j \rangle = \delta_{ij} (m + n + 1)$. We then gave the code some arbitrary functions of x_1 and x_2 and

checked the matrix elements using Mathematica. In Mathematica, we did not use any tricks such taking advantage of the Fourier transform for the kinetic energy; we calculated the matrix elements using the basic, naïve and slow integrals. The results are consistent.

Next, we checked that the machinery for calculating the density matrix and the natural orbitals was working correctly. Instead of first truncating our basis in N_{\max} truncation before calculating the eigenvalues, we left it in single-particle truncation. In this case, the energy spectra in the original basis and the natural orbital basis should be identical, since the two bases span the exact same space. The two spectra were identical for any potential, particularly the

relative potential.

Finally, since the code built specifically for the relative Hamiltonian is somewhat different than that for any given potential (using (7),(8) and (9) rather than(5)), we did a final check of the original Hamiltonian matrix using Mathematica, which confirmed that everything was working properly. The same density matrix code is used in both cases, so that needed no extra verification.

This entire project is done using Python 3.2 for all computations. Mathematica is used occasionally to check that certain calculations are accurate. The scipy package is used for calculation of eigenvalues and eigenvectors. Integration is done using the Romberg variation of the trapezoidal rule for single integrals, and a generalized trapezoidal rule for double integrals.

Results

We hope to show that in N_{\max} truncation, using the natural orbital basis improves accuracy of an observable for a given basis size. In addition, we want to see how the size of the basis affects the accuracy of calculations as the basis size is increased. The observable studied here is the ground-state energy of a relative Hamiltonian.

For the Hamiltonian $H = \frac{1}{2m}(p_1 - p_2)^2 + \frac{1}{2}(x_1 - x_2)^2$ we saw the following rather

useless, though not unexpected, results:

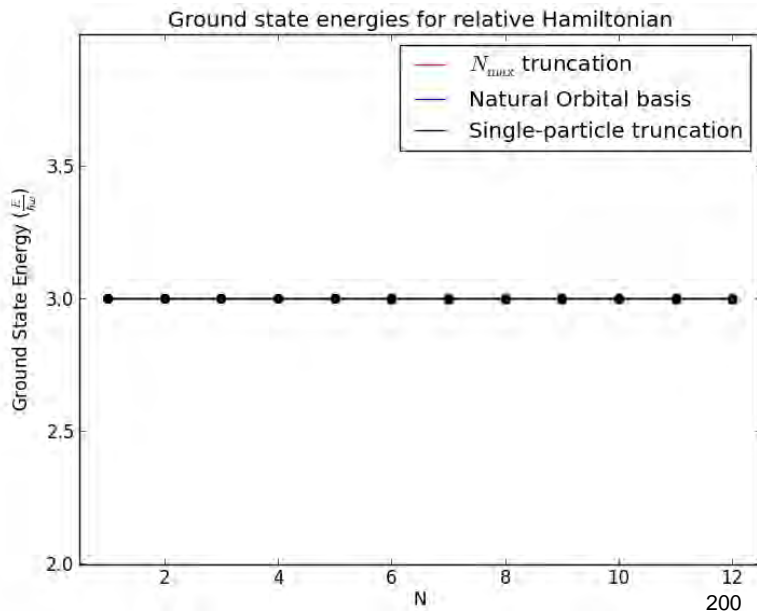


Fig. (1): Ground state energy for the relative potential.

Since this Hamiltonian is so similar to the two-particle harmonic oscillator Hamiltonian, the ground state in both bases was simply the state $|01\rangle$

Since the Hamiltonian is so similar to the Hamiltonian for which our basis functions are eigenfunctions, namely that the “spring constant” is the same, the ground state in both the original basis and the natural orbital basis is simply the state $|01\rangle$, regardless of basis size.

More interesting is what happens when we explore a potential with a different spring constant K :

$$H = \frac{1}{2m}(p_1 - p_2)^2 + \frac{1}{2} \cdot K \cdot (x_1 - x_2)^2 \quad (13)$$

Since our basis functions are for a Hamiltonian with $K = 1$, using different K gives us more interesting and useful results:

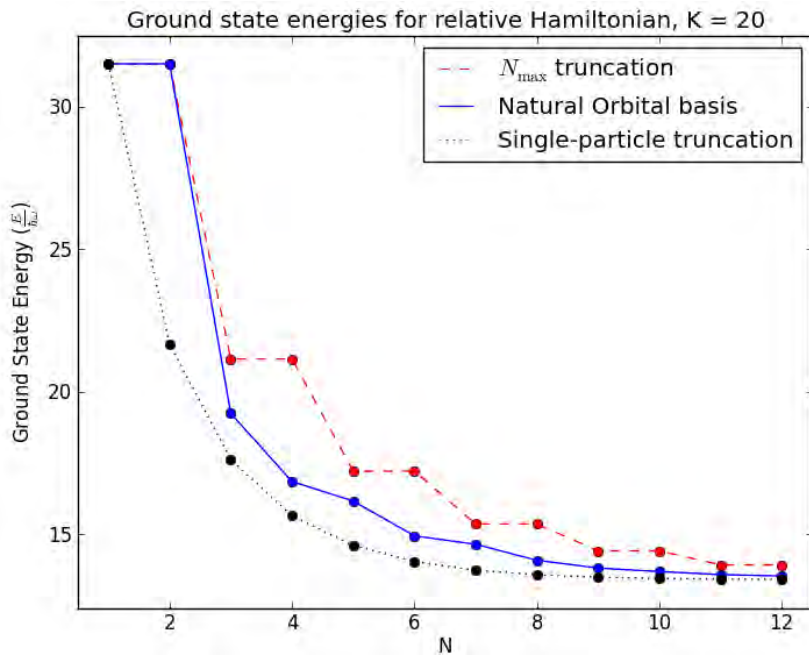


Fig. (2): Ground state energy of the dilated Hamiltonian with $K = 20$.

Here we can clearly see the improved accuracy of the natural orbital basis compared to the N_{\max} basis. Note also that at $N=12$, the calculations have yet to converge

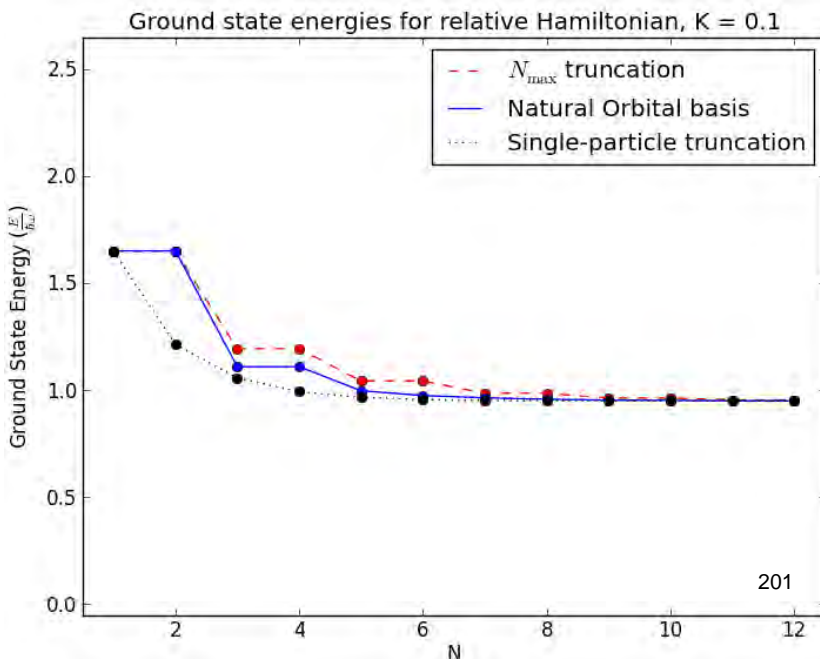


Fig. (3): Ground state energy of the dilated Hamiltonian with $K = 0.1$

This figure supports the idea that the natural orbitals are more accurate for any K , and therefore hopefully any relative potential

Here, it is obvious that the natural orbital basis in blue is superior to the N_{\max} basis in red. The black single-particle truncated basis is better than both; however, this matrix is only relevant in the two-particle case. For many particles, the size of this matrix grows extremely large and calculations using it would no longer be feasible

Conclusion

Through our exploration of a one-dimensional two-particle system, we have shown that the use of natural orbitals has great potential for use in the nuclear many-body problem. For our dilated relative harmonic-oscillator potential, as shown in figures (2) and (3), calculations using a basis built from natural orbitals are more accurate than calculations using the harmonic oscillator basis up to a certain maximum basis size, where all calculations converge. However, further analysis of the use of natural orbitals is necessary; their applicability in three dimensions, for more particles, for more exotic potentials, and for different observables cannot be directly inferred from our results. That being said, the superiority of natural orbitals in our test case shows they may be useful for the translationally invariant problem of the nucleus, and the prospect for their use in the above situations is promising. Furthermore, much of the code behind this project was designed with generality in mind, meaning that much of it can be recycled in examining the more complicated scenarios of real nuclei.

References

- [1] Löwdin, Per-Olav. "Quantum Theory of Many-Particle Systems. I." *Physical Review* 97.6 (1955): 1474-1489.
- [2] Löwdin, Per-Olav, and Harrison Shull. "Natural Orbitals in the Quantum Theory of Two Electron Systems." *Physical Review* 101.6 (1956): 1730-1739.
- [3] Davidson, Ernest R. "Properties and Uses of Natural Orbitals." *Reviews of Modern Physics* 44.3 (1972): 451-64.
- [4] Suhonen, Jouni. "Fock Space: Particle Creation and Annihilation." *From Nucleons to Nucleus*. Berlin: Springer, 2007. 64-66. Print.

**Search for a Higgs-Top Quark Pairing
In the Opposite-Charged Dilepton Channel**

Patrick Moran

2014 NSF/REU Program

Physics Department, University of Notre Dame

Advisors:

Dr. Kevin Lannon

Dr. Michael Hildreth

Abstract

Experimental verification of the coupling of the Higgs Boson and the massive top quark can provide evidence for the properties of the Higgs with respect to the Standard Model. A search for Standard Model Higgs Boson production in association with a top-quark pair ($t\bar{t}H$) using an opposite-charged dilepton analysis is presented. Previous studies of $t\bar{t}H$ production have not focused on Higgs decays to opposite-charged dileptons, and findings from this analysis can provide another perspective to the understanding of the Higgs-top quark coupling. Using Boosted Decision Tree (BDT) techniques, Higgs dilepton decays were separated from Higgs decays resulting in zero or one lepton, using distinguishing characteristics of each decay signature. These two decay channels were then further separated based on number of jets in order to optimize signal sensitivity. Another BDT analysis was used to isolate all $t\bar{t}H$ decays from background events. A median upper limit of 8.9 times the Standard Model prediction is expected for $t\bar{t}H$ production.

1. Introduction

In 2012, the ATLAS and CMS experiments at the Large Hadron Collider (LHC) confirmed the discovery of a new particle at a mass of about $125 \text{ GeV}/c^2$. Experimental analyses have confirmed that this new particle bears many of the same properties, such as spin and parity, as the long sought-after Standard Model Higgs Boson.¹ The Higgs Boson, which serves as the final piece of the Standard Model, is responsible for giving mass to the other particles. Those particles which couple strongly to the Higgs field have manifestly large masses, while those which couple weakly (or not at all) with the Higgs have low masses (or are massless).

One striking feature of the Standard Model is the strong coupling between the Higgs Boson and the massive top quark. The mass of the top quark is about $173 \text{ GeV}/c^2$, over 40 times larger than the next most massive quark, and heavier than the Higgs Boson. Therefore, the

coupling between the Higgs Boson and the top quark cannot be determined directly by the decay of Higgs Bosons into top quarks, as this decay is kinematically impossible. However, assuming no contribution from any physics beyond the Standard Model (BSM), the Higgs/top quark coupling can be determined by measurements of Higgs Boson production via a fermion loop (Fig. 1a), as well as a fermion loop via Higgs Boson decay (Fig. 1b).¹

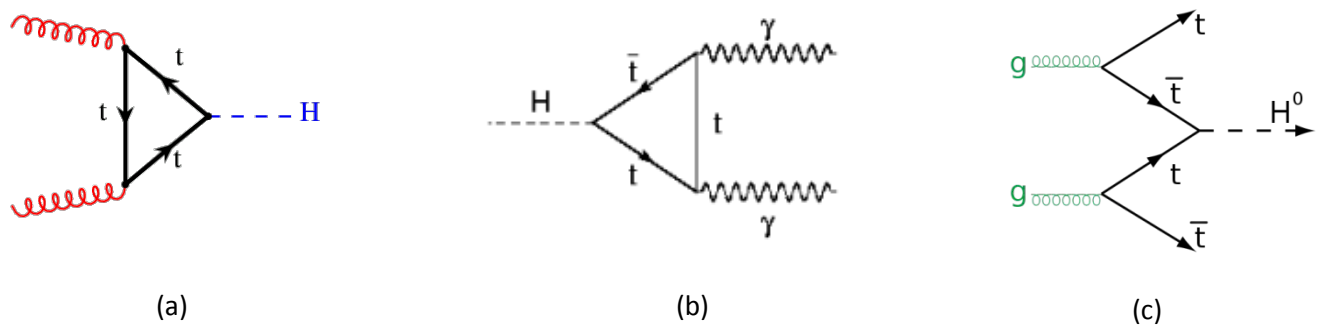


Figure 1. Feynman diagrams involving Higgs Boson and top quark: (a) Higgs Boson production from gluon fusion via fermion loop, (b) Higgs Boson decay to diphotons via fermion loop, (c) Higgs/top quark production via gluon fusion

However, in order to exclude contributions to these loop diagrams from BSM physics, and to test directly the accuracy of the Standard Model prediction for Higgs/top quark coupling, the production of a Higgs Boson in association with a top quark must be measured. The production of a Higgs Boson and top-anti top quark pair ($t\bar{t}H$) via gluon fusion (Fig. 1c) satisfies this requirement.¹

1.2 Decay Channels

Because of the small $t\bar{t}H$ production rate, $t\bar{t}H$ decay signatures must be exploited in order to collect enough data on this interaction. Due to the short lifetime of the Higgs Boson and top quarks, $t\bar{t}H$ production is identified by its decay products, such as electrons, muons, and photons, which can be detected by the CMS detector (see section 2.1). Top quarks decay nearly 100% of

the time to a bottom quark and a W boson.¹ Due to QCD confinement, the bottom quark produces a spray of hadrons and other particles known as a jet (a b-jet, in the case of a bottom quark). The W boson decays about two-thirds of the time to a quark and an anti-quark, which decay to a pair of jets. The other third of the time, the W boson decays to an electron, muon, or tau lepton, plus a neutrino. The tau lepton decays to either an electron or a muon (with neutrinos), or a jet.

The Higgs Boson decays to a pair of bottom quarks with a branching fraction of about 57%, which likewise produce a pair of b-jets.² The Higgs decays to a pair of W bosons about 21% of the time, and a tau/anti-tau pair about 6.3% of the time. The remaining Higgs decays include a pair of photons, a pair of Z bosons, and a pair of gluons, among other lesser contributions.² This paper focuses on the search for $t\bar{t}H$ production by analyzing the decay channels in which the Higgs decays to opposite charged leptons in collaboration with the CMS experiment.

2. Methods

A Monte Carlo model was used to simulate events from proton-proton collisions at 8 TeV at an integrated luminosity of 19.5 fb^{-1} . The $t\bar{t}H$ signal events and background events were simulated using particle physics event generator software, such as PYTHIA and MadGraph. The CMS detector response was simulated using Geant4. Signal sensitivity was increased using multivariate statistical techniques such as Boosted Decision Trees (BDT) to separate signal events of interest from background events.

2.1 CMS Detector

The Compact Muon Solenoid (CMS) detector is one of four detectors at the LHC, located in an underground cavern in Cessy, France. Measuring 21.6 meters long and 15 meters in diameter, the barrel-like CMS detector provides four distinct layers of detection technology.³

From innermost (closest to the beam) to outermost, these include: the tracking system, the Electromagnetic Calorimeter (ECAL), the Hadron Calorimeter (HCAL), and the muon tracker. Surrounding the tracker, ECAL, and parts of the HCAL is a solenoid 6 meters in diameter, creating a 4 Tesla magnetic field parallel to the beamline.

The tracking system consists of 3 cylindrical layers of silicon pixel detectors and 10 layers of silicon strip detectors. As particles travel outward from the point of collision, perpendicular to the beamline, they make contact with these tracker detectors, dislodging electrons in the process that send an electrical output signal to give 3-dimensional information on the location of the particle. Charged particles will be deflected by the magnetic field perpendicular to their direction of motion, causing to follow a circular path. The radius of this path provides information about the momentum of the particle, with a particle of higher momentum traveling with less curvature.

The ECAL consists of over 60,000 lead tungstate scintillation crystals along the barrel region, with endcaps to detect particles with a large component of motion parallel to the beamline. The ECAL crystals are excited by incoming electrons and photons, with photodetectors attached to the crystals to amplify the signals.

The HCAL consists of dense absorber plates and plastic scintillation tiles used to detect hadrons. The HCAL includes endcaps and a “forward” section perpendicular to the beamline in order to capture particles traveling at all angles from the beamline.

The muon detector from which CMS derives its name is the outermost layer and is specialized for detecting muons, which are the only detectable particles that travel beyond the inner detectors. An iron yoke creates a 2 T magnetic field within the muon detector, causing the charged muons to curve and provide information about their momentum. Three kinds of

detectors are triggered when bombarded by a muon, creating an electrical signal that identifies the 3-D position of the muon.

2.2 $t\bar{t}H$ Opposite-Sign Dilepton

In order to understand $t\bar{t}H$ production, decay channels were analyzed in which an event decays to a pair of opposite charged muons, electrons, or an opposite-signed muon/electron pair. Of particular interest were events in which both of these leptons came from the Higgs Boson, with either W boson or tau particle intermediaries. In the case that the sole leptons in a $t\bar{t}H$ process come from the Higgs, the top quarks should decay fully to jets, six altogether (assuming faithful reconstruction of the event by the detector, which is not always the case). Other scenarios are possible in which one lepton comes from the Higgs and one from the top quark, or both from the top quark, in which case the final $t\bar{t}H$ decay could include 4 or 5 jets. Furthermore, initial cuts were made that excluded uninteresting background events. For example, the leptons were required to have transverse momentum (component of momentum perpendicular from the beamline) of at least 20 GeV and 10 GeV.

2.3 Boosted Decision Trees

Boosted decision tree learning is a form of machine learning that can be used to separate signal events from background events based on distinguishing characteristics of each type of event. By inputting variables to the BDT algorithm in which signal events differ significantly on average from background events, the algorithm will analyze each event and determine a threshold value that best separates signal from background. If another variable exists that can further increase the signal and background purity, then the process will repeat with that variable, forming another branch of the tree. Each intermediate separation is referred to as a node, and each terminus is referred to as a leaf.

For example, in Figure 2, setting a threshold value for the invariant mass of a pair of leptons at $46.4 \text{ GeV}/c^2$ is found to give good separation between signal and background in this case. The signal purity for all events with invariant mass above this threshold is higher than that for all events together, with the ratio of signal to all events $\left(\frac{S}{S+B}\right)$ increasing from 0.498 to 0.759. On the other hand, signal purity decreases (or background purity increases) among events below this invariant mass threshold. The background-like events with invariant mass less than $46.4 \text{ GeV}/c^2$ can then be further separated using the transverse mass (MT) of the missing transverse energy (MET) and a pair of leptons.

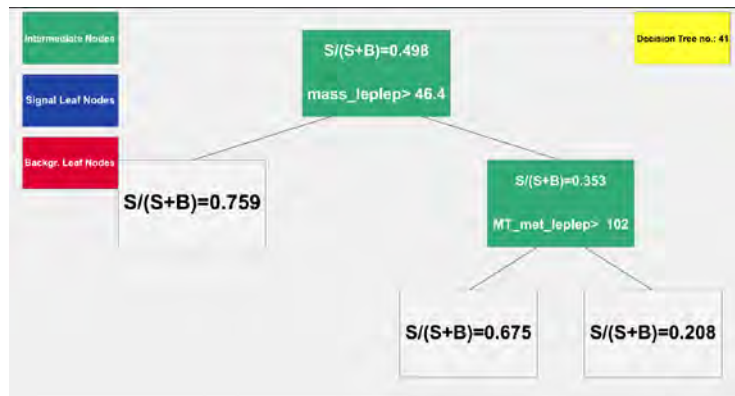


Figure 2. Decision Tree for $t\bar{t}H$ events

Hundreds of trees similar to that of Figure 2 are created and weighted according to their separation power. Events are then assigned a BDT score between -1 (for background-like events) and +1 (for signal-like events) according to their classification in each of the decision trees. The process by which the algorithm takes a known set of signal events and background events, separates, and determines the weighting of each separation is known as training. Once the BDT is trained, it is fed events that are not identified beforehand as signal or background, in

a process known as testing. Testing ensures that the BDT is functioning properly, and is truly able to distinguish signal from background solely from the variable parameters of each event.

3. Results

An initial BDT, which will be called BDT1, was taken to separate two types of $t\bar{t}H$ decay processes: events in which both leptons come from Higgs Boson decays from those in which one or both leptons come from a top quark. The former category includes Higgs decays to W bosons to a pair of leptons and Higgs decays to tau particles to a pair of leptons. The latter category consists of decays of the Higgs to bottom quarks, or Higgs decays to W bosons or taus in which one of the W bosons/taus decays to a jet. Figure 3a shows the strong separation achieved by the BDT, with the signal in blue with high BDT values and the red background events with low BDT values.

It was noticed that above a BDT1 score of -0.5, about 95% of the signal is retained while 50% of the background events are discarded (Fig. 3b). Therefore, further BDTs were performed with $t\bar{t}H$ and background events by setting a floor threshold of -0.5 score on BDT1 to separate out $t\bar{t}H$ events in which both leptons come from the Higgs. Similarly, BDTs were performed with $t\bar{t}H$ and background events by setting a ceiling threshold of -0.5 score on BDT1 to separate out $t\bar{t}H$ events in which one or both leptons come from the top quarks.

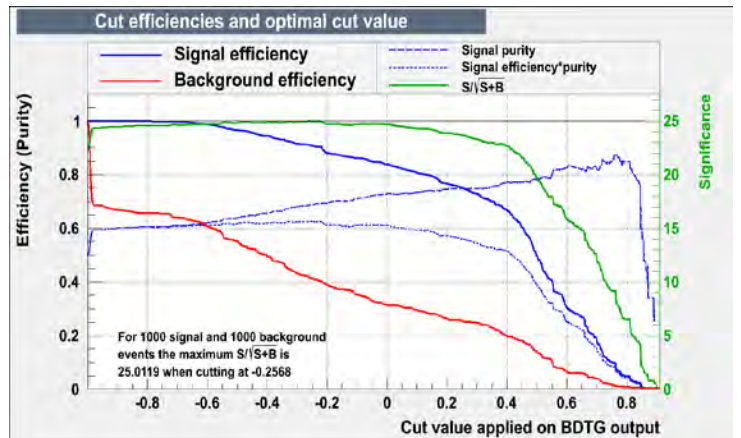
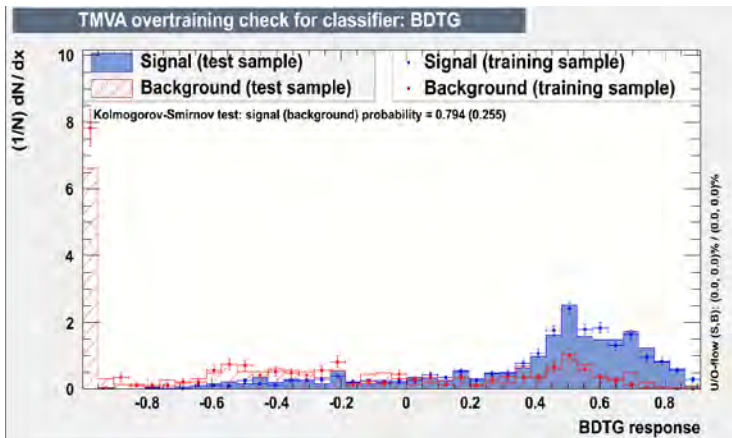
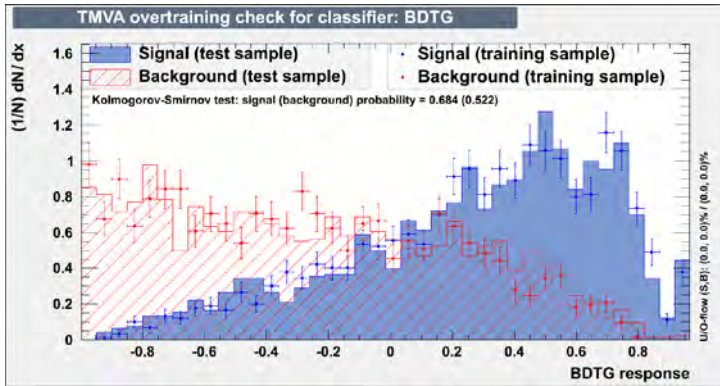
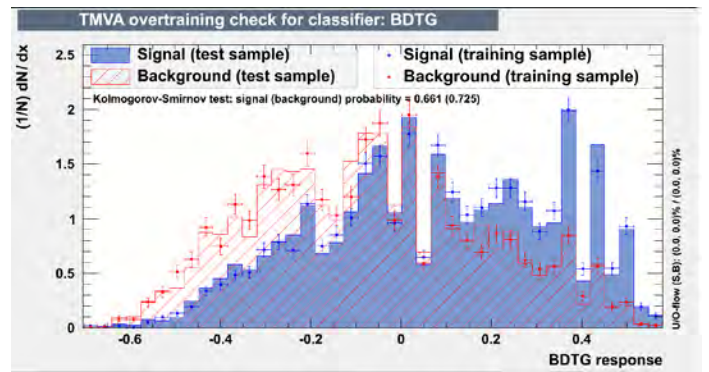


Figure 3. $t\bar{t}H$ BDT plots: (a) separation between $t\bar{t}H$ with dileptons from Higgs (signal) vs. $t\bar{t}H$ with one or two leptons from top quarks; (b) Cut efficiencies for initial BDT.

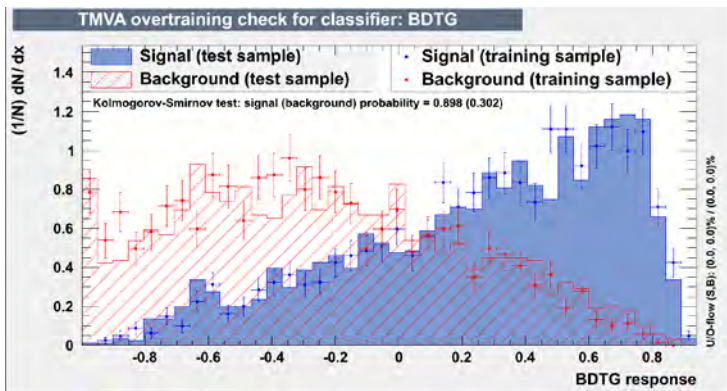
These BDTs were trained separately for different jet categories: first for all events with 6 jets or more, and then for all events with 5 jets. Figure 4 shows the separation obtained in each category between $t\bar{t}H$ and background for each BDT category.



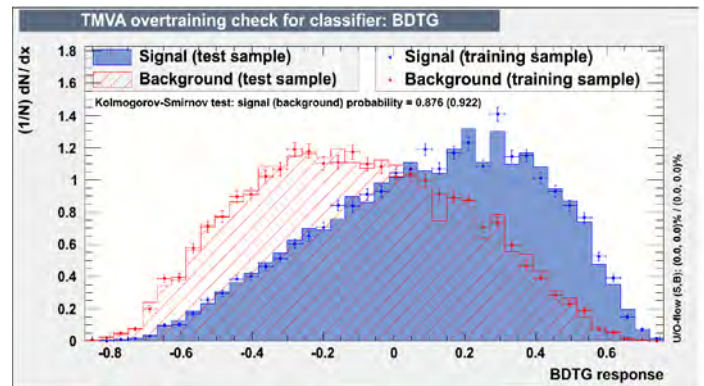
(a)



(b)



(c)



(d)

Figure 4. BDT Separations: (a) $H \rightarrow ll$ vs background, > -0.5 BDT1, ≥ 6 jets; (b) $t\bar{t}H$ vs background, < -0.5 BDT1, ≥ 6 jets; (c) $H \rightarrow ll$ vs background, > -0.5 BDT1, 5 jets; (d) $t\bar{t}H$ vs background, 5 jets

A BDT was not trained for events with 5 jets and a BDT1 score less than -0.5 due to the difficulty of separation. Instead, the BDT corresponding to Figure 4d was trained on $t\bar{t}H$ vs background events with 5 jets.

These BDT variables were then used to determine expected upper limits for $t\bar{t}H$ production at 8 TeV. In order to determine $t\bar{t}H$ production from events with 4 jets, the 5 jet BDT variables were used. A median expected 95% confidence level upper limit of 8.9 was obtained. This means that given the data that we expect to see based on a theoretical understanding of the proton-proton collisions at the LHC, statistical fluctuations in the background events could mimic $t\bar{t}H$ signal in excess of 8.9 times the Standard Model, provided that $t\bar{t}H$ production does not take place, 50% of the time.

An upper limit of 8.9 for $t\bar{t}H$ production is comparable to that found from analyses involving other $t\bar{t}H$ decay channels. The results found in this analysis will be used together with analyses into other decay channels to help aid in the discovery of $t\bar{t}H$ production.

Acknowledgements

I would like to thank Dr. Lannon and Dr. Hildreth for all of their help this summer to make this research possible. I would also like to thank the graduate students in the NDCMS lab for their invaluable help: Andrew Brinkerhoff, Anna Woodard, Charlie Mueller, and Matthias Wolf. Many thanks to Dr. Garg and the National Science Foundation for allowing me to be here this summer. Also thanks to Sue Coyne for all of her hard work in making this summer program great.

References

CMS Collaboration, “Search for Higgs Bosons Produced in Association with Top-Quark Pairs and Decaying to Bottom Quarks, Photons, or Leptons”, 2014, Submitted for Publication.

²A. Denner, S. Heinemeyer, I. Puljak, D. Rebuszi, and M. Spira, “Standard Model Higgs-Boson Branching Ratios with Uncertainties”, *Eur. Phys. J. C*, 71, 1753, (2011).

³CMS Website, “About CMS”: <http://cms.web.cern.ch/content/about-cms>

Analyzing Deuteron Scattering at 100 MeV/u
Through Optical Model Parameters

Emily Morgan

2014 NSF/REU Program

Physics Department, University of Notre Dame

Advisor: Umesh Garg

1 Abstract

Nuclear incompressibility, K_∞ , is the curvature of the equation of state of infinite nuclear matter at saturation density. The only direct method through which we can study and then constrain incompressibility is the isoscalar giant monopole resonance (ISGMR), the breathing mode of the nucleus. Using the nuclear optical model to both fit elastic scattering patterns and reproduce inelastic scattering patterns, we identify parameters with which we can predict and analyze the behavior of the ISGMR, eventually progressing to a calculation of incompressibility. The advent of radioactive beam facilities has introduced significant experimental advancements. From here we begin to discern which probes are ideal for use in our analysis of the interaction. Deuterium is presently being tested for its feasibility. The Research Center for Nuclear Physics at Osaka University in Japan was home to just such an experiment. A 196 MeV deuteron beam was impinged on ^{116}Sn and ^{58}Ni targets to measure the elastic and inelastic cross-sections at various angles. These angular distributions have been analyzed using the hybrid optical model, whose effectiveness is investigated.

2 Introduction

An inherent property of infinite nuclear matter, the compression modulus, is important in the understanding of numerous nuclear and astrophysical phenomena, including the strength of collapse in supernovae explosions, collective-flow in high-energy

heavy ion collisions, and properties of neutron stars [1]. One might conceptualize K_∞ as the “stiffness” of the nucleus. Mathematically, nuclear incompressibility, K_∞ , is the curvature of the equation of state at saturation density, as seen in Eq. (1),

$$K_\infty = 9\rho_0^2 \frac{d^2(\frac{E}{A})}{d\rho^2} \Big|_{\rho_0} \quad (1)$$

where E and ρ_0 are the binding energy and the saturation density, respectively [2]. Through constraining its value, we in turn improve our understanding of the equation of state of nuclear matter. With this understanding comes a better grasp on astrophysical phenomena and the origin of atomic elements. At this point in the pursuit, however, an exact incompressibility constant remains inaccessible, limiting our ability to clearly delineate the equation of state.

The most direct way to extract incompressibility is through analysis of isoscalar giant monopole resonances (ISGMR). ISGMR is often referred to as the “breathing mode” of the nucleus for its in and out oscillations,. The exact relation comes from the centroid energy of the ISGMR and is illustrated in the form of Eq. (2).

$$E_{ISGMR} = \hbar \sqrt{\frac{K_A}{m \langle r^2 \rangle}} \quad (2)$$

Where m is the nucleon mass and $\langle r^2 \rangle$ is the ground state mean-square radius [3]. Note here the use of K_A as opposed to K_∞ . ISGMR only provides information about

the compressibility of finite nuclear matter, however, from K_A we can extrapolate K_∞ .

3 Procedure

Before obtaining E_{ISGMR} , K_A , and ultimately K_∞ , it is possible to fit and calculate the elastic and inelastic experimental angular distributions. This process includes fitting a set of optical model parameters to elastic distributions and confirming with the low-lying discrete state angular distributions by comparing the calculated cross sections with those experimentally obtained. The optical model parameter set search is run by the program ECIS which employs an iterative technique that searches for the one unique solution among the many which correspond to local minima in the χ^2 , [4]. Since a wide range of parameter combinations can achieve a satisfactory fit, an extensive, manual scan of local and global minima is required before the final set is found. These same parameters will eventually be used to calculate low-lying discrete state distributions and thus determine the validity of the set through a direct comparison of the calculated and experimental angular distributions. Once validated, the set is used to predict behavior of high-lying excitations, such as the ISGMR.

The nuclear optical model is the method of choice for modeling the interaction potential given its ability to account for the “refraction” and “absorption” like behavior of the scattering pattern through its inclusion of both real and complex terms, respectively [5]. The optical potential is employed in this analysis in the form

$$V(r) = -V_{vol}(r) - iW_{vol}(r) + V_{SO}(r) + V_{coul}(r) \quad (4)$$

in which the real volume term is calculated with the double folding distribution and the imaginary volume and real spin-orbit terms are calculated using the Woods-Saxon shape factor [6].

The double folding distribution and Woods-Saxon shape factor are separate and specific methods for defining the potentials. There are a several proposed phenomenological and theoretical techniques to choose from, but this work utilizes a hybrid approach in which the real volume potential is calculated with a double folding formalism and the imaginary volume and spin-orbit potentials with Woods-Saxon shape form, as shown in Eq. (4). In the double folding model, the (nuclear) interaction V is taken to be a sum of effective two-body nucleon-nucleon interactions between target and projectile nuclei[7]. The method takes into account mass and charge distributions to make this calculation. The Woods-Saxon shape factor is defined as

$$f(r) = \frac{1}{1 + \exp(\frac{r-R}{a})} \quad (5)$$

where R is the radial parameter defined as $R = r_0 A^{1/3}$ and a is the diffuseness parameter[5]. These parameters are presented as they correspond to ^{116}Sn and ^{58}Ni in

Tables 1 and 2.

In this analysis, we've employed deuterium as our projectile with targets of ^{116}Sn and ^{58}Ni to explore the efficiency of deuterons as a probe and investigate the ability of the hybrid optical model to reproduce the scattering's angular distributions. The experiment was carried out at the ring cyclotron facility of the Research Center for Nuclear Physics, Osaka University, Japan, using inelastic scattering of 196 MeV deuterium particles at extremely forward angles, including 0° . Scattered particles were momentum analyzed with "Grand Raiden", a high-resolution magnetic spectrometer. The vertical and horizontal positions of the scattered particles were measured with the focal-plane detector system composed of two position-sensitive multiwire drift chambers and two scintillators [8].

4 Results and Analysis

Presented in this work are two analyses which aptly convey the strengths and weaknesses of the hybrid optical model. For ^{116}Sn , the parameter search was performed with encouraging results. Not only were the elastic fit and 2^+ calculations in close agreement with the experiment, but we found moderate success at the 3^- state as well with a reproduction that only misses one valley. Figure 1 is the elastic fit and showcases its efficiency at following the structure of the pattern. Figure 2 displays the inelastic calculation for the 2^+ state, which again, follows the experimental angular distribution of the experiment well. Finally, Figure 3 further supports the validity

of the parameter set by highlighting agreements between calculation and experiment at almost every angle at the 3^- state.

Potentials	Parameters				
	Normalization	Depth (MeV)	r_0 (fm)	a (fm)	R
Real Volume	0.602				
Imaginary Volume		35.66	1.26	0.55	6.14
Real Spin Orbit		0.95	1.47	0.94	7.16

Table 1: Parameter set for hybrid optical model of ^{116}Sn

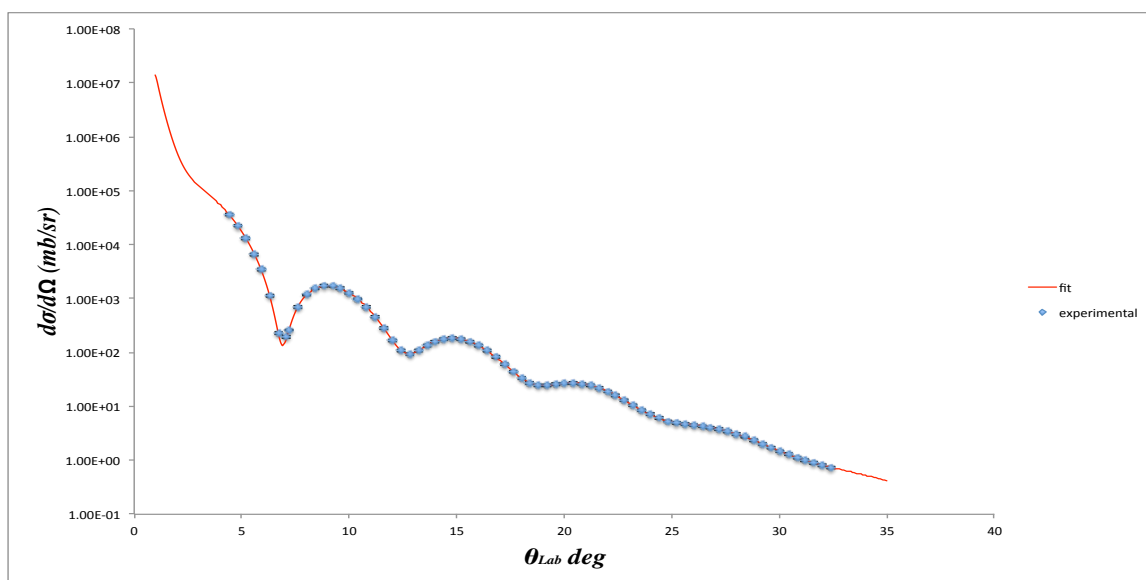


Figure 1: ^{116}Sn Elastic Fit

The next analysis performed was on ^{58}Ni . While the elastic state was originally quite easy to fit, none of the corresponding 2^+ calculations could replicate the shape of the distribution. The parameter set which could simultaneously fit the elastic state and reproduce low-lying 2^+ angular distributions was adopted. While the presented parameter set reproduces the experimentally obtained low-lying 2^+ angular

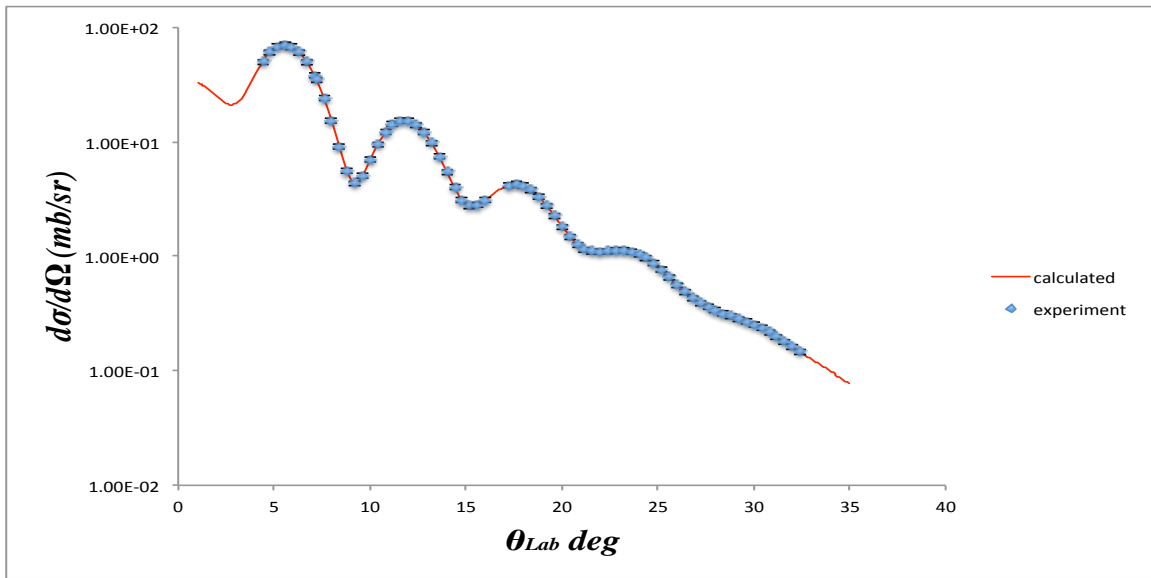


Figure 2: $^{116}\text{Sn } 2^+$ Model

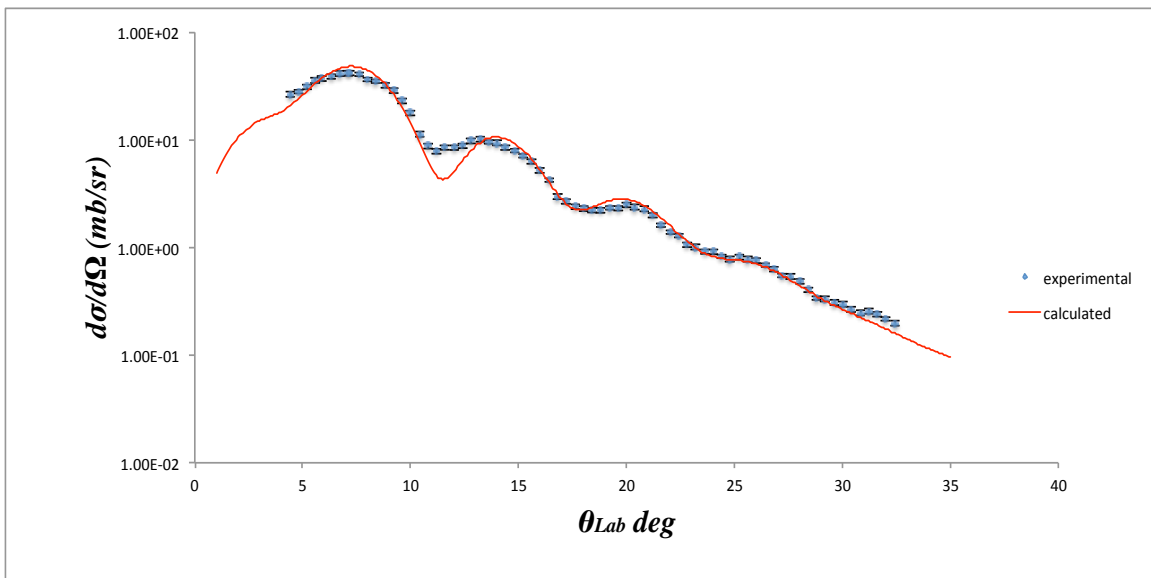


Figure 3: $^{116}\text{Sn } 3^-$ Model

distribution with roughly the same structure of the experimentally obtained 2^+ distribution, it is not without missing the first valley of the elastic fit. Even then, an

additional decrease of 20% in the adopted B(E2) transition probability was necessary to reconcile a significant inconsistency with the experimental distribution. Figure 4 displays the elastic fit which is clearly unable to reproduce the first valley just before 10° . In Figure 5, the 2^+ state, the model produced by our parameter set achieves the general shape of the scattering but still slightly misses almost every point.

Potentials	Parameters				
	Normalization	Depth (MeV)	r_0 (fm)	a (fm)	R
Real Volume	0.95				
Imaginary Volume		10.47	1.59	0.687	40.53
Real Spin Orbit		1.83	1.28	0.683	7.08

Table 2: Parameter set for hybrid optical model of ^{58}Ni

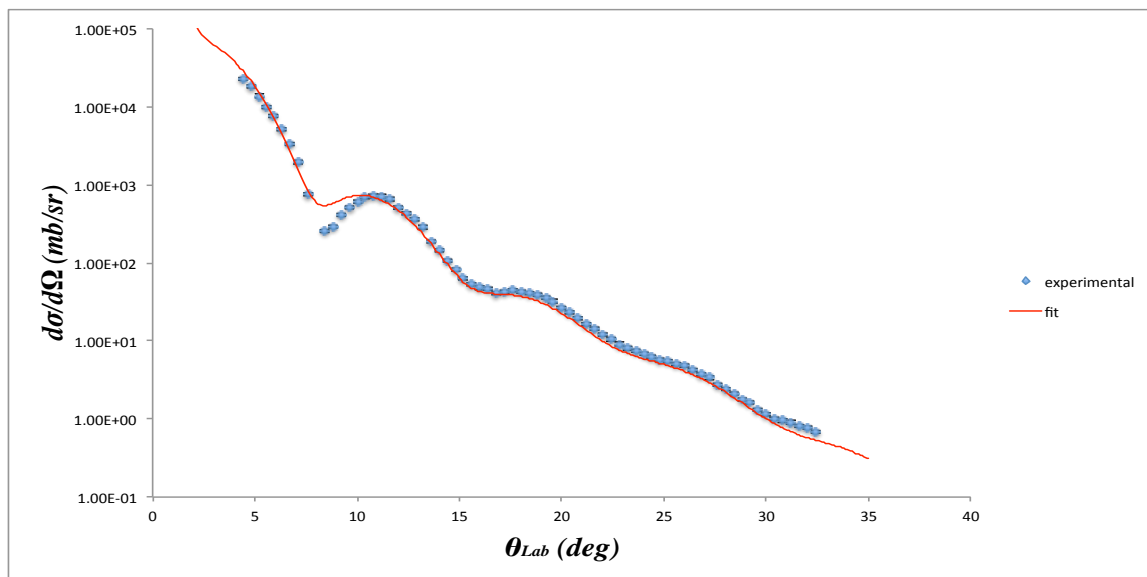


Figure 4: ^{58}Ni Elastic Fit

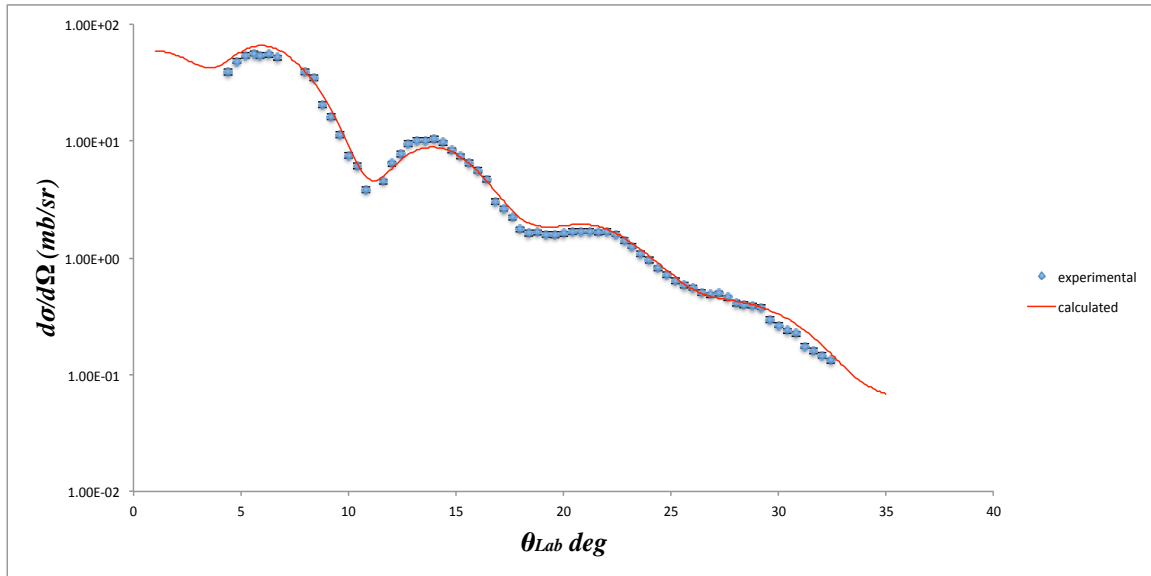


Figure 5: $^{58}\text{Ni } 2^+$ Model

5 Conclusion

At this time, a definitive declaration of the hybrid model's capabilities to reproduce experimental distributions is yet to be determined. Nonetheless, its effectiveness with modeling the ^{116}Sn states is significant, proving its ability, at the very least, for higher masses. There remains more searching to be done on the ^{58}Ni optical model parameters. As for deuterium's efficacy as a probe, the findings thus far suggest its merit and a further investigation of its effectiveness could solidify this.

6 Acknowledgments

I would like to thank the University of Notre Dame College of Science for providing me with more than sufficient funding to perform this research. I am immensely

grateful to Professor Umesh Garg for allowing me to join his group and providing me with the opportunity to begin research for the first time. Special thanks also to graduate student Darshana Patel for exercising the utmost patience and offering invaluable guidance throughout this process, along with the rest of Garg's research group.

7 References

- [1] J. Piekarewicz, *Phys. Rev. C* **66**, 034305 (2002)
- [2] A. Kolomiets, V. M. Kolomietz, and S. Shlomo, *Phys. Rev. C* **59**, 6 (1999)
- [3] J.P. Blaizot, *Nuclear Physics A* **591** (1995) 435–457
- [4] J. Raynal, computer program ECIS97 (1998), - O.E.C.D.Nuclear Energy Agency, Paris, France
- [5] P.E. Hodgson *Rep. Prog. Phys.* 1971 **34** 765-819
- [6] W. W. Daehnick, *Phys. Rev. C* **21**, 6
- [7] D.T. Khoa, G.R. Satchler, *Nuclear Physics A* **668** 2000. 3-41
- [8] T. Liu, U. Garg, *Phys. Rev. C* **81**, 034309 (2010)

Simulating a Multi-Reflection Time-of-Flight Mass Spectrograph for the Purification of Radioactive Isobars

Catherine Nicoloff

2014 NSF/REU Program

Physics Department, University of Notre Dame

Advisor:

Professor Maxime Brodeur

Abstract:

A Multi-Reflection Time-of-Flight mass spectrograph (MR-TOF) is being designed for the future Notre Dame Radioactive Ion Beam facility. The MR-TOF will provide isobarically pure beams to experiments. Design considerations for the MR-TOF include its geometry, its electrode voltages, and the choice of ion extraction scheme. These considerations were investigated using SIMION simulations. As a benchmark, we first optimized the electrode voltages of the ISOLTRAP MR-TOF geometry. The preliminary simulations involved varying two electrode voltages with the remaining electrodes held fixed and resulted in a mass resolving power $\langle TOF \rangle / \Delta TOF \approx 45,000$. Further simulations to optimize the remaining three electrodes will be required to reach higher mass resolving power.

Introduction:

The rapid capture of neutrons, known as the r-process, is an astronomical phenomenon that is partially responsible for the observed abundance of elements heavier than iron. Therefore, understanding the r-process is crucial to the understanding of heavy element formation in the universe. To that end, radioactive ion beams are necessary. Using ion traps, it is possible to measure nuclear properties of importance. However, to perform these measurements, pure beams containing solely the ion of interest are required. An MR-TOF will therefore be a vital component of the Radioactive Ion Beam facility that is being constructed at Notre Dame. Radioactive ions will be produced by a fission process that results in not only the ion of interest but contaminant ions as well. As these ions exist far from the valley of stability, the number of contaminant ions created can far exceed the number of ions of interest [1].

Ion beams can usually be purified of non-isobaric contamination by using conventional dipole analyzing magnets. An analyzing magnet works by subjecting incoming ions to an

unchanging magnetic field that is normal to the beam path. The magnet is also curved along the path of ion travel. Charged particles that enter the analyzing magnet will feel a central force $F = q_i v_i B$, giving the relation $\frac{m_i v_i^2}{r_i} = q_i v_i B$ which, if solved for r , yields a radius of curvature for a given particle of $r = \frac{m_i v_i}{q_i B}$. Assuming that B is constant, the radius of curvature of an ion inside the analyzing magnet is proportional to its mass and velocity and inversely proportional to its charge. Unwanted ions will collide with the walls of the analyzing magnet, thus removing them from the ion beam.

Analyzing magnets do not work for the purification of some radioactive ion beams due to the presence of isobar contamination. Isobars are atoms which contain the same number of nucleons. For example, Potassium-40 contains 19 protons and 21 neutrons (mass 39.96399848 u) while Calcium-40 contains 20 protons and 20 neutrons (mass 39.96259098 u). The difference in mass between these two isobars is due to minute differences in the binding energies of each nucleus. A dipole magnet does not have the mass resolving power to differentiate between isobars. A more sensitive instrument is required.

A Multi-Reflection Time-of-Flight mass spectrograph (MR-TOF) is just such an instrument. An MR-TOF separates ions of different mass by the differences in their times of flight. The working principles of the MR-TOF are as follows: First, the potential of the first electrostatic mirror is dropped, permitting a mixed ion bunch to enter the MR-TOF. The mirror potentials are then raised, preventing escape. The strong positive potential at the extraction end causes the positively charged ions to slow down and change direction, accelerating back towards the injection end, where they are again turned around by a strong positive potential. Ions in the MR-TOF may repeat this back and forth cycle a hundred or more times in just a few milliseconds.

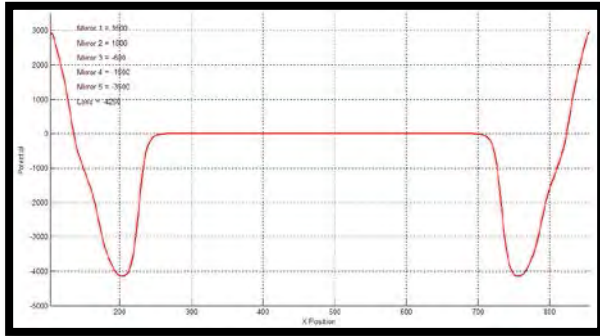


Fig 1: Potential distribution inside the simulated MR-TOF

As the ions fly from end to end of the MR-TOF, they oscillate inside a potential well they cannot escape (see Fig 1). Ions of different species, with only slight variations in mass, will travel at different velocities based on their mass and charge and thus take different amounts of

time to fly from one end of the MR-TOF to the other. These differences in velocity accumulate with the number of revolutions n until the original mixed ion bunch has resolved into separate bunches of ions, each containing only a single isobar. Once these bunches are separated by enough time, it is possible to extract the purified bunch corresponding to the ions of interest from the MR-TOF by raising the lift electrode or dropping the electrostatic mirror potentials at the right instant.

In practice, a typical MR-TOF is a compact device containing two arrays of mirror electrodes, one at each end (see Fig 2). There may also be a lift electrode at the center to assist with ion extraction.

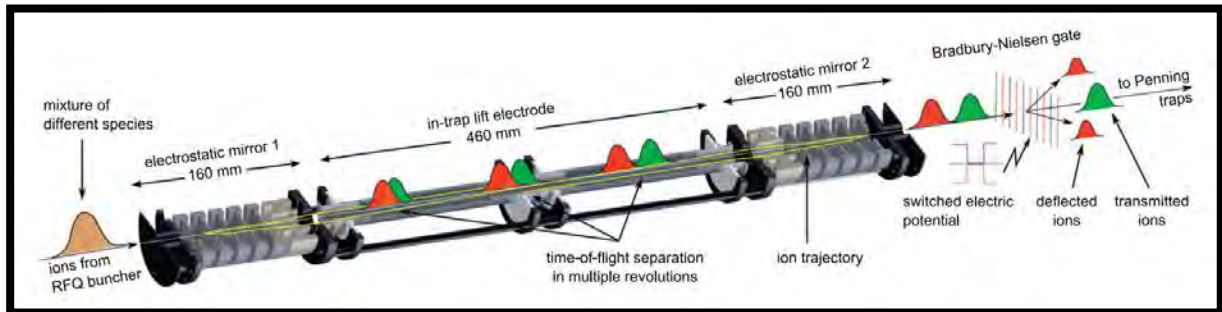


Fig 2: MR-TOF layout as depicted in R.N. Wolf, et al [1].

Simulation:

For the initial simulation, the geometry of the ISOLTRAP MR-TOF from the ISOLDE facility at CERN was used. By using the dimensions given in R.N. Wolf et. al., a SIMION geometry file was

created that defined all the individual electrodes [2]. For simplicity, only electrically relevant structures were defined (see Fig 3). In a physical MR-TOF, there would be the supporting beam pipe, insulators, electrical connections, and other necessary hardware.

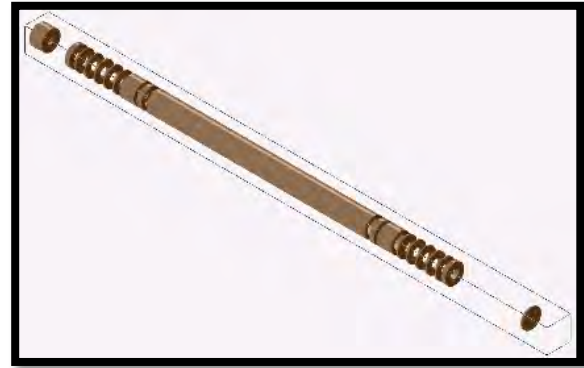


Fig 3: MR-TOF geometry as it appears in SIMION

Once the SIMION geometry was created, it was necessary to write a LUA script that would then dynamically control important aspects of the simulation. At the time of ion injection, the script drops the mirror electrode voltages to permit entrance into the simulated MR-TOF. The script then sets the mirror voltages to their operating voltages while the ions are circulating. Finally, at extraction time, the script raises the lift electrode voltage to propel the ion bunches out of the potential well and thus out of the MR-TOF.

Optimizing the MR-TOF:

There are five mirror electrodes at each end of the simulated MR-TOF. To begin the task of calculating ion times of flight, these five electrodes needed to be set to some initial value. R.N. Wolf, et al. provided a graph (Fig 4) showing the potential distribution inside the

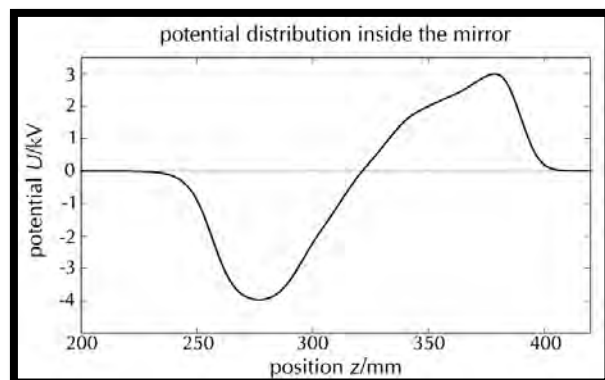


Fig 4: Potential distribution as depicted in R.N. Wolf, et al [2].

ISOLTRAP MR-TOF's electrostatic mirrors [2]. Since the geometry of the MR-TOF is also known, it was possible to locate each mirror's position on the graph and then estimate a mirror value that

would produce a similar potential at that location. The initial estimated values were (starting from the injection end): 2000, 2500, 2000, 750, -1500.

These estimates were then tested by flying a single, uncharged ion through the simulated MR-TOF and logging its potential at each position. The resulting potential graph was then compared to the one from ISOLTRAP [2] and further refinements were

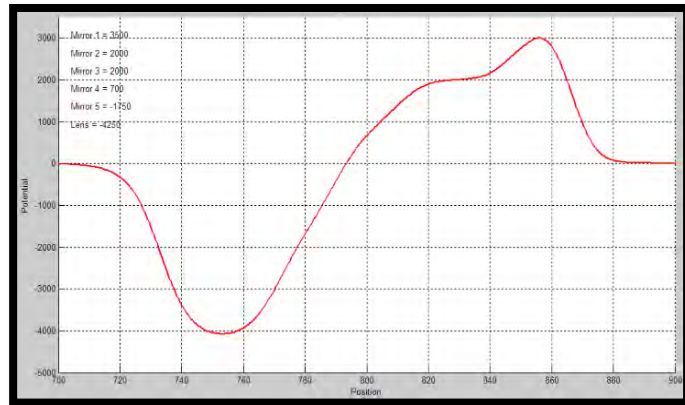


Fig 5: Estimated mirror potentials

made until the potentials seen inside SIMION closely resembled those seen inside the ISOLTRAP MR-TOF (see Fig 5). The final estimated values were: 3500, 2000, 2000, 700, -1750.

Simulation and optimization could then begin. To optimize the simulated MR-TOF, the ratio of mean time of flight ($\langle \text{TOF} \rangle$) to the full width at half maximum of the time of flight (ΔTOF) must be maximized. This involves logging time of flight and round trip data for each simulated ion.

At the time the ion is created, a line of data is logged to file. This line of data includes the ion number, the time of flight (which is zero at $t = 0$), and the x, y, and z positions of the ion. Additionally, every time the ion circles around and passes the plane of $x = 480$ at the center of the MR-TOF, another line of data is logged to the same file. Once the extraction time is reached, the ion goes splat and another ion is created.

The simulated ions were given a mass of 40u, an initial kinetic energy of 2000eV, and a charge of +1. They were also set up as a Gaussian 3D distribution of approximately 3mm in

diameter in each of the x, y, and z dimensions, centered at x = 480. This was to simulate the discrete ion packets that come from the RFQ cooler and buncher.

The first test of the estimated mirror potentials was a time of flight test for a single round trip. A flight of 1000 ions was flown through the simulated MR-TOF, with each ion completing one round trip. The results were then put into a histogram and

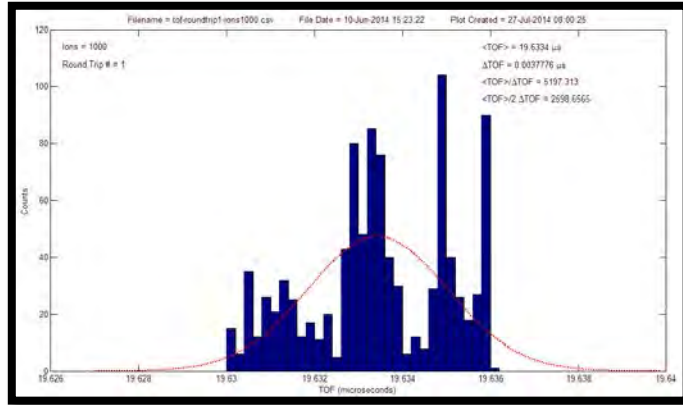


Fig 6: The initial estimated mirror potentials were not optimal.

analyzed: the initial single packet of ions had turned into three distinct peaks on the histogram. Some of the ions were speeding ahead of the bunch and some were lagging behind, resulting in a wide non-Gaussian distribution (see Fig 6). It was clearly necessary to optimize the MR-TOF mirror potentials.

It was initially decided to focus on Mirror 3, which is in the center of the five electrode array. The LUA code for the simulation was edited to permit sequential SIMION runs thus: Mirror 3 could be set to a range of voltages with a step factor per increment and would start at the lowest value in its range. Mirror 3 would be progressively incremented by the step value until it reached the highest value in its range. At each step, 100 ions would be flown for 100 round trips. For the first run, the range of Mirror 3 was set from -100 to 900, in steps of 100.

Again, the results were unexpected. The $\langle \text{TOF} \rangle / \Delta \text{TOF}$ was plotted per round trip per Mirror 3 voltage. Instead of smoothly climbing curves, which would indicate that the ions in the

bunch were better resolved in time, the curves climbed to a peak and then begin to descend (see Fig 7), indicating that the ions in the bunch were initially converging but later spreading out.

At first, it was theorized that the ion bunches were spreading out because the mirror voltages had not been tuned. The LUA code controlling the simulation was modified to permit nested sequential runs thus: Mirror 4 and

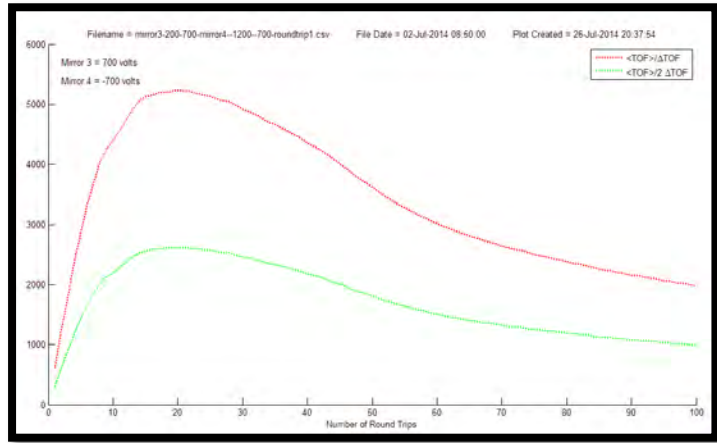


Fig 7: $\langle TOF \rangle / \Delta TOF$ lines decreasing at longer times of flight

Mirror 3 could each be set to a range of voltages with a step factor per increment. Each would start at the lowest value in its range. Mirror 3 would be progressively incremented by the step value until it reached the highest value in its range. At each step, 100 ions would be flown for 100 round trips. Then Mirror 4 would be incremented by its step value and the cycle would repeat until all combinations of Mirror 4 and Mirror 3 voltages had been simulated. The $\langle TOF \rangle / \Delta TOF$ was plotted per round trip per Mirror 3/Mirror 4 voltage pair. These graphs had the same basic curve structure as previously, with an initial increase followed by a decrease at longer times of flight.

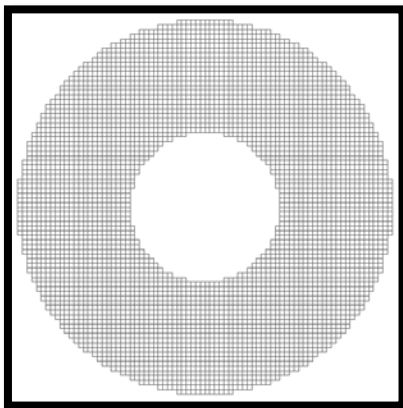


Fig 8: Scaling of 1mm per grid unit

This problem was solved by using a finer mesh to create the electrode structure. The original MR-TOF geometry file had a scale of 1mm per grid unit. This left the round electrodes blocky and angularly asymmetric (see Fig 8). It was decided that a smaller scale of 0.0625mm per grid unit would result in a

rounder, smoother electrode (see Fig 9). This, in turn, would make the field inside the MR-TOF more accurate and angularly symmetric.

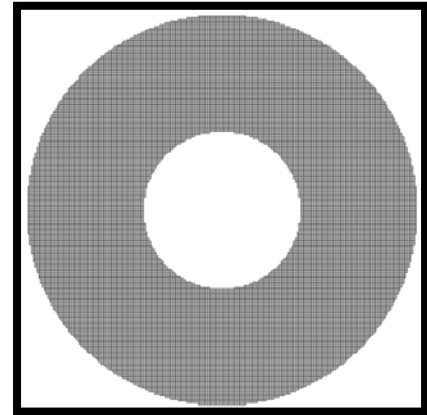


Fig 9: Scaling of 0.0625mm per grid unit

After changing the scaling of the MR-TOF geometry, the downward trend of the $\langle \text{TOF} \rangle / \Delta \text{TOF}$ graphs resolved into the expected trend lines (see Fig 10). The scaling change also had the effect of dramatically improving the mass resolving power. Unfortunately, the finer mesh also increased total simulation time due to increasing the complexity of SIMION's calculations. It now takes a little over a day to simulate a range of five Mirror 4 voltage steps versus a range of five Mirror 3 voltage steps.

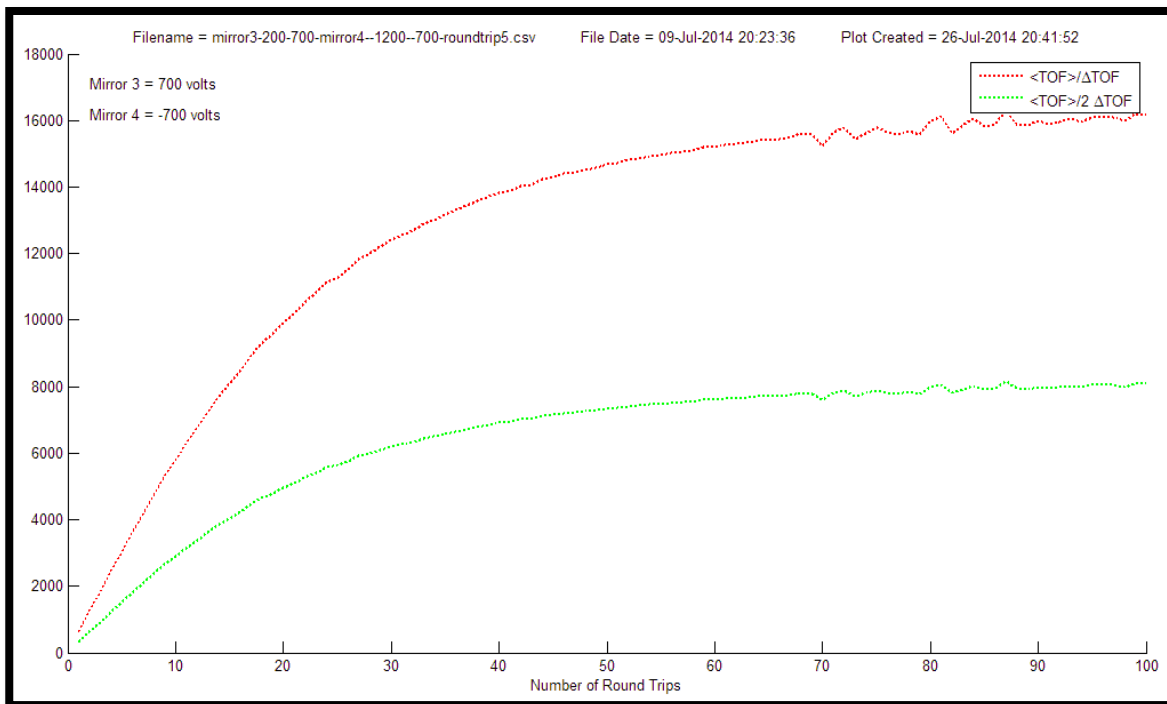


Fig 10: Post-scaling, the $\langle \text{TOF} \rangle / \Delta \text{TOF}$ graph is as expected

With the simulated MR-TOF behaving as expected, it was finally possible to hold Mirror 1, 2, and 5 fixed while scanning Mirror 3 and Mirror 4 ranges to find the maximum mass resolving

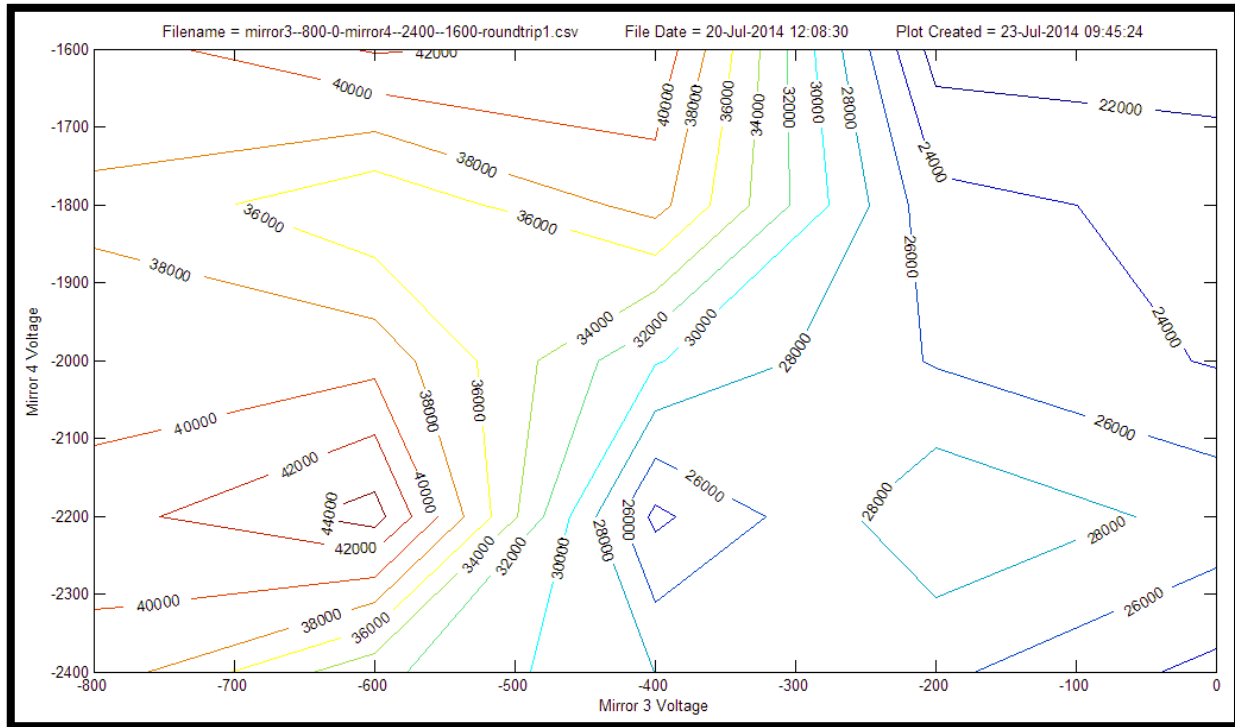


Fig 11: Contour plot of the best mass resolving power to date

power for those two electrodes. As shown in Fig 11, this maximum occurs when Mirror 3 is at -600 and Mirror 4 is at -2200.

Future work:

There is much work to be done to optimize all five mirror electrodes within the current geometry. Mirror 3 is now fixed at -600 while Mirrors 2 and 4 are being varied across ranges to see if a new maximum mass resolving power can be located. This process will repeat iteratively until all five mirror electrodes have acceptable values. The target for $\langle \text{TOF} \rangle / \Delta \text{TOF}$ after full optimization is approximately 100,000.

References:

- [1] Wolf, R. N., et al.: Nuclear Instruments and Methods in Physics Research A. 686 (2012) 82-90.
- [2] Wolf, R. N., et al.: Hyperfine Interact. 199 (2011) 115-122.

Filaments: Understanding the Math that Defines them

Marina Paggen

2014 NSF/REU Program

Physics Department / University of Notre Dame

Advisor: Dr. Lara Phillips

ABSTRACT. Filaments are tube-like structures filled with matter, gas, and heat which give the universe a web-like appearance. In order to study the significance of these large scale structures, numerous structure finding algorithms were created in order to simulate tubes in computational models. The aim of this paper is to determine the mathematical underpinnings of a few select structure finding algorithms and understand which parts of the filament these algorithms are recreating. This was done by selecting three astronomical structure finding algorithms and one medical imaging algorithm. The equations and their spatial significance were compared in order to understand what these algorithms offer. It was determined that in order to ensure proper tracing of the filaments, centerline extraction used in medical imaging would provide better data. Using python, the equation used for centerline extraction was written in a way that it could attempt to be adapted to astronomical computations. Incorporating other features of the physical attributes of filaments, such as Gibbs Free Energy, would allow more significant study of the nature of such large scale structures. For future work, Gibbs Free Energy could be determined based on the initial data and then compared to the structure finding algorithm(s).

1. INTRODUCTION

In order to advance our understanding of intricate networks of biological entities or the vastness of space, computer modeling is a method for testing and observing changes in these systems. Structure finding algorithms are used in medical imaging and astronomical simulations. In order to better study and treat the networks of blood vessels within the brain, the use of medical imaging is utilized in order to better direct the use of a successful surgery. In order to

study the patterns of our universe from a distance a computer model is necessary to assess the information and determine patterns in galaxy formation [1].

The cosmic web was divided into some basic large scale structures. These structures include filaments, walls, voids, and clumps. They have distinct features geometrically. A filament is a tube like structure. Voids are areas of relatively empty space. Clumps and walls are structures that resemble their names. Numerous studies with simulations were done on these structures in order to determine their nature and function[2,3,4]. In this paper the focus is on filaments. Filaments contain gas and matter that are thought to be “pathways for matter to accrete on forming galaxies”[3,4,5].”

There are a number of structure finding algorithms where the purpose is to distinguish the structures from the data presented by the databases of information such as the Sloan Digital Sky Survey or SDSS [2,3,4,5,6,7,8,9,10,11,12]. Additionally, it has been observed that similar structure finders in medical imagery such as Frangi’s vesselness measure can be adapted to be used for cosmology applications. NEXUS is based on the Multiscale Morphology Filter technique [10]. The authors claim that this algorithm can be used for a variety of inputs to include: “tidal field, shear, density, and velocity divergence.”[10]. Multiscale Geometric Flow, a medical imaging algorithm, used to evaluate data of protein density to find tubular blood vessels.[13,14] The author claims that the algorithm can determine blood vessels and determine the flow within the vessels thus improving MRI images.[13] The methods used to enhance the MRI images can also be adapted astronomical algorithms to find filaments.

The marked point process can be executed with raw density information without smoothing [12]. The authors claim that the probability approach of the marked point process constructs a model more true to what can be detected by the eye [12]. The three dimensional

Smoothed Hessian Major Axis Filament Finder or SHMAFF is based on ideas behind a two dimensional program that uses a method to divide the field into a pixelized grid [2,8,9,11]. The author's claim that this method is more accurate for classifying filaments [2,8,9]. The Multiscale Morphology Filter or MMF technique employs the use of dark matter haloes and their orientation in order to distinguish the difference between structures [6,7]. Combining the Hessian matrix calculation with a deliberate extraction of a ridge or spine was performed in medical imaging algorithms, but not in astronomical algorithms compared in this paper. The direction of this paper will be the comparison of four algorithms and an attempt to write the medical imaging centerline extraction formula in a way that can be inserted into astronomical algorithms.

2. ANALYSIS AND COMPARISON OF ALGORITHMS

Four algorithms were chosen to compare techniques. This includes MMF, SHMAFF, the marked point process, and Descoteaux's Multiscale Geometric Flow. The algorithms were compared in three areas: the technique for smoothing the initial density field data, the computation and source of eigenvalues, and the use of extracting a centerline or spine of the structure in order to confirm location of structure.

To begin the algorithm, a density field is chosen and set up. MMF uses the Delauney Triangulation/Tessellation Field Estimator (DTFE) to set up the density field and then uses scale-space filtering to smooth the field at different scales [6,7]. The following filtering formula uses an "hierarchy of spherically symmetric Gaussian filters having different widths." [6]

$$\rho_{\sigma}(\mathbf{x}) = \int \rho(\mathbf{x}') \rho_{\sigma}(\mathbf{x}, \mathbf{x}') d\mathbf{x}' \quad [6]$$

$$\rho_{\sigma}(\mathbf{x}, \mathbf{x}') = \exp\left(-\frac{(\mathbf{x}-\mathbf{x}')^2}{2\sigma^2}\right) \frac{1}{(2\sigma^2)^{\frac{3}{2}}} \quad [6]$$

$\rho(\mathbf{r}) =$

$$(\sqrt{2})^{-3} \sum_{\mathbf{r}_i} \rho(\mathbf{r}_i) \exp\left(-\frac{|\mathbf{r} - \mathbf{r}_i|^2}{2\sigma^2}\right) \quad [6]$$

SHMAFF “generates the density field and its second derivatives” with Gaussian smoothing kernels [2]. The “density field is initially the sum of delta functions and integration by parts yields the smoothed Hessian.”[2] The formula appears different from MMF formulas but is based on same idea.

$$\rho(\mathbf{r}) = \int \rho(\mathbf{r}') \exp\left(-\frac{|\mathbf{r} - \mathbf{r}'|^2}{2\sigma^2}\right) d\mathbf{r}' \quad [2]$$

Tempel’s marked point process does not require smoothing of the raw data field. Descoteaux’s program does not specifically state that it uses smoothing. This could be due to the fact that it is using medical imaging data and it is based on a protein density field. There is mention of the Hessian matrix “computed over 10 logscases”. [13]

Once the field is established the next step for most of the algorithms is to generate the Hessian matrix. The Hessian matrix is a symmetric matrix with the double derivative of each component. Wikipedia states that the Hessian “describes the local curvature of a function of many variables.” This matrix is then solved for its eigenvalues which can be used to describe geometrically an ellipsoid. [14] MMF’s Hessian matrix is based on the data provided by the DTFE. The eigenvalues are “computed at each point of the smoothed density field.” [6] SHMAFF’s Hessian matrix is also based on a density field. However, his smoothed density field is computed differently from MMF’s field. Thus, the eigenvalues maybe similar but are not exactly the same. The marked point process does not use the Hessian matrix but instead uses the Bisous model to generate cylinders for the filaments. [12] Descoteaux uses the Hessian matrix and the data for this matrix is based on a protein density field.

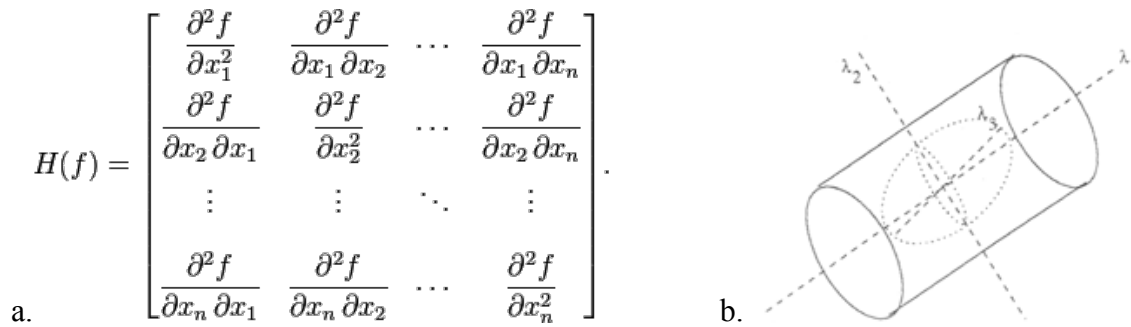


Figure 1: a.) The general form of the Hessian matrix. (source Wikipedia) b.) The ellipsoid generated by the eigenvalues. [14]

Once the geometry of the bulk of the filaments is determined, the final touch of the algorithms is to finely tune the position and end points of the structure. Most programs do this by establishing a spine or centerline to the tube. MMF does not search for a centerline or extract a spine, instead the program uses thresholds to make a final determination of the structures.[6] SHMAFF determines an “axis of structure” using the eigenvalues which represent the principal axes.[2,8,9] The “axis of structure” becomes the axis of the filament.[2,8,9] The marked point process does perform a “spine detector” that uses the “stochastic information.”[12] Stated by the authors “the spines are situated at the highest density regions outlined by the filament probability maps.”[12] Descoteaux uses Frangi’s vesselness measure to extract a centerline.[13] The area of highest vesselness measure gives the centerline of the tube.[13,14] The equation to generate this measure follows: [13,14]

$$V(\sigma) = \begin{cases} 0 & \text{if } \lambda_2 < 0 \text{ or } \lambda_3 < 0 \\ (1 - \exp(-\frac{R_A^2}{2\alpha^2})) \exp(-\frac{R_B^2}{2\beta^2}) (1 - \exp(-\frac{S^2}{2c^2})) & \end{cases}$$

Table 1	MMF (Multi-scale Morphology)	SHMAFF (Smoothed Hessian Major)	marked point process	Multi-scale Geometric Flow (Medical)
---------	------------------------------	---------------------------------	----------------------	--------------------------------------

	Filter)	Axis Filament Finder)		Imaging)
Smoothing Technique	DTFE (Delauney Triangulation/ Tessellation Field Estimator) followed by Scale-Space Filtering	Guassian smoothing kernel	No smoothing required. Density data is used as is.	No direct mention of smoothing but does calculate data at different scales.
Eigenvalues	Eigenvalues are determined from a density based Hessian matrix.	Eigenvalues are determined from a density based Hessian matrix.	No eigenvalues used. Algorithm is based on the Poisson Process.	Eigenvalues are determined from a density based Hessian matrix.
Extraction of Centerline or Spine	MMF does not extract a line but instead uses a matrix norm parameter to establish thresholds.	SHMAFF exhausts the geometric characteristics of the Hessian matrix and uses the eigenvalues to determine an “axis of structure”	Tempel does extract a spine based on where the probability data is at its highest density.	Frangi’s vesselness measure is used to extract the location of the centerline. The highest measure depicts where the centerline is.

One unique aspect in the marked point process was the use of Gibbs Free Energy. In this program the energy is used in order to align and connect the cylinders. Tempel *et al* includes Gibbs Free energy during the calculation of the Poisson process as indicated by the following equation [12]:

$$p(\mathbf{y}|\theta) = \frac{\exp[-U(\mathbf{y}|\theta)]}{Z(\theta)}$$

Gibbs free energy is the sum of U_d the data energy and U_i the interaction energy: [12]

$$U(\mathbf{y}|\theta) = U_d(\mathbf{y}|\theta) + U_i(\mathbf{y}|\theta)$$

The energy acts as a method to align and connect the cylinders [12]. It also serves as an additional method to determine the existence of a filament if one of the energies is too strong. [12]

3. PROGRAM

The equation known as the vesselness measure was determined to be the base of extracting a centerline for cosmic filaments. Using Python, a preliminary program was written where it would start by using the eigenvalues calculated by the Hessian matrix and calculate the vesselness measure. Descoteaux and Frangi use the Frobenius matrix norm in the calculation of one of the parameters known as the S parameter [9,10]. The equation is as follows [13,14]:

$$S = \sqrt{\lambda_1^2 + \lambda_2^2 + \lambda_3^2}$$

It was noted by Aragon-Calvo et al that the Frobenius method favors blob formations and MMF uses a different matrix norm called the S morph to calculate thresholds. [6] It was determined that one of the key places to manipulate the program would be the selection of the matrix norm for the S parameter. The equation is as follows: [6]

$$S_{\text{morph}} = \left(1 - \frac{|\lambda_3|}{|\lambda_1|}\right) \cdot \frac{|\lambda_3|}{|\lambda_2|}$$

Additional matrix norms could be tested to determine the best fit for the centerline extraction. At this time the program is not running due to bugs in the program.

4. CONCLUSION

The benefits of using the Hessian matrix are noted by Bond, Nicholas *et al* “with the eigenvalues and eigenvectors of the Hessian matrix, we can determine the type and orientation of structures in a continuous two- or three-dimensional density field.”[2] Both in astronomical

algorithms and the medical imaging algorithm, the use of this matrix does a good job at detecting and distinguishing three of the four main structures. Voids are not detected using this method and are simply defined by what is left after the other structures were classified. [6] The Bisous model is adaptable to look for all major structures and does not require smoothing of the density field. [12] All the programs have problems with determining the ends of the tubular structures. Descoteaux addresses this problem by adding the centerline extraction in the medical imaging algorithm. [13] Further work concentrated on distinguishing the ends of the tubular structures is necessary and can be done by using different centerline extraction methods as suggested by Descoteaux and analyzing the Gibbs Free Energy of the field and comparing with the structures.

5. REFERENCES

- [1] Davé, R., Finlator, K., Hernquist, L., Katz, N., Kereš, D., Papovich, C., et al. (2005). Building galaxies with simulations. (arXiv:astro-ph/0510625v1)
- [2] Bond, J. R., & Wadsley, J. W. (1997). The Lyman alpha forest within the cosmic web (arXiv:astro-ph/9703125v1)
- [3] Kereš, D., Katz, N., Weinberg, D. H., & Davé, R. (2005). *How do galaxies get their gas?*(doi:10.1111/j.1365-2966.2005.09451.x)
- [4] Tanaka, M., Hoshi, T., Kodama, T., & Kashikawa, N. (2007). A huge filamentary structure at $z=0.55$ and star formation histories of galaxies at $z < 1$. *Monthly Notices of the Royal Astronomical Society*, 379(4), 1546-1556.
- [5] Bond, N. A., Strauss, M. A., & Cen, R. (2010). Crawling the cosmic network: Identifying and quantifying filamentary structure.(arXiv:1003.3237v2)

- [6] Aragón-Calvo, M. A., Jones, B. J., van de Weygaert, R., & Van Der Hulst, J. (2007). The multiscale morphology filter: Identifying and extracting spatial patterns in the galaxy distribution (arXiv:0705.2072v2)
- [7] Aragón-Calvo, M. A., van de Weygaert, R., Jones, B. J., & Van Der Hulst, J. (2007). Spin alignment of dark matter halos in filaments and walls. *The Astrophysical Journal Letters*, 655(1), L5.
- [8] Bond, N. A., Strauss, M. A., & Cen, R. (2010). Crawling the cosmic network: Exploring the morphology of structure in the galaxy distribution. *Monthly Notices of the Royal Astronomical Society*, 406, 1609-1628.
- [9] Bond, N. A., Strauss, M. A., & Cen, R. (2010). Crawling the cosmic network: Identifying and quantifying filamentary structure. *Monthly Notices of the Royal Astronomical Society*, 409(1), 156-168.
- [10] Cautun, M., van de Weygaert, R., & Jones, B. J. T. (2013). NEXUS: Tracing the cosmic web connection. *Monthly Notices of the Royal Astronomical Society*, 429(2), 1286-1308.
- [11] Moody, J., Turner, E. L., & Gott, J. R. (1983). Filamentary galaxy clustering: A mapping algorithm. *The Astrophysical Journal*, (273), 16.
- [12] Tempel, E., Stoica, R. S., Martínez, V. J., Liivamägi, L. J., Castellan, G., & Saar, E. (2014). Detecting filamentary pattern in the cosmic web: A catalogue of filaments for the SDSS. *Monthly Notices of the Royal Astronomical Society*, 438, 3465-3482.
- [13] Descoteaux, M., Collins, L., & Siddiqi, K. (2004). Geometric flows for segmenting vasculature in MRI: Theory and validation. *Medical image computing and computer-assisted Intervention—MICCAI 2004* (pp. 500-507) Springer.

[14] Frangi, A., Niessen, Wiro J., Vincken, Koen L., Viergever, Max A.(1998). Multiscale Vessel Enhancement Filtering. *Medical image computing and computer-assisted Intervention–MICCAI 1998* (pp. 130-137) Springer

Fluid Dynamics—From Helping Messi Goal to Modeling the Evolution of a Galaxy

Adrián A. Rivera Torres

2014 NSF/REU Program

Physics Department, University of Notre Dame

Advisor: Dr. Lara Phillips

Title

Fluid Dynamics – From Helping Messi Goal to Modeling the Evolution of a Galaxy

Abstract

We wish to model the evolution of the feedback materials from a galaxy moving in a filament. An accurate model can be obtained by inputting the galaxy's parameters and solving the compressible Navier-Stokes equations using a numerical solver that uses a fractional step method. Because there is material flowing in and out of the galaxy, this solver can tell us where the material is flowing to and if the orientation of the galaxy will have an effect on other galaxies or on the distribution of material in the filaments.

Introduction

The field of astronomy and astrophysics has greatly advanced throughout the past decades. Because of this, we are rethinking our approach to modeling galaxies and filaments that form part of the cosmic web. Astrophysicists have always modeled the evolution of a galaxy's structure, but only in a limited view, not taking into consideration where the inflow material is coming from or where the feedback material is flowing to. We might assume that the effect the feedback material has is negligible, but there is reason to believe it might actually have a profound effect on neighboring galaxies and material distribution in the filament. And this would mean that we would definitely have to change our outlook on galaxy modeling now that we've seen the bigger picture.

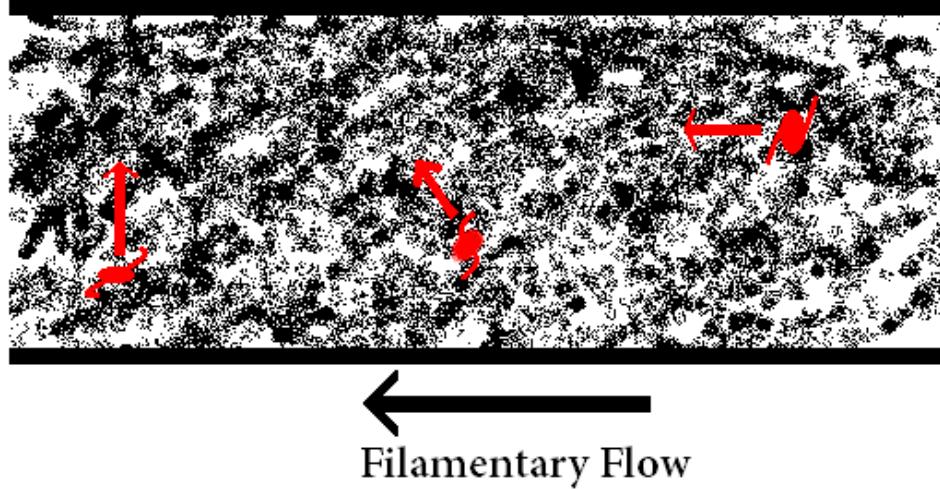


Figure 1.

This diagram represents galaxies moving across a filament, the red arrows show the galaxies' outflow orientation. If this model is an accurate representation, it is safe to assume that not only is the amount of feedback material held accountable for any change of material distribution in the host filament or the material flowing into neighboring galaxies, but the galaxies' orientation on the filament as well.

How can we model the evolution of a galaxy's structure?

Galaxies are mostly composed of gas and dust, and each point in space-time has a value for pressure, temperature, velocity components, density, viscous stress tensor components and heat flux components. So we can treat galaxies as if they were large fluids and find the values we want by solving the Navier-Stokes equations. This would require the appropriate boundary (initial) conditions, which can be obtained from databases that provide good theoretical values for whatever galaxy we're working with.

We tasked ourselves to write a computer program that would solve the compressible Navier-Stokes equations (referred to from this point on as the CNSE) using a numerical method. Last year some research was done to solve the incompressible Navier-Stokes equations for constant density, but this would prove to be an unrealistic and impractical model for this problem. Unfortunately there is still a lot we don't know about the general Navier-Stokes equations (such as the existence of a unique analytical solution to the equation,) so numerical methods of finding the solution are rather scarce, which is why there was no existing template of a program that would solve the equation, meaning we would have to write it from scratch.

A look at the equations and the fractional-step method involved

The CNSE arise from three basic physical principles: conservation of mass, conservation of momentum and conservation of energy, which are properly addressed in this set of equations, respectively:

$$\frac{\partial \rho}{\partial t} = -\frac{\partial}{\partial x_j}(\rho u_j)$$

$$\frac{\partial}{\partial t}(\rho u_i) + \frac{\partial}{\partial x_j}(\rho u_i u_j) + \frac{\partial p}{\partial x_i} = \frac{\partial \sigma_{ij}}{\partial x_j}$$

$$\frac{\partial}{\partial t}(\rho E) + \frac{\partial}{\partial x_j}((\rho E + p)u_j) = \frac{\partial}{\partial x_j}(u_i \sigma_{ij}) - \frac{\partial q_j}{\partial x_j}$$

Where ρ corresponds to the density, u_n is the velocity component ($n=1, 2, 3$), p is the pressure, σ_{ij} is the viscous stress tensor component, E is the energy density, and q_j is the

heat flux component. This notation (as well as the idea behind the numerical solver) comes from a paper published by Kunlun Liu and Richard H. Pletcher—there is another paper included in the references that tackles this problem but it uses heavy mathematical notation and was not taken into consideration for this project.

We start with what we'll refer to as the value vector $\vec{v} = [\rho, u_1, u_2, u_3, T]$, where each component \widehat{v}_n holds a value that follows the CNSE, i.e. $\vec{v} \cdot \widehat{v}_1 = \rho$ the pressure value. The objective is to give an initial guess as to what those values are, calculate the variance for each component by multiplying the vector by the Jacobian matrix, a preconditioning matrix (to accelerate convergence,) and a factorizing multiplier matrix, then add it to the initial guess and repeat this process until we have obtained a value with a good residual error.

How the program works

The grid's dimensions are 40 horizontal plot points, 40 vertical plot points, and n time steps, adding up to 1600n data points. Each data point has a five-dimensional value vector \vec{v} associated to it, meaning we are working with 8000n values distributed in a four-dimensional array referred to as datastore from this point on. This program can be used to solve problems of any magnitude (from a small pond to an entire galaxy,) but for this particular case the spatial intervals are equal to 1.00kpc and the time interval is equal to 10,000 years. These values were chosen because the Milky Way is roughly 37.0kpc in diameter and the evolution of galaxies' structure takes millions of years. We initialize datastore (the four-dimensional array of dimensions (n, 40, 40, 5) used to store the important data) to have all values equal to zero.

At a certain point in time ($t=0$) there is a known value vector for each point in space in the galaxy, referred to as the galaxy's initial values from this point on. These would serve as the boundary conditions for the solver, so we need accurate values in order to have an accurate simulation. A function can be coded and used to rewrite the initial values on datastore (values that correspond to $n=1$) using a file that contains those values—unless you feel like manually inputting 8000 values. We define functions for all values involved in the CNSE that provides us initial guesses of what the real values are supposed to be, run it through the numerical solver and then save it to datastore. We also need guesses for the values a time step before the origin time in order to make sure the derivative works.

The time derivative for any function F is approximated using the Euler Backwards Method:

$$\frac{\partial F}{\partial t}(x_1, x_2, t) \approx \frac{\delta F}{\delta t}(x_1, x_2, t) = \frac{3F(x_1, x_2, t) - 4F(x_1, x_2, t - 1) + F(x_1, x_2, t - 2)}{2\Delta t}$$

While the spatial derivative for any function F and any direction x_i is approximated using the Central Difference Formula (where $i \neq j$):

$$\frac{\partial F}{\partial x_i}(x_i, x_j, t) \approx \frac{\delta F}{\delta x_i}(x_i, x_j, t) = \frac{F(x_i + 1, x_j, t) - F(x_i - 1, x_j, t)}{2\Delta x_i}$$

These discretizations are necessary to help us calculate the material derivative (a concept originally proposed by the CNSE,) and it is defined as:

$$\frac{\bar{D}}{Dt} \equiv \frac{\partial}{\partial t} + u_i \frac{\partial}{\partial x_i} \approx \frac{\delta}{\delta t} + u_i \frac{\delta}{\delta x_i}$$

We want to calculate the variance (δ_m) of each component from the value vector, add it to the initial guess and then run the process again. For that we need to find the values for F_i first, where the sub index i stands for the value vector component you're working with, and they are calculated using the following formulas (to simplify matters, each variable is the variable evaluated at the coordinates (x_1, x_2, t) except in the cases where there is a square brace next to it, meaning one of the values changes according to what's inside the square brace):

$$\begin{aligned}
-F_1 &= \frac{1}{2\Delta t} (-3\rho + 4\rho[t - 1] - \rho[t - 2]) \\
&\quad + \frac{1}{2\Delta x_j} ((\rho[x_j - 1] - \rho[x_j + 1])u_j + (u_j[x_j - 1] - u_j[x_j + 1])\rho) \\
-F_{i+1} &= \frac{1}{2\Delta t} ((-3\rho + 4\rho[t - 1] - \rho[t - 2])u_i + (-3u_i + 4u_i[t - 1] - u_i[t - 2])\rho) \\
&\quad + \frac{1}{2\Delta x_j} ((\rho[x_j - 1] - \rho[x_j + 1])u_i u_j + (u_i[x_j - 1] - u_i[x_j + 1])\rho u_j \\
&\quad + (u_j[x_j - 1] - u_j[x_j + 1])\rho u_i + \sigma_{ij}[x_j - 1] - \sigma_{ij}[x_j + 1]) \\
&\quad + \frac{1}{2\Delta x_i} (p[x_i - 1] + p[x_i + 1]) \\
-F_5 &= \frac{1}{2\Delta t} ((-3\rho + 4\rho[t - 1] + \rho[t - 2])E + (-3E + 4E[t - 1] + E[t - 2])\rho) \\
&\quad + \frac{1}{2\Delta x_j} ((\rho[x_j - 1] - \rho[x_j + 1])E u_j + (E[x_j - 1] - E[x_j + 1])\rho u_j \\
&\quad + (u_j[x_j - 1] - u_j[x_j + 1])E \rho + (u_i[x_j - 1] - u_i[x_j + 1])\sigma_{ij} \\
&\quad + (\sigma_{ij}[x_j - 1] - \sigma_{ij}[x_j + 1])u_i + q_j[x_j - 1] - q_j[x_j + 1])
\end{aligned}$$

Then we multiply each value by the preconditioning matrix P, given by Liu's paper. Once those values have been calculated we need to calculate $\delta_m W_i$, which is associated to the variance for each component of the value vector. Those can be calculated using the following equations for $i=1,2,3$:

$$\frac{\bar{D}}{Dt} (\delta_m W_{i+1}) = -PF_{i+1}$$

$$\delta_m W_1 = -PF_1 - b \frac{\delta}{\delta x_1} \delta_m W_i$$

$$\frac{\bar{D}}{Dt} (\delta_m W_5) = \Delta t \left(-PF_5 - c \frac{\delta}{\delta x_2} \delta_m W_i \right)$$

Where b, c and e are values given by the paper written by Liu. All that's left is calculating $\delta_m p$, $\delta_m u_i$, and $\delta_m T$ using the following equations:

$$\left(\frac{1}{R} \frac{\bar{D}}{Dt} - b \Delta t \frac{\delta}{\delta x_i} e \frac{\delta}{\delta x_i} \right) \delta_m p = \delta_m W_1$$

$$\delta_m u_i = \delta_m W_{i+1} - e \Delta t \frac{\delta}{\delta x_i} \delta_m p$$

$$\delta_m T = \delta_m W_5 + c (\Delta t)^2 \frac{\delta}{\delta x_i} e \frac{\delta}{\delta x_i} \delta_m p$$

We now renew the variables in the program such that $p' = p + \delta_m p$, $u'_i = u_i + \delta_m u_i$ and $T' = T + \delta_m T$. Then we go back to the first step and repeat this process multiple times—the more times we run this process, the more accurate our value is. For this program I propose running this procedure 20 times, giving us a residual error of 10^{-2} . Once we have

calculated the values for pressure, velocity components and temperature for that particular data point, we move on to the next data point and continue this process until values for all data points have been found.

Future work and research

Since the general idea behind the program has been laid out, all that's necessary is coding the program, debugging it and running it once it's finished. Some pieces of code have already been written and defined, so it's not necessary to write the entire program from scratch. Once the program is fully operational, we import the values from datastore to a graphing program, which can then be adapted into an animation of how the galaxy's structure changes over time. But most importantly, we can keep track of the feedback material and determine its effects on neighboring galaxies and the distribution of material in the filament.

References

- [1] Liu, Kunlun and Pletcher, Richard H. (2007). A Fractional-Step Method for Solving the Compressible Navier Stokes Equations. *Journal of Computational Physics* 226(0),1930—1951.
- [2] Schütz, J. and G, May (2012). A Hybrid Mixed Method for the Compressible Navier-Stokes Equations. *AICES-2012* 11(2).

Analysis of Schematic One-Level and Two-Level Nuclear Shell Models

Jason Saroni
2014 REU Program
Department of Physics, University of Notre Dame

Advisor:
Professor Mark Caprio

Analysis of schematic one-level and two-level nuclear shell models

August 1, 2014

Abstract

In the nuclear shell model, nuclei with several nucleons outside closed major shells have a prominent short-range residual interaction which can approximately be accounted for through pairing forces and deformation-inducing quadrupole forces. Here these forces are considered in a valence space of one and two shells. The calculated results are compared to test cases using the ArbModel code. The ultimate goal is to map out the competition between the pairing and quadrupole forces.

1 Introduction

Nuclei with several nucleons outside closed shells are called open shell nuclei. Most open shell nuclei are either deformed and rotational or spherical and superconducting. On the one hand, towards the middle of the open shell the nucleus becomes less spherical and more deformed which quadrupole forces can account for. On the other hand, short-range components of the residual interaction scatter nucleons out of their orbits in such a way that the interaction shows as pairing correlations between nucleons which pairing forces can account for. The one-level and two-level results from [1] will be considered along with the appropriate input to the ArbModel code for the pure pairing one-level case. Then results from [2] will be used to compare the pairing force to the quadrupole force for general j-level.

2 Evidence for pairing forces

If only a part of a j shell is occupied, the angular momenta of the nucleons may result in different total angular momenta depending on the coupling. The energy, however, does not depend on the coupling, because in the single-particle model it is simply given by the sum of the single-particle energies of the occupied states. Thus we get degeneracy of the various total angular momenta. Any lifting of this degeneracy is due to residual interactions. Pairing forces account for the short-range part of this residual interaction and they occur predominantly for zero angular momentum. Evidence for this is firstly given by the experimental observation that for even-even nuclei the ground state always has zero angular momentum because the residual interaction lowers this particular state with respect to the other angular-momentum combinations. Secondly even-even nuclei are bound more tightly than odd nuclei because all the nucleons can pair up. Thirdly in even-even nuclei there is an energy gap of 1-2 MeV between the ground state and the lowest single-particle excitation. To formulate the pairing interaction for nucleons in the same j shell coupled to zero angular momentum, we start from the following wave function without spin or antisymmetrization for simplicity

$$\begin{aligned}\Psi(r_1, r_2) &= \sum_{m_1 m_2} (j m_1 j m_2 | 00) \varphi_{m_1}(r_1) \varphi_{m_2}(r_2) \\ &= \frac{1}{\sqrt{2j+1}} \sum_m (-1)^{j-m} \psi_m(r_1) \psi_{-m}(r_2)\end{aligned}$$

This can be written in bra-ket formalism as

$$|j=0\rangle = \frac{1}{\sqrt{2j+1}} \sum_{m=-j}^j (-1)^{j-m} |jm\rangle |j-m\rangle$$

The second quantization operator creating the state is

$$\hat{A}^\dagger = \frac{1}{2} \sum_{m=-j}^j (-1)^{j-m} \hat{a}_m^\dagger \hat{a}_{-m}^\dagger$$

This is known as the pair creation operator. The pairing potential is tentatively constructed for the one level case

$$V_{PAIR} = -G \sum_{mm' > 0} c_{jm}^\dagger \tilde{c}_{jm}^\dagger \tilde{c}_{jm'} c_{jm'}$$

with $G > 0$ being the pairing strength. G is given by

$$G \doteq -2 \langle jj; 0 | V | jj; 0 \rangle \hat{j}^{-2}$$

The appropriate input Hamiltonian for the ArbModel is in spherical tensor operator notation, so the operator in this form is given by,

$$V_{RES} = -\frac{1}{2} \sum_J \hat{J} \langle jj; J | V | jj; J \rangle \left[\left[c_j^\dagger c_j^\dagger \right]_J \left[\tilde{c}_j \tilde{c}_j \right]_J \right]_{00}$$

For the one-level case, we consider 2 particles in the shell. The two particle basis is

$$A_{jm}^\dagger |0\rangle = c_{jm}^\dagger \tilde{c}_{jm}^\dagger |0\rangle, m > 0$$

The Hamiltonian matrix is

$$\begin{aligned} \langle 0 | A_{jm} V_{PAIR} A_{jm'}^\dagger | 0 \rangle &= -G \sum_{m_1 m_2 > 0} \langle 0 | \tilde{c}_{jm} c_{jm} \tilde{c}_{jm_1} \tilde{c}_{jm_1}^\dagger \tilde{c}_{jm_2} c_{jm_2} c_{jm'}^\dagger \tilde{c}_{jm'}^\dagger | 0 \rangle \\ &= -G \end{aligned}$$

By calculating the characteristic equation and setting it equal to zero, the matrix is diagonalized and the eigenvalues

$$E_1 = -\Omega G, E_i = 0 \quad i = 1, 2, 3, \dots$$

are obtained. A value v is assigned to represent the number of unpaired particles developing the seniority model with more general eigenvalues. It can be seen that the Hamiltonian is such that only zero angular momentum paired particles are at lower energy than they would otherwise be unpaired. The seniority model accounts for situations in which some nucleons are unpaired. The seniorities can be assigned to angular momentum eigenstates by comparing seniority degeneracies to angular momentum degeneracies.

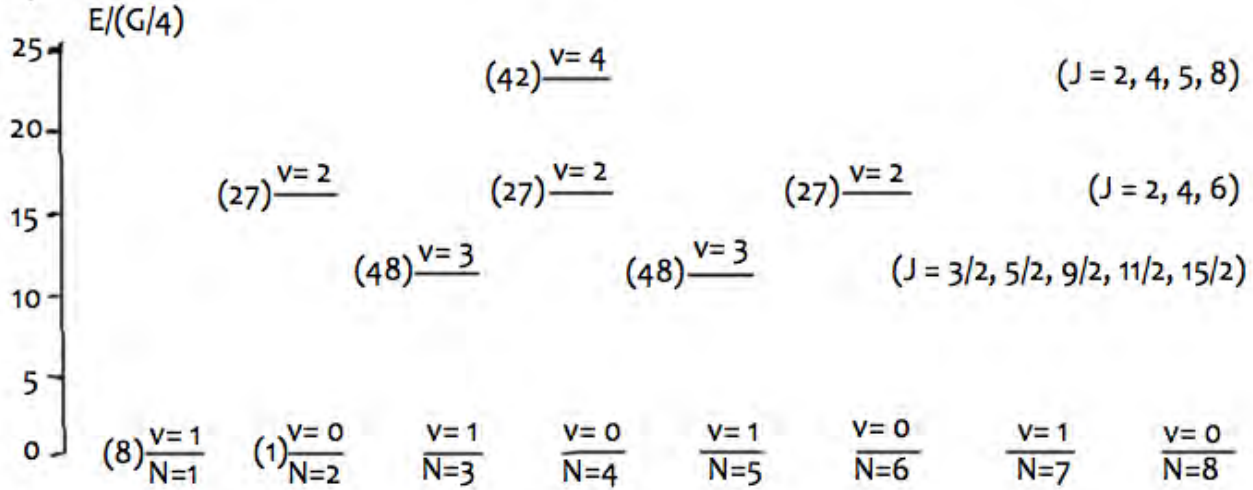


figure 1.

The energies in the diagram depend on whether N is even or odd and on the states realized as can be seen in experiments. This is because excitation energies differ depending on whether N is even or odd as the lowest seniority for the even case is 1 and the lowest seniority for the odd case is 0.

3 Two-level model

The two-level model is for seniority zero and valence space with two shells. The pair creation operator for the two level case can be written as

$$A_j^\dagger = \frac{1}{\sqrt{2}} [c_j^\dagger c_j^\dagger]_{00} = \frac{1}{\sqrt{\Omega_j}} \sum_{m>0} c_{jm}^\dagger \tilde{c}_{jm}^\dagger$$

where j represents j1 and j2

The number operators are

$$\hat{n}_j = \sum_m c_{jm}^\dagger c_{jm} = \sum_{m>0} (c_{jm}^\dagger c_{jm} + \tilde{c}_{jm}^\dagger \tilde{c}_{jm})$$

and in spherical tensor operator form which is the preferred format of the ArbModel they are

$$\hat{n}_j = -\hat{j}_j (c_j^\dagger \times \tilde{c}_j)_0^0$$

If n is the number of pairs in j_1 and m is the number of pairs in j_2 , then the normalized two-level basis is

$$|nm\rangle = \frac{1}{\sqrt{[n]_{j_1}! [m]_{j_2}!}} \left(A_{j_1}^\dagger\right)^n \left(A_{j_2}^\dagger\right)^m |0\rangle$$

The Hamiltonian is then

$$H_{PAIR} = \varepsilon_{j_1} \hat{n}_{j_1} + \varepsilon_{j_2} \hat{n}_{j_2} - G \sum_{jj'} \sqrt{\Omega_j \Omega_{j'}} A_j^\dagger A_{j'}$$

The matrix elements are

$$\begin{aligned} & \langle nN - n | H_{PAIR} | n'N - n' \rangle \\ &= -G \delta_{n', n+1} \sqrt{(n+1)(\Omega_{j_1} - n)(N - n)(\Omega_{j_2} - N + n + 1)} \end{aligned}$$

where

$$N = n + m$$

Considering two particles in this two-level scheme, Hamiltonian matrix elements are

$$\begin{aligned} & \langle 10 | H_{PAIR} | 10 \rangle \\ & \langle 10 | H_{PAIR} | 01 \rangle \\ & \langle 01 | H_{PAIR} | 10 \rangle \\ & \langle 01 | H_{PAIR} | 01 \rangle \end{aligned}$$

Defining g and diagonalizing gives the eigenvalues which can be written using symmetric shell energies as

$$E_{\mp} = -g \mp \sqrt{\varepsilon^2 + g^2}$$

where $\varepsilon_{j_1} = -\frac{1}{2}\varepsilon$ and $\varepsilon_{j_2} = +\frac{1}{2}\varepsilon$

4 Competition between pairing and quadrupole forces

This section is based on results from [2]. Evidence for deformed nuclei by quadrupole forces is given by rotation bands similar to those of diatomic molecules. The competition can be mapped out by considering a Hamiltonian of the form

$$H = \alpha H_1 + (1 - \alpha) H_2$$

Where H_1 is the Hamiltonian for rotational motion given by

$$H_{RM} = \frac{1}{2m} \sum_n^A p_n^2 + \frac{1}{2} m \omega^2 \sum_n^A r_n^2 + V(Q)$$

and H_2 is the pairing Hamiltonian for general j -level

$$H_{SC} = \sum \varepsilon_j a_{jm}^\dagger a_{jm} - \sum G_{jj'} a_{jm}^\dagger a_{j\bar{m}}^\dagger a_{j'\bar{m}'} a_{j'm'}$$

Dynamical symmetries of the rotational and spherical phase are incompatible meaning that it is not possible to diagonalize the linear combination of the Hamiltonians. The rotational phase can be simplified using quadrupole tensor operators to get

$$H_1 = -\chi Q \cdot Q$$

with spectrum

$$E(\lambda\mu J) = -\chi C_2(\lambda\mu) + 3\chi J(J+1)$$

Putting all single particle energies equal the spherical phase can be simplified to

$$H_2 = -GS_+S_-$$

where

$$S_+ = \sum_{jm>0} (-1)^{j+m} a_{jm}^\dagger a_{j-m}^\dagger$$

$$S_- = \sum_{jm>0} (-1)^{j+m} a_{j-m}^\dagger a_{jm}^\dagger$$

which has a Hamiltonian spectrum given by

$$E(N, s) = -Gs(s + 1) + \frac{1}{4}G(N - 2s)(N - 2s - 2)$$

Here N is the number of particles and s the seniority. In this form, the dynamical symmetries are now compatible and the spectrum is given by

$$E_j(\alpha) = E_j(0) + \alpha[G \langle S_+ S_- \rangle_0 - 4\chi \langle C_2 \rangle_0 + 3\chi J(J + 1)]$$

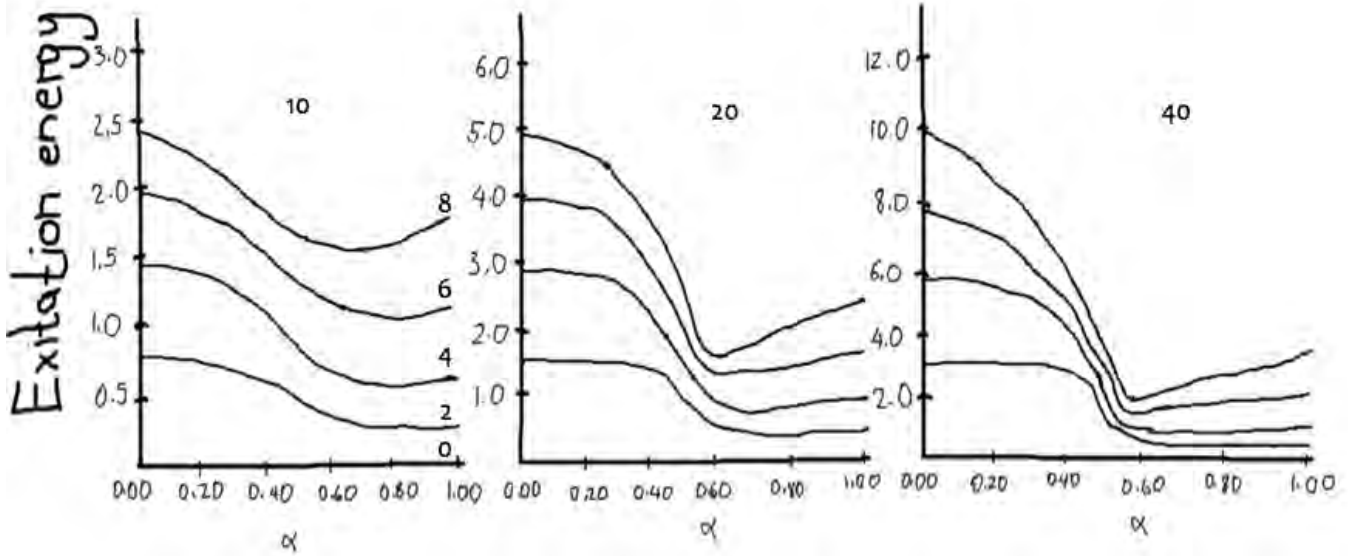


figure 2.

10, 20 and 40 are the total number of particles and 2, 4, 6, 8 the total angular momentum states.

5 Conclusion

For the one-level pairing force, there is only one non-trivial eigenvalue corresponding to the lowering energy by the pairing force for the $J=0$ state. The two-level pairing force, there are two eigenvalues representing the lowering of energy in each level symmetrically. By considering the excitation energies graph with α going from 0 to 1 for the general level in mapping out the competition between the pairing and quadrupole force, we see that the

pairing force creates more energy separation between angular momentum states than the quadrupole force for spins close to zero. This shows that pairing forces lower energy more than quadrupole forces around $J=0$.

6 References

- [1] Suhonen, Jouni. From Nucleons to Nucleus. : Springer, 2007. Print.
- [2] Rowe, David. "Exactly Solvable Model of a Superconducting to Rotational Phase Transition." Physical Review Letters 80: n. pag. Print.
- [3] Caprio, Mark. "Dual algebraic structures for the two-level pairing model." Journal of Physics A: Mathematical and Theoretical: n. pag. Print.
- [4] Bohr, Aage. "Rotational motion in nuclei." 48: n. pag. Print.

Implementation of OpenACC for GPU Acceleration Of Astrophysical Fluid Dynamics Code

Ethan Sauer
2014 REU Program
Department of Physics, University of Notre Dame

Advisor:
Professor Dinshaw Balsara

Abstract:

Computational schemes which provide numerical solutions to partial differential equations have myriad uses in the realm of physics and beyond, from electrodynamics to analytical finance. One of the primary limitations of high-resolution schemes is the speed and efficiency with which the model can be executed. This project sought to explore the use of a Graphics Processing Unit (GPU) to accelerate code which models three-dimensional hydrodynamic shocks. The primary advantage of utilizing a GPU over the more traditional CPU for compute-intensive numerical simulations is the presence of a much larger number of cores. In this case, the GPU used was the NVIDIA Titan Black, which contains 2880 cores. The code used was previously written by Prof. Balsara in Fortran and the acceleration directives were in OpenACC, a recently developed language for expressing high-level parallelism. This implementation intends to demonstrate the potential of GPU acceleration as a viable alternative to more costly multi-CPU systems.

Introduction:

Recently, GPUs have increasingly been used for supercomputing applications, perhaps most notably at the Titan supercomputer at Oak Ridge National Laboratory, which added 18,688 Nvidia Tesla GPUs to create a hybrid CPU and GPU system which has achieved 17.59 petaFLOPS (10^{15} Floating-point Operations Per Second) [1]. The potential of using GPUs for scientific computing, especially because of their relatively low cost and high computational yield, has made them an area of growing interest. This project began with preliminary investigations into the effectiveness of OpenACC in parallelizing simple iterative code, such as a two-dimensional solver for Laplace's Equation, and then moved on to the RIEMANN code written by Professor Dinshaw Balsara. The RIEMANN code is a one to three-dimensional hydrodynamic simulation which is second order accurate. It is capable of using two different

methods of spatial interpolation and limiting, either Total Variation Diminishing (TVD) or Weighted Essentially Non-Oscillatory (WENO). TVD was initially proposed by Bram van Leer in his 1979 paper, “Towards the Ultimate Conservative Difference Scheme. V. A Second-Order Sequel to Godunov’s Method” [2] and essentially means that at a given point of a numerical scheme, if:

$$\textit{Total Variation} = \sum_j |u_{j+1} - u_j|$$

Where “u” is the equation which is being solved for, then the next step of the method should have a total variation that is less than or equal to that of the previous step. WENO methods involve using a combination of possible polynomials for interpolation, instead of choosing what is determined to be the best single polynomial, and are stable and non-oscillatory, making them particularly suited to dealing with strong shocks and other discontinuities. The first WENO method was presented in a 1994 paper by Liu, Osher, and Chan [3]. The RIEMANN code as a whole operates according to a predictor-corrector method, in which an initial prediction is refined in a second corrector stage. The results are then used to build fluxes and evaluate the time step in the simulation before moving on to the next iteration. At given intervals, image files of the simulation are written out.

Initial Exploration:

In order to test the viability of using OpenACC to accomplish GPU parallelism, several test programs were parallelized. The most notable test was a simple Laplace Equation solver which made use of a Jacobi iteration method over a fairly large mesh of points. The Laplace Equation in two dimensions can be expressed as:

$$\Delta u = \frac{\partial^2 u}{\partial x^2} + \frac{\partial^2 u}{\partial y^2} = 0 \quad [4]$$

In order to solve for this equation, the Jacobi iterative technique is used, which constructs a second-order estimate for a given point on the point mesh using its neighboring values:

$$u_{new}(i, j) = 0.25 * (u(i+1, j) + u(i-1, j) + u(i, j-1) + u(i, j+1))_{[5]}$$

This estimate is then iterated over in two dimensions (the “i” and “j” indices) until the mesh is complete. In order to parallelize this code, the two iterative loops needed to be parallelized across the various GPU cores. This was initially accomplished using the OpenACC “kernels” directive, which simply tells the compiler to attempt to automatically generate code for the GPU for the given region. Though this did parallelize the section of code, large amounts of data were being copied over to and from the GPU when they did not need to be, which took a significant toll on the performance of the code. Data transfers between the CPU side of the computer and the GPU side are highly costly to performance primarily because of the bottleneck of the connection between the two, so eliminating nonessential data movement was a clear next step.

The reduction of the data transferred was accomplished using OpenACC “data regions”: section of code which are executed on the GPU and for which certain data transfer rules have been specified. The general implementation of the data region programming was as follows:

```
!$ACC DATA COPY(A), CREATE(Anew), COPYOUT(B)
!$ACC KERNELS
  do j=1,m-2
    do i=1,n-2
      Anew(i,j) = 0.25_fp_kind * ( A(i+1,j ) + A(i-1,j ) + &
                                A(i ,j-1) + A(i ,j+1) )
      error = max( error, abs(Anew(i,j)-A(i,j)) )
      if (i .gt. x1 .and. i .lt. x2 .and. i .gt. y1 .and. i .lt.y2) then
        B(i,j)=Anew(i,j)
        A(i,j)=Anew(i,j)
      endif
    end do
  end do
!$ACC END KERNELS
!$ACC END DATA
```

In this instance, the two-dimensional array A was copied both in and out of the GPU in the data region, Anew was created on the GPU and left there, and B was only brought out of the data region (B was a test array for only bringing subsections of the arrays back.) The use of data regions was highly beneficial to the performance of the code, as seen in the timing results below. OpenMP, a language for CPU parallelism analogous to OpenACC, was used for multi-core comparison:

	2048x2048	4096x4096
1 CPU Core	64.55	243.07
2 CPU Cores	32.87	122.63
4 CPU Cores	23.05	85.01
8 CPU Cores	25.37	80.86
GPU	1.42	4.76

In this table, the runtimes (in seconds) of the program for two different mesh sizes reveal the significant performance gap between the 2880 cores of the Nvidia Titan Black GPU and the 8 cores of the AMD FX-8350 CPU. These promising results encouraged the step attempting to accelerate the much more complex hydrodynamic code written by Prof. Balsara.

Hydrodynamic Code Implementation:

The first part of the code to be targeted for parallelization was a computationally heavy subroutine named `make_ader_updt_euler`, which constructs the ADER (Arbitrary DERivative in space and time) update for the simulation in one step for the hyperbolic partial differential equations which characterize the system (Balsara et al, 2010) [6]. The same type of implementation as in the Laplace solver was used, with some adjustments for the new code. The new code can be outlined as:

```

SUBROUTINE MAKE_ADER_UPDT_EULER (Arguments)
....
Initialize variables
....
!$ACC DATA COPYIN (In variables), COPY (In and out variables)
....
For x-fluxes:
!$ACC KERNELS LOOP, PRIVATE (Private variables)
DO izz = 1 - MIN0 ( 1, ioffz), iz1 + MIN0 ( 1, ioffz)
  DO iyy = 1 - MIN0 ( 1, ioffy), iy1 + MIN0 ( 1, ioffy)
!$ACC LOOP VECTOR
  DO ix = 0, ix1 + 1
    ....
    Computation code
  ....
  END DO
  END DO
END DO
!$ACC END KERNELS
....
Above repeated for y and z fluxes
....
!$ACC END DATA
RETURN
END SUBROUTINE MAKE_ADER_UPDT_EULER

```

The GPU parallelization of this subroutine was successful, but despite attempts to minimize data transfer required, the run time was only marginally reduced. Issues with the compiler that was being used for OpenACC began to crop up, which greatly slowed progress and was an indicator of the immaturity of the support for OpenACC, which was introduced in 2012. The root of the problems stemmed from the nested subroutine calls built into the code, which the compiler had difficulty processing correctly for the GPU. Since actual calls of subroutines are not supported in OpenACC 1.0, the initial approach was to instruct the compiler to inline (replace subroutine calls with the contents of the subroutine itself) automatically, but this proved difficult to execute successfully, as some of the compilation flags required caused errors not sufficiently documented to easily resolve. In an effort to get around these issues, the Notre Dame Center for Research

Computing was asked to update the compiler to the latest version, which included support for OpenACC 2.0 [7]. OpenACC 2.0 presented new possibilities for maintaining the call structure, as it supports the creation of GPU versions of subroutines and calling them in a manner similar to on the CPU. However, preliminary test programs failed to successfully make use of the new compiler's features, and some progress was made on the inlining approach, so that was pursued instead. After finding a configuration of statements and compiler instructions that was successful, the other four most computationally expensive subroutines were parallelized. These are listed below, along with the actual computation time recorded by the GPU (not counting times for data movement and additional assorted time costs):

Subroutine	GPU Time (s)	CPU Time (s)
limit_all_slopes_euler	0.0388	25.53
make_ader_updt_euler	0.0104	36.05
make_euler_flux_ptwise_x	0.0028	23.25
make_euler_flux_ptwise_y	0.0039	24.87
make_euler_flux_ptwise_z	0.0035	31.05

There is a clear and massive difference between the profiled computation times, though unfortunately the actual running time for the program was similar to that of the original code. This difference can be attributed to the multitude of times which large arrays had to be moved to and from the GPU and various inefficiencies in the data region scheduling.

Simulation Results:

Results yielded by the parallelized code match those produced by the original serially executed code, which verifies that the transition to GPU calculation has not had a negative effect on the

accuracy of the code’s simulation. An example of the expected results, taken from Balsara, Meyer, Dumbser, Du, and Xu’s “Efficient Implementation of ADER Schemes for Euler and Magnetohydrodynamical Flows on Structured Meshes -- Comparison with Runge-Kutta Methods” [6], is shown below, along with comparative images from the accelerated code: From left to right, the images depict blast density, pressure, and velocity magnitude.

Conclusions:

This project was a successful exploration into the potential of making use of a GPU for the calculation of a full, complex code. It imparted insights into both the power and limitations of

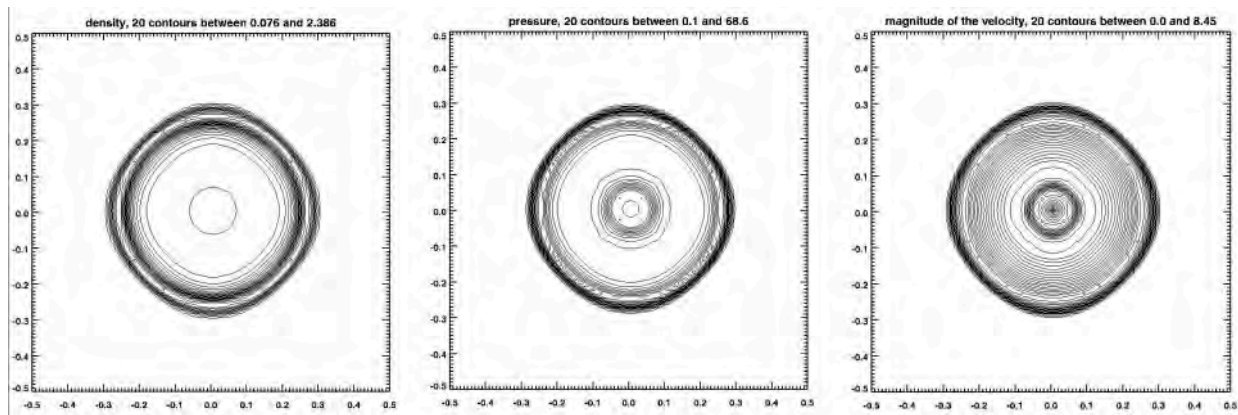
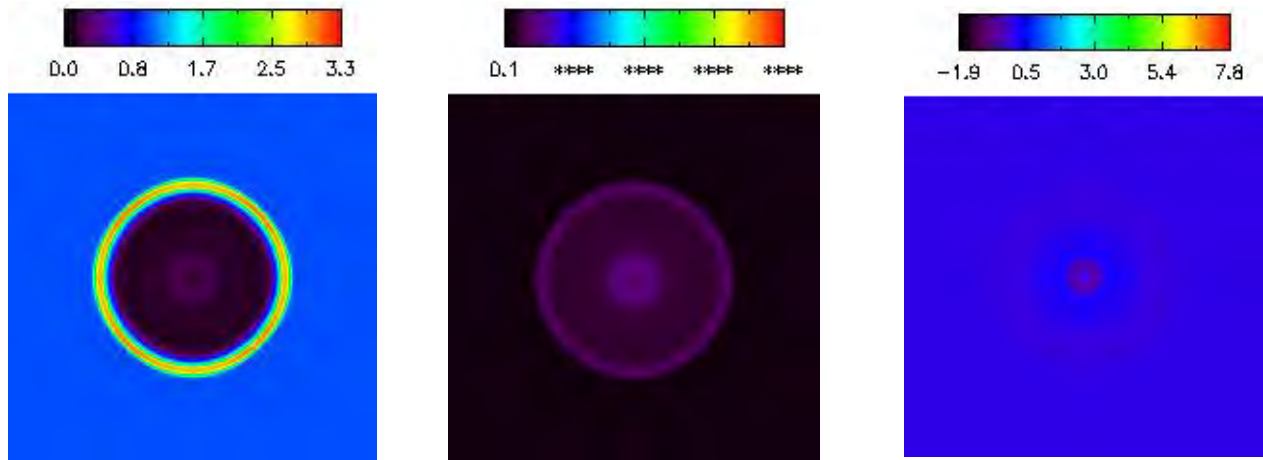


Fig. 5) Shows the density, pressure and magnitude of the velocity for the hydrodynamical blast wave problem run with an ADER-WENO scheme and linearized Riemann solver at fourth order. 20 contours were fit between the lowest and highest values shown on each figure.

OpenACC and GPU utilization; precise and complete parallelization can be hugely rewarding,



but reaching it can be made very challenging by the incomplete support and quirks which come along with OpenACC and its compilers being in something of a developmental stage. There is definite room for improvement and refining of the accelerated code, which is planned to continue. With the further progression of this project, OpenACC could still fully deliver on its promises of minuscule execution time and low-cost computational power.

Acknowledgements:

I would firstly like to thank Prof. Dinshaw Balsara for sharing his expertise, guidance, and (perhaps most crucially) patience during this project. Sudip Garain and Chad Meyer also provided valuable insights, along with Paul Brenner and Dodi Heryadi from the Center for Research Computing. Additional thanks are due to Prof. Umesh Garg and Susan Coyne for deftly running the REU program. Finally, I would like to thank my friends and family for their support and companionship over the summer.

References:

- [1] Oak Ridge National Laboratory, <https://www.olcf.ornl.gov/titan/>
- [2] Bram van Leer, “Towards the Ultimate Conservative Difference Scheme. V. A Second-Order Sequel to Godunov’s Method”, Journal of Computational Physics, July 1979
- [3] Xu-Dong Liu, Stanley Osher, Tony Chan, “Weighted Essentially Non-oscillatory Schemes”, Journal of Computational Physics, November 1994
- [4] Anthony Pierce, http://www.math.ubc.ca/~peirce/M257_316_2012_Lecture_24.pdf
- [5] Los Alamos, <http://www.nongnu.org/freepooma/tutorial/tut-01.html>
- [6] Dinshaw S. Balsara, Chad Meyer, Michael Dumbser, Huijing Du, Zhiliang Xu, “Efficient Implementation of ADER Schemes for Euler and Magnetohydrodynamical Flows on Structured Meshes -- Comparison with Runge-Kutta Methods”, Journal of Computational Physics, February 2013
- [7] OpenACC API, http://www.openacc.org/sites/default/files/213462%2010_OpenACC_API_QRG_HiRes.pdf

Coupling Algorithm for $\mathrm{Sp}(3, \mathbb{R})$ Irreducible Representations

James St. Germaine-Fuller

2014 NSF/REU Program

Physics Department, University of Notre Dame

Anna McCoy

Prof. Mark Caprio

Abstract

The nuclear symplectic model based on $\text{Sp}(3, \mathbb{R})$ – the smallest algebra that contains both the shell model Hamiltonian and the rotor algebra – connects the microscopic shell model to collective rotational behavior and naturally extends the Elliot $\text{SU}(3)$ model to multiple shells. However, $\text{Sp}(3, \mathbb{R})$ is only an approximate symmetry of the nucleus, where the symmetry can be broken by spin-orbit interactions, tensor force interactions, and pairing. The Hamiltonians in most physical situations will break $\text{Sp}(3, \mathbb{R})$ symmetry, causing their eigenstates to become linear combinations of symplectic irreducible representations (irreps). Calculations with those eigenstates will then involve multiple irreps. We report a computer algorithm for coupling symplectic irreps that should assist in performing such multi-irrep calculations and facilitate computing symplectic coupling coefficients.

1 Introduction

The algebra of the symplectic group $\text{Sp}(3, \mathbb{R})$ is the simplest algebra that simultaneously contains two of the most significant nuclear models, namely, the shell model and the collective model [1, 2]. The shell model approximates the nuclear potential as a quadratic (harmonic oscillator) potential. The starting point for the shell model is to build states of the nucleus by placing nucleons in harmonic oscillator shells, similar to how electrons are placed into different orbitals in the atomic model. More generally, shell model states are linear combinations of such states. The nuclear collective model looks at the nucleus as a whole, where, instead of particles carrying the degrees of freedom, the dynamical variable in the theory is the shape of the nucleus.

This report presents a computer algorithm for coupling $\text{Sp}(3, \mathbb{R})$ irreducible representations (irreps). More specifically, the result of coupling two $\text{Sp}(3, \mathbb{R})$ irreps may be any one of several product irreps. We list the irreps in that set. This is known as decomposing the Kronecker product of two irreps [3]. Just as $\text{SO}(3)$ coupling plays an important role in many quantum-mechanical calculations involving angular momentum, the coupling algorithm for $\text{Sp}(3, \mathbb{R})$ should facilitate many symplectic calculations, especially those involving several irreps.

2 U(3) coupling

Sp(3,ℝ) coupling will be done using the algebra chain Sp(3,ℝ) ⊃ U(3) ∼ U(1) × SU(3). Hence, we need to cover U(3) coupling. U(3) irrep labels can be written in two equivalent forms: “Cartesian form” $[\sigma_1\sigma_2\sigma_3]$ and “Elliott form” $N(\lambda\mu)$. The physical meaning of Cartesian form is that σ_1 , σ_2 , and σ_3 count the number of quanta of excitations in the x , y , and z directions respectively, specifically, $\sigma_i = n_i + A/2$, where n_i is the number of excitations in the i th direction and A is the total number of nucleons. Valid U(3) quantum numbers have

$$\sigma_1 \geq \sigma_2 \geq \sigma_3 \geq 0. \quad (1)$$

Since U(3) is isomorphic to U(1)×SU(3), we can break the U(3) label into a U(1) label N and an SU(3) label $(\lambda\mu)$. The Elliot $N(\lambda\mu)$ form is more useful for doing the actual coupling. Cartesian and Elliot form labels are related through

$$N = \sigma_1 + \sigma_2 + \sigma_3 \quad (2)$$

$$\lambda = \sigma_1 - \sigma_2 \quad (3)$$

$$\mu = \sigma_2 - \sigma_3. \quad (4)$$

Before giving the U(3) coupling rules, we briefly review SO(3) coupling. An SO(3) state $|jm\rangle$ has total angular momentum j where $m = -j, -j + 1, \dots, j$ is the projection of the angular momentum onto the z -axis. Coupling two total angular momenta $|j_1\rangle$ and $|j_2\rangle$ from two different spaces could result in the following total angular momenta $|j\rangle$:

$$|j_1\rangle \times |j_2\rangle = \bigoplus_{|j_1-j_2| \leq j \leq j_1+j_2} |j\rangle. \quad (5)$$

For the SO(3) algebra see [4, 5, 6].

Suppose $N_1(\lambda_1\mu_1)$ couples to $N_2(\lambda_2\mu_2)$ to give $N(\lambda\mu)$. The U(1) part of the coupling is

simply

$$N = N_1 + N_2. \quad (6)$$

The SU(3) part of the coupling is given by [7]

$$\begin{aligned} (\lambda\mu) &= (\lambda_1\mu_1) \times (\lambda_2\mu_2) \\ &= \bigoplus_{\substack{0 \leq k \leq \min(\mu_2, \lambda_1 + \mu_1) \\ 0 \leq j \leq \min(\mu_1, \lambda_2, \lambda_1 + \mu_1 - k) \\ \max(0, j - \mu_1 + k) \leq i \leq \min(\lambda_2 - j + k, \lambda_1)}} (\lambda_1 + \lambda_2 - j - 2i + k, \mu_1 + \mu_2 + i - j - 2k) \end{aligned} \quad (7)$$

3 Enumerating the states in an Sp(3,ℝ) irrep

The Sp(3,ℝ) operators can be written in terms of the harmonic oscillator raising and lowering operators b_{si}^\dagger and b_{si} that increase or decrease, respectively, the number of excitations of the s th nucleon in the i th direction. The raising and lowering operators satisfy the commutation relations $[b_{si}, b_{tj}^\dagger] = \delta_{st}\delta_{ij}$. In terms of these raising and lowering operators, the symplectic operators are

$$A_{ij} = \sum_{s=1}^{A-1} b_{si}^\dagger b_{sj}^\dagger \quad (8)$$

$$B_{ij} = \sum_{s=1}^{A-1} b_{si} b_{sj} \quad (9)$$

$$C_{ij} = \frac{1}{2} \sum_{s=1}^{A-1} (b_{si}^\dagger b_{sj} + b_{sj} b_{si}^\dagger) \quad (10)$$

where the A_{ij} are Sp(3,ℝ) raising operators, the B_{ij} are Sp(3,ℝ) lowering operators, the C_{ij} are the U(3) operators, and A is the total number of nucleons [1]. The raising and lowering operators (A_{ij} and B_{ij}) add and subtract, respectively, two oscillator quanta from the states they act on. Additionally, the raising and lowering operators connect states of the same N in an irrep.

$\text{Sp}(3, \mathbb{R})$ irreps are labeled by a $\text{U}(3)$ label σ . The states in such a symplectic irrep are $|\sigma n \omega \rho \alpha\rangle$ where σ, n, ω are $\text{U}(3)$ labels, ρ is an integer, and α , which we will often omit, is an extra set of quantum numbers needed to fully specify states within the $\text{U}(3)$ irrep ω . Here σ signifies that the state belongs to the σ irrep, n is the label of a “raising polynomial” which will be explained shortly, ω is a member of the $\text{U}(3)$ product $\sigma \times n$, and $1 \leq \rho \leq M$ where M is the outer multiplicity of ω , i.e., M is the multiplicity of ω in the product $\sigma \times n$.

The bandhead is defined as the state annihilated by the lowering operator, that is, $|\sigma n \omega \rho\rangle$ is a bandhead if $B_{ij}|\sigma n \omega \rho\rangle = 0$. The bandhead of the σ irrep is $|\sigma, 0(00), \sigma, 1\rangle$. Since the lowering operator annihilates the bandhead, all other states in the σ irrep are obtained by repeatedly raising the bandhead. The raising operator A is a $\text{U}(3)$ tensor operator that carries $\text{U}(3)$ label $2(20)$. Raising the bandhead one time produces the states

$$A^{2(20)}|\sigma, 0(00), \sigma, 1\rangle = |\sigma, 2(20) \times 0(00), 2(20) \times \sigma, \rho\rangle = |\sigma, 2(20), 2(20) \times \sigma, \rho\rangle \quad (11)$$

where ρ is the multiplicity of $2(20) \times \sigma$ and we have used the fact that $u \times 0(00) = u$ for any $\text{U}(3)$ number u . The RHS of (11) describes a set of states because multiple $\text{U}(3)$ numbers result from the coupling $2(20) \times \sigma$. Raising the bandhead multiple times is done using

$$A^{2(20)}A^{2(20)}\dots A^{2(20)}|\sigma, 0(00), \sigma, 1\rangle = (AA\dots A)^n |\sigma, 0(00), \sigma, 1\rangle = |\sigma, n, n \times \sigma, \rho\rangle \quad (12)$$

where n runs over the $\text{U}(3)$ labels that the A 's can couple to. In particular, $n = [n_1, n_2, n_3]$ is a member of the product $2(20) \times 2(20)\dots 2(20)$ with $n_i \in 2\mathbb{Z}$. Since the raising operator A physically represents adding two oscillator quanta to the shell model configuration in question, $AA\dots A$ should represent adding an even number of oscillator quanta and this is why we require the n_i to be even. Additionally, for $n = N(\lambda\mu)$ we call N the order of the raising polynomial label. Repeated application of the $\text{U}(1)$ coupling rule (6) shows that $N = 2N_A$ where N_A is the number of A 's appearing in the product in (12). In essence, raising a bandhead comes down to calculating the raising polynomials n and then doing the

coupling $n \times \sigma$.

Rather than performing the multitude of $U(3)$ couplings in $2(20) \times 2(20) \dots 2(20)$ and then restricting n to be one of the results of the coupling with even Cartesian coefficients, there is a shortcut for producing the labels for the raising polynomials. The raising polynomial labels must certainly satisfy $n_1 \geq n_2 \geq n_3 \geq 0$ because n must be a valid $U(3)$ number and furthermore the n_i 's must be even because n is the raising polynomial label of a bosonic raising operator. In other words, the set P_N of raising polynomial labels of order N is a subset of

$$S_N = \{[n_1, n_2, n_3] | n_i \in 2\mathbb{Z} \text{ and } n_1 \geq n_2 \geq n_3 \geq 0 \text{ and } n_1 + n_2 + n_3 = N\}. \quad (13)$$

We make the stronger claim that $P_N = S_N$. Physically, we expect that we should be able to add oscillator quanta however we desire without any restrictions except that we add an even number of quanta. S_N is the set of raising polynomial labels with precisely these properties. In short, to raise a bandhead, S_N must be calculated and then applied to (12).

There is an additional complication for irreps with $\sigma_3 < 3$. For these irreps, the branching rule in (12) produces excess states. The procedure required to eliminate the extraneous states is given in [8]. In this report we will only deal with irreps with $\sigma_3 \geq 3$.

Finally, we slightly extend how we notate states. In the next section, we will encounter situations where there are multiple bandheads with the same $U(3)$ labels. If we have k bandheads with the same $U(3)$ labels, then we will write the bandheads as $|\beta, \sigma, 0(00), \sigma, 1\rangle$ where $\beta = 1, 2, \dots, k$. The states produced by raising these bandheads will be written as $|\beta\sigma n\omega\rangle$.

4 Description of the coupling routine

In this section we describe the $Sp(3, \mathbb{R})$ coupling algorithm. The algorithm lists the $Sp(3, \mathbb{R})$ irreps $\sigma_{f1}, \sigma_{f2}, \dots$ produced by coupling σ_1 to σ_2 (see Figure 1 for a pictorial repre-

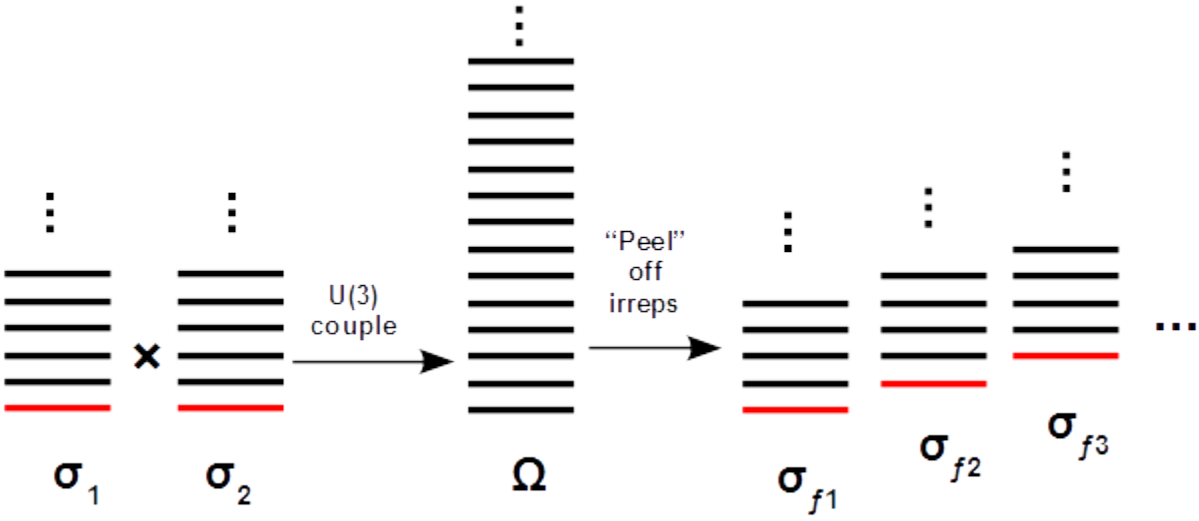


Figure 1: This diagram shows the process behind the $\text{Sp}(3, \mathbb{R})$ coupling algorithm. The symplectic irreps σ_1 and σ_2 couple to produce $\sigma_{f1}, \sigma_{f2}, \dots$. Bandheads are shown in red and the states obtained by raising those bandheads are shown in black. The algorithm constructs Ω by taking the ω 's appearing in the states $|\sigma_1 n \omega \rho\rangle$ and U(3) coupling them to the ω 's in the states $|\sigma_2 n \omega \rho\rangle$. The final irreps $\sigma_{f1}, \sigma_{f2}, \dots$ are obtained by peeling procedure described in the text.

sentation of the coupling routine). The algorithm does this coupling at the ω level, that is, σ_1 is $\text{Sp}(3, \mathbb{R})$ -coupled to σ_2 by U(3)-coupling the ω 's of the states in the σ_1 and σ_2 irreps. The algorithm begins by enumerating the states in the σ_1 bandhead and placing them in a list which we will call $\{|\sigma_1 n \omega \rho\rangle\}$ (the bandhead is shown in red in the figure and the states obtained by raising the bandhead are shown in black above the bandhead). Of course it is computationally impossible to list all states in $\{|\sigma_1 n \omega \rho\rangle\}$ because there are infinitely many raising polynomials. Thus the algorithm only lists the states in $\{|\sigma_1 n \omega \rho\rangle\}$ with raising polynomial order less than some cutoff N_{\max} .

We compile a list called Ω_1 of all the ω 's (and their multiplicities) appearing in $\{|\sigma_1 n \omega \rho\rangle\}$. Similarly, Ω_2 contains all the ω 's that come from the states in the σ_2 irrep up to raising polynomial order N_{\max} . Although infinitely many irreps $\sigma_{f1}, \sigma_{f2}, \dots$ result from coupling σ_1 and σ_2 , N_{\max} indirectly limits the number of final states actually calculated. (Specifically, the algorithm produces all final irreps σ_{fi} with $N_{\sigma_{fi}} \leq N_{\sigma_1} + N_{\sigma_2} + N_{\max}$). Every ω in Ω_1 is U(3) coupled to every ω in Ω_2 and the resulting U(3) states, along with their multiplicities,

are placed in Ω .

Now Ω has to be decomposed into $\text{Sp}(3, \mathbb{R})$ irreps. This is accomplished by the following “peeling” process [3, 9]. This peeling process is based on the idea that Ω should be the same as the collection of all the ω ’s belonging to all the states in all the final irreps $(\sigma_{f1}, \sigma_{f2} \dots)$. We will number the remaining steps in the algorithm for clarity.

1. **Obtain ω_0 :** Let $\omega_0 = N_0(\lambda_0 \mu_0)$ be the $\text{U}(3)$ label in Ω with the smallest N_0 . There may be multiple ω ’s with the same smallest N_0 in which case we may consider any one of these.
2. **ω_0 is a final irrep:** We claim that ω_0 is in fact the $\text{U}(3)$ label of one of the final irreps. We know ω_0 must be some state $|\beta \sigma n \omega_0 \rho\rangle$. If $|\beta \sigma n \omega_0 \rho\rangle$ is not a bandhead, it must be obtained from raising a bandhead of lower N . However, we chose ω_0 to have the lowest N so $|\beta \sigma n \omega_0 \rho\rangle$ must be a bandhead. In particular, $\sigma_{f1} = \omega_0$. Furthermore, ω_0 appears β times in Ω so σ_{f1} will appear β times in the symplectic product $\sigma_1 \times \sigma_2$.
3. **Remove ω ’s from Ω :** Since ω_0 is in the set Ω , Ω must also contain all ω ’s in $|\beta \omega_0 n \omega \rho\rangle$ that come from raising the ω_0 bandhead. Removing all such ω ’s from Ω produces the new Ω .
4. **Repeat:** Repeating steps 1 through 3 with this new Ω yields σ_{f2} . Repeating steps 1 through 3 until Ω is empty produces all the final irreps $\sigma_{f1}, \sigma_{f2} \dots$

The part of the coupling algorithm described in steps 1 through 4 is called a “peeling” process because we repeatedly remove subsets of Ω from Ω .

5 Checking the coupling algorithm

To verify the algorithm was working properly, we checked it against the $\text{U}(3)$ shell model configurations of the carbon-12 (^{12}C) nucleus which is made of 6 neutrons and 6 protons.

	13(0,2):1		14(0,1):2		14(1,2):1	
13(0,2):1	26 (0,4):1	26 (1,2):1	27(0,3):2	27 (1,1):2	27 (0,3):1	27(1,1):1
	26 (2,0):1	28 (0,2):3	29 (0,1):4	29(1,2):4	27(1,4):1	27(2,2):1
14(0,1):2	27(0,3):2	27 (1,1):2	28 (0,2):4	28(1,0):4	28 (0,2):2	28(1,3):2
	29 (0,1):4	29(1,2):4	30(0,0):4	30(1,1):8	28(2,1):2	30(0,0):2
14(1,2):1	27 (0,3):1	27(1,1):1	28 (0,2):2	28(1,3):2	28(0,2):1	28(0,5):1
	27(1,4):1	27(2,2):1	28(2,1):2	30(0,0):2	28(1,0):1	28(1,3):2

Table 1: The first three 6-proton irreps from $\{\sigma_p\}$ are shown along the top (columns) of the table with the first three 6-neutron irreps from $\{\sigma_n\}$ shown along side (rows). Irreps are notated as $N(\lambda, \mu)$:multiplicity. The entries in the table show the first four irreps produced by coupling the irrep in the column to the irrep in the row. For example, the entry under column 13(0,2):1 and in row 14(1,2):1 shows the first four irreps in $13(0, 2) : 1 \times 14(1, 2) : 1$.

The $U(3)$ irreps representing ^{12}C were obtained using the computer code LSU3shell [10]. From the $U(3)$ irreps, we extracted the set $\{\sigma_C\}$ of $\text{Sp}(3, \mathbb{R})$ irreps. Similarly, the set of symplectic irreps $\{\sigma_p\}$ for a 6-proton nucleus and the set of symplectic irreps $\{\sigma_n\}$ for a 6-neutron nucleus were obtained from the $U(3)$ irreps produced by [10] for the 6-proton nucleus and the 6-neutron nucleus. If the coupling algorithm is working properly, then combining a 6-proton nucleus with a 6-neutron nucleus should produce the ^{12}C nucleus. (Note that $\{\sigma_n\}$ and $\{\sigma_p\}$ actually contain the same irreps.) Each irrep in $\{\sigma_p\}$ was coupled to each irrep in $\{\sigma_n\}$ using the symplectic coupling algorithm described in the previous section. The set of irreps produced by this coupling matched $\{\sigma_C\}$, indicating that symplectic coupling was performed correctly.

Table 1 shows a few of the irreps produced by coupling $\{\sigma_n\}$ to $\{\sigma_p\}$, where irreps in the table are notated as $N(\lambda, \mu)$:multiplicity. The table shows the first three irreps in $\{\sigma_n\}$ and $\{\sigma_p\}$ and, for each σ_1 in $\{\sigma_n\}$ and each σ_2 in $\{\sigma_p\}$, the table shows the first four irreps in $\sigma_1 \times \sigma_2$. To expand on the limited number of irreps from $\sigma_1 \times \sigma_2$ shown in Table 1, we include the first 16 irreps from $13(0, 2) : 1 \times 14(0, 1) : 2$ in Table 2. Although neither of the tables show irreps $N(\lambda\mu)$ in $\sigma_1 \times \sigma_2$ with N higher than 31, comparison with $\{\sigma_C\}$ was carried out to $N = 34$.

To avoid unnecessary complications, we only considered configurations in $\{\sigma_p\}$, $\{\sigma_n\}$, and $\{\sigma_C\}$ with spin zero. Furthermore, we could have coupled other nuclei to obtain ^{12}C . For

27 (0,3):2	27 (1,1):2	29 (0,1):4	29 (1,2):4	29 (2,0):2	29 (2,3):2
29 (3,1):2	31 (0,2):2	31 (0,5):2	31 (1,0):4	31 (1,3):4	31 (2,1):8
31 (3,2):4	31 (4,0):2	31 (4,3):2	31 (5,1):2		

Table 2: This table shows the first 16 irreps produced by coupling $13(0,2):1$ with $14(0,1):2$. These first 16 irreps include all members $N(\lambda\mu)$ of $13(0,2) : 1 \times 14(0,1) : 2$ with $N \leq 31$.

example, coupling the 5-proton 1-neutron nucleus to the 7-proton 11-neutron nucleus would also lead to ^{12}C . However, combining 5 protons with 7 protons (and similarly combining 1 neutron with 11 neutrons) requires knowledge of the Pauli principle that is not natively included in the symplectic coupling algorithm. For this reason we choose to couple a 6-neutron nucleus to a 6-proton nucleus.

6 Conclusion

In conclusion, this report examined the symplectic group $\text{Sp}(3, \mathbb{R})$. The algebra of $\text{Sp}(3, \mathbb{R})$ is of interest because it is the simplest algebra connecting the nuclear shell model and the collective model. The primary purpose of this report is to present an algorithm for coupling $\text{Sp}(3, \mathbb{R})$ irreps. The essence of the algorithm is captured in Figure 1. In order to couple the symplectic irreps σ_1 and σ_2 to obtain the set of final irreps $\sigma_{f1}, \sigma_{f2}, \dots$, the algorithm raises each of the σ_1 and σ_2 bandheads. The algorithm then $\text{U}(3)$ couples the ω_1 's from each state $|\sigma_1 n_1 \omega_1 \rho_1\rangle$ in the σ_1 irrep to the ω_2 's from each state $|\sigma_2 n_2 \omega_2 \rho_2\rangle$ in the σ_2 irrep. The set of ω 's obtained from the $\omega_1 \times \omega_2$ coupling can be peeled off to obtain the set of final irreps $\sigma_{f1}, \sigma_{f2}, \dots$. Finally, we checked the symplectic coupling routine against the $\text{U}(3)$ shell model configurations of ^{12}C .

References

- [1] D. J. Rowe, *Microscopic theory of the nuclear collective model*, Re. Prog. Phys. **48** (1985) 1419.
- [2] T. Dytrych, K. D. Sviratcheva, J. P. Draayer, C. Bahri and J. P. Vary, *Ab initio symplectic no-core shell model*, J. Phys. G: Nucl. Part. Phys. **35** (2008) 123101.
- [3] B. G. Wybourne, *Classical Groups for Physicists*, Wiley, New York, 1974.
- [4] J. Suhonen, *From Nucleons to Nucleus: Concepts of Microscopic Nuclear Theory*, Springer, New York, 2007.
- [5] R. Shankar, *Principles of Quantum Mechanics, 2nd Ed.*, Plenum Press, London, 2008.
- [6] J. J. Sakurai, *Modern Quantum Mechanics, 2nd Ed.*, Addison-Wesley, Boston, 2010.
- [7] M. F. O'Reilly, *A closed formula for the product of irreducible representations of $SU(3)$* , J. Mat. Phys. **23** (1982) 2022.
- [8] D. J. Rowe, B. G. Wybourne, and P. H. Butler, *Unitary representations, branching rules, and matrix elements for the non-compact symplectic groups*, J. Phys. A: Math. Gen. **18** (1985) 939.
- [9] M. A. Caprio, K. D. Sviratcheva, A. E. McCoy, *Racah's method for general subalgebra chains: Coupling coefficients of $SO(5)$ in canonical and physical bases*, J. Math. Phys. **51** (2010) 093518.
- [10] T. Dytrych, computer code LSU3shell, <http://www.sourceforge.net/projects/lsu3shell>.

Finding optimal parameters for use of position-sensitive ionization chamber

Daniel Votaw

2014 NSF/REU Program

Physics Department, University of Notre Dame

Advisor: Dr. Dan Bardayan

Abstract

This paper details work done in the development and testing of various components of what is to become an ionization chamber with two position-sensitive boards and a downstream scintillation counter. The ionization chamber is intended to be used for fast particle identification of high-current heavy ion beams. Work was supervised by Dr. Dan Bardayan and Dr. Patrick O'Malley of the Notre Dame Nuclear Science Laboratory (NSL). The design is loosely based on the design of another ionization chamber at Oak Ridge National Laboratory (ORNL).^[1] Optimal bias voltage and gas (P10) pressure for the electrodes were determined using a standard chamber and an α -source containing ^{148}Gd and ^{228}Th . A prototype for the 700 μin -diameter, gold-coated tungsten wire position-sensitive boards was built using a printed circuit board and 0.1 mm wire of the same kind.

1 Introduction

Ionization chambers are remarkably simple, yet effective particle detectors. As their name implies, they rely on the ionization of matter to detect particles. The basic components of an ionization chamber are electrodes used to apply an electric field and a chemically inert gas. When ionizing radiation passes through the inert gas, it ionizes the gas molecules. The free elec-

trons drift in an applied electric field be collected on the biased anodes and a signal can be read out. The amount of free charge produced gives information about the energy of the incident radiation. While ionization chambers may not have resolution as high as semiconductor detectors, they are much more durable, so they can handle much higher beam intensities, and they tend to have very high efficiencies.

2 Setup

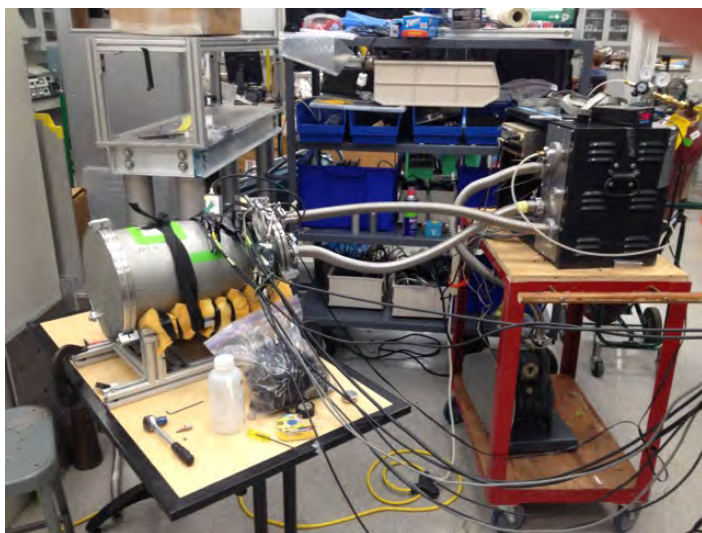


Figure 1: Picture of setup.

Our ionization chamber is a cylindrical tube, sealed from the ambient air by vacuum flanges, and filled with an array of wire grids. Towards the front of the cylinder we are developing two position-sensitive wire grids.

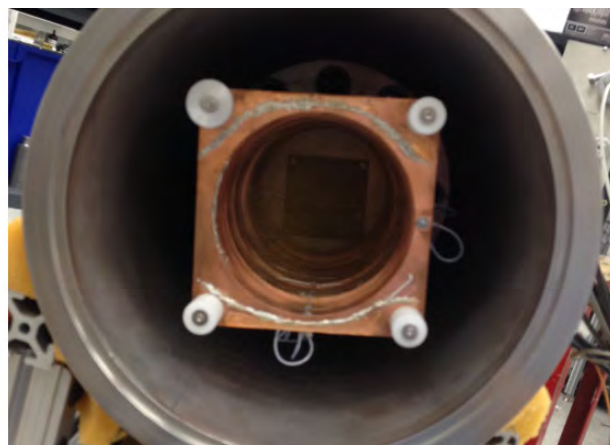


Figure 2: Electrodes inside cylindrical housing.

The wires are soldered into a printed circuit board, and each wire is individually read out via a pin, all of which connect to a ribbon cable. Just downstream from the position boards is a series of alternating wire grid elec-

trodes. They alternate between one cathode (grounded to the outside of the chamber), and one anode (positively biased by an exterior high voltage power supply). This is done to keep the field as uniform as possible throughout the active area. The electrodes will be tilted at 45° above the horizontal in order to reduce electron-ion recombination^[1], which would allow us to use the chamber at higher rates than the untilted grids would allow for. With untilted electrodes, free electrons and ions would tend to drift in the beamline, possibly recombining with other ions and electrons along the way, which can be a big problem for high-current beams. With tilted electrodes, the electric forces on the free charges have components perpendicular to the beamline, working to move them out of the way and reduce the chance of recombination.

While testing for the best pressure and voltage settings, the electrodes were placed in a cylindrical housing (the silver cylinder on the left of Figure 1) without the position boards or the scintillator. They were also oriented perpendicular to the "beam" (the beam was just an α -source, collimated with aluminum foil and taped to the inside of the front flange of the chamber). The cathodes were collectively connected to an external ground and each pair of anodes was connected to an external HV power source (three in total), effectively separating the chamber into three detection regions. The black box on the right side of Figure 1 is the gas handling system, which allows for slow pumping of the chamber and efficient circulation of the P10 gas into the chamber. The purity of the gas inside the chamber is of great importance, since the ionization of the gas is involved in the method of detection. A standard vacuum pump (the object on the bottom of the cart in the right side of Figure 1) was used to pump the air out of the chamber to a low vacuum (when the chamber is being used in experiment, it will be pumped down to the milliTorr range), and then pump in P10 gas from an external canister (the red tank in the top right corner of Figure 1). P10 is a gaseous mixture of 90% argon and 10% methane used in ionization chambers. Argon is used for its high specific ionization energy, but it must be diluted to 90% by a quenching gas (methane in our case) to prevent discharge at high voltages.^[2] Methane was chosen over other quenching gases like isobutane since it's not as flammable. The drift velocity of free electrons in P10 is plotted as a function of field strength normalized by pressure in Figure 4. The pressure of the P10 gas and anode bias voltages were varied and data was recorded in order to find the best settings.

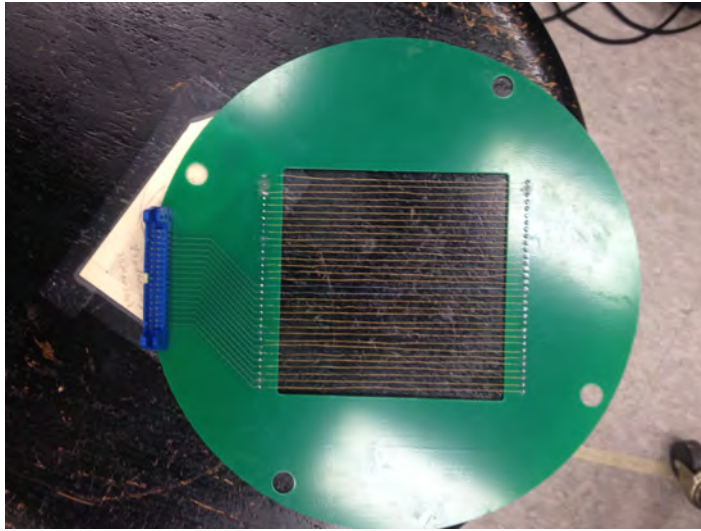


Figure 3: The position board prototype.

The signals from the anodes were taken out of the chamber through three high voltage feedthroughs. They were connected to pre-amplifiers, which then sent the signals to three Ortec amplifiers on a rack. The amplifiers sent the amplified and shaped signals to the analog-to-digital converter (ADC), and then to the data acquisition system (DAQ).

Once the optimal settings were determined, the prototype position board was made (Figure 3). The prototype was made with 0.1 mm-diameter gold-coated tungsten wire, but the real boards will be made with 700 μin (0.017 mm) diameter wire. On the prototype, the wire was threaded through the holes in the printed circuit

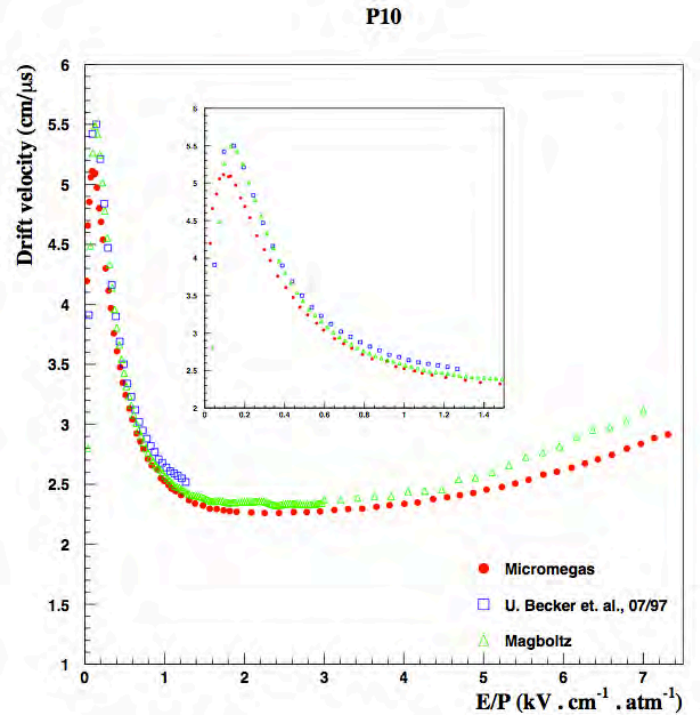
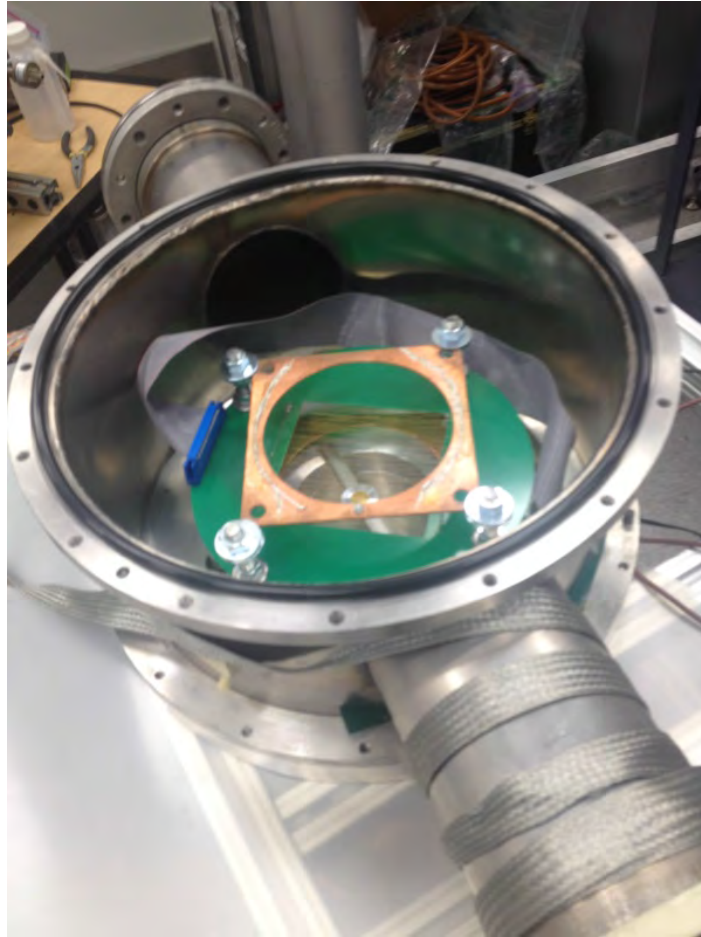


Figure 4: Electron drift velocity in P10 gas.^[3]

The ADC also had a logic signal fed into it that was true whenever one of the sets of anodes received a large enough signal. This was used as a strobe to trigger data collection. The data were recorded and analyzed in a data analysis program written at ORNL called DAMM.

board, soldered on one end, pulled taut, and then soldered on the other end. Careful measures were taken to make sure the tension stays relatively constant in each wire, as the resistivity of the wire is a function of its tension. When the real boards are made, the wires will be tensioned by a weighted bob to keep the tension in each

Figure 5: The setup used to test the position board.



the same as the others. It is very important to pull the wires as tight as possible, because any curves or kinks in the wire could distort the electric field in the active region of the chamber, affecting the signal that is read out.

The position board was tested in a different chamber (Figure 5). The board was supported by four metal dowels (the wires remained electrically isolated from the dowels), sandwiched in between two electrode grids that were grounded to the outside of the chamber by contact with the metal dowels. This chamber had ribbon cable feedthroughs, one of which was connected to the position board and read out through a special pre-amplifier designed to take signals from ribbon cables. Test were done near what had already been determined to be the optimal settings: +200 V on the anode (the position board) relative to ground (0 V), and P10 pressure around 200 Torr.

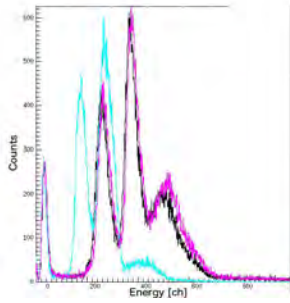


Figure 6: Anode set 1.

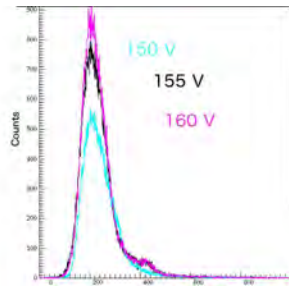


Figure 7: Anode set 2.

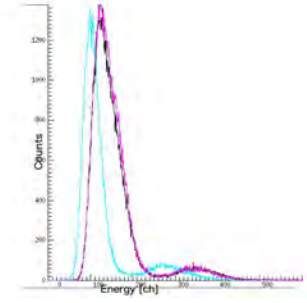


Figure 8: Anode set 3.

3 Results

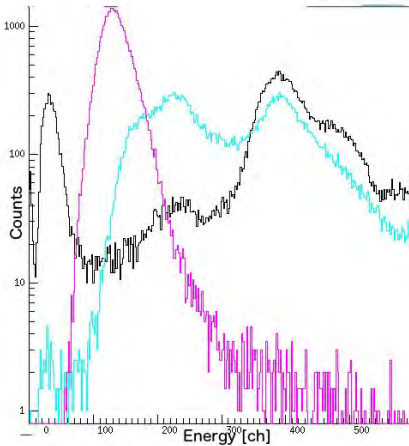
The first test resulted in the size of the detected signal not increasing above some critical bias voltage, which was determined to be around 155 V. This is the voltage at which the ion collection as a function of bias voltage begins to level off, signifying the beginning of the "ionization chamber region" (sometimes known as "complete collection") for gaseous ionization detectors.^[2] The sudden stagnation of gain indicates that almost all of the free electrons are being collected. Further increase in field strength into the "proportional" region would lead to avalanching, and the gain would increase proportionally with voltage. Figures 6-8 show each set of anodes at 150 V (blue), 155 V (black), and 160 V (pink), each at the same pressure. The plots are

1D histograms with energy [channels] on the horizontal axis and counts on the vertical axis. It is clear that there is very little change in the gain of the signal at voltages right around 155 V, which is consistent with where the ionization chamber region is expected to be.^[2] Also, the ideal pressure for the chamber seemed to be around 200 Torr. When the pressure was too low there was not enough gas being ionized, so the rate at which data was being acquired was not high enough; and when the pressure was too high some of the energy information was lost due to the high number of collisions with gas molecules lowering the mean free path of the electrons. This worsened the energy resolution at high pressures. The data from the three anode sets are plotted together in Figure 9.

Unfortunately, we were unable to get definitive results with the prototype position board. We only had a limited time to use the chamber we needed to per-

form the tests. There were grounding issues with the pre-amplifiers we were using and the ribbon cable connectors we had on hand. We were not able to see the α

Figure 9: Plot of all three anodes at optimal settings.



particles of interest due to persistent grounding issues. Also the wires used in the board were adopted from an older project, so some of them were kinked or had had the gold coating stripped off, both of which could have distorted the electric field in the active region of the chamber.

4 Conclusions

We have concluded that the design of our ionization chamber is feasible, and we know the best settings at which to operate it. It is planned to be built soon, and will be put to use in experiment shortly afterwards. In the future the real position boards will be wired with a standard tension and have thinner and straighter wires, the electrodes will be angled as previously described, and there will be a downstream scintillation counter

behind the electrodes. This setup should be ideal for a position-sensitive, high efficiency detector for high-current nuclear beams.

5 Acknowledgements

I would like to thank the entire staff of the Notre Dame REU program for providing me with this research opportunity. I would also like to thank the physicists and supporting staff of the Notre Dame NSL. I would also like to personally thank Dr. Dan Bardayan, Dr. Patrick O'Malley, Matthew Hall, and Shannon Massey for working with me and making my time at Notre Dame a fun and rewarding experience. Finally, I would like to thank the National Science Foundation for funding the REU program.

6 References

^[1]K. Y. Chae, et al., "Construction of a fast ionization chamber for high-rate particle identification," Nucl. Instrum. Meth. A. 751 (2014) 6-10.

^[2]W. R. Leo, *Techniques for Nuclear and Particle Physics Experiments*, (Springer Verlag, Berlin, Germany, 1987) pp. 120-148.

^[3]P. Colas, et al., "Electron drift velocity measurements at high electric fields," Elsevier Science (preprint) 27, March 2001.

High Purity Germanium Detectors and the
Angular Distribution of $^{27}\text{Al}(p,\gamma)^{28}\text{Si}$

André M. Wilson II

2014 NSF/REU Program

University of Notre Dame Department of Physics

Advisor: Ed Stech

Student Collaborators:

Bryant Vande Kolk, University of Notre Dame Graduate Student

Qian Liu, University of Notre Dame Graduate Student

Eleanor Dunling, University of Surrey Undergraduate Student

Abstract

The purpose of this research was to study high purity germanium detector systems, and to calculate and compare absorption ratios of $^{27}\text{Al}(p,\gamma)^{28}\text{Si}$. Work with the germanium detector online array for gamma ray spectroscopy in nuclear astrophysics in the Nuclear Science Laboratory at the University of Notre Dame, also known as Georgina, including energy calibrations and work with software and hardware logic, provided the necessary background information and experience with high purity germanium detectors and angular distribution of gamma rays. The knowledge taken from work with the Georgina detectors was then applied to the analysis of $^{27}\text{Al}(p,\gamma)^{28}\text{Si}$. Previous experimental data of $^{27}\text{Al}(p,\gamma)^{28}\text{Si}$ was analyzed using the 1778.9 gamma energy in the $E_p = 992$ keV resonance. The data used was taken from a 2010 experiment completed in the Nuclear Science Laboratory at the University of Notre Dame using the 4MV KN particle accelerator. A 1977 paper by A. Anttila and J. Keinonen with analysis of the same reaction using the $E_p = 992$ keV resonance was used for the energy calibration and gamma energies. Peak fitting and background reduction of the spectra were completed using analysis software, *jtek*. Angular distribution ratios from a ^{56}Co source were used for the normalization of the ^{27}Al data. Angular dependent absorption factors were used to analyze the angular distribution of γ -rays from the ^{27}Al beam target. With these absorption factors, relative γ -ray intensity measurements of $^{27}\text{Al}(p,\gamma)^{28}\text{Si}$ were calculated.

I. Introduction

In a nuclear reaction, protons are accelerated and collided with a target for a period of time. As a result, a yield of gamma rays are emitted in all directions. The goal of the experiment is to detect and study these scattered particles. As much as physicist wishes every particle can be detected, it is not possible, because the detector can only perceive the particles that interact with it. The detector is placed at a solid unmoving angle and a small fraction of the total gamma ray yield is detected. Angular distribution is the ratio of observed emissions at various angles of the detector. The angular distribution of particles must be know in order to calculate the total reaction yield from the number of observed emissions. The following research was centered

around finding the total gamma ray reaction yield of an $^{27}\text{Al}(p,\gamma)^{28}\text{Si}$ reaction using high purity germanium detectors (Rolfs 295).

Germanium detectors are P-I-N structured semi-conductor diodes with the intrinsic region sensitive to ionizing radiation, particularly x and gamma rays (Knoll). A PIN diode is a diode with a wide, lightly doped, intrinsic semiconductor region between p-type semiconductor and an n-type semiconductor regions. Unlike the typically heavily doped p-type and n-type regions, the lightly doped intrinsic region makes the PIN diode an inferior rectifier, but makes it suitable for high voltage electronics applications (Knoll).

Under reverse bias, an electric field extends across the intrinsic, or depleted, region. When protons interact with the material within a detector, charge carriers are produced and shifted into the P and N nodes by the electric field (Knoll).

The thickness of a detector's depletion region is dependent on the reverse bias voltage (V), and the net impurity concentration (N).

$$d = (2\epsilon V_0 / eN_a)^{.5}$$

At a given applied voltage, greater depletion depths can only be achieved by lowering the value of N through further reductions in the net impurity concentration (Knoll). To lower N, scientists seek refining techniques capable of reducing the impurity concentration. At 10^{10} atoms/cm³ in germanium, the equation predicts that the depletion depth of 10mm can be reached using a reverse bias voltage of less than 1000V. These germanium detectors are called High-Purity Germanium Detectors (HPGeD) with depletion levels nearing 10 mm (Knoll).

Germanium detectors are preferred for the analysis of complex gamma ray spectra because of their superior energy resolution. Because germanium has a relatively low band gap, the detectors must be cooled to liquid nitrogen temperatures to reduce the thermal generation of

charge carriers. If the detector gets too warm, leakage current induced noise will destroy the detector's energy resolution (Canberra). To prevent this, a liquid nitrogen cryostat is a critical component in germanium detector that ensures the detector's long term performance. The detector components are also placed under vacuum to protect the detector from moisture and condensable contaminants (Canberra).

The University of Notre Dame GERmanium detector Online aRray for Gamma ay spectroscopy In Nuclear Astrophysics, otherwise known as GEORGINA, is a specially designed array of five Canberra high purity germanium detectors. The system, located in the Nuclear Science Laboratory, is designed to measure g-transitions of about 10 MeV and a multiplicity of less than 5¹. Georgina's detectors fit closely around a beam line from Notre Dame's 5U particle

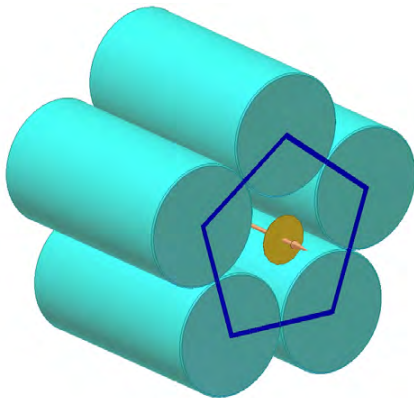


Figure 1: Sketch of GEORGINA detectors positioned around beam line

accelerator and have a dedicated 16-channel MPA-3 data acquisition system (Isnap). Georgina is unique because of the logic systems that allow coincidence measurements be taken. Like other HPGe detectors, Georgina has a charge sensitive preamplifier mounted directly to the detector. This converts the charge to a voltage pulse. The voltage pulse is sent to the timing filter amplifier that turns the slow pulse from the

preamplifier into a fast signal appropriate for a constant fraction discriminator. From there, the constant fraction discriminator establishes a threshold and removes pulses below that threshold from the signal. Hardware logic then opens up the opportunity for coincidence measurements.

¹ One of the detectors was missing due to a damaged dewar, so multiplicity during the summer of 2014 was limited to less than 4.

The last step for the signal is the analog-to-digital converter that allows all of these data signals to be seen on the computer for analysis.

There were two main purposes in the research. The first included calibrating the Georgina detectors and calculating energy efficiencies for the array. These very same detectors were to be used in an experiment centered on finding the angular distribution of gamma rays emitted from a proton beam incident on an ^{27}Al beam target. This experiment was already conducted in 2010 and the data had been left unanalyzed and smaller detectors were used at farther distances from the target to get the angular information. This information would have helped to better understand the data that could have been collected from the close geometry of Georgina. The benefit of the large Georgina detectors in close geometry is covering a larger solid angle. The downside is that the data analysis is a more complicated process because of increased summing effects and the coverage of a wide range of angles. Unfortunately, because of issues with the 5U particle accelerator, beam could not be delivered for the experiment. Therefore, the focus fell on analyzing the angular distribution data without its interaction with Georgina.

II. Experimental Procedure

Experimental procedure occurred in several stages. Initially, the Georgina array was to be used to observe an $^{27}\text{Al}(p,\gamma)^{28}\text{Si}$ reaction. In preparation for this experiment, Georgina's inaugural run, the detectors' energy calibration and detection efficiency had to be calculated. To find the detector efficiency, the spectra from ^{60}Co , ^{137}Cs , and ^{22}Na sources were first acquired. A mount for the sources was created so that each source could be placed at a fixed position 3cm from the detectors. After finding the number of gammas detected from the sources, the current activities

of the sources were found using the exponential decay law. The energy efficiencies were calculated using the equation

$$\epsilon = N_D/AT$$

where ϵ is efficiency, N_D is the number of gammas detected, A is current activity, and T is time of the run.

The original goal was to conduct an experiment using an $^{27}\text{Al}(p,\gamma)^{28}\text{Si}$ reaction. Due to issues with the 5U particle accelerator, the goal shifted to data analysis. The data was taken in a 2010 experiment in the Nuclear Science Laboratory at Notre Dame using the 4MV KN particle accelerator. In the experiment, ten runs were completed using a proton beam and an ^{27}Al target.

Each experimental run corresponded to a different angle of the germanium detector with angles $\theta = 0, 15, 30, 45, 60, 75, 89, 110, 120,$ and 130° as shown in Figure 2. Experimenters used 15° intervals because it results in equidistant data points. The target was placed 10 inches from the detectors to reduce the likelihood of

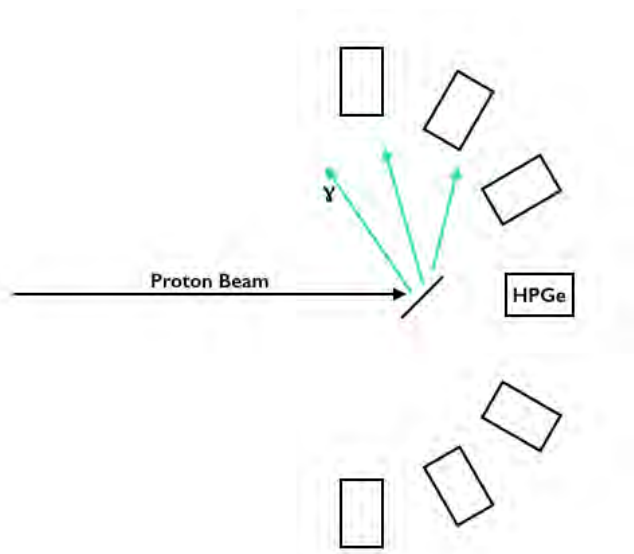


Figure 2: Angular distribution experimental setup

energy summing. The experiment also

included angular distribution measurements at the same angles as well as 55° with a ^{56}Co source.

The source was placed 10 inches away from the detectors just as the ^{27}Al beam target was in the subsequent runs. The ^{56}Co source data was analyzed and the angular distribution correction factors normalized to 55° were provided in the data. Using the data taken in this 2010

experiment, the goal was to look at the first excited state in ^{28}Si in the $^{27}\text{Al}(p,\gamma)^{28}\text{Si}$ reaction and calculate absorption ratios and compare the relative gamma ray intensity at each angular position of the germanium detector.

The gamma energies in the $E_p = 992$ keV resonance were analyzed using *jtek*. The software, developed by Joacchim Goerres at Notre Dame, includes programing that allows the user to fit background noise from a spectrum before fitting the peak at a particular gamma energy, thereby making data fits more accurate. This feature made *jtek* a valuable tool during the analysis of the $^{27}\text{Al}(p,\gamma)^{28}\text{Si}$ spectra. A 1977 paper by A. Anttila and J. Keinonan provided the peaks of interest for the spectral analysis. The energy calibration also made it simpler to account for doppler shift in the spectra. Using *jtek*, the peaks, along with their likely escape peaks, were isolated from surrounding background counts and fitted. Both of these fits comprised the total number of counts recorded for each gamma energy. Including the escape peaks in the total count rates was significant because escape peaks often comprise upwards of 50% of the total number of counts at higher energies.

After analyzing the spectra using *jtek* and calculating the total number of counts for the gamma energies emitted from the decay of the resonance, the data was then normalized with charge of the beam used in that particular run. The angular distribution factors calculated from the ^{56}Co source and normalized to the 55° angle were also used to normalize the $^{27}\text{Al}(p,\gamma)^{28}\text{Si}$ data. After normalization with charge and ^{56}Co absorption factors, the ^{27}Al data was normalized once more using the data from the 45° run. This was done because the beamspot is significantly larger than the source so that it impacts the effective angles of the detector and the ^{27}Al data did not include a 55° detector angle and that angle is optimal because observations show that 55° between the beam and detector minimizes angular distribution at 0° . Normalizing to 45° was the

closest angle to 55° available in the ^{27}Al data. All of these normalizations provided the relative efficiency of the detectors' angular position for each peak in the ^{27}Al spectrum.

III. Measurements & Results

The energy efficiencies of the Georgina detectors and a plot of the change in efficiency with the change in energy per detector are displayed in Figure 3 and Figure 4. After the normalizations were completed, plots of relative efficiency vs. angle were created for each gamma energy. The 1778.9, 2838.9, 4497.6, and 4743 keV graphs are shown below along with a plot of both ^{56}Co and ^{27}Al angular distribution correction factors.

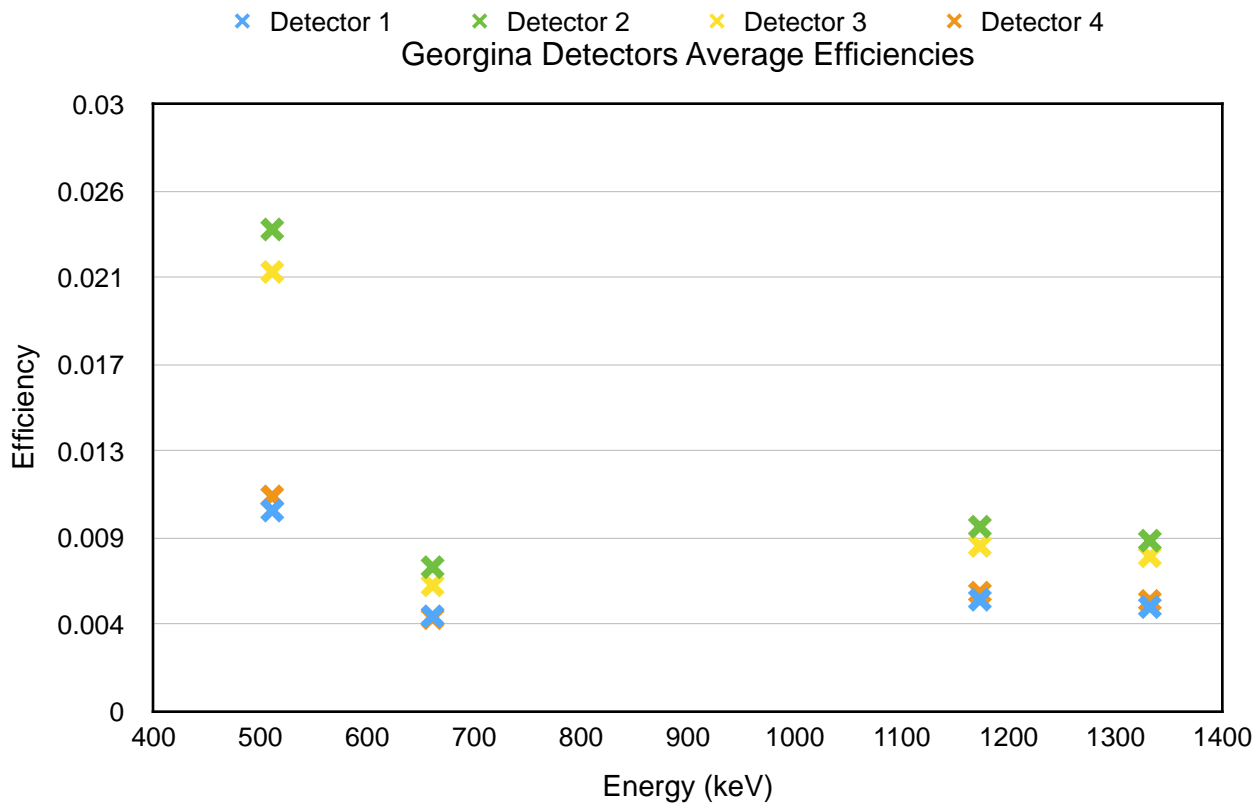


Figure 3: Georgina detector efficiencies

Source	Energy (keV)	Detector 1	Detector 2	Detector 3	Detector 4
60	1332	0.00513	0.00841	0.00764	0.00543
60	1173	0.00549	0.00910	0.00815	0.00584
137	661	0.00467	0.0071	0.0062	0.00458
22	511	0.0099	0.0238	0.0217	0.0106

Figure 4: Georgina detector efficiencies

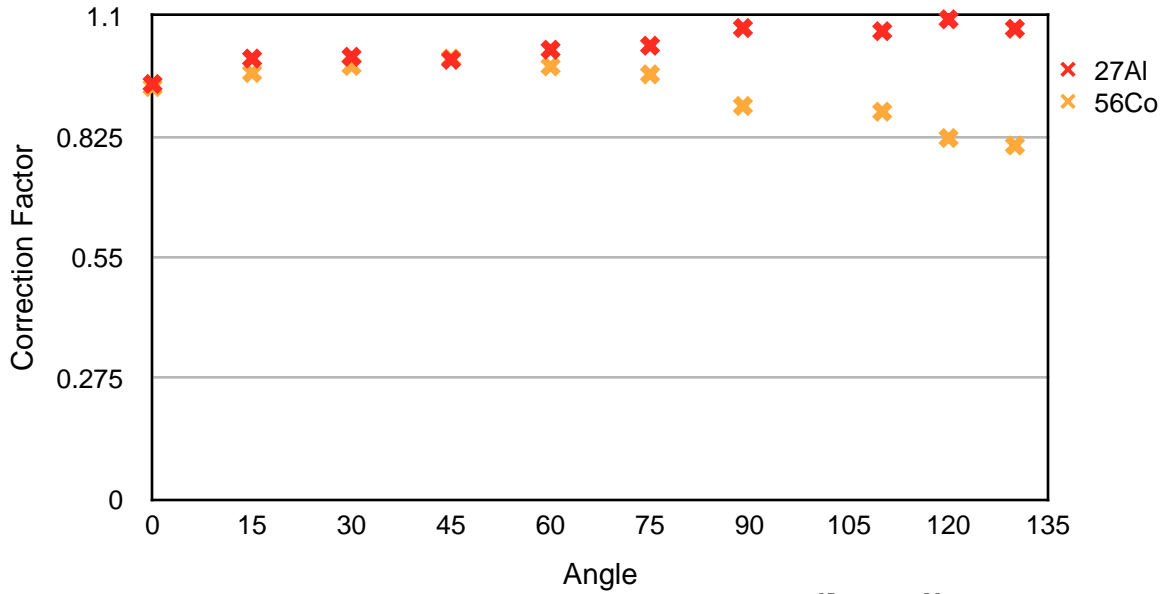


Figure 5: Graph of angular correction factors for ²⁷Al and ⁵⁶Co

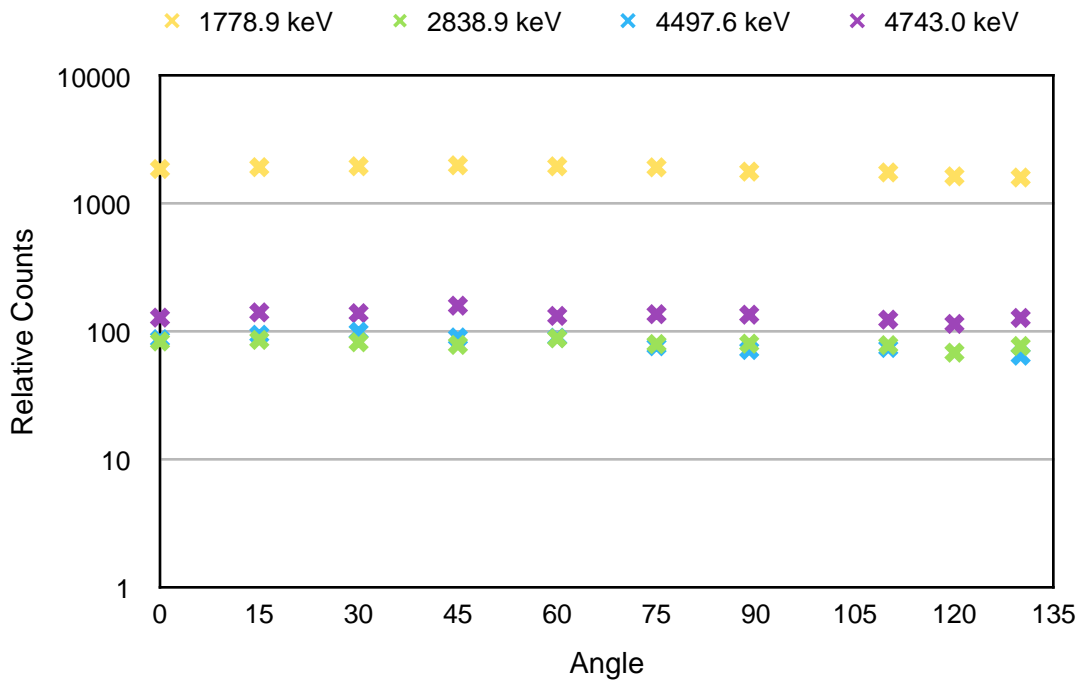


Figure 6: Graph of relative counts of energies over various angles

IV. Discussion & Conclusions

That data shown above represents the angular distribution calculations for the $^{27}\text{Al}(p,\gamma)^{28}\text{Si}$ reaction. It is interesting to note that the correction factors of ^{27}Al and ^{56}Co align until the 75° detector angle. After that point, the ^{27}Al correction factors begin to climb while the ^{56}Co factors begin to drop. The efficiencies of Georgina detectors 2 and 3 were consistently higher than the efficiencies of detectors 1 and 4. This is particularly unusual because all four detectors are identical and the mount designed allowed the source to be accurately placed in the center of the array. As expected, the number of relative counts of gamma rays at the 1778 keV was significantly higher than the counts at any other energy.

Unfortunately, the work was constrained by a short ten week time span. Work with this data and experiment will be continued and conducted by researchers at in the Nuclear Science Laboratory in the future. Moving forward, the values calculated using *jtek* will be compared to the values that were expected. Using the angular distribution ratios and number of observed emissions, the total reaction yield will be calculated. Upward efficiencies will also be studied in future work with the $^{27}\text{Al}(p,\gamma)^{28}\text{Si}$ reaction. It is also possible that the experiment can be run with the 5U particle accelerator and see how the calculated angular efficiency and gamma ray yield translates to the wide angle of the Georgina array.

References

- Anttila, A., J. Keinonan, M. Hautala and I. Forsblom, Nucl. Instr. and Meth. 147 (1977) 501
- Rolfs, C. and W. Rodney. Cauldrons in the Cosmos. Chicago: The University of Chicago Press, 1988. Print.
- Knoll, G. Radiation Detection and Measurement. New York: Wiley, 1979. Print.
- "High-purity Germanium (HPGe) Detectors ." . Canberra, 1 Jan. 2014. Web. 1 Aug. 2014. <<http://www.canberra.com/products/detectors/germanium-detectors.asp>>.
- "Georgina." Isnap, 28 Jun, 2012. Web. 1 Aug. 2014. <http://isnap.nd.edu/html/research_georgina.html>.